Supported Pd and Pd/Alloy Membranes for Water-Gas Shift Catalytic Membrane Reactors

by

Alexander Sullivan Augustine

A PhD Thesis

Submitted to the faculty of the

Worcester Polytechnic Institute

In partial fulfillment of the requirement for the

Degree of Doctor of Philosophy

In Chemical Engineering

by

_____

February 2013

APPROVED

Professor Yi Hua Ma, Advisor	**Professor Nikolaos K. Kazantzis, Advisor**
Professor Robert W. Thompson, PhD Committee	**Professor Richard D. Sisson, PhD Committee**

ACKNOWLEDGEMENTS

I would like first and foremost to thank Professor Yi Hua Ma (James H. Manning Professor) for his profound patience in me. When I first began my PhD in September 2007, I was a very stubborn person, and it is only through Professor Yi Hua Ma's perseverance and guidance that I have reached where I am today. Only recently have I even remotely come close to fully appreciating all of the effort that Professor Yi Hua Ma has invested in mentoring me, and for this I will forever be indebted to him.

Over the past six years Professor Yi Hua Ma has served as an exemplary teacher, leader, and mentor to all who have worked under him. He has diligently encouraged those in his lab to become more thorough investigators and more confident scientists. Under his tutelage I was able to publish several research articles and present at several scientific conferences. Professor Yi Hua Ma allowed considerable freedom of research to those working under him such that I have become a more independent thinker. In addition, he successfully procured funding such that those of us working under him were able to fully devote ourselves to research. Professor Yi Hua Ma's open door policy enabled all of us to receive input and guidance regarding the direction of our work, greatly facilitating all of our efforts.

Next, I would like to thank my co-advisor Professor Nikolaos K. Kazantzis for his instrumental mentorship over the past six years. Professor Nikolaos K. Kazantzis' meticulous feedback and guidance have been critical to the peer-reviewed papers and presentations I have completed over the years. Additionally, Professor Nikolaos K. Kazantzis taught an exceptional course titled "Mathematical Analysis in Chemical Engineering", which was an inspiration to me during my early graduate years at WPI.

In addition to my two advisors, I would also like to thank my PhD committee members, Professor Robert W. Thompson and Professor Richard D. Sisson for their valuable advice over the course of my research and in the shaping of my thesis. It is no small task to review and judge the quality of a PhD candidate and I am so thankful that they have accepted this responsibility. I would lastly like to thank Professor Robert W.

Thompson for teaching an exceptional course, “Chemical Reactor Design”, which was been greatly beneficial to my graduate studies.

Worcester Polytechnic Institute has been an exceptional place to spend my six years of graduate studies. Throughout that time I have met many distinguished professors and students who have conveyed to me a great love of learning. I cannot imagine a better environment to foster the development of a PhD student as this one. Thank you to all those who have made WPI what it is today.

I would like to thank my co-workers in the lab: Dr. Ivan Mardilovich, Dr. M. Engin Ayturk, Dr. Federico Guazzone, and Dr. Jacopo Catalano. They have each, upon many occasions, listened to my ramblings and aided me in brainstorming solutions to the problems discussed in this thesis. Both Ivan and Engin have, on several occasions, guided me through membrane syntheses and contributed membranes to the work reported here. Both Federico and Jacopo have, on several occasions, proofread my drafts and made pertinent suggestions regarding my conference presentations.

I would next like to thank my peers, all of whom have now graduated: Dr. Rajkumar Bhandari, Dr. Natalie Pomerantz, Dr. Mike Chen, and Dr. Reyyan Koc. I have fond memories (both in lab and outside) with each of them and hope that I may see and work with them again.

During my PhD I have authored two peer reviewed articles (“High pressure palladium membrane reactor for the high temperature water-gas shift reaction”, *International Journal of Hydrogen Energy* and “Durability of PSS-supported Pd-membranes under mixed gas and water-gas shift conditions” *Journal of Membrane Science*). I would like to highlight and thank all the authors on those papers for their help and contributions: Professor Yi Hua Ma, Professor Nikolaos K. Kazantzis, and Dr. Ivan Mardilovich.

There are numerous people in the Department of Chemical Engineering to whom I owe gratitude. I would like to thank Giac Ferraro for help fabricating experimental components on many occasions. I would like to thank Doug White for help constructing electrical components of our test systems. I am greatly indebted to Paula Moravek and Rebecca Evanoff, without whom I don’t know that anything ordered would ever arrive. I

have also greatly appreciated Felicia Vidito and Tiffany Royal for coping with my goofiness and allowing me to accumulate massive amounts of department coffee in my desk.

The work conducted here would also not have been possible without the financial support of the U.S. Department of Energy. I am greatly appreciative to Technology Manager Dr. Daniel Driscoll and Project Manager Mr. Jason Hissam for overseeing our work in the projects titled “Composite Pd and Pd Alloy Porous Stainless Steel Membranes for Hydrogen Production and Process Intensification” (Award Number: DE-FC26-07NT43058) and “Engineering Design of Advanced H_2 – CO_2 Pd and Pd/Alloy Composite Membrane Separations and Process Intensification” (Award Number: DE-FE0004895).

Lastly I would like to thank my wife Christina Liu and my parents Sullivan and Linda Augustine for their loving support over the course of my research. Without their encouragement I would not have had the confidence and strength to complete this work.

ABSTRACT

This work describes the application of porous metal supported Pd-membranes to the water-gas shift catalytic membrane reactor in the context of its potential application to the Integrated Gasification Combined Cycle (IGCC) process. The objective of this work was to develop a better understanding of Pd-membrane fabrication techniques, water-gas shift catalytic membrane reactor operation, and long-term behavior of the Pd-membranes under water-gas shift conditions.

Thin (1.5 – 16 μm) Pd-membranes were prepared by electroless deposition techniques on porous metal supports by previously developed methods. Pd-membranes were installed into stainless steel modules and utilized for mixed gas separation (H_2/inert, H_2/H_2O, dry syngas, and wet syngas) at 350 – 450°C and 14.5 atma to investigate boundary layer mass transfer resistance and surface inhibition. Pd-membranes were also installed into stainless steel modules with iron-chrome oxide catalyst and tested under water-gas shift conditions to investigate membrane reactor operation in the high pressure (5.0 - 14.6 atma) and high temperature (300 – 500°C) regime. After the establishment of appropriate operating conditions, long-term testing was conducted to determine the membrane stability through He leak growth analysis and characterization by SEM and XRD. Pd and Pd/Au-alloy membranes were also investigated for their tolerance to 1 – 20 ppmv of H_2S in syngas over extended periods at 400°C and 14.0 atma.

Water-gas shift catalytic membrane reactor operating parameters were investigated with a focus on high pressure conditions such that high H_2 recovery was possible without a sweep gas. With regard to the feed composition, it was desirable to operate at a low H_2O/CO ratio for higher H_2 recovery, but restrained by the potential for coke formation on the membrane surface, which occurred at a H_2O/CO ratio lower than 2.6 at 400°C. The application of the Pd-membranes resulted in high CO conversion and H_2 recovery for the high temperature (400 – 500°C) water-gas shift reaction which then enabled high throughput. Operating at high temperature also resulted in higher membrane permeance and less Pd-surface inhibition by CO and H_2O.

The water-gas shift catalytic membrane reactor was capable of stable CO conversion and H_2 recovery (96% and 88% respectively) at 400℃ over 900 hours of reaction testing, and 2,500 hours of overall testing of the Pd-membrane. When 2 ppmv H_2S was introduced into the membrane reactor, a stable CO conversion of 96% and H_2 recovery of 78% were observed over 230 hours. Furthermore, a $Pd_{90}Au_{10}$-membrane was effective for mixed gas separation with up to 20 ppmv H_2S present, achieving a stable H_2 flux of 7.8 m^3/m^2-h with a moderate H_2 recovery of 44%. The long-term stability under high pressure reaction conditions represents a breakthrough in Pd-membrane utilization.

EXECUTIVE SUMMARY

The results and discussion presented in this thesis pertain to the application of Pd and Pd-alloy membranes to the separation of hydrogen from syngas and to the water-gas shift catalytic membrane reactor. Several gaps still exist in the relevant literature regarding Pd-membrane fabrication techniques, water-gas shift catalytic membrane reactor operation, irreversible poisoning by coking, irreversible poisoning by H_2S, and long-term membrane leak development under WGS conditions. The work presented here aims to develop a better understanding of these issues.

Lab-scale Pd-membranes (25 cm^2) were prepared by electroless deposition of 1.5 – 16 μm of palladium onto α-alumina graded porous stainless steel supports by previously developed methods. These membranes were initially tested in pure H_2 for up to 1,000 hours and exhibited stable H_2 permeance as high as 61.7 m^3/m^2-h-$atm^{0.5}$ at 400°C, with stable H_2/He selectivity as high as 75,000. A $Pd_{90}Au_{10}$-membrane was also prepared by a previously developed method and had a H_2 permeance of 38.0 m^3/m^2-h-$atm^{0.5}$ at 400°C with a stable H_2/He selectivity of 25,000. The method of membrane fabrication which was comprised of sequential grading of large (greater than 10 μm) to small (0.02 μm) α-alumina particles proved reproducible, assuming good support quality, potentially justifying pilot scale production.

After initial testing, membranes were utilized to separate H_2/inert, H_2/H_2O, dry syngas, and wet syngas mixtures at 350 – 450°C and 14.5 atma. H_2 fluxes as high as 47.0, 19.4, 33.1, and 14.2 m^3/m^2-h were achieved with each mixture respectively at 400°C. At low feed flow rates of less than 1.2 L/min, H_2 recovery of 90% was achieved for all gas mixtures. It was demonstrated that reversible adsorption by the water-gas species CO and H_2O significantly inhibited the H_2 permeance of the Pd-membrane below 400°C, but had little effect at higher temperatures. Gas boundary layer resistance was found to be significant over the entire range of feed rates utilized (up to 9 L/min).

Pd-membranes were loaded into the water-gas shift catalytic membrane reactor with iron-chrome oxide catalyst and tested under water-gas shift conditions (CO + H_2O and simulated syngas mixtures fed at 0.23 - 1.2 L/min, 300 – 500°C, and 4.4 – 14.6 atma).

The reactor operation was characterized with respect to the feed composition, feed flow rate, system pressure, and temperature. CO conversion and H_2 recovery as high as 98% and 88% respectively were achieved at 450°C and 14.4 atma. The removal of H_2 by the membrane resulted in an increased CO conversion, which was greater than that achieved by a packed bed reactor, due to Le Chatelier's principle. Increasing H_2O in the feed resulted in increased CO conversion due to the equilibrium nature of the reaction, but also decreased H_2 recovery due to the dilution of H_2 in the reaction mixture. Increasing the feed flow rate resulted in a lower CO conversion and H_2 recovery due to lower residence time, but a higher net flux of H_2. Increasing the system pressure resulted in a significant gain in H_2 flux and recovery by both raising the residence time and increasing the driving force for H_2 flux. The equilibrium CO conversion, which was pressure invariant in the packed bed case, was significantly pressure dependent in the membrane reactor due to the increased H_2 recovery associated with higher pressure. Notably, the high reaction pressure utilized in this study distinguished it from the previous literature. A maximum in CO conversion with respect to temperature was observed at approximately 450°C due to the interplay between the membrane permeance (which was covariant with temperature) and the equilibrium constant (which was contravariant with temperature). A better understanding of membrane reactor performance was developed which was paramount to its effective incorporation into the IGCC process.

Coke formation was found to be problematic in the water-gas shift catalytic membrane reactor for steam to carbon ratios of less than 2.6. The rate of coke formation was highly erratic and was perhaps catalyzed by the contact between the iron-chrome catalyst particles and the Pd-surface. The development of a better analysis framework for coke formation was important as a restraint upon operating conditions for the membrane reactor.

Pd and Pd/Au-membranes were utilized to separate shifted syngas (enriched in H_2 and depleted in CO) containing 1 – 20 ppmv H_2S at 400°C and 14.0 atma. For the pure Pd-membrane, a H_2 flux of 12.3 m^3/m^2-h with a H_2 recovery of 76% was achieved with 2.5 ppmv H_2S in the feed. For the Pd/Au-membrane, a H_2 flux of 7.8 m^3/m^2-h with a H_2

recovery of 44% was achieved with 20 ppmv H_2S in the feed. The Pd/Au-membrane had no clear advantage over the pure Pd-membrane when exposed to 1 - 2.5 ppmv H_2S. Pd_4S was observed slightly on both membranes, but to a lesser extent than what was previously observed in the literature, indicating some interaction of the water-gas shift species with H_2S.

After operating conditions were refined, membranes were tested for extended periods of time (65 – 1,000 hours) under mixed gas and water-gas shift reaction conditions. Several of the membranes exhibited stable H_2 permeance and gradual He permeance growth (as low as $1.0*10^{-7}$ m^3/m^2-h^2-atm) which was in agreement with pure H_2 testing. Experiments with H_2/H_2O mixtures indicated that H_2O did not adversely affect the membrane selectivity. Long-term testing under WGS conditions also indicated that CO and CO_2 did not increase the leak growth rate or decrease the H_2 permeance of the membranes. The gradual leak growth observed under WGS conditions agreed with the pinhole formation mechanism. Moreover, due to the stable membrane behavior, stable CO conversion and H_2 recovery of 96% and 88% respectively were achieved for over 900 hours for the water-gas shift catalytic membrane reactor. Given the low leak growth rates observed in several membranes tested under reaction conditions, a membrane lifetime of greater than 10 years was projected to be possible.

Lastly, a pure Pd-membrane was tested under water-gas shift conditions with 2 ppmv H_2S present and achieved a stable CO conversion and H_2 recovery of 96% and 78% respectively for 230 hours. The final H_2/He selectivity of the membrane remained above 2,500. No Pd_4S was detected on the membrane surface indicating that the presence of the WGS species increased the H_2S threshold for irreversible poisoning. The understanding of H_2S tolerance by Pd-membranes was also directly relevant to their commercial application since there is a high cost associated with H_2S removal.

The successful application of the porous stainless steel supported Pd-membranes to the water-gas shift catalytic membrane reactor represents a significant potential process intensification for the IGCC process. Over the coming decades the IGCC process incorporating Pd-membranes may prove to be a pivotal stepping stone in efficient energy production.

TABLE OF CONTENTS

LIST OF FIGURES

LIST OF TABLES

1. INTRODUCTION

Fossil fuels currently account for approximately 86% of the total energy consumed in the United States each year in terms of electricity, heating, and transportation, all of which are ubiquitous in our everyday lives (US EIA, 2008). In the United States the current electricity consumption is approximately $1.5x10^{16}$ BTU and will continue to increase over the next 20 years as hybrid and electric vehicles become increasingly adopted (Obama, 2011). Currently, approximately 50% of electricity consumption is met by coal combustion and an additional 19% is met by natural gas combustion (US EIA, 2008). These two fuels are paramount due to their low cost and nearly inexhaustible supply.

Unfortunately, the use of fossil fuel produces a significant amount of CO_2, over 21 billion tons per year, which has potentially begun to result in global climate change (Keeling *et al.,* 2009). Due to concerns over climate change, CO_2 emission has come under increasing regulations in Europe, and more recently in the United States. Renewable technologies such as wind, solar, and biomass, which could potentially replace coal as a major electricity provider, are still in their infancy. Nuclear power, which is well developed and cost effective on a large scale, suffers from increasing safety concerns, preventing its further proliferation. Based on this potential energy bottleneck, it is prudent to develop efficient means by which energy from coal and natural gas could still be utilized but without the emission of CO_2.

A midterm (20 – 40 years) solution to this problem is the potential sequestration of CO_2 underground. It has been demonstrated that relatively pure CO_2 can be sequestered in some geologic formations with relatively low compression cost (Shukla *et al.,* 2010). The energy sub-sector to which CO_2 sequestration could be best applied is coal based power plants. Coal based (and natural gas based) power plants are built on an economy of scale at which CO_2 processing and storage is feasible, with costs of approximately 13% overall process efficiency (Li *et al.,* 2008a). While that cost is high, CO_2 capture from other fossil fuel use such as homes and/or vehicles is completely unrealistic. Depending on the stringency of the CO_2 regulation, home heating and

transportation may be forced to move in the direction of electricity and/or hydrogen as the energy transport medium, further increasing the demand for coal based gasification and power plants.

The most advanced coal-fired power plants with 90% CO_2 capture by Acid Gas Removal (AGR) have a limiting efficiency of approximately 36% (Li *et al.,* 2008a). The Integrated Gasification Combined Cycle (IGCC) plant, a relatively young technology, has already demonstrated an efficiency of 35% with 90% CO_2 capture by AGR. In contrast to a coal-fired power plant, an IGCC plant can separate out most of the carbon as CO_2 in an intermediate step at significant cost savings over a post-combustion separation. If IGCC plants can be modified with membranes capable of separating H_2, either incorporated into, or immediately following the Water-Gas Shift (WGS, equation **1.1**) reaction step, the overall efficiency can be as high as 43% (Bracht *et al.,* 1997). This technology has the added bonus of producing high purity H_2, which can either be sold directly or burned on-site for electricity generation depending on market demand (Koc, 2012).

$$\mathbf{CO + H_2O \underset{catalyst}{\longleftrightarrow} H_2 + CO_2} \qquad \mathbf{1.1}$$

In the IGCC, coal/water slurry is burned with a minimal quantity of O_2 enriched air to generate syngas (H_2, CO, and CO_2). The syngas is cleaned of mercury and sulfur, and then put through the WGS reaction (equation **1.1**) in two steps: high temperature (300 - 400℃) for high through-put, then low temperature (200 - 250℃) for increased equilibrium CO conversion. The CO_2 in the effluent stream can then be separated by AGR for sequestration. The remaining gas is composed primarily of H_2 and can be burned in a gas turbine or a fuel cell to generate electricity, or used in a chemical process. Using a WGS Catalytic Membrane Reactor (CMR) to replace the high-temperature shift, the low temperature shift, and the AGR steps of the IGCC has the potential to increase the overall process efficiency by a significant amount (Bracht *et al.*, 1997). If only the AGR step of the process is replaced by a Pd-membrane separator, the overall efficiency could be increased by up to 2.9% (Gray *et al.,* 2009).

The ability of palladium membranes to separate hydrogen from gas mixtures has been well-known and studied for over a century. In recent years, Porous Stainless Steel (PSS) supported Pd-membranes have been prepared as thin as 8 μm (Mardilovich *et al.,* 2006). These membranes have both high H_2 permeance (68.5 $m^3/m^2h*atm^{0.5}$ at 500°C) and high selectivity (greater than 140) over testing periods of up to 1,400 hours. The mechanical strength provided by the PSS supports is also greatly desirable for industrial applications. The application of Pd-membranes to H_2 producing, equilibrium limited reactions has been highlighted in the literature because of the potential for process intensification and to drive the reaction conversion beyond the traditional equilibrium via the *in situ* removal of the product H_2 (Shu *et al.,* 1991). WGS CMR experiments with thin Pd-membranes have thus demonstrated CO conversion in significant excess of the thermodynamic equilibrium conversion (Basile *et al.,* 1996a; 1996b; 2001; Damle *et al.,* 2008; Iyoha *et al.,* 2007a; Uemiya *et al.,* 1991a).

Despite the apparent viability of PSS supported Pd-membranes to the WGS step of the IGCC process, several obstacles still exist. Cost effective membrane fabrication has not yet been extensively demonstrated. H_2 separation from syngas and from the WGS CMR at high pressure (greater than 10 atma) has not yet been thoroughly investigated. Poisoning phenomenon (by H_2S and coke) on the Pd-surface from syngas mixtures are not yet fully understood. Lastly, few long-term stability studies have been conducted with Pd-membranes under syngas separation conditions or in the WGS CMR, making life-time estimation difficult.

The application of Pd-membranes to the IGCC process is dependent on the development of a simple and reproducible fabrication method that is at least somewhat independent of the support quality. There is a wide variance in PSS support costs, with highly uniform supports costing up to five times more than the lowest cost alternative. Unfortunately, no studies have yet demonstrated reproducible fabrication techniques that could be applied to the lower cost supports. Better fabrication methodology is necessary before investment in a pilot scale operation can be considered.

The separation effectiveness of the Pd-membrane may be impaired by several effects: mass transfer resistance in the dense Pd-layer, gas phase mass transfer resistance,

reversible surface inhibition by adsorbed species, and irreversible surface inhibition due to surface reactions (Catalano *et al.,* 2009; 2010; 2011; Li *et al.,* 2000; 2007b; Gallucci *et al.,* 2007). Depending on the membrane characteristics as well as the feed conditions, any one of the above effects can serve to significantly limit the percentage of separated H_2 and/or the rate of the separation. A better understanding of the H_2 separation at high pressures and under the above limitations is necessary before a pilot scale design could be proposed.

Considering the WGS CMR, little work exists in the literature studying the high pressure, high temperature operating regime. Indeed, the majority of literature studies have utilized a sweep gas (of up to 100 times the feed flow rate) to establish a driving force for H_2 across the membrane, which would be counter-productive for high-purity H_2 production. The use of a high reaction pressure can allow for H_2 recovery above 90% without a sweep gas and with high through-put (Damle *et al.,* 2008). A better understanding of the relationship between feed conditions and reactor operation in the high pressure regime is necessary so that optimal operating parameters can be determined.

While coke formation has not typically been a concern in the WGS system (Newsome, 1980), coke formation can be a significant problem in the WGS Pd-CMR. First, a low H_2O/CO ratio is preferred for high H_2 recovery and secondly, the Pd-surface most likely has some catalytic propensity for coke formation (Li *et al.,* 2007b; 2008b). The coke formation in the WGS Pd-CMR has the potential to block active H_2 adsorption sites on the Pd-surface over time, limiting the long-term efficacy of the reactor. Additionally, several studies have suggested that carbon may dissolve in the Pd-lattice to some extent, causing increased strain and therefore leak growth in Pd-membranes (Selman *et al.,* 1970; Li *et al.,* 2007b). A better understanding of the coke formation thermodynamics and kinetics in the WGS CMR is important as a constraint upon the possible system design and operating conditions.

For a Pd-membrane to be utilized in the IGCC process, at least a small degree of tolerance to H_2S is necessary. The exit stream from the coal gasifier typically contains 0.7 mol% of H_2S, which can then be reduced down to 15 ppmv at a reasonable cost by

the Selexol AGR process (Klara *et al.,* 2007; Korens *et al.,* 2002). It is known in the literature that pure Pd-membranes cannot tolerate 15 ppmv of H_2S in pure H_2 over the temperature range of 300 – 500°C, but that Pd/Au and Pd/Cu-membranes can. Still undocumented in the literature is the effect that other reversibly adsorbed gases (such as CO and H_2O) will have on H_2S poisoning of pure Pd, Pd/Au, and Pd/Cu membranes. It is possible that competitive adsorption of the CO and H_2O will prevent some poisoning by H_2S. Additionally, reactions between the H_2S, CO, and H_2O may either prevent or promote irreversible poisoning of the Pd-surface. A better understanding of H_2S poisoning phenomena is essential to establishing the required level of sulfur removal for the IGCC process incorporating a Pd or Pd/alloy-membrane.

Lastly, a key performance requirement for PSS supported Pd-membranes to be applied in a commercial setting is long-term permeance and selectivity stability. Relatively few studies have unambiguously demonstrated robust Pd-membrane stability over periods on the order of 1,000 hours. Furthermore, no long-term WGS CMR experiments have been conducted in the literature to demonstrate the stability of PSS supported Pd-membranes under reaction conditions. Through better characterization of leak growth mechanisms under high-pressure syngas and WGS reaction conditions, a better life-time estimation could be achieved such that the economic case for supported Pd-membrane commercialization can be made.

The overall aim of this thesis is to develop a better fundamental understanding of the operating principles and impediments which are relevant to the application of the WGS CMR to the IGCC process. The development of this understanding will aid in solving the engineering problem of how to best utilize the WGS CMR in a commercial setting. The specific objectives supporting this goal are as follows:

(1) Develop a better understanding of synthesis methodology which allows for the production of highly permeable, robust, and reproducible membranes.

(2) Understand the membrane separation effects which limit H_2 flux and recovery: mass-transfer resistance of the Pd-layer, gas phase mass transfer resistance, reversible inhibition, and irreversible inhibition by surface species.

(3) Understand the operation of the WGS CMR incorporating a PSS supported Pd-membrane in terms of H_2O/CO ratio, temperature, pressure, and feed flow rate. A focus was made on high pressure to more closely align with industrial conditions.

(4) Understand the kinetic and thermodynamic factors which result in coke formation in the WGS CMR system such that coke formation can be avoided.

(5) Understand the effect that reversibly adsorbed gas species (such as CO and H_2O) might have on the H_2S poisoning of Pd and Pd/Au-membranes under mixed gas and WGS conditions.

(6) Understand and characterize leak growth mechanisms which may occur under mixed gas and WGS conditions, but otherwise may not be present during pure H_2 and inert gas testing.

2. LITERATURE REVIEW

2.1. The water-gas shift (WGS) reaction

The reaction of carbon monoxide and steam, commonly known as the Water-Gas Shift (WGS) reaction yields hydrogen and carbon dioxide as in equation **2.1**.

$$\mathbf{CO + H_2O \rightarrow CO_2 + H_2} \qquad \mathbf{2.1}$$

Town-gas or water-gas, referring to a gas mixture of carbon monoxide and hydrogen, was first named for being the product of steam reforming of coke by the reaction given in equation **2.2**. This gas was first distributed in England in 1828 for gas heating and lighting (Singer, 1954). The use of water-gas in this way was continued in many cities and towns around the world up to the 1970's.

$$\mathbf{C(s) + H_2O \rightarrow CO + H_2} \qquad \mathbf{2.2}$$

The use of the WGS reaction for the industrial production of hydrogen first began in the United States in 1870 in a process invented by Thaddeus Lowe (Christain and Boyd, 1949), steam reforming of coke followed by the WGS. The WGS reaction is still used industrially for the production of hydrogen from natural gas, coal, and biomass.

The WGS reaction is reversible and weakly exothermic with a reaction enthalpy of -40.6 kJ/mol. The reaction also has a negative Gibbs free energy and therefore occurs less preferentially at higher temperatures. The equilibrium constant is below unity at temperatures above 800℃ and does not exceed 20 until the temperature is below 350℃. A good approximation of the equilibrium constant is given by equation **2.3** (Moe, 1962). A highly accurate expression for the equilibrium constant was derived by Bisset (1977) and can be found in Appendix A.1.

$$\boldsymbol{K = e^{\frac{4577.8}{T} - 4.33}} \qquad \mathbf{2.3}$$

Figure 2.1 shows a plot of equilibrium conversion versus temperature for a 1:1 mixture of steam and carbon monoxide calculated using equation **2.3**.

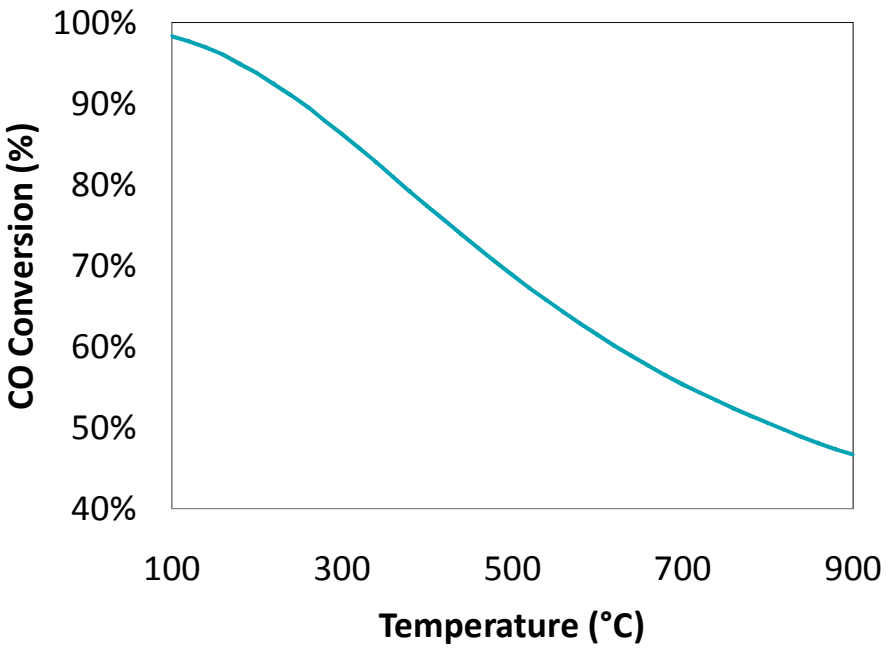

Figure 2.1. Equilibrium conversion versus temperature for a 1:1 mixture of CO and H_2O.

Due to the equilibrium limitation, high conversion for the reaction is not possible at elevated temperatures. Unfortunately, the uncatalyzed reaction proceeds very slowly at temperatures lower than approximately 600℃ (Bustamante and Enick, 2004), so the reaction is always catalyzed in industry (Newsome, 1980).

Many types of materials were found to catalyze the water-gas shift reaction in the temperature range of 100 - 500℃ in order to maximize both the conversion and the throughput. The most common of these catalysts are iron-chrome oxide (Fe_2O_3/Cr_2O_3) and copper-zinc oxide (Cu/ZnO). The iron-chrome oxide catalyst is generally known as a “high-temperature” WGS catalyst since it has better activity at temperatures of 320 - 450℃. Copper-zinc oxide is generally known as a “low-temperature” WGS catalyst since it has better activity at temperatures of 180 - 250℃ (Newsome, 1980).

Despite the equilibrium conversion being greater in the lower temperature range, the catalytically enhanced reaction rate is always greater at higher temperatures. To achieve maximum throughput in the industrial process, a combination of catalysts is

utilized in two steps, first higher, then lower temperature to obtain a high conversion with a high throughput. The reaction is first performed at higher temperatures to take advantage of the high catalytically enhanced rate, then at lower temperature to take advantage of the high equilibrium conversion. The majority of the CO is shifted at the higher temperature where the rate is highest, and then most of the remaining CO is shifted at the lower temperature where a higher conversion is thermodynamically permitted.

2.1.2. Iron-chrome oxide catalyst

The iron-chrome oxide catalyst is generally used in the bulk form as porous pellets. The Cr_2O_3 content is generally less than 14 wt%, which is the maximum amount of chromium oxide that will form a homogeneous solid solution with ferric oxide. The iron-chrome oxide catalyst has typically been produced by co-precipitation of Fe(III) and Cr(III) nitrates with excess ammonium hydroxide followed by filtration and mechanical formation into pellets. The catalyst produced in this way was shown to be very cheap and robust under WGS conditions (Christain and Boyd, 1949).

The rate of the WGS reaction on iron-chrome oxide has been extensively studied in the range of 250 - 500℃, and many different forms of the rate equation have been proposed. Rates based on the Eley-Rideal model, the oxidation-reduction model, the Hulburt-Vasan model (Hulburt *et al.*, 1961), the Tempkin model (Kul'kova and Temkin, 1949), and the Kodama model (Kodama *et al.*, 1955) have been largely dismissed in more recent literature since they didn't fit modern experimental studies conducted over larger pressure ranges (Podolski and Kim, 1974). The rate equations which have survived intense scrutiny are the empirical rate equation and the Langmuir-Hinshelwood rate equation. The empirical rate equation, given by equation **2.4**, was not based on a model or kinetic mechanism but instead approximated the rate as proportional to the concentration of each species raised to a constant power.

$$r_{CO} = kP_{CO}{}^{m}P_{H2O}{}^{n}P_{CO2}{}^{o}P_{H2}{}^{p}(1-\beta) \qquad \textbf{2.4}$$

where $\beta = \mathrm{P_{CO2}P_{H2}}/K_{EQ}\mathrm{P_{CO}P_{H2O}}$, $k = k_0\mathrm{e}^{E_a/RT}$, P_i [atma] is the partial pressure of species i, k_0 [mol/g-s] is the pre-exponential factor, E_a [kJ/mol] is the activation energy for the

reaction, and *m*, *n*, *o*, and *p* are adjustable parameters. k_0, E_a, and the exponents *m*, *n*, *o*, and *p* were typically estimated by a series of up to 16 experiments with differing feed concentrations and at multiple temperatures. The empirical parameters calculated by various experimental studies are given in Table 2.1.

Table 2.1. Empirical parameters as calculated by various studies.

ln(k_0)	E_a [kJ/mol]	*m*	*n*	*o*	*p*	Reference
8.61	114.7	0.90	0.25	-0.60	0	Bohlbro, 1961
7.61	118.9	0.81	-0.024	-0.16	-0.044	Podolski and Kim, 1974
11.4	95.0	1.1	0.53	0	0	Keiski *et al*., 1996
8.52	122.0	0.84	0.08	-0.4	0	Koukou *et al*., 1998
11.7	112	1	0	0	0	Rhodes *et al*., 2002
6.55	111	1.0	0	-0.36	-0.09	Hla *et al*., 2009
1.52	88	0.9	0.31	-0.16	-0.05	Hla *et al*., 2009

The alternate rate equation that was favored in the literature was based on the Langmuir-Hinshelwood model (Keiski *et al*., 1996; Podolski and Kim, 1974). The Languir-Hinshelwood model assumed that the reaction took place first by adsorption of each species onto the surface, then surface reaction, then desorption of each species from the surface. A high surface coverage of any single species adversely affected the amount of other species (reactants or products) that could be adsorbed and reacted. When the model was applied to the WGS reaction five elementary steps were indicated as shown in Mechanism I (Keiski *et al*., 1996). One step was for the adsorption of each species, equations **2.5 - 2.8**, and one step was for surface reaction, equation **2.9**.

Mechanism I

1) $\boldsymbol{CO} + * \leftrightarrow \boldsymbol{CO} *$ **2.5**

2) $\boldsymbol{H_2O} + * \leftrightarrow \boldsymbol{H_2O} *$ **2.6**

3) $\boldsymbol{CO_2} * \leftrightarrow \boldsymbol{CO_2} + *$ **2.7**

4) $\boldsymbol{H_2 * \leftrightarrow H_2 + *}$ **2.8**

5) $\boldsymbol{CO * + H_2O * \leftrightarrow CO_2 * + H_2 *}$ **2.9**

Generally surface adsorption and desorption took place very fast so steps 1 - 4 were assumed to be at equilibrium, allowing their overall rates to be set equal to zero. Equation **2.10** gave the overall rate of adsorption, r_i [mol/g-s], for species *i*, which was valid for all species in equations **2.5 - 2.8**. Equation **2.10** was simplified to result in equation **2.11**, the gas-surface equilibrium expression.

$$\boldsymbol{r_i = 0 = k_i[P_i][*] - k_{-i}[S_i]} \quad \textbf{2.10}$$

$$\boldsymbol{[S_i] = K_i P_{S_i}[*]} \quad \textbf{2.11}$$

where k_i [mol/g-s-atm] was the forward rate constant for species *i*, k_{-i} [mol/g-s] was the reverse rate constant, [*] was the dimensionless concentration of unoccupied surface sites, [S_i] was the concentration of adsorbed species *i* on the surface, and $k_i/k_{-i} = K_i$ [atm^{-1}] was called the Langmuir adsorption equilibrium constant for species *i*.

The rate equation for step 5 (equation **2.9**), given by equation **2.12**, was the rate limiting step.

$$\boldsymbol{r_5 = k_5[CO *][H_2O *] - k_{-5}[H_2 *][CO_2 *]} \quad \textbf{2.12}$$

By utilizing the material balance for the surface coverage given by equation **2.13** as well as the gas-surface equilibrium expression for each species given by equation **2.11**, the overall rate, r_5 [mol/g-s], could be simplified to that given by equation **2.14**.

$$\boldsymbol{C_s = [*] + [CO *] + [H_2O *] + [CO_2 *] + [H_2 *]} \quad \textbf{2.13}$$

$$\boldsymbol{r_5 = \frac{k K_{CO} K_{H2O} P_{CO} P_{H2O} (1-\beta)}{(1 + K_{CO} P_{CO} + K_{H2O} P_{H2O} + K_{CO2} P_{CO2} + K_{H2} P_{H2})^2}} \quad \textbf{2.14}$$

Where $k = k_5 * C_s^2 = k_0 e^{-Ea/RT}$, C_s [mol/m^2] was the concentration of all surface sites, and $K_{EQ} = k_5 K_{H2} K_{CO2} / k_{-5} K_{CO} K_{H2O}$.

The overall rate of equation **2.14** was promoted by an increase in the concentration of the reacting species, CO and H_2O, and so those species were found in the numerator of

equation **2.14** to the first power. The overall rate was also inhibited by an increase in the concentration of any one of the four species since that species would cover the surface and lower the concentration of free sites. The inhibition effect was represented by the terms in the denominator of equation **2.14**. The concentration of each of the reactant species, therefore, had either a promoting or an inhibiting effect on the overall reaction rate depending on the concentration. The values of the Langmuir adsorption equilibrium constants, K_i [atm^{-1}], were defined by equation **2.15** and with the parameters listed in Table 2.2.

$$\boldsymbol{K_i = \exp\left(-\frac{\Delta H_i}{RT} + \frac{\Delta S_i}{R}\right)} \qquad \textbf{2.15}$$

Table 2.2. Parameters for equations **2.14** and **2.15**, for iron-chrome oxide catalyst (ΔS in J/mol-K, ΔH in kJ/mol, E_A in kJ/mol, and k_0 in mol/g-s).

ΔH_{CO}	ΔS_{CO}	ΔH_{H2O}	ΔS_{H2O}	ΔH_{CO2}	ΔS_{CO2}	ΔH_{H2}	ΔS_{H2}	E_A	ln(k_0)	Reference
-12.8	-28.2	26.0	53.4	-52.5	-77.2	-	-	122.9	8.01	Podolski and Kim, 1974
-43.1	N/R*	-	-	-8.8	N/R*	27.6	N/R*	N/R*	N/R*	Keiski *et al.*, 1996

* Not reported

The activation energy and pre-exponential factor for the Langmuir-Hinshelwood model was very near that of the empirical model. The absolute reaction rate was also very similar between both equation sets and only differed significantly at high reaction pressure (greater than 10 atma) and where the partial pressure of any one reaction component was much greater than all the other species, resulting in a significant inhibition by occupying the majority of surface sites (Podolski and Kim, 1974).

An additional aspect of reaction modeling was the unsteady state reaction behavior. It was shown that the iron-chrome oxide catalyst underwent oxidation and reduction over the course of the reaction so that the unsteady state behavior could potentially be modeled by an oxidation-reduction mechanism like that shown by Mechanism II, equations **2.16 - 2.20** (Salmi *et al.*, 1988; Tinkle and Dumesic, 1987). Step 1, equation **2.16**, represented the reaction of gas phase CO with an adsorbed oxygen atom. Steps 2

and 3, equations **2.17** and **2.18**, represented adsorption and desorption of CO_2 and H_2O from the surface. Step 4, equation **2.19**, represented the dissociation of surface H_2O to surface bonded atomic H and O. Step 5, equation **2.20**, represented the association of surface bonded atomic H and subsequent desorption of H_2. It was demonstrated experimentally by reactions with ^{13}C labeled CO that the rate limiting steps were Steps 1 and 5 resulting in the approximated rate given by equations **2.21** and **2.22** (Tinkle and Dumesic, 1987).

Mechanism II

1) $\boldsymbol{CO + O* \leftrightarrow CO_2 + *}$ **2.16**

2) $\boldsymbol{CO_2* \leftrightarrow CO_2 + *}$ **2.17**

3) $\boldsymbol{H_2O + * \leftrightarrow H_2O*}$ **2.18**

4) $\boldsymbol{H_2O* + 2* \leftrightarrow 2H* + O*}$ **2.19**

5) $\boldsymbol{2H* \leftrightarrow H_2 + 2*}$ **2.20**

$$\boldsymbol{r_{CO2} = k_1 P_{CO}(1-\beta)} \quad \textbf{2.21}$$

$$\boldsymbol{r_{H2} = k_2 L^2 (1-\theta_O)^2} \quad \textbf{2.22}$$

where r_i [mol/g-s] was the rate of formation of species i, $\boldsymbol{k_n = k_{0,n} e^{\frac{E_n}{RT}}}$, with values for $k_{0,1}$ [mol/g-s-atm], $k_{0,2}$ [mol-m^4/g-s-mol$_{SS}^2$] and E_n [kJ/mol] defined in Table 2.3 as reported by Salmi *et al*. (1988), P_{CO} [atm] was the partial pressure of CO, L [mol$_{SS}$/m^2] was the concentration of surface sites on the catalyst, and θ_O was the fraction of oxygenated Surface Sites (SS).

Equations **2.21** and **2.22** were simplified from more complex equations (Salmi *et al*., 1988) based on the following assumptions. In transient experiments CO_2 was found to evolve immediately while the evolution of H_2 from the catalyst was significantly delayed. Based on the lag-time for the evolution of H_2, and calculations of available surface sites, the surface coverage of the oxygenated sites was assumed to be nearly total. The immediate appearance of CO_2 in transient experiments suggested that the adsorption and desorption of CO and CO_2 took place very fast compared to the adsorption and desorption of H_2O. Also, the H_2O/CO ratio was assumed to be greater than 1.0.

Table 2.3. Parameters for k_1 and k_2 in equations **2.21** and **2.22**.

$\ln(k_{0,1})$	E_1 [kJ/mol]	$\ln(k_{0,2})$	E_2 [kJ/mol]	Reference
5.67	97.2	4.37	-26.5	Salmi *et al.*, 1988

2.1.3. Copper-zinc oxide catalyst

Copper based catalyst, which typically contained around 20 mol% ZnO as a promoter and up to 25 mol% Cr_2O_3 as a stabilizer, came into study and use in the 1960's (Newsome, 1980). These catalysts had exceptional activity in the temperature range of 100 - 300°C and were utilized in the second step of the industrial WGS process.

Copper based catalysts were prepared by kneading zinc oxide, copper hydroxide, and chromium oxide together, followed by extrusion into pellets, and calcination at 250°C. The optimal composition of CuO and ZnO was found experimentally to be 29 mol% Cu (Uchida *et al.*, 1967). A plot of the reaction rate constant, k_{180} in mol/atm-mL_{cat}-h, versus Cu/Zn ratio at 180°C is shown in Figure 2.2. With increasing Cu/Zn ratio, the rate increased to a maximum at a Cu/Zn ratio of 0.4, then decreased slightly in the range of 0.4 - 2.0, then further decreased at a Cu/Zn ratio of greater than 2.0.

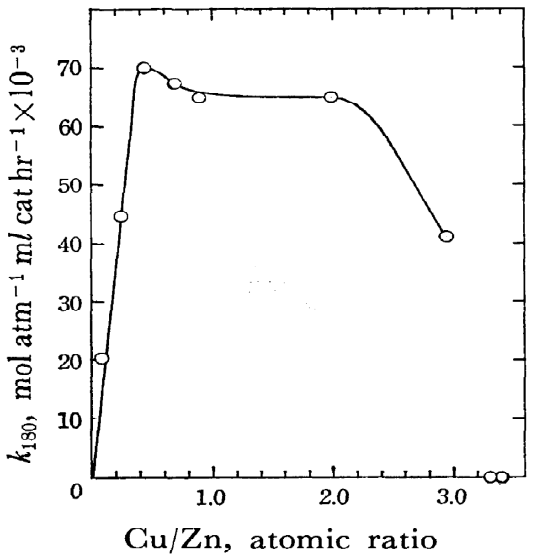

Figure 2.2. Rate constant versus Cu/Zn atomic ratio at 180°C (Uchida *et al.*, 1967).

In a subsequent study, Uchida *et al*. (1968) studied the porosity, surface area, and surface morphology of catalyst samples with varying Cu/Zn ratios. They concluded that the optimal activity occurring at a Cu/Zn ratio of 0.4 was due to an optimal catalyst structure at that Cu/Zn ratio. They found that the majority of the catalytic activity occurred on the copper and that the zinc oxide acted as a support. At high percentages of copper however, the copper particles tended to aggregate and sinter under reaction conditions lowering the available surface area. The optimal balance between high catalyst surface area and low extent of sintering was achieved at approximately 29 mol% Cu.

The rate of the WGS reaction on copper-zinc oxide catalyst, in the temperature range of 100 - 400℃, has been thoroughly studied in the literature (Newsome, 1980). The predominant forms of the rate equation seen in the literature were also the empirical rate law and the Langmuir-Hinshelwood based rate law (Amadeo and Laborde, 1995; Newsome, 1980; Salmi and Hakkarainen, 1989). The empirical rate law, equation **2.23**, was largely agreed to be dependant only on the concentrations of CO and H_2O, and not on CO_2 or H_2 (Salmi and Hakkarainen, 1989). Additionally the exponents *m* and *n* have been found to vary with temperature over the range of 130 - 410℃. Salmi and Hakkarainen (1989) reported the varying *m* and *n* values as well as the rate constant data for that range.

$$\boldsymbol{r = k[CO]^m[H_2O]^n(1-\beta)} \qquad \textbf{2.23}$$

Since the empirical rate law, equation **2.23**, did not adequately express the temperature dependence of the reaction, the Langmuir-Hinshelwood rate law, equation **2.14**, was generally utilized. The parameters for the Lagmuir isotherm constants and the rate constants are given in Table 2.4.

Table 2.4. Parameters for Langmuir-Hinshelwood rate equation **2.14** for copper-zinc oxide catalyst.

ΔH_{CO}	ΔS_{CO}	ΔH_{H2O}	ΔS_{H2O}	ΔH_{CO2}	ΔS_{CO2}	ΔH_{H2}	ΔS_{H2}	E_A	$\ln(k_0)$	Reference
-0.84	6.59	-1.32	-7.62	-22.8	-44.6	-13.3	-24.6	5.94	0.049	Amadeo and Laborde, 1995

2.1.4. Other WGS catalysts

A third type of catalyst, cobalt-molybdenum based catalyst, has also been extensively studied and has come into mainstream use but to a lesser extent than the other two catalysts (Newsome, 1980). This catalyst was usually supported on silica or alumina and promoted cesium salts. In contrast to the iron-chrome and copper-zinc oxide catalysts, the cobalt-molybdenum catalyst was made more active by the presence of sulfur in the WGS reaction mixture. In the intermediate temperature range, 250 - 350°C, and in the presence of 2 mol% sulfide species, cobalt-molybdenum catalysts have shown activity as high as five times that of copper-zinc oxide catalyst for the same feed mixture, excluding the sulfide (Newsome, 1980). For this reason, Co/Mo catalysts are not typically used in situations where sulfide species were absent from the WGS feed mixture.

In recent years alternative catalysts have been developed based on both transition metals such as iron, nickel, and cobalt (Hilaire *et al*., 2004) as well as noble metals such as palladium, gold, platinum, and rhodium (Kim and Thompson, 2005; Burch, 2006; Iida and Igarashi, 2006). These catalysts have been designed primarily to operate in the 100 - 300°C temperature range where a high equilibrium conversion was possible and increased catalytic activity was greatly sought after. Practically all novel transition metal catalysts failed to compete with commercially available Zn/Cu-oxide catalyst in the low temperature range (Hilaire *et al*., 2004). A few of the best examples of these catalysts are listed in Table 2.5. The catalytic activity is presented as a multiple of the catalytic rate of a commercial copper-zinc oxide catalyst.

Table 2.5. Composition and catalytic activity of experimental WGS catalysts as a multiple of the activity of Zn/Cu oxide, at the same temperature.

Catalyst	Temperature (°C)	Activity ($\frac{\text{Reaction Rate}}{\text{Rate on ZnCuO}}$)	Reference
$CoMoCs/Al_2O_3$	300	5.24*	Newsome *et al.*, 1980
Au/CeO_2 – 400	240	3.81 - 2.0	Kim and Thompson, 2005
Pt/TiO_2 (rutile)	250	1.24	Iida and Igarashi, 2006
Pd/CeO_2	227	0.1	Hilaire *et al.*, 2004
Ni/CeO_2	227	0.1	Hilaire *et al.*, 2004
Co/CeO_2	227	<0.01	Hilaire *et al.*, 2004

*2 mol% H_2S utilized in the feed

Despite many synthesis attempts, all but a few noble metal catalysts (primarily Au and Pt) have shown lower catalytic activity than commercial Zn/Cu oxide catalysts in the 100 - 300°C temperature range (Burch, 2006). It was believed that the activity of these catalysts was strongly influenced by the microstructure of the support material and the noble metal. Kim and Thompson (2005) developed a ceria supported gold catalyst by the deposition of chloroauric acid onto basic aqueous suspended ceria which proved to have significantly higher activity than the commercial Zn/Cu oxide catalyst at a temperature of 240°C. The catalyst prepared by Kim and Thompson (2005) showed an initial activity of 3.81 times that of the commercial Zn/Cu oxide reference catalyst although its activity declined by 48% over 10 hours. Iida and Igarashi (2006) prepared several supported platinum catalysts on titanium dioxide, zirconium dioxide, and alumina by evaporation of aqueous platinum chloride solution onto each support followed by calcination. Of the four supported Pt-catalysts prepared by Iida and Igarashi (2006), only the Pt/TiO_2(rutile) sample showed catalytic activity slightly higher than the commercial alternative. Burch (2006) reviewed over 20 experimental papers presenting gold and platinum supported catalysts and showed that the most important aspects of the supported noble metal catalysts were the noble metal particle size (smaller particles being better) and the extent of contact between the particles and the support (more intimate contact being better). Burch (2006) postulated that the mechanism of the WGS

reaction on the noble metal catalysts involved not only the metal surface but also metal-support interface.

The relatively minor gains in catalytic activity achieved by noble metal catalysts in recent years have not been great enough to outweigh the added cost of the noble metal use.

2.2. Palladium membranes

The solubility of hydrogen in palladium was first discovered in 1863 by Deville and Troost (Graham, 1866). The first separation of hydrogen by thin palladium tubes was performed shortly thereafter by Thomas Graham in 1866. Despite the early discovery of this unusual property of palladium, little research was done until the 1930's. Palladium is capable of occluding vast quantities of hydrogen in a non-stoichiometric way and, at elevated temperatures, transporting that hydrogen throughout the metal lattice (Lewis, 1967). The quantity of hydrogen dissolved in palladium is dependent on both temperature and pressure. Figure 2.3 shows the partial pressure of hydrogen as a function of solubility (given by the atomic ratio, H/Pd) for different isotherms. Figure 2.3 also indicates that there are two distinct phases of dissolved hydrogen. Below the critical temperature of 298°C two distinct phases exist which are separated by the dashed parabola. The α-phase exists to the left of the parabola and the β-phase exists to the right of the parabola. Under the parabola both phases are present as a heterogeneous mixture in the metal.

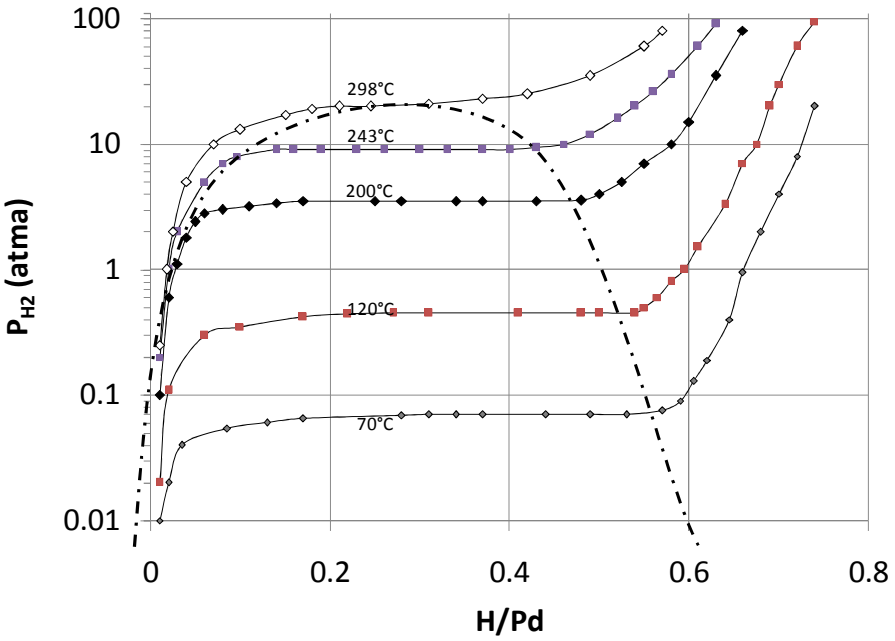

Figure 2.3. Pressure isotherms of the Pd-H system at several temperatures (Reproduced from Frieske and Wicke, 1972).

Since transitions between the α and β-phases were accompanied by a large change in the lattice constant, 3.89 to 4.02Å, significant stress and deformation could occur in the metal during the transition (Lewis, 1967; Smith, 1948). When palladium foils were subjected to repeated α/β transitions, deformations were observed on both the macroscopic and microscopic levels. Thin membranes subjected to α/β transitions have developed pinholes and cracks due to these deformations in a process known as hydrogen embrittlement. An example of a thin supported membrane put through an α/β transition is shown in Figure 2.4 (Guazzone *et al.,* 2006).

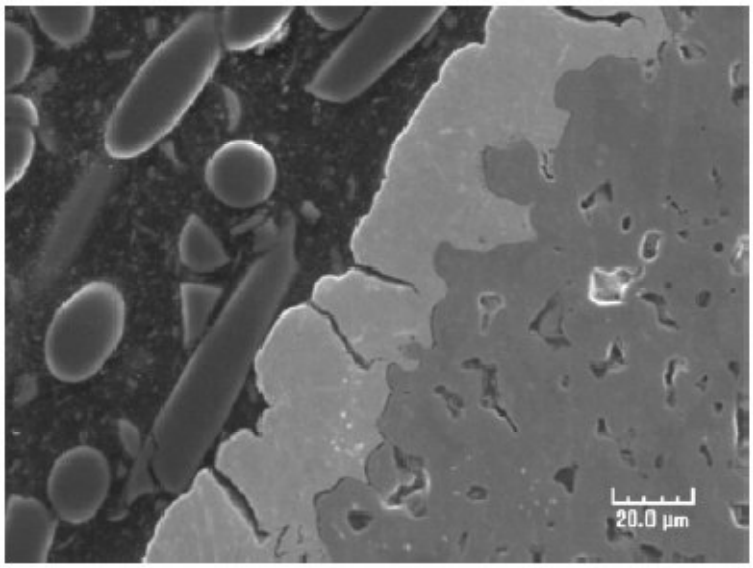

Figure 2.4. SEM image of a PSS supported Pd-membrane which has undergone hydrogen embrittlement (Guazzone *et al.,* 2006).

At temperatures above 298°C there are no distinct α and β-phases so the increase to higher H-concentration happens smoothly, with far less stress and deformation (Guazzone *et al*., 2006). Pure palladium membranes are typically utilized at temperatures of greater than 298°C to avoid possible failures due to hydrogen embrittlement. Alternatively at lower temperatures a Pd-membrane can be kept clear of the α/β transition by keeping the hydrogen partial pressure below the transition pressure. Alloying the palladium with other metals, silver for instance, also lowers the temperature at which the distinct α and β-phases can coexist. A $Pd_{60}Ag_{40}$-alloy has no distinct two phase region at temperatures as low as 50°C (Lewis, 1967).

2.2.1. H_2 permeability of thin Pd foils

The permeation of pure hydrogen through a palladium foil happens in several steps. Hydrogen is first adsorbed on the surface and dissociates. The dissociated hydrogen atoms then dissolve into the metal lattice. Both of these steps are reversible and occur at both sides of the foil. The hydrogen diffuses through the lattice and can thereby cross

the foil (Barrer, 1951). Figure 2.5 shows the adsorption, dissociation, dissolution, and diffusion process.

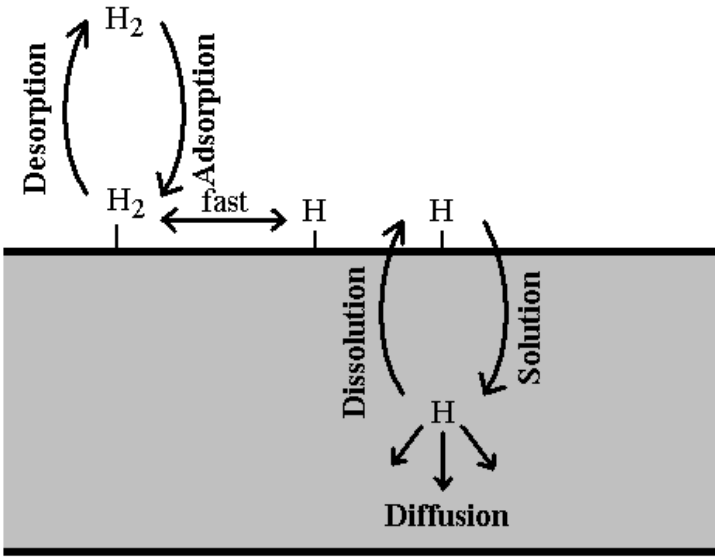

Figure 2.5. Mechanism of hydrogen permeation into a metal.

The flux of hydrogen permeating through a thin palladium layer depended mainly on the diffusion of hydrogen through the bulk palladium, which was the rate determining step for membranes thicker than approximately 1 µm (Shu *et al.,* 1991). For membranes thinner than approximately 1 µm, the mass transfer resistance in the bulk can become very low such that it is no longer rate limiting. In this case, the H_2 flux can be limited by the desorption step on the low pressure side of the membrane (Ward and Dow, 1999). For thicker membranes the permeation flux, J_H [mol_H/m^2-h] at steady state was obtained by the integration of the Fick's law across the foil, resulting in equation **2.24**.

$$\boldsymbol{J_H = (D_H/\delta_{Pd})(C_1 - C_2)} \qquad \textbf{2.24}$$

Where D_H [m^2/h] was the diffusion coefficient for atomic hydrogen in the lattice, δ_{Pd} [m] was the thickness of the foil, and C_x [mol_H/m^3] was the concentration of hydrogen immediately beneath surface *x* on one side of the foil. The concentration can be defined

as a constant, $\boldsymbol{\kappa}$ = 1.130*10^5 mol$_{Pd}$/m^3, multiplied by the H/Pd atomic ratio, $\boldsymbol{\nu}$, as in equation **2.25**.

$$\boldsymbol{C_x \equiv \kappa \nu_x} \qquad \textbf{2.25}$$

The following derivation was elucidated by Shu *et al*. (1991), a list of all terms and their definitions can be found in the Nomenclature section, and a more thorough derivation of the following equations can be found in Appendix A.2. For surface *x* of the membrane the flux of adsorption/desorption, J_a [m$_{H2}$^{3}/m^2-h], is given by equation **2.26**.

$$\boldsymbol{J_a = k_a P_x (1 - \theta_H)^2 - k_d \theta_H^2} \qquad \textbf{2.26}$$

Where the two terms are rate expressions for adsorption and desorption, k_a [m$_{H2}$^{3}/m^2-h-atm] and k_d [m$_{H2}$^{3}/m^2-h] are the rate constants for adsorption and desorption respectively, P_x [atma] is the partial pressure of hydrogen in the gas phase adjacent to surface *x*, and θ_H is the fraction of surface covered by dissociated hydrogen.

The flux of dissolution into the lattice, J_d [mol$_{H2}$/m^2-h] is given by equation **2.27**.

$$\boldsymbol{J_d = \kappa k_i \theta_H (1 - \nu_x) - \kappa \nu_x k_o (1 - \theta_H)} \qquad \textbf{2.27}$$

Where the two terms are rate expressions for dissolution of surface H_2 into the lattice and evolution of H_2 from the lattice to the surface, and k_i [m/h] and k_o [m/h] are the rate constants for dissolution into and out of the dense Pd respectively.

Since diffusion has been shown experimentally to be the rate limiting step for membranes thicker than approximately 1 μm, the flux will be given by equation **2.24**. The rates of equations **2.26** and **2.27** are much greater, allowing for the assumption that those processes are at equilibrium. Equations **2.26** and **2.27** can therefore be set equal to zero and simplified to generate an expression for concentration, C_x, inside the bulk palladium and close to surface *x*. The expression for H-concentration near surface *x* was given by equation **2.28**.

$$\boldsymbol{C_x = \frac{\kappa}{K_s}\sqrt{P_x}(1 - \nu_x) \cong \frac{\kappa}{K_s}\sqrt{P_x}} \qquad \textbf{2.28}$$

Where K_s [atm$^{0.5}$-mol$_H$/mol$_{Pd}$] is known as Sieverts' constant, $\boldsymbol{K_s = (k_o/k_i)\sqrt{(k_d/k_a)}}$. Sieverts' constant is an equilibrium constant relating the partial pressure of hydrogen in contact with a metal surface to the concentration of hydrogen, $\boldsymbol{\nu_x}$, just below the surface, $\boldsymbol{K_s = \sqrt{P}/\nu}$. The equation is simplified greatly by the assumption that $\boldsymbol{\nu \ll 1}$ (the last term in equation **2.28**), meaning that the hydrogen concentration in the metal is very low. The acceptable conditions which validate the $\boldsymbol{\nu \ll 1}$ assumption can be found from Figure 2.3 ($\boldsymbol{\nu} = \text{"H/Pd"}$), the α-phase region to the left of the dashed parabola.

Incorporating equation **2.28** into equation **2.24** gives the equation known as Sieverts' law, equation **2.29**. Sieverts' law is the most common expression for the relationship between hydrogen flux and partial pressure in Pd-membranes.

$$\boldsymbol{J = \frac{D\kappa}{\delta_{Pd} K_s}\left(\sqrt{P_1} - \sqrt{P_2}\right)} \qquad \textbf{2.29}$$

Equation **2.29** expresses that the flux of hydrogen across the foil is dependent on the difference in square root partial pressures of hydrogen on both sides of the foil. The flux is directly proportional to the diffusion coefficient and inversely proportional to the thickness of the foil. If the assumption, $\nu \ll 1$, is not justified, for example at low temperature and/or very high pressure, then the total flux across the barrier is given by equation **2.30**, derived directly from the substitution of equation **2.28** into equation **2.24** with no further assumptions or simplifications.

$$\boldsymbol{J = \frac{D\kappa}{\delta_{Pd}}\left(\frac{\sqrt{P_1}}{K_s+\sqrt{P_1}} - \frac{\sqrt{P_2}}{K_s+\sqrt{P_2}}\right)} \qquad \textbf{2.30}$$

A more thorough derivation of equation **2.30** is given in Appendix A.2. As can be seen, at lower pressure, when $\sqrt{P_x} \ll K_s$ for both sides of the foil, equation **2.30** simplifies to equation **2.29**. When this simplification cannot be made due to high pressure the flux no longer obeys a square root dependence on pressure.

The permeability of hydrogen in a metal, defined by Q_{H2} [m^3-μm/m^2-h-atm$^{0.5}$] = $D\kappa/K_S$, can also be expressed as the diffusivity, D [m^2/h], multiplied by the solubility, S [m$^3_{H2}$/m$^3_{Pd}$], where S = κ/K_S. Incorporating the above definition of permeability of hydrogen in a metal into equation **2.29** results in equation **2.31**.

$$J = \frac{Q_H}{\delta_{Pd}}\left(\sqrt{P_1} - \sqrt{P_2}\right) \qquad \textbf{2.31}$$

The permeability of hydrogen is a temperature-dependant property of the metal which can differ significantly between metals and alloy compositions. For ideal membranes the flux is dependent on the square root partial pressure difference as given by equation **2.29** but for supported membranes the dependence may not well fit the ½ power due to support resistance, surface adsorption resistance, or leaks. For membranes that are not ideal an empirical equation, **2.32**, has been used to characterize the H_2 flux.

$$J = \frac{Q_{H2}}{\delta_{Pd}}\left(P_1^n - P_2^n\right) \qquad \textbf{2.32}$$

where *n* is the exponent of the pressure dependence.

In non-ideal membranes, different effects can alter the *n*-value in predictable ways. For very thin films (less than 1 μm) the flux can cease to be limited by the diffusion of hydrogen in the metal lattice and instead become partially limited by the desorption of hydrogen from the downstream metal surface, equation **2.26** (Ward and Dao, 1999). The pressure dependence of equation **2.26** is first order, so that if the flux becomes partially limited by desorption the *n*-value in equation **2.32** will approach one. Additionally, the hydrogen flux of membranes supported on microporous supports can be partially limited by the mass transfer resistance in the support. The flux through microporous media occurs through Knudsen diffusion which is also first order with respect to partial pressure difference and would cause the *n*-value of equation **2.32** to approach one (Knudsen, 1995). When the membrane is being utilized to separate a gas mixture, a concentration boundary layer will form above the surface such that a concentration gradient will exist between the bulk gas phase and the surface (Caravella *et al*., 2009). The flux across the boundary layer is first order with respect to partial pressure so if there is significant mass transfer resistance in the boundary layer it will also cause the *n*-value of equation **2.32** to approach one.

An important aspect of non-ideal membranes is that they may have leaks. Guazzone and Ma (2008) studied leak growth in Pd membranes supported on PSS and found that above approximately 400°C, in a H_2 atmosphere, pinholes formed due to sintering and

rearrangement of the Pd crystallites. Microscopic defects and pinholes will allow a flux of otherwise non-permeable gas. For this reason the separation factor, $\boldsymbol{\alpha_{H2-i}}$, of the membrane must be defined, equation **2.33**.

$$\boldsymbol{\alpha_{H2-i} = \frac{y_{H2}/y_i}{x_{H2}/x_i}} \qquad \textbf{2.33}$$

where y_{H2} [mol/mol] is the mole fraction of H_2 in the permeate, y_i [mol/mol] is the mole fraction of gas species *i* (non-hydrogen gas) in the permeate, x_{H2} [mol/mol] is the mole fraction of H_2 in the retentate, and x_i [mol/mol] is the mole fraction of gas species *i* in the retentate. An alternate way to characterize the efficacy of a membrane is by the ideal separation factor, $\boldsymbol{\alpha^i_{H2-i}}$, as defined by equation **2.34**.

$$\boldsymbol{\alpha^i_{H2-i} = J_{H2}/J_i} \qquad \textbf{2.34}$$

where J_{H2} [m^3/m^2-h] and J_i are the fluxes of pure hydrogen and pure non-permeable gas species *i* respectively, measured at the same temperature and pressure difference. The 'real' separation factor (equation **2.33**) will frequently be less than the ideal separation factor (equation **2.34**). In many types of membranes, chemical or physical interactions between one gas species and the surface, can affect the permeability of the membrane to a different gas species. A specific example dealing with Pd-membranes is H_2 permeation inhibition caused by CO, H_2O, or H_2S (Hou and Hughes, 2002; Unemoto *et al*., 2007; Peters *et al.,* 2012), causing a lower membrane permeance to H_2 and the 'real' separation factor, $\boldsymbol{\alpha_{H2-i}}$, to be less than the ideal separation factor.

2.2.2. H_2 permeability of Pd/Alloys

The permeability of hydrogen in a metal is dependent on temperature as in equation **2.35**.

$$\boldsymbol{Q_H = Q_0 \exp\left(-E_A/RT\right)} \qquad \textbf{2.35}$$

where Q_0 [m^3-μm/m^2-h-$atm^{0.5}$] is a pre-exponential factor and E_A [kJ/mol] is the activation energy of hydrogen permeation. The pre-exponential factor and the activation energy are unique for different alloy compositions. Table 2.6 lists the pre-exponential

factors and activation energies for the hydrogen permeation of several different palladium alloy foils.

Table 2.6. Pre-exponential factor and activation energy for Pd and Pd-alloy foils.

Material	Q_0 [m^3-$\mu m/m^2*h*atm^{0.5}$]	E_A [kJ/mol]	T [℃]	P_{H2} [atma]	Reference
Pd	$4.397x10^3$	13.81	350 - 900	1.0 - 27.3	Morreale *et al*., 2003
Pd	$6.59x10^3$	15.48	100 - 620	$3x10^{-7}$ - $7x10^{-5}$	Balovnev, 1974
Pd	$8.47x10^3$	18.26	300 - 700	0.001 - 1	Latyshev and Bystritskiy, 1991
$Pd_{75}Ag_{25}$	$1.986x10^3$	6.60	300 - 500	6.8 - 68	Ackerman and Koskinas, 1972
$Pd_{85}Ag_{15}$	$9.40x10^3$	17.43	400 - 700	0.001 - 1	Latyshev and Bystritskiy, 1991
$Pd_{60}Cu_{40}$	$9.24x10^2$	10.77	350 - 450	1 - 26	Howard *et al*., 2004
$Pd_{80}Cu_{20}$	$1.67x10^3$	18.60	350 - 950	1 - 26	Howard *et al*., 2004
$Pd_{90}Au_{10}$	$2.32x10^3$	10.70	350 - 500	1.0 - 6.9	Gade *et al.,* 2010
$Pd_{80}Au_{10}$	$1.43x10^3$	7.95	350 - 500	1.0 - 6.9	Gade *et al.,* 2010

Pd/Ag, Pd/Au, and Pd/Cu membranes prepared by McKinley (1967) as well as Pd/Au and Pd/Cu membranes prepared by Knapton (1977), demonstrated permeabilities in excess of pure Pd membranes for some alloy compositions: less than approximately 35 at% Ag, less than 15 at% Au, and approximately 40 at% Cu. Figure 2.6 shows the permeability of different Pd/Ag, Pd/Au, and Pd/Cu compositions as a fraction of the permeability of pure Pd, and at 350℃.

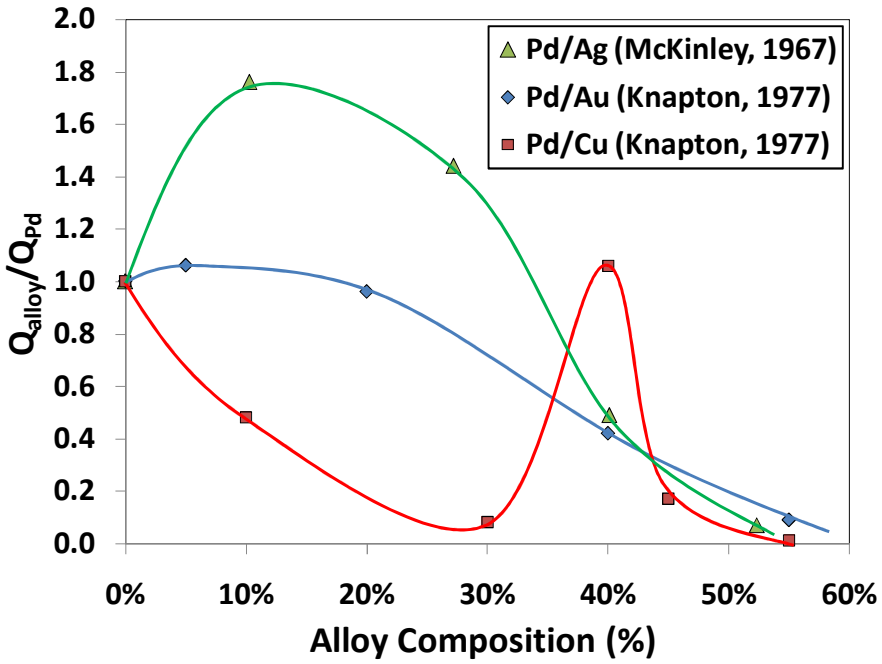

Figure 2.6. Permeability of Pd-alloy divided by that of pure Pd versus alloy composition at 350℃.

Lewis (1967) suggested that the improved permeability of Pd/Ag-alloys with less than approximately 35 at% Ag was caused by the lattice dilation which significantly increased the solubility of H-atoms in the alloy. Knapton (1977) and McKinley (1967) both suggested that the higher or lower H_2 permeability of the Cu and Au alloys was also due to the higher or lower lattice constant caused by the fraction of the alloying metal. For the Pd/Au-alloy, the lattice constant increased approximately linearly with increasing Au composition. For copper, a spike in permeability was seen at approximately 40 at% Cu, caused by the formation of a body-centered cubic (bcc) phase which had very high H_2 diffusivity, resulting in high H_2 permeability (Knapton, 1977).

2.2.3. Synthesis of supported membranes

A variety of synthesis techniques have been developed to produce thin foils or thin supported membranes of palladium and palladium alloys for hydrogen separations. Since the flux of such membranes was inversely proportional to their thickness,

substantial effort has been made to produce thinner membranes. In addition, the majority of membrane synthesis efforts have been directed towards supported or composite membranes instead of free standing foils. Supported membranes generally have better mechanical strength and durability than thin foils. Thin foils (less than 100 µm thick) have been attached by various means (such as mechanical clamping, welding, or diffusion welding) to different types of porous supports in order to improve their mechanical strength. Thin layers of dense metal have also been synthesized on top of porous supports in a variety of ways, the most common of which were electroplating, magnetron sputtering, chemical vapor deposition, and electroless plating. Table 2.7 lists the synthesis methods and properties of several dense metallic membranes that have been prepared in the literature.

2.2.3.a. Supported foils

One way of producing a supported membrane has simply been to attach a piece of foil onto a porous support; the foil accomplished the separation, the support provided the mechanical stability. Tosti (2003) bonded a $Pd_{76}Ag_{24}$-foil (42 µm thick) to Ni/Ag coated stainless steel mesh by diffusion welding (heating to above the Tamman temperature and applying mechanical pressure). They observed a hydrogen permeance of 0.98 $m^3/m^2h*atm^{0.5}$ with an assumed infinite selectivity at 350°C. DeRosset (1960) tested a 20 µm palladium foil held at the edges of a PSS disk by a diaphragm. The author reported a permeance of 6.0 $m^3/m^2h*atm^{0.8}$ at 450°C and an *n*-value of 0.8. The author did not report selectivity or stability over time. Peters *et al*. (2008) synthesized a 2.2 µm $Pd_{77}Ag_{23}$-foil by magnetron sputtering (discussed in section 2.2.3.c) onto a silicon substrate, then removed the foil from the substrate and clamped it to a tubular Porous Stainless Steel (PSS) support. They reported a flux of 150.8 $m^3/m^2h*atm^{0.54}$ at 400°C, an *n*-value of 0.54, and a selectivity of over 650 for up to 500 hours of testing. Peters *et al*. (2009) synthesized another supported foil, 2.6 µm $Pd_{77}Ag_{23}$, and tested it for up to 2,400 hours in a 50/50 mixture of hydrogen and nitrogen, at 350 - 450°C; they observed an initial H_2/N_2 separation factor of 550 which declined to 50 over the testing time. They determined that the leak development was due to grain growth in the Pd-layer, and that the rate of leak growth at 400°C led to a projected membrane lifetime of 2.5 years.

Table 2.7. Synthesis methods and properties of a selection of membranes reported on in the literature.

Deposition Method	Support	Composition	Thickness [µm]	H_2 Permeance [m^3/m^2h*atm^n]	*n*-value	Temperature [°C]	Selectivity [F_{H2}/F_{He}]	Testing Time [h]	Reference
Foil	SS Mesh	PdAg	42	0.98	0.5	350	N/R	N/R	Tosti, 2003
Foil	PSS	Pd	20.3	5.97	0.8	450	N/R	N/R	deRosset, 1960
Foil	PSS	$Pd_{77}Ag_{23}$	2.2	150.8	0.52	400	N/R	500	Peters *et al.*, 2008
Vacuum EP	PSS	$Pd_{78}Ni_{22}$	1	105.9	1	550	600	N/R	Nam *et al.*, 1999
			1	141.2	1	550	2700	N/R	
			1	150.0	1	550	4700	N/R	
Vacuum EP	PSS	$Pd_{63}Cu_{37}$	2	68.4	1	550	70,000	960	Nam and Lee, 2001
Vacuum EP	PSS	$Pd_{82}Ni_{18}$	3	26	1	450	4500	1400	Nam and Lee, 2005
MS	Ceramic	$Pd_{76}Ag_{24}$	1	90	1	462	800	N/R	Zhao *et al.*, 2000
MS	Silicon	$Pd_{77}Ag_{23}$	0.75	153.2	0.5	450	1500	N/R	Gielens *et al.*, 2002
MS	PSS	$Pd_{77}Ag_{23}$	2.6	24.1	0.5	0.5	8700	2400	Peters *et al.,* 2009
CVD	Ni-PSS	Pd	5	141.1	1	450	1600	48	Jun and Lee, 2000
		$Pd_{80}Ni_{20}$	22	17.6	1	450	400	48	
		$Pd_{70}Nb_{30}$	N/R	21.2	1	450	120	48	
CVD	Alumina	Ir	8.3	34.7	0.5	500	93	15	Kajiwara *et al.*, 2000
		Rh	17.3	30.2	0.5	500	80	15	
CVD	Alumina	Pd	3.2	80.3	0.5	500	240	15	Uemiya *et al.*, 2001
		Pt	5.8	22.6	0.5	500	210	15	
		Ru	3.3	45.2	0.5	500	120	15	
Electroless	Alumina	$Pd_{77}Ag_{23}$	2.2	49.2	1	410	330	N/R	Keuler and Lorenzen, 2002
Electroless	PSS	Pd	8	38.5	0.5	500	800	N/R	Tong *et al.*, 2004
Electroless	PSS	Pd	6	24.4	0.5	500	∞	300	Tong *et al.*, 2005
Electroless	Alumina	$Pd_{90}Cu_{10}$	1.0	95.0	0.5	350	1390	8	Roa *et al.*, 2002
Electroless	Alumina	$Pd_{60}Cu_{40}$	1.5	97.9	0.52	350	93	N/R	Roa *et al.*, 2003a
Electroless	Alumina	$Pd_{81}Cu_{19}$	11.6	36.5	0.5	500	170	480	Roa *et al.*, 2003b
		$Pd_{91}Cu_{9}$	12.0	56.1	0.5	500	1400	624	
		$Pd_{70}Cu_{30}$	1.5	46.3	0.5	350	47	144	
Electroless	PSS	Pd	7.9	68.5	0.5	500	149	1388	Mardilovich *et al.*, 2006
Electroless	P-Hastelloy	Pd	4.0	42.4	0.5	400	100,000	2286	Guazzone and Ma, 2008

With the exception of Peters *et al*. (2008; 2009), the hydrogen permeances achieved by the other two investigators (Tosti, 2003; DeRosset, 1960) were significantly lower than those achieved with supported membranes prepared by alternate methods, most likely due to the thickness of the membranes utilized in these studies, 42 and 20 µm. The membranes synthesized by Peters *et al*. (2008) were exceptionally thin, but upon longer testing at up to 450°C experienced a substantial decline in selectivity and so may not be suitable for industrial applications.

2.2.3.b. Electroplating

Electroplating (EP) is a plating technique characterized by the use of a direct electric current in an electrolyte solution to reduce metal ions from the solution directly onto a substrate. Typically the metal salt to be plated is dissolved along with stabilizing ligands to moderate its availability in the solution. A platinum mesh is usually used as the anode due to its inert nature. The sample to be plated is made to be the cathode by wire attachment or by placement in a metallic tray. For electroplating to be successful the sample to be plated must be highly conductive. The anode and the cathode are submerged in the solution with stirring and a voltage is applied across them in order to reduce the metal ions in solution directly onto the support. A good control of the plating rate can be achieved by adjusting the voltage and the concentrations of different species in the solution. Membranes as thin as 1 µm have been synthesized in this manner (Nam *et al*., 1999; Nam and Lee, 2000; 2001; 2005).

Nam *et al*. (1999) produced $Pd_{78}Ni_{22}$-membranes approximately 1 µm think on porous stainless steel supports by vacuum electroplating of both metals simultaneously onto one side of the support, while applying vacuum on the opposite side. Their best membrane had a hydrogen permeance of 150 m^2/m^2h*atm at 550°C. They observed a selectivity of 4,500 and an *n*-value of approximately one, but did not report the testing time. In a subsequent study Nam and Lee (2001a) also produced $Pd_{53}Cu_{47}$-membranes approximately 2 µm thick on PSS graded with silica. One of these membranes had a hydrogen permeance of 68 m^3/m^2h*atm and a selectivity of 70,000 at 550°C with stability over 960 hours of testing. In another study (Nam and Lee, 2000) they treated their support with a titanium nitride barrier deposited by radio-frequency vacuum

sputtering in order to prevent intermetallic diffusion of the support metals into the membrane. They then electroplated a 3 µm layer of $Pd_{82}Ni_{18}$ onto treated support. The membrane they prepared had a hydrogen permeance of 26 m^3/m^2h*atm and a stable selectivity of 4,500 at 450°C over 1,440 hours of testing. The authors indicated that the use of either the silica or titanium nitride as an intermediate layer simultaneously smoothed the support surface for good deposition morphology and acted as an intermetallic diffusion barrier, leading to good long-term permeance and selectivity stability.

Membranes demonstrating very good permeance and selectivity as well as high mechanical strength have been prepared by vacuum electroplating. Due to the nature of electroplating, only metallic or highly conductive samples can be plated, which limits this technique almost exclusively to porous metal supports. Complex shapes also present a challenge since all surfaces of the support must be nearly equidistant from the anode for uniform plating. Nam *et al*. (1999) and Nam and Lee (2000; 2001; 2005) have thus far only utilized porous disks as supports.

2.2.3.c. Magnetron sputtering

Magnetron Sputtering (MS) is a technique which uses high energy plasma, usually generated from high-voltage gas discharge, to vaporize metal atoms from the surface of a target sample. The vaporized metal atoms then condense on a nearby substrate. The type of plasma as well as its temperature affect the rate of vaporization, and the position and the gas flow characteristics around the substrate affect the rate and properties of the deposition. Particularly thin supported membranes (0.75 µm) have been synthesized by this technique (Gielens *et al*., 2002).

Zhao *et al*. (2000) produced $Pd_{76}Ag_{24}$-membranes approximately 1 µm thick on porous ceramic graded with γ-alumina by magnetron sputtering. They measured an H_2 permeance of 90 m^3/m^2h*atm, with a selectivity of 50 at 462°C. They observed a columnar grain structure in the deposited layers when the substrate temperature was low (less than 350°C). They achieved better selectivity by utilizing a higher substrate temperature (350 - 400°C) which allowed for greater diffusion of surface Pd-atoms,

suppressing the columnar structure during the deposition. Regardless, their best membranes still lost selectivity when changing temperatures in the range 300 - 500°C. They suggested that the loss of selectivity by leak growth was due to sintering of the Pd/alloy-grains at temperatures greater than 411°C. It was unclear if they had good selectivity stability below 411°C because the testing times were not reported.

Gielens *et al*. (2002) synthesized a 0.75 µm thick $Pd_{77}Ag_{23}$-membrane on a non-porous silicon substrate by magnetron sputtering; they then chemically etched 5 µm pores into the substrate from the reverse side. They measured a hydrogen permeance of 153.2 $m^3/m^2h*atm^{0.5}$ with a selectivity of 1,500 at 450°C, utilizing an inert sweep gas to establish a partial pressure difference. The membranes prepared by magnetron sputtering were roughly the same thickness and had nearly the same permeance as those prepared by vacuum electroplating. Unfortunately, no long-term testing of these membranes has been conducted so no statements could be made on their selectivity stability.

2.2.3.d. Chemical vapor deposition

Chemical Vapor Deposition (CVD) is a plating technique accomplished by the decomposition of an organo-metallic species on the surface of the object to be plated. An organo-metallic such as palladium bis(acetylacetonate)-complex is evaporated at a low pressure and circulated around a hot (200 - 300°C) substrate. When the organo-metallic species comes in contact with the substrate, decomposition occurs leaving the metal deposited on the substrate. By controlling the pressure, the temperature of evaporation, and the temperature of deposition, the rate of deposition can be well controlled. Membranes as thin as 3.2 µm have been prepared on porous substrates with this technique (Uemiya *et al*., 2001).

Jun and Lee (2000) synthesized Pd, $Pd_{80}Ni_{20}$, and $Pd_{70}Nb_{30}$-membranes by CVD of metal-$(C_3H_5)(C_5H_5)$ precursors onto nickel-powder-graded PSS. Their best performing membrane was a pure Pd-membrane, 5 µm thick, with a permeance of 141.1 m^3/m^2h*atm and a selectivity of 1,600 at 450°C. They reported *n*-values of one for all membranes. Their pure Pd-membrane had a significantly better selectivity than their

Pd/Ni and Pd/Nb-membranes because the H_2 permeability of the pure Pd was higher than either of the alloys, resulting in higher H_2 flux. The inert gas flux (0.001 – 0.002 m^3/m^2-h at a ΔP of 1 atm) was similar for each membrane, suggesting that the integrity of the CVD deposited layer was not dependent on the alloy composition.

Kajiwara *et al*. (2000) and Uemiya *et al*. (2001) synthesized membranes of pure iridium, rhodium, palladium, platinum, and ruthenium by chemical vapor deposition of metal-bis(acetylacetonato) precursors onto porous alumina substrates. Their best performing membrane was also the pure Pd-membrane (3.2 μm thick) with a permeance of 80.3 m^3/m^2h*atm and a selectivity of 240 at 500°C. They suggested that for Rh and Ir, the rate limiting step was surface adsorption in conjunction with surface diffusion of H-atoms, which significantly limited the H_2 flux through those metal-layers. The properties of the membranes prepared by these different investigators can be found in Table 2.7.

2.2.3.e. Electroless plating

Electroless plating is plating of metal ions out of an electrolyte solution by reaction with a chemical reducing agent. The metal salts to be plated are dissolved along with stabilizing ligands to moderate their availability in the solution. A solution of the reducing agent (NH_2HN_2, NaH_2PO_2, $(CH_3)_2S$*BH_3, etc.) is added and the substrate is immersed in the solution. The reaction is autocatalytic so the substrate is usually activated chemically in advance by some manner. A typical palladium electroless plating bath composition is shown in Table 2.8.

Table 2.8. Palladium electroless plating bath composition (Ma *et al*., 2008).

Component	Concentration
$Pd(NH_3)_4Cl_2$*$2H_2O$	4.0 g/L
NH_4OH (28%)	198 mL/L
Na_2EDTA*$2H_2O$	40.1 g/L
NH_2NH_2 (1M aq.)	5.7 mL/L

Keuler and Lorenzen (2002) synthesized $Pd_{77}Ag_{23}$-membranes by electroless plating on porous α-alumina supports with thicknesses in the range of 1.4 - 2.2 µm. Their best performing membrane had a hydrogen permeance of 49.2 m^3/m^2h*atm with a selectivity of 330 at 410°C. They reported the *n*-value to be one. They identified the leak growth mechanism as pinhole formation, which they suggested was accelerated by changing temperature while the membrane was in H_2. They achieved the high H_2 permeance by first annealing in Ar at 550°C, followed by surface oxidation in air at 310°C, followed by surface reduction in H_2 at 400°C. They suggested that this procedure both annealed the Pd/Ag-layer to allow for good selectivity stability and increased the surface roughness to allow for a high H_2 flux.

Tong *et al*. (2004; 2005) synthesized pure Pd-membranes by electroless plating on PSS with aluminum hydroxide grading. Their best performing membrane had an approximate thickness of 8 µm and a hydrogen permeance of 38.5 $m^3/m^2h*atm^{0.5}$ at 500°C. They reported a selectivity of 800 but did not report the length of testing. They indicated that the thin Pd-layer with high selectivity was a result of plugging the support pores with the porous aluminum hydroxide grading.

Roa *et al.* (2002; 2003a; 2003b) synthesized a series of Pd/Cu-membranes (1 - 12 µm thick) by sequential electroless plating of copper and palladium on porous alumina supports. Their best performing membrane was 1.0 µm thick (10 at% Cu), had a hydrogen permeance of 95.0 $m^3/m^2h*atm^{0.5}$, and a selectivity of 1,390 at 350°C. They attributed the remarkable selectivity stability of one membrane over 1,400 hours to accidental air exposure during testing at 350°C, followed by additional Pd/Cu plating to achieve a high selectivity. They suggested that the nano-porous structure of the Pd-oxide layer created by the accidental air exposure had very good surface properties for the plating of the additional Pd/Cu-layer.

Ayturk *et al*. (2007) and Ma *et al*. (2007) developed a method for preventing intermetallic diffusion from the support by oxidizing the support surface, followed by application of a porous Pd/Ag-layer, followed by the dense Pd-layer. The oxide layer prevented intermetallic diffusion of the support elements into the Pd-layer. The Pd/Ag-layer both prevented intermetallic diffusion and allowed for a smoother surface for

dense Pd-plating. That same group reported a 7.9 µm thick membrane with a hydrogen permeance of 68.5 $m^3/m^2h*atm^{0.5}$ and a selectivity of 149. They also reported permeance and selectivity stability over 1,400 hours of testing, made possible by the intermediate oxide and porous Pd/Ag-layers (Mardilovich *et al.*, 2006).

Electroless plating results in a uniform layer regardless of membrane shape or surface contours, allowing for easy scale-up. Non-toxic and only moderately corrosive solutions for electroless plating (such as that described in Table 2.8) make the technique amenable to commercial use. Lastly, membranes possessing high permeability and selectivity as well as good long-term stability have been prepared by electroless deposition making this technique very attractive for industrial applications.

2.3. WGS catalytic membrane reactor

Most commonly, the term "Catalytic Membrane Reactor" (CMR) refers to a reactor where a membrane is utilized to introduce a reactant into a reacting mixture as well as to potentially catalyze the reaction on the membrane surface. For the purposes of this study however, CMR will refer to a subtype of Packed Bed Reactor (PBR) in which a selective membrane extends along the length of the reactor and is in contact with the reacting mixture. The membrane, which is selectively permeable to one of the reaction products, continuously separates the product from the reacting mixture (Shu *et al.*, 1991; Marcano and Tsotsis, 2002). CMR's have been utilized to improve yields on many dehydrogenation reactions through the selective removal of hydrogen. Sheintuch and Dessau (1996) performed the dehydrogenations of propane and of isobutane utilizing $Pd_{75}Ag_{25}$-tubes to selectively remove hydrogen from the reaction mixture. They observed yields of propylene and isobutene in significant excess of the traditional PBR for a variety of the experimental conditions tested. Uemiya *et al.* (1991b) performed methane steam reforming using a porous glass supported Pd membrane to selectively remove hydrogen from the reaction mixture. They also observed CH_4 conversions in significant excess of the equilibrium values. The *in situ* separation of products is often beneficial in at least two ways: process intensification and overcoming equilibrium limitation. The coupling of the separation step of a process (by the membrane) with the reaction step can increase throughput and lower the energy and cost associated with

that process. Economic analyses suggest that many industrial processes could be optimized by the use of a membrane reactor although few have yet been employed (Shu *et al*., 1991; Marcano and Tsotsis, 2002).

According to Le Chatelier's principle, when a change (in pressure, temperature, concentration, etc.) is imposed on a chemical system in equilibrium, the system will react by opposing that change. If a reaction product is removed from the system causing the concentration of that product to be reduced, the system will respond by forming more of that product. In the case of a WGS reactor incorporating a palladium membrane, hydrogen is removed from the reacting gas mixture *in situ,* which causes the system to shift further in the direction of H_2 and CO_2 formation.

The WGS reaction is also amenable to the application of a CMR, resulting in both process intensification and increased hydrogen yield, beyond the equilibrium conversion (Kikuchi *et al*., 1989; Uemiya *et al*., 1991a). A cut-away drawing of a shell and tube WGS CMR is shown in Figure 2.7. The reaction occurs in the catalyst bed surrounding the membrane while hydrogen is selectively separated from the reaction mixture. The resulting effluent streams are composed primarily of hydrogen in the permeating stream and primarily of CO_2 and H_2O in the retentate stream.

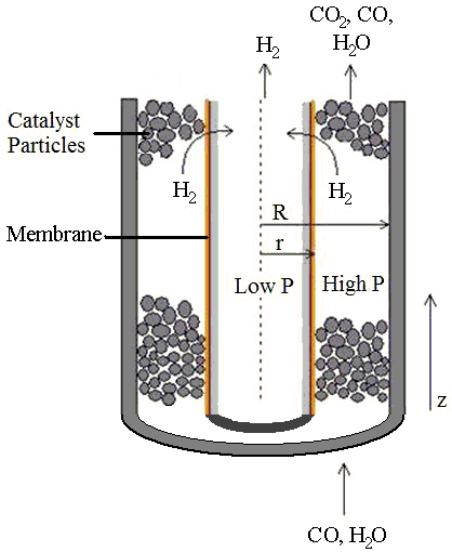

Figure 2.7. Axial cross-section of a shell and tube WGS CMR.

2.3.1. The WGS CMR system

Several studies in the literature exploring the fundamental characteristics of the WGS reaction in CMR's have been performed. A variety of palladium membranes have been used in these studies including self supported foils, Pd-alloy/ceramic supported membranes, Pd-alloy/porous glass supported membranes, and Pd-alloy/PSS membranes. The selective layers used were Pd, Pd/Ag, Pd/Cu, as well as microporous silica. All of these studies have demonstrated that yields in significant excess of the PBR equilibrium conversion were possible for both CO/H_2O and syngas feeds.

Kikuchi *et al*. (1989) and Uemiya *et al*. (1991a) performed WGS CMR experiments with 20 μm thick Pd-membranes supported on microporous glass tubes, including iron-chrome oxide catalyst. Their most successful result was 98% CO conversion (20% in excess of equilibrium) at 400°C, 5 atma, a steam to carbon ratio of 1.0, and a gas hourly space velocity (GHSV at STP) of 630 h^{-1} (Kikuchi *et al*., 1989). They also utilized a permeate side sweep flow of Ar with an Ar/CO ratio of 16. They utilized an one-dimensional steady state model to simulate the WGS CMR, finding excellent agreement between their simulation and experimental results (Uemiya *et al*., 1991a). They utilized the model to determine the relationship between membrane thickness and CO conversion for various feed rates. They found that reducing the membrane thickness increased conversion until the membrane was approximately 10 μm thick, after which the system was reaction rate limited and no further advantage was gained. They also found a clear relationship between the reaction pressure and the conversion; higher pressure resulted in higher conversion due to the removal of H_2 from the system and the greater residence time for the reaction. They found a clear relationship between conversion and GHSV; lower GHSV resulted in higher conversion for the same reason (removal of H_2 and greater residence time). The group collected a broad range of consistent data, concluding that the extent of hydrogen removal by any means was responsible for the increased CO conversion.

Basile *et al*. (1996b) performed WGS CMR experiments with Pd membranes supported on porous ceramic tubes synthesized by MS, Physical Vapor deposition (PVD), and CVD, and including copper-zinc oxide catalyst. Their MS membranes were 10 μm thick,

their PVD membranes were 1.0 μm thick, and their CVD membranes were approximately 0.1 μm thick. Their best result was 98% CO conversion for their 0.1 μm thick CVD membrane at 323°C and a steam to carbon ratio of 2.2. Unfortunately, some of the experimental conditions (pressure, GHSV, and the use of a sweep gas) were unclear in their report. They concluded that the membrane prepared by CVD achieved the best results due to its low thickness, resulting in higher H_2 flux and recovery. The same group also experimented with a 0.2 μm thick Pd-membrane prepared by CVD on an alumina support (Basile *et al*., 1996a). The best conditions identified in that study resulted in greater than 99.8% CO conversion at 323°C, 1.2 atma, a steam to carbon ratio of 3.85, and a $GHSV_{STP}$ of 518 h^{-1}. They employed a permeate side sweep flow of N_2 with N_2/CO ratios of 0.09, 0.45, and 1.8. Their results displayed a maximum in CO conversion versus temperature at approximately 323°C which they attributed to a compromise between the kinetic reaction rate and thermodynamic considerations (the equilibrium value). They also observed that CO conversion in the greatest excess of the equililbrium CO conversion (94%, 10% in excess of the equilibrium conversion), was achieved with a low steam to CO ratio of 0.96. Although Basile *et al*. (1996b) did not offer a reason for this, it was most likely due to a lesser dilution of (and therefore greater removal of) hydrogen from the reaction mixture, with respect to that which occurred with more steam present.

The same group later experimented with 70 μm thick Pd-foils on tubular ceramic supports packed with copper-zinc oxide catalyst (Criscuoli *et al*., 2000). This study utilized simulated syngas mixtures as feeds; the feed gas compositions, on a dry basis, are listed in Table 2.9. They pointed out that the equilibrium conversion for any mixture of syngas and steam would be lower than that for a mixture of CO and H_2O (at the same temperature, with the same steam to CO ratio) because the mixture was already shifted to some extent. In this case, the membrane reactor was even more necessary to achieve high CO conversion because the presence of H_2 and CO_2 in the syngas had an adverse effect on further CO conversion. The best result obtained by Criscuoli *et al*. (2000) was 99.5% conversion (16% in excess of the PBR equilibrium conversion) for Gas A (Table 2.9) at 322°C, 1.0 atma, a steam to carbon ratio of 1.1, and a $GHSV_{STP}$ of 350 h^{-1}. They employed a permeate side sweep flow of N_2 with a N_2/CO ratio of 3.2.

They concluded that the greatest CO conversion values could be achieved by using mixed gas feeds which were initially very far from thermodynamic equilibrium (meaning that the PBR equilibrium conversion for the conditions was high).

Table 2.9. Syngas mixtures utilized in literature studies, on a dry basis.

	% CO	% CO_2	% H_2	% N_2	% CH_4	Reference
Gas A	32	12	4	52	-	Criscuoli *et al*., 2000
Gas B	12.3	11.5	75	-	1.2	Criscuoli *et al*., 2000
Gas C	27	-	73	-	-	Criscuoli *et al*., 2000
Gas D	28.6	71.4	-	-	-	Tosti *et al*., 2003
Gas E	53	12	35	-	-	Iyoha *et al*., 2007a
Gas F	15.6	7.1	75.2	-	2.1	Damle *et al*., 2008

The same group later experimented with Pd (70 μm thick) and Pd/Ag (50 μm thick) foils supported on porous ceramic tubes (Basile *et al*., 2001). The best result obtained was 99.0% CO conversion (15% in excess of equilibrium conversion) utilizing the pure Pd membrane at 331°C, 1.0 atma, a steam to CO ratio of 1.0, and a $GHSV_{STP}$ of 210 h^{-1}. They employed a permeate side sweep flow of N_2 with a N_2/CO ratio of 12.3. Here they noted that the use of the permeate side sweep allowed for a higher H_2 driving force across the membrane, and therefore greater H_2 recovery, and therefore higher CO conversion. The same group again experimented with 50 μm thick Pd/Ag foils supported on porous ceramic tubes (Tosti *et al*., 2003). They presented excellent results with greater than 98% CO conversion at 325°C, 1.0 atma, steam to CO ratios of 1.0 and 1.5, and GHSV's of 420 – 2,500 h^{-1}. They utilized a permeate side sweep of N_2 with N_2/CO ratios of 3 - 14. Additionally they performed WGS CMR experiments with a mixed gas feed (Table 2.9, Gas D). They achieved a CO conversion of 96.6% at 325°C, 1.0 atma, a steam to CO ratio of 1.5, a $GHSV_{STP}$ of 2,500 h^{-1}, and a N_2/CO sweep ratio of 6. They observed the same basic relationships with pressure and GHSV as most previous studies did and attributed them to the same reason (greater H_2 recovery at higher

pressure and lower GHSV). They also observed a clear relationship between the steam to CO ratio and the CO conversion; a higher steam to CO ratio resulted in higher CO conversion. They concluded that the CMR could achieve significantly higher CO conversions than could be achieved at lower steam to CO ratios (less than 2.0) in a PBR. Utilizing a lower steam to CO ratio (less than 2.0) in the CMR was important because it allowed for a greater H_2 recovery via a higher H_2 partial pressure in the reaction mixture. The data collected by this group (Basile *et al*., 1996a; 1996b; 2001; Criscuoli *et al*., 2000; Tosti *et al*., 2003) was exceedingly wide ranging in both reaction conditions used as well as the types of membranes applied. This group was also the first to investigate the WGS reaction with a syngas feed in the CMR. In regards to syngas feed experiments, they concluded that all the same trends were present regarding feed composition, temperature, and pressure conditions as when only CO and steam were used as the feed.

Iyoha *et al*. (2007a) experimented with 125 μm thick Pd and $Pd_{80}Cu_{20}$ self supported foils and mixed gas feed (Table 2.9, Gas E). Their setup utilized no WGS catalyst. The best result obtained was 99.7% CO conversion for the Pd membrane (65% in excess of the equilibrium conversion) at 900°C, 4.1 atma, a steam to carbon ratio of 1.5, and a $GHSV_{STP}$ of 1,800 h^{-1}. The high testing temperature allowed for the reaction to proceed uncatalyzed. They experimented at such a high temperature in order to test sulfur resistance of the $Pd_{80}Cu_{20}$-alloy. They utilized a counter-current sweep gas of an unspecified composition and flow rate. They concluded that high conversion could be achieved with a membrane reactor at 900°C with no catalyst present. They hypothesized that most of the reaction was occurring on the surface of the Pd and Pd/Cu-membranes. They also pointed out that with the (presumably high rate of) counter-current sweep gas, H_2 recovery of over 95% was possible, shifting the CO conversion to a very high level (99.7%) based on Le Chatelier's principle. They noted that the presence of up to 60 ppm H_2S in the feed caused a significant drop in H_2 recovery because of the blocking of Pd-surface sites for H_2 adsorption, and also a significant drop in CO conversion because of the reduced catalytic activity of the Pd-surface for the WGS reaction. Iyoha *et al*. (2007a) performed several long-term WGS CMR experiments lasting over 70 hours each. They did not observe any degradation of

the membranes under WGS conditions (when no H_2S was present) although this was unsurprising given the thickness (125 μm) of the membranes tested.

Brunetti *et al*. (2007a) performed WGS CMR experiments with an 1 μm thick silica membrane supported on PSS, and incorporating copper-zinc oxide catalyst. The best result obtained was 95% CO conversion (8% in excess of the equilibrium conversion) at 228°C, 4 atma, a steam to carbon ratio of 1.0, and a $GHSV_{STP}$ of 2,000 h^{-1}. No sweep gas was used. The silica membrane had separation factors ranging from 15 - 45 for H_2/N_2, H_2/CO, and H_2/CO_2 (and depending on temperature) determined by GC measurement of mixed gas permeation experiments. Separation factors this low were inadequate for the production of high-purity hydrogen, but still high enough to allow for a CO conversion in excess of the equilibrium conversion. They observed that at a higher pressure (greater than 4 atma) the CO conversion was no longer aided by a further increase in pressure. At a higher pressure the separation factor of the membrane was lower, so the permeation of CO and CO_2 significantly affected the overall CO conversion. The results made clear that a highly selective membrane was necessary for high reaction pressure operation.

Barbieri *et al*. (2008) performed WGS CMR experiments with a 60 μm thick self supported Pd/Ag-foil. They designed a CMR with the membrane mounted only in the second half of the catalyst bed, essentially a PBR in series with a CMR. They postulated that their design would be optimal for WGS feed mixtures with low H_2 concentrations since the partial pressure of H_2 would not allow for permeation until some WGS conversion had taken place. The best result obtained was 94% CO conversion (8% in excess of the equilibrium conversion) at 300°C, 6 atma, a steam to carbon ratio of 1.0, and a $GHSV_{STP}$ of 2,070 h^{-1}. The reactor design allowed for significantly less membrane area (and therefore a lower cost), while still achieving high CO conversion and H_2 recovery with regard to the moderate feed flow rate (2,070 h^{-1}). The primary difficulty with utilizing thin, self supported foils was that no significant trans-membrane pressure could be applied; this study was limited to a pressure difference of 5 atm. These studies, as well as others (Brunetti *et al.,* 2007b; Barbieri *et al.,* 2008;

Damle *et al.,* 2008) have shown that a higher trans-membrane pressure was beneficial to the H_2 recovery and the CO conversion.

Damle *et al*. (2008) experimented with 4 µm thick Pd membranes supported on PSS, incorporating iron-chrome oxide catalyst, with mixed gas feed (Table 2.9, Gas F). The best result obtained was 84% CO conversion (35% in excess of equilibrium conversion) at 375°C, 10.2 atma, and a steam to carbon ratio of 1.2. No sweep gas was used and the GHSV was unclear. Damle *et al*. (2008) constructed and tested a pilot scale WGS CMR with a total membrane area of 300 cm^2 in a three tube configuration. They ran experiments in the temperature range of 375 - 550°C and operated at high pressures (6.8 - 10.2 atma), achieving a H_2 production rate as high as 14 L/min. Their results demonstrated the scalability of the WGS CMR and the effectiveness of a multi-tube-in-tube reactor design. They pointed out that the production rate of H_2 was strongly dependant on the pressure due to the driving force of H_2 across the membrane. They also pointed out that the H_2 production rate was strongly dependent on the H_2 recovery (with higher production rates occurring at lower values of H_2 recovery) although they did not discuss the reason for this trend.

The pressure and temperature ranges for the literature studies discussed in this section are outlined in Figure 2.8. For each literature study, the highest CO conversion is noted with a star.

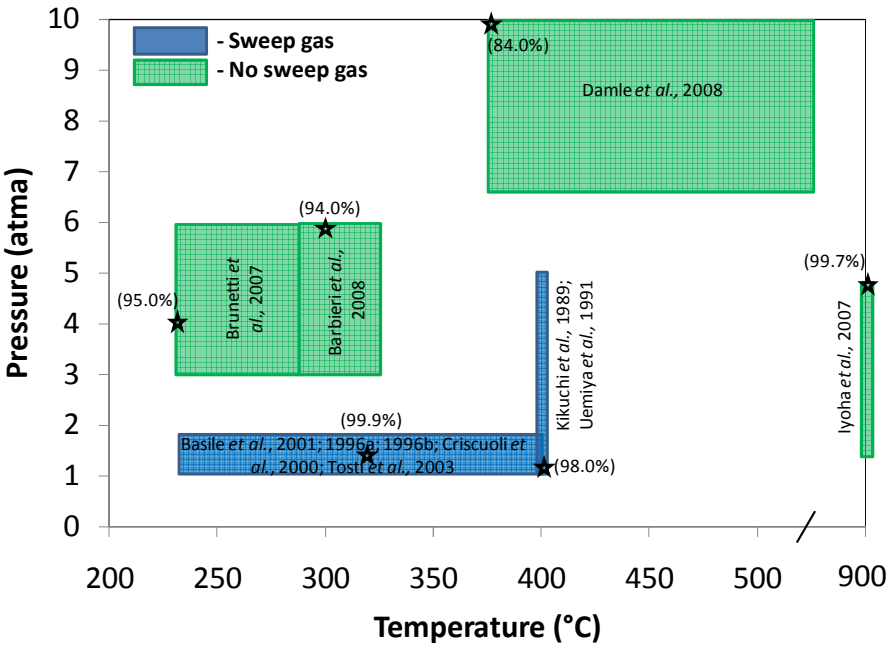

Figure 2.8. WGS CMR studies in the literature with regards to the feed conditions.

More important than the specific results achieved in the various studies were the trends identified in those studies between the feed conditions and the resulting yields. As in traditional PBR's, the CO conversion in the WGS CMR was enhanced by higher steam to carbon ratios (Basile *et al.*, 1996a; 1996b; Uemiya *et al.*, 1991a). It was clear that the higher CO conversion in the membrane reactor over a packed bed reactor was a direct result of the *in situ* removal of hydrogen from the reacting gas mixture (Damle *et al.*, 2008; Uemiya *et al.*, 1991a). Effects either with regards to the feed conditions or the membrane properties that maximized the H_2 recovery subsequently increased the CO conversion. Lowering the feed rate also allowed for increased CO conversion, both through greater residence time with the catalyst as well as more complete H_2 recovery (Basile *et al.*, 1996b; Kikuchi *et al.*, 1989; Uemiya *et al.*, 1991a). Membranes with greater H_2 permeances, either through thickness reduction, alloying, or composite design also proved effective in increasing H_2 recovery and CO conversion, but only in situations where the gas phase mass transfer was not rate limiting (Basile *et al.*, 1996b). A greater H_2 partial pressure difference across the membrane either by increasing the

total pressure difference or by the use of a permeate side sweep gas has also been shown to result in a greater CO conversion (Barbieri *et al*., 2008; Basile *et al*., 1996b; Kikuchi *et al*., 1989).

The effect of the reaction temperature on WGS CMR yield was not as simple as the effects of the other feed conditions. At lower temperatures the equilibrium constant was higher but the reaction rate was lower and the permeance of Pd-based membranes was lower. At higher temperatures the reaction rate was higher and the permeance of Pd membranes was also higher, but the equilibrium constant was lower. The presence of these opposing factors suggested the possibility of a maximum in CO conversion at some intermediate temperature. Several of the studies listed above performed WGS CMR experiments at several temperatures with identical feed conditions. Basile *et al*. (1996b) observed a maximum in CO conversion with regard to temperature at 323°C, 1.1 atma, a steam to CO ratio of 0.96, and GHSV's of 210 and 420 h^{-1}, utilizing a 0.2 μm Pd/alumina membrane. Barbieri *et al*. (2008) observed a maximum in CO conversion with regard to temperature at 300°C, 6 atma, a steam to CO ratio of 1.0, and GHSV's of 2,070, 3,180, and 4,550 h^{-1}, utilizing a 60 μm unsupported Pd/Ag membrane. They also observed a maximum in the CO conversion with regard to temperature at 300°C with similar conditions in their traditional packed bed reactor. Both of these studies utilized low-temperature shift copper-zinc oxide catalyst. Unfortunately, no studies presented temperature trend data utilizing high-temperature shift iron-chrome oxide catalyst. Additionally, the composition of the mixed gas feed would likely affect the optimal reaction temperature but no studies have been conducted to quantify that relationship.

2.3.2. Modeling of the WGS CMR system

There is a great deal of modeling work available in the literature dealing with membrane reactors in general as well as several dealing specifically with the WGS CMR. The WGS CMR system is inherently two-dimensional (2-D). The flow of the reaction gas mixture is axial, while the separation of H_2 through the membrane is radial, therefore concentration gradients can exist in both dimensions. A 2-D WGS CMR model was utilized by Chiappetta *et al*. (2006; 2008) and Tiemersma *et al*. (2006) to simulate the radial concentration profiles for the WGS and Methane Steam Reforming (MSR) CMR's. If the

aspect ratio of the reactor (length divided by characteristic width) is greater than approximately ten, the assumption can be made that no significant radial concentration gradient exists (Kumar *et al.*, 2006). This assumption simplifies the model immensely and allows for a one-dimensional (1-D) set of equations to be applied. Ayturk *et al.* (2009) utilized a 1-D model to simulate a MSR CMR. To validate the model they reproduced the CH_4 conversions of nine experimental and modeling studies performed in the literature, including both PBR and CMR cases; the simulation results correlated to within 99% of the reported data.

Two types of 1-D models have typically been applied to membrane reactors, a steady state model which assumes plug flow behavior, and an unsteady state model which approximates a PBR by several Continuous Stirred Tank Reactors (CSTR's) in series. The 1-D steady state model is diagramed in Figure 2.9 (Ayturk *et al.*, 2009; Barbieri *et al.*, 2001; Basile *et al.*, 2003; Brunetti *et al.*, 2007b; Kumar *et al.*, 2006).

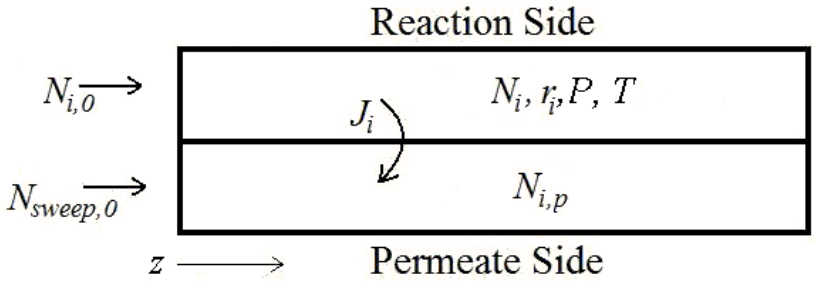

Figure 2.9. Diagram of a 1-D, non-isothermal, steady state membrane reactor system.

In Figure 2.9 N_i [kmol/h] is the molar flow rate of component *i* on the reaction side, with *i* representing each gas species present, $N_{i,p}$ [kmol/h] is the molar flow of each species on the permeate side, r_i [kmol/kg-h] is the rate of formation or consumption of species *i*, *P* [atma] is the pressure, and *T* [K] is the temperature. The system was represented mathematically by a mass balance (*dF/dz*) for each species in the reaction and permeate mixtures, energy balance (*dT/dz*), and a momentum balance (dP/dz), all as a function of reactor position *z* [m]. This model did not take into account any thermal or

mass dispersion in the axial direction. It also did not take into account any mass, heat, or momentum transfer in the radial direction.

This model has been solved by integrating numerically along *z* with Euler's method and, more recently, by the more precise Runge-Kutta method. Uemiya *et al*. (1991a) utilized this model to simulate the WGS CMR system varying GHSV, steam to CO ratio, reaction pressure, and membrane thickness. They found that CO conversion increased with lower GHSV, higher steam to CO ratio, higher reaction pressure, and lower membrane thickness (their results were discussed in greater detail in Section 2.3.1). Barbieri *et al.* (2001) used this model to demonstrate the operating capabilities of a MSR CMR employing only a sweep gas to establish a driving force across the membrane, and operating at the relatively low temperature of 350°C. They determined that a very high sweep rate (F_{sweep}/F_{feed} greater than 100) would be necessary in order to achieve the optimal conversion of CH_4. The same group also solved this model for a WGS CMR equipped with a counter-current sweep gas which utilized a Monte Carlo method to match feed and effluent conditions for the permeate side (Basile *et al.,* 2003). They demonstrated that operating with a counter-current sweep gas resulted in up to 2% greater conversion (99.9% overall) than could be achieved by using a co-current sweep for otherwise identical systems. The same group also solved this system of equations for a WGS CMR (minus the energy balance) in order to demonstrate the possible size reduction for a CMR achieving equivalent performance with a PBR, which was possible when using a higher reaction pressure (Brunetti *et al*., 2007b). They reported that a WGS CMR could be up to 65% smaller by volume than a WGS PBR while still achieving the same throughput and conversion. Ayturk *et al*. (2009) utilized the 1-D model to demonstrate a framework, involving a parameter called the Δ-index, by which the advantage of a CMR over a PBR could be quantified. They characterized the Δ-index for the operating parameters of the MSR CMR.

The alternative, but equally valid method of modeling a plug flow reactor (with or without a membrane) is to treat it as several CSTR's in series (Battersby *et al*., 2009; Luyben, 2000; Marigliano *et al*., 2003; Ramaswami *et al*., 2005; Reyes and Luyben, 2000). In each theoretical CSTR reaction conversion occurs on $1/N^{th}$ (for a system of N-

segments) of the catalyst bed and separation occurs on 1/Nth of the membrane area with ideal mixing in each segment. The 1-D unsteady state model is diagramed in Figure 2.10.

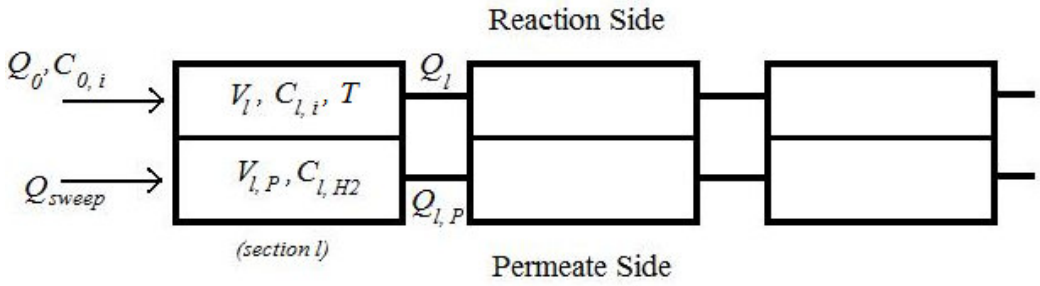

Figure 2.10. Diagram of a 1-D, non-isothermal, unsteady state membrane reactor system.

In Figure 2.10 $C_{l,i}$ [kmol/m^3] is the concentration of component *i* in the *l* segment, V_l [m^3] is the volume of the *l* segment, $V_{l,p}$ [m^3] is the volume of the permeate side of the *l* segment, T_l [K] is the temperature of the *l* segment. The system was represented mathematically by a mass balance (*dC/dt*) for each species in the reaction and permeate mixtures, and energy balance (*dT/dt*), both as a function of time for each segment. The total number of equations will be equal to the number of segments, times the number of species, times two (for reaction side and permeate side).The advantages of this model are that the time dependent mass balance equations can be established with little difficulty and if the right number of CSTR's are used, axial dispersion can also be approximated (Battersby *et al*., 2009).

This model has been solved by integrating numerically over time with the Runge-Kutta method or the Adams-Bashforth method, for each of *n*-segment sequentially. Luyben (2000) and Reyes and Luyben (2000) solved similar systems of equations for a WGS CMR which included control systems. Marigliano *et al*. (2003) utilized this model to demonstrate the maximum conversion which could be achieved by the use of a membrane reactor, for either the MSR or the WGS reaction, over a range of different feed and temperature conditions. They demonstrated that almost 100% conversion

could be achieved for both MSR and WGS reactions at 500 and 300°C respectively, with high sweep (F_{sweep}/F_{feed} equal to 10), and that such conversions were only limited in experimental systems by the activity of the catalyst and/or the permeance of the membrane. Battersby *et al*. (2009) also used this model for a WGS CMR in order to determine the effects of different operating parameters on the performance of the system. They found that higher conversion was achieved at lower feed rates, higher pressures, higher temperatures, and higher sweep rates, which agreed well with the experimental studies in the literature.

2.3.3. Economic considerations

The most significant barrier at present to the commercialization of the WGS CMR is the mechanical strength and long term stability of the palladium membranes (Hagg, 2009). The unsupported membranes prepared by cold rolling techniques (Barbieri *et al*., 2008; Basile *et al*., 2001; Tosti *et al*., 2003) had a limiting thickness of approximately 50 µm and were extremely fragile with thicknesses below 200 µm. Unsupported membranes were typically utilized with a sweep gas to establish a partial pressure driving force as they would be unable to withstand a larger total pressure difference. Membranes chemically deposited or sputtered onto porous ceramics or porous glass have been produced and were extremely thin, 0.2 - 10 µm (Basile *et al*., 1996b; Hou and Hughes, 2002), but were brittle and had low mechanical strength. The most promising membrane design for commercial CMR applications has been porous metal supported Pd or Pd-alloy membranes. Peters *et al.* (2008) prepared a 2.2 µm foil by magnetron sputtering and then supported it on a porous stainless steel tube. Damle *et al*. (2008) prepared 4 µm Pd membranes by electroless deposition onto yittria stabilized, zirconia graded stainless steel supports. Thin Pd-membranes, 5 - 20 µm, have been prepared by electroless deposition of Pd onto α-alumina graded stainless steel supports (Lin and Rei, 2001; Mardilovich *et al*., 2006). Membranes prepared in these ways have shown good long term stability as well as good mechanical strength, making them suitable for use in high pressure, commercial applications.

Four significant economic feasibility studies have been done to determine the potential industrial application of the WGS CMR (Criscuoli *et al*., 2001; Bracht *et al*., 1997; Damle

et al., 2008; Koc, 2012). Bracht *et al*. (1997) utilized a model developed by Koukou *et al*. (1996) as well as a hypothetical silica membrane to demonstrate that with a WGS CMR operating at the end of an IGCC plant, 80% CO_2 capture could be achieved at a cost of only 3.3% overall efficiency, down from 46.7% (efficiency for a plant with no CO_2 capture). Unfortunately the authors did not clearly explain the methodology of the calculations, resulting in seemingly unsupported conclusions. Criscuoli *et al*. (2001) used previously acquired experimental data (Criscuoli *et al*., 2000) to estimate the specifications for a CMR syngas plant of equivalent throughput to a syngas plant located in Augusta Italy. They demonstrated that the use of a membrane reactor with a Pd-membrane thickness of less than 20 µm both enhanced yields and reduced costs when compared to the existing syngas plant, largely by preventing the need for pressure-swing adsorption in the gas separation step. Damle *et al*. (2008) used the experimental data from their own pilot scale system in order to estimate the cost of hydrogen produced by a hypothetical syngas plant. They demonstrated that with a 4 µm Pd/PSS membrane hydrogen could be produced at a cost of $0.28/kg less than the existing techniques.

Koc (2012) utilized a Monte Carlo method to evaluate the net present value of an IGCC plant in the presence of uncertainty, incorporating a WGS CMR. She found that for a 550 MW plant, producing only electricity, having a total capital cost of $1.5 billion, and operating under a CO_2 tax of $25/ton, there was a net present value of up to $1.0 billion for the incorporation of a WGS CMR. The necessary membrane area was approximately 13,000 m^2, with an estimated capital cost of $134 million for the membrane reactor module. The positive net present value of the IGCC incorporating a WGS CMR over other methods of electricity generation (pulverized coal combustion and methane combustion) indicated the favorability of that process if a moderate CO_2 tax of $25/ton was enacted.

2.3.4. Other considerations

The separation of hydrogen by a palladium membrane is by no means a trivial or easily modeled process. Depending on the gas composition, the permeability of the membrane, and the flow properties, the concentration polarization around the

membrane could significantly impede the separation efficiency (Caravella *et al*., 2009; Peters *et al*., 2008). It has also been found that both steam and CO can lower the effective permeance of the membrane significantly by reversibly binding to the palladium surface and blocking the adsorption of H_2 (Hou and Hughes, 2002; Peters *et al*., 2008). Several mixed gas permeation studies have been done to determine the separation characteristics of palladium membranes operated under syngas feed streams. Hou and Hughes (2002) found that 2.2% of CO in H_2 caused an 18, 12, and 6% decrease in H_2 permeate flux from that of an equivalent mixture of H_2/N_2 at 275, 325, and 400°C, respectively for a Pd/Ag alumina supported membrane. The trend they observed suggested that the inhibitory effect of CO was greater at lower temperature which agreed with the physical adsorption mechanism. Gallucci *et al*. (2007) performed a series of experiments with varying compositions of H_2/N_2, H_2/Ar, H_2/CO_2, and H_2/CO at 250 and 350°C. They found that CO_2 caused an almost undetectable decrease in flux as compared with N_2. They also found that CO caused a 21 - 44% flux decrease for 5 - 50% CO in H_2 at 250°C; they did not observe any flux decrease for CO mixtures at 350°C. They suggested that CO did not bind significantly to the membrane surface at temperatures of 350°C and above. All of the above mentioned studies concluded that the permeation inhibition caused by CO was reversible. Reversible surface binding indicated a relatively low binding energy and a surface coverage equilibrium that was greater at lower temperatures. Brunetti *et al*. (2006) found that 50% CO caused no effect on permeance at 252 and 291°C when compared to a 50/50 mixture of H_2/N_2, for a silica membrane supported on PSS. This result was unsurprising since the transport of material through a silica membrane occurred through porous diffusion, not surface adsorption followed by solution and diffusion.

There was some discrepancy in the literature regarding the effects of steam on the H_2 permeance of Pd membranes. Hou and Hughes (2002) found that 2.0% of H_2O in H_2 caused a 61, 53, and 37% decrease in H_2 permeate flux compared to that of an equivalent mixture of H_2/N_2 at 275, 325, and 400°C respectively with their Pd/Ag membrane. Unemoto *et al*. (2007) observed a 54% decrease in H_2 permeance with 9.5% steam present at 172°C, but no detectable decrease with 9.5% steam present at 358°C with a Pd/Ag-membrane. Iyoha *et al*. (2008) reported very little effect (less than

3% permeance decrease when compared to an inert gas mixture) from the presence of 50% steam at 350 to 900°C in their Pd/Cu-membrane. It is yet unclear how steam affects the permeance of Pd/alloy-membranes. It is also unknown if some alloys may possess greater tolerance to surface inhibition by either CO or steam.

A potential obstacle to the commercialization of palladium CMR's is the chemical reactivity of palladium to trace impurities that are often found in industrial process streams. Industrial coal gasification streams often contain in excess of 1,000 ppm H_2S, a poison which is particularly harmful to palladium membranes as well as various catalysts. Only a minimal number of studies have attempted to characterize H_2S poisoning of palladium membranes and of those studies only a few have yielded some success in mitigating the poisoning effects by alloying. Pd/Au and Pd/Cu-alloys have shown limited resistance to lower ppm concentrations of H_2S at temperatures in the range of 300 - 500°C (McKinley and Nitro, 1976; Li *et al*., 2000; Iyoha *et al.,* 2007a; Pomerantz and Ma, 2009).

Pomerantz and Ma (2009) demonstrated that a porous stainless steel supported $Pd_{92}Cu_8$-alloy membrane retained 20% of its permeance when exposed to 43 ppm H_2S at 500°C. The alloy was synthesized by plating a layer of Cu on the surface of a pure Pd membrane followed by annealing at 500°C. They also performed similar poisonings at 350, 400, and 450°C. After poisoning with H_2S they again tested with pure H_2, noting the extent to which the H_2 permeance returned to its pre-poisoned level, they termed this as "recovery" ($F_{H2,f}/F_{H2,i}$, where $F_{H2,f}$ was the pure H_2 permeance after poisoning and $F_{H2,i}$ was the permeance before poisoning). They found that the poisoning effect was less at higher poisoning temperatures and that the extent of recovery was greater at higher recovery temperatures (up to 100% recovery at 450 and 500°C). They attributed this to the thermodynamic equilibrium of the sulfur adsorption, with a higher degree of surface coverage at lower temperature.

McKinley and Nitro (1976) demonstrated that a $Pd_{60}Au_{40}$-membrane retained 65% of its permeability when exposed to 20 ppm H_2S at 350°C. Iyoha *et al*. (2007a) investigated the effects of sulfur poisoning on the membrane in a WGS membrane reactor (with no catalyst present) for both pure Pd and Pd/Cu 125 µm thick unsupported membranes.

They found relatively little effect of up to 1,000 ppm H_2S at temperatures of 900°C. The results of the studies conducted by Pomerantz and Ma (2009) and Iyoha *et al*. (2007a) indicated that the testing temperature played a key role in the H_2S tolerance, with higher temperature allowing for greater resistance to poisoning. Pomerantz and Ma (2009) observed significant poisoning with a relatively low concentration of H_2S while Iyoha *et al*. (2007a) observed no poisoning with a high concentration of H_2S, but at a much higher temperature. The reaction that occurs between H_2S and Pd to form bulk Pd_4S has a negative Gibbs free energy, and therefore occurs to a greater extent at lower temperatures (Mundschau *et al.,* 2006; Chen, 2011). Mundschau *et al*. (2006) demonstrated that a $Pd_{80}Cu_{20}$-membrane retained 80% of its permeability when exposed to 20 ppmv H_2S at 320°C although their results were not well documented. A more thorough discussion of the H_2S poisoning phenomenon is presented in Chapter 9.

2.4. Summary

A great deal of work has been done to fabricate thin, supported Pd-membranes, resulting in high permeance (greater than 50 m^3/m^2-h-$atm^{0.5}$) and high selectivity (greater than 1,000) membranes that seem complimentary to the IGCC process. Unfortunately, relatively few membranes have been fabricated on lower cost stainless steel supports and with well established, reproducible methods. An additional shortcoming is that few of the membranes in the literature have been tested for extended periods of time under mixed gas and reaction conditions. A good deal of work has been done in the application of Pd-membranes to the WGS reaction in order to both increase reaction conversion and simultaneously separate H_2 from the reaction mixture. Up until now the majority of the studies have utilized low temperatures (250 – 350°C), low pressures (less than 6 atma), and low feed rates (less than 1,000 h^{-1}) due to the fragile nature of the membranes used. A more comprehensive testing of the WGS CMR and the supported Pd-membranes, with conditions approaching that of the IGCC process is needed.

3. EXPERIMENTAL

3.1. Introduction

This chapter thoroughly describes the experimental apparatus and procedures utilized in this thesis. Section 3.2 describes specific methods for membrane synthesis, by which most of the membranes utilized were prepared. The membrane synthesis methods were initially developed by Ma *et al*. (2000; 2004; 2007; 2010), Ma and Guazzone (2010), Ayturk *et al*. (2006), and Koc (2012). Aberrations from the published methodology, for the preparation of some specific membranes are discussed in Chapter 4. Section 3.3 describes the method for coupon synthesis which was also based on previous literature (Ma *et al.,* 2000; 2007). Sections 3.4 and 3.5 describe the experimental setups for the mixed gas and WGS CMR experiments. The experimental apparatus in those sections were designed based on systems used by colleagues in the Center for Inorganic Membrane Studies (Ayturk, 2007; Chen, 2011; Guazzone, 2005), with modifications for H_2O vaporization, pre-heating, pre-mixing, H_2O condensation, better temperature control, better pressure control, and analysis of gas composition. Sections 3.4 and 3.5 also explicitly describe the protocol by which mixed gas and WGS CMR experiments were conducted. Amendments to that protocol for the utilization of H_2S containing mixtures are described in Chapter 9. Section 3.6 describes the post-testing characterization procedures. Leak testing, SEM, and XRD analysis were conducted by similar procedures as those utilized by colleagues in our laboratory (Ayturk, 2007; Guazzone, 2005).

3.2. Porous metal supported Pd-membrane synthesis

The membrane supports used in this study were PSS_{316L} and porous Inconel (PI) tubes (6 cm length, 1.3 cm OD, Media Grade 0.2 μm), capped at one end, and welded to a stainless steel tube at the other, purchased from either Mott Metallurgical Corp. (Farmington, CT) or Chand Eisenmann Metallurgical (Burlington, CT). A block diagram of the specific membrane synthesis procedure, Synthesis Method A, is shown in Figure 3.1[a]. The support tubes were heated in air for 12 hours at 600°C (PSS) (or 700°C for

PI) to generate an oxide layer as the intermetallic diffusion barrier layer and then graded with 0.02 - 1.0 µm γ and α-alumina slurry mixture (Alfa Aesar, 99.98% min) via the method reported by Ma *et al*. (2007). A composite Pd/Ag-layer, acting as additional grading and intermetallic diffusion barrier was prepared via the method reported by Ma *et al.* (2007) and Ayturk *et al*. (2006). Pd was then plated by electroless deposition until the membrane became dense. The composite Pd/Ag-layer was not thought to alloy significantly with the subsequent Pd-layers (Ayturk *et al*., 2006) so the completed membrane was supposed to have properties in line with pure Pd-membranes. In some cases where higher temperature testing (greater than 450℃) was not planned, membranes were prepared without a composite Pd/Ag-layer. In these cases, additional grading steps were conducted to establish a smooth surface. A block diagram of the specific membrane synthesis procedure, Synthesis Method B, is shown in Figure 3.1[b] with grading layers based on Koc (2012) and Ma and Guazzone (2010). A detailed account of both synthesis procedures as well as the composition of all prepared solutions is presented in Appendix B.

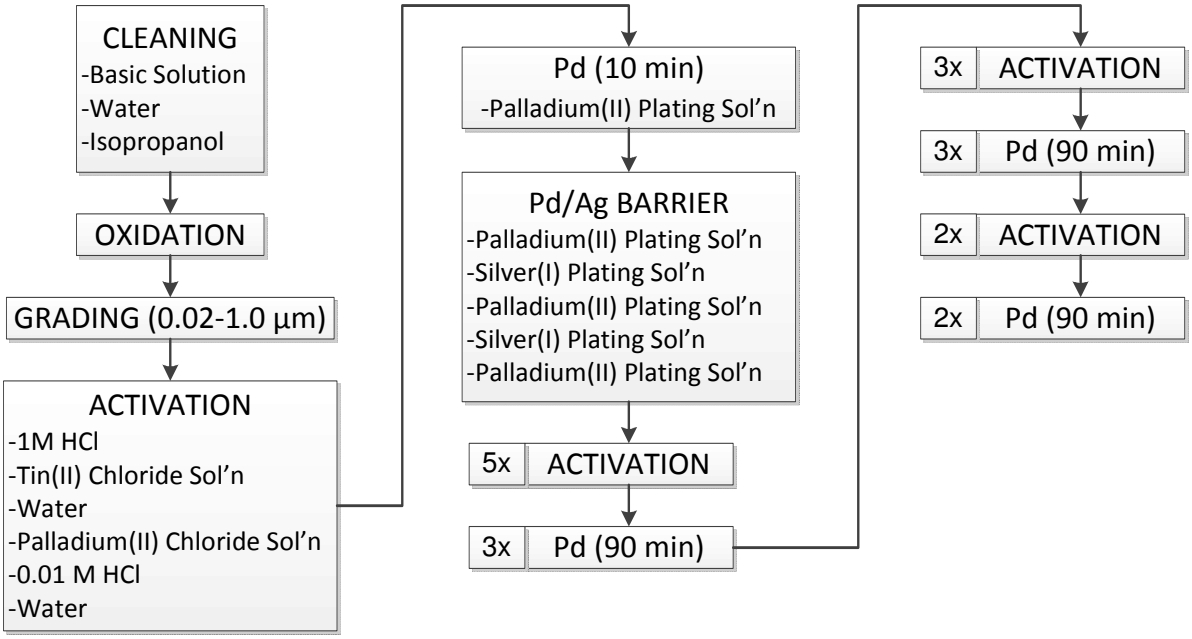

[a]

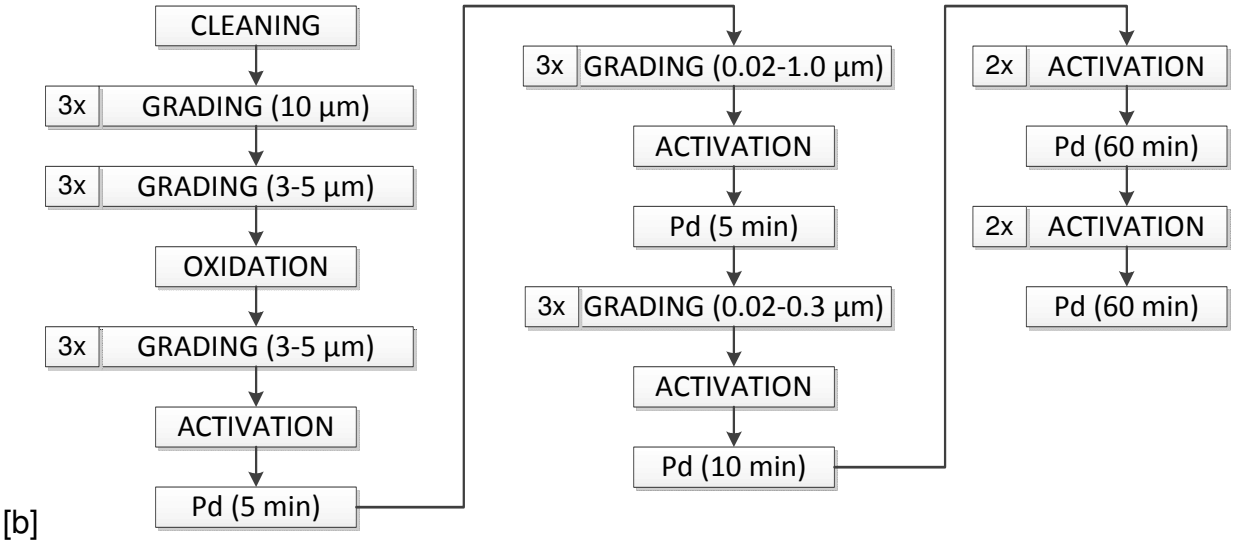

[b]

Figure 3.1. Block diagram of the membrane synthesis [a] Synthesis Method A [b] Synthesis Method B (Further details given in Appendix B).

The appearance of the completed membrane ranged from a dull steel color to a mirror finish depending on the aggressiveness of the polishing treatments employed as shown in Figure 3.2[a] and [b] of membranes AA-29 and AA-14 respectively. Membrane AA-29 was not polished during the synthesis, membrane AA-14 was aggressively polished after most synthesis steps and buffed after the final step.

[a]

[b]

Figure 3.2. Pictures of synthesized membranes [a] Membrane AA-29, unpolished [b] Membrane AA-14, polished and buffed.

3.2.1. Gravimetric thickness

The gravimetric thickness, δ_{Pd} [μm], of the deposited metal was estimated by dividing the weight gain after plating, Δw [g], by the plated area, A [cm^2], and the density of the metal, ρ_{Pd} [g/cm^3], as shown in Eq. **3.1**.

$$\delta_{Pd} = \frac{\Delta w}{A * \rho_{Pd}} * (10^4 \mu m/cm) \qquad \textbf{3.1}$$

The thickness could be underestimated by this technique if there was any corrosion of the support due to the strongly alkaline plating solution. Additionally, the thickness could be overestimated by this technique if the plating solution was not completely rinsed from the support before drying, resulting in trapped salts and EDTA.

3.2.2. IPA bubble test

Defects on the membrane surface were identified by the Isopropyl Alcohol (IPA) bubble test in which a pressure of 1.3 – 2.0 atma was applied to the tube-side and then the membrane was submerged in IPA. Bubbles were then visible emerging from any defects. During the membrane synthesis this technique was used to determine if any additional Pd-plating was required on specific areas of the membrane surface. Pd-plating on a specific area involved covering the membrane with Teflon tape, leaving the defective area exposed, then electroless plating 5 – 10 μm of additional Pd.

3.2.3. Mechanical polishing

Membranes were mechanically polished for two different reasons, either to smooth the surface features and/or to lower the overall thickness of the dense Pd-layer. Mechanical polishing was conducted by mounting the membrane tube in a lathe and rotating at 100 – 200 rpm and polishing first with a fine SiC paper (600 grit, ca. 16 μm particles) then with a finer (1200 grit, ca. 8 μm particles). For each stage of polishing 1 - 5 strips (1 x 10 cm) of the paper were cut, then hand-held at both ends for application to the rotating membrane. The strip was held so that it was in contact with about $1/4^{th}$ of the circumference of the membrane, then slid from one end to the other along the axis of the membrane, while maintaining gentle to moderate pressure. By gravimetric thickness

measurements, one strip of 600 grit SiC-paper would remove about 0.2 μm of dense Pd, if greater removal was desired more strips were used. After polishing with SiC-paper the membrane was rinsed thoroughly with IPA and H_2O to ensure that all SiC-particles were removed. If washing was not thorough further Pd-plating would be non-uniform. Alternatively, P1500 grit Al_2O_3 paper (ca. 13 μm particles) could be used in the same way and had the same effect. Al_2O_3-paper was preferred since it did not seem to interfere with further Pd-plating.

If an extraordinarily smooth Pd-surface was desired, the membrane was buffed with a cloth wheel rotating at ~7,500 rpm with blue rouge (sub-micron particles of Al_2O_3 binded together with grease). The membrane was moved quickly (within 1 second) across the wheel 1 – 3 times on each $1/8^{th}$ of the membrane circumference resulting in a mirror-like finish. A photograph of the buffed membrane AA-14 was shown in Figure 3.2[b]. After buffing the membrane was submerged in acetone for two ten-minute intervals to remove any grease.

3.2.4. Electro-deposition of gold

For the purpose of H_2S resistance, some membranes were prepared with a thin layer (0.5 – 2 μm) of Pd/Au-alloy on the surface of the membrane. This layer was fabricated by electro-deposition of gold from Gold 25 ES RTU Solution (Technic Inc., Cranston, RI). A platinum clad niobium mesh (diameter = 2.5 cm) was used as the anode and the membrane was attached as the cathode. The electro-deposition was conducted at 60°C with a current density of 3 mA/cm^2 (V = 0.89 v) for 10 minutes. Within seconds of initiating the current, the color of the membrane changed to yellow/gold.

3.2.5. Defect repair by electro-deposition

For the purpose of defect repair, copper was electro-deposited on the defective regions of one finished membrane. The objective of the electro-deposition was to block defective regions with 20 – 100 μm of either copper, chromium, or nickel. The elements were chosen because of their low cost, low chemical reactivity, and simple electro-deposition methods from commonly available starting materials. A copper plating solution composed of 200 g/L $CuSO_4 \bullet (H_2O)_5$ and 25 mL/L H_2SO_4 (conc.) in H_2O was

utilized. A copper foil (total area = 10 cm^2) was used as the anode bent around the membrane and the membrane was attached as the cathode. The electro-deposition was conducted at 20°C with a current density of 24 mA/cm^2 (V = 1.0 v) for four cycles of 60 minutes each.

Chromium was electro-deposited on the defective regions of one finished membrane. A chromic acid solution composed of 224 g/L CrO_3 and 2.4 mL/L H_2SO_4 (conc.) in H_2O was utilized. Three lead strips (total area = 63 cm^2) were used as the anode and positioned around the membrane. The membrane was attached as the cathode. The electro-deposition was conducted at 45°C with a current density of 175 mA/cm^2 (V = 6 v) for 60 minutes.

Nickel was electro-deposited on the defective regions of one finished membrane. A nickel plating solution composed of 235 g/L $NiSO_4•(H_2O)_6$, 50 g/L $NiCl_2•(H_2O)_6$, 30 g/L H_3BO_4, and 0.1 g/L sodium dodecyl sulfate in H_2O was utilized. A nickel mesh was used as the anode, wrapped around the membrane at a distance of 1.5 cm, and the membrane was attached as the cathode. The electro-deposition was conducted at 50°C with a current density of 20 mA/cm^2 (V = 0.63 v) for 60 minutes.

3.3. Pd-coupon synthesis

Coupons were used in some instances to investigate possible coke formation on the Pd-surface. Coupons were prepared by cutting a sheet of Hastelloy (0.1 µm grade) into 1 x 1.5 cm squares with a sand-stone cutting wheel. Hastelloy was utilized because of its availability and because it was considered irrelevant which metal was underneath the Pd-layer for the coking experiments. A small (1/16") hole was drilled at the corner of each coupon for mounting purposes. The coupons were oxidized at 700°C in air for 12 hours (Ma *et al.*, 2000, 2007). The coupons were hung from stainless steel hooks attached to a sample holder. 12 pieces were hung from the sample holder such that they could all fit into a 400 mL beaker without touching one another. The coupons were put through 5 activation cycles (see Figure 3.1) and Pd-plated for three periods of 90 minutes. Since the coupons appeared somewhat blotchy they were polished with 600

grit SiC paper. The coupons were then put through an additional three activation cycles and Pd-plated for three periods of 90 minute.

3.4. Mixed gas experimental

3.4.1. H_2 and mixed gas setup

The pure H_2 and mixed gas testing system is diagramed in Figure 3.3.

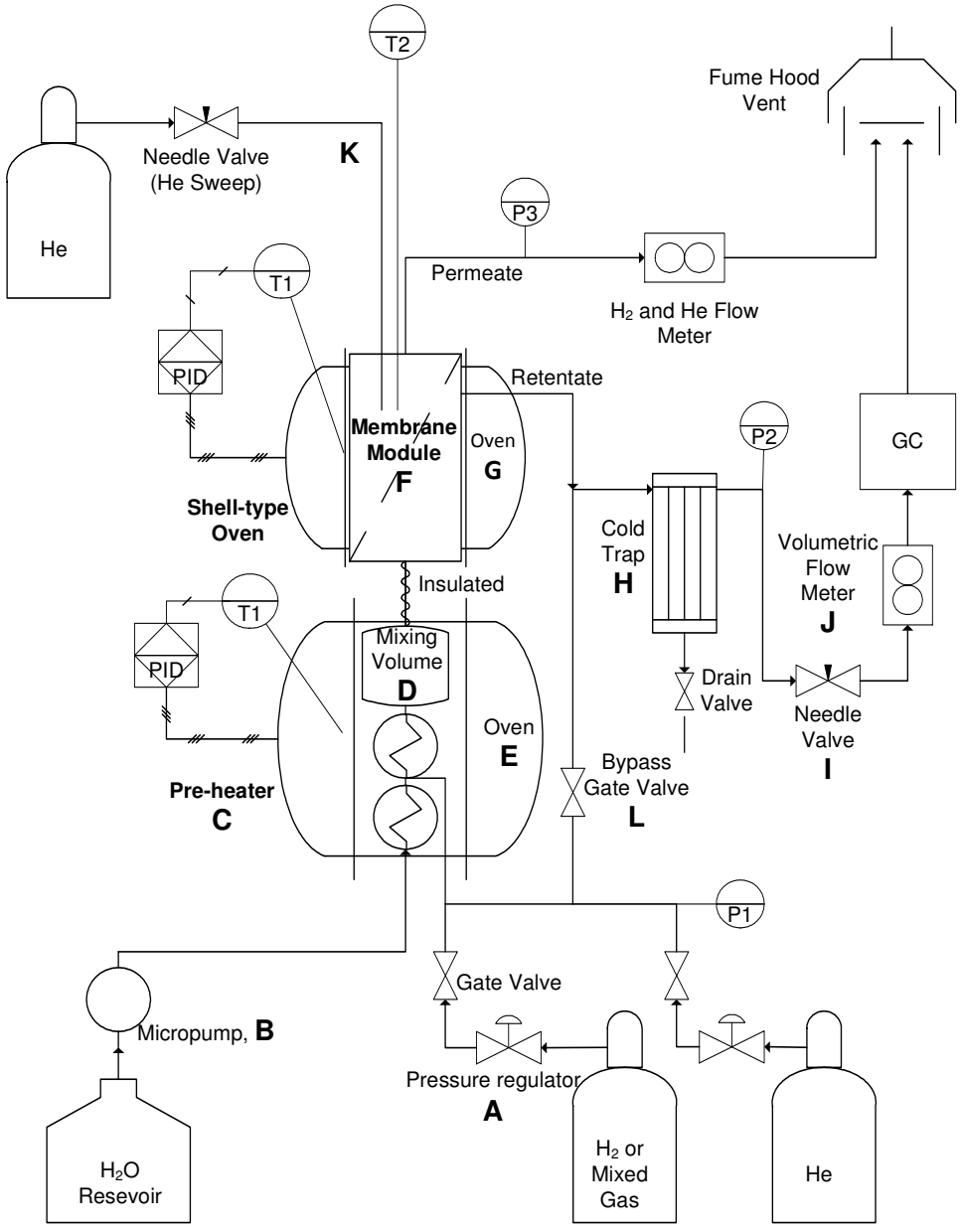

Figure 3.3. Schematic of the pure H_2 and mixed gas testing system.

Pressure regulators **A** (Swagelok KPR1B1C3GA10A01 for 1.2 – 10 atma and SGC Inc. Model 3101-500-350NV for 10 – 21 atma) were used to control the pressure of the H_2, He, or mixed gas supplied to the membrane. De-ionized water was supplied via the micropump **B** (Harvard Apparatus Series I Pump). The pre-heater **C** consisted of a coiled 0.16 cm OD and 90 cm long (1/16" x 3') SS tube, a coiled 0.64 cm OD and 120 cm long (1/4" x 4') SS tube, a tubing union, and a mixing volume **D** (150 mL, packed with 1 cm quartz Raschig rings). The water was vaporized in the 0.16 x 90 cm tube, mixed with the feed gas at the union then heated additionally in the 0.64 x 120 cm tube. The feed/steam mixture was then mixed thoroughly in the mixing volume **D**. The pre-heater was encased in a ceramic tubular oven **E** (Watlow) with a thermocouple and PID controller to control the temperature of the feed/steam mixture. The membrane was mounted in a shell consisting of a 2.54 cm OD and 25.4 cm long (1" x 10") SS tube. The membrane was mounted with a Swagelok® stainless steel ferrule and nut assembly which was essential for high pressure (greater than 6 atma) use. The membrane and shell **F** were encased in a ceramic tubular oven **G** (Watlow) with a thermocouple and PID controller to control the temperature of the membrane. Thermal tape controlled by a variable autotransformer (Staco Inc., Type 2PF 1010) was fitted to the outlet end of the reactor apparatus and its power adjusted to minimize the axial temperature gradient along the membrane (not shown in Figure 3.3). A thermocouple was mounted inside the membrane to measure the membrane temperature. A mass flow meter (MKS) was used to measure the hydrogen flux permeating the membrane. A stainless steel cold trap **H** (180 mL internal volume, maintained at room temperature) was used to condense the steam from the retentate gas mixture. A needle valve **I** was used to regulate the flow of the retentate gas. A volumetric flow meter **J** (GCA Precision Scientific) was used to measure the retentate flow rate. A 0.32 cm OD (1/8") SS tube **K** was positioned inside the membrane and provided a flow of He sweep gas (approximately 15 sccm) to the permeate side. The sweep gas was used to purge the permeate side of the membrane before and after experiments, not to increase the H_2 partial pressure driving force. A gas chromatograph (HP 5890 Series II) with a Carboxen 1000 column for permanent gas separation, and a thermal conductivity detector was used to analyze both the permeate and the retentate gas streams in the case of mixed gas feeds. The GC method and

calibration details can be found in Appendix C. A bypass **L** was in place before the pre-heater to divert feed gas directly to the GC for feed composition analysis. Pressure sensors (MKS, 722A14TCD2FA), labeled P1, P2, and P3 in Figure 3.3, were attached at the inlet of the pre-heater, the outlet of the membrane module, and the permeate outlet respectively.

3.4.2. Mixed gas testing procedure

In a typical mixed gas experiment the following procedure was used. Prior to the experiment, the mixed gas was delivered to the system at 100 sccm and a pressure of 4.4 atma (P_{H2} > 1.0 atma) for at least one hour to ensure that the system was thoroughly purged. The pressure was then raised to 14.4 atma over several minutes. The retentate flow was adjusted by means of a needle valve **I** (Figure 3.3). Once the pressure and retentate flow were adjusted the system was allowed to reach steady state for at least 10 minutes before measurements were taken. Flow measurements of the retentate and the permeate streams were taken by the volumetric flow meter **J** (GCA/Precision Scientific). Samples of the retentate and permeate streams were analyzed via the HP 5890 Series II GC. The retentate flow rate was increased and measurements were taken at intervals of 300 sccm up to 6,000 sccm. At retentate flow rates in excess of 4,000 sccm, the temperature was adjusted by the PID controller to ensure that the system temperature remained stable despite convective cooling.

3.5. WGS CMR experimental

3.5.1. WGS CMR Setup

The WGS CMR setup consisted of the reactor system diagramed in Figure 3.4 and was similar to the H_2 and mixed gas system with the following exceptions. Mass flow controllers **A** (Brooks 5850E) were used to deliver feed gases to the pre-heater during reaction experiments. A back pressure regulator **B** (SGD Inc. Model 12-253) was in line after the cold trap to control the system pressure. For long-term (greater than 20 hour) reaction experiments an infrared continuous gas analyzer **C** (Siemens, Ultramat 6) was utilized to measure the level of CO in the permeate stream. For experiments in which H_2S was present in the feed, a second GC **D** (SRI Model 8610C) equipped with a 1/32”

MXT stainless steel capillary column and a Flame-Photometric Detector (FPD) was used in line with the first. The GC method and calibration details for this device can also be found in Appendix C.

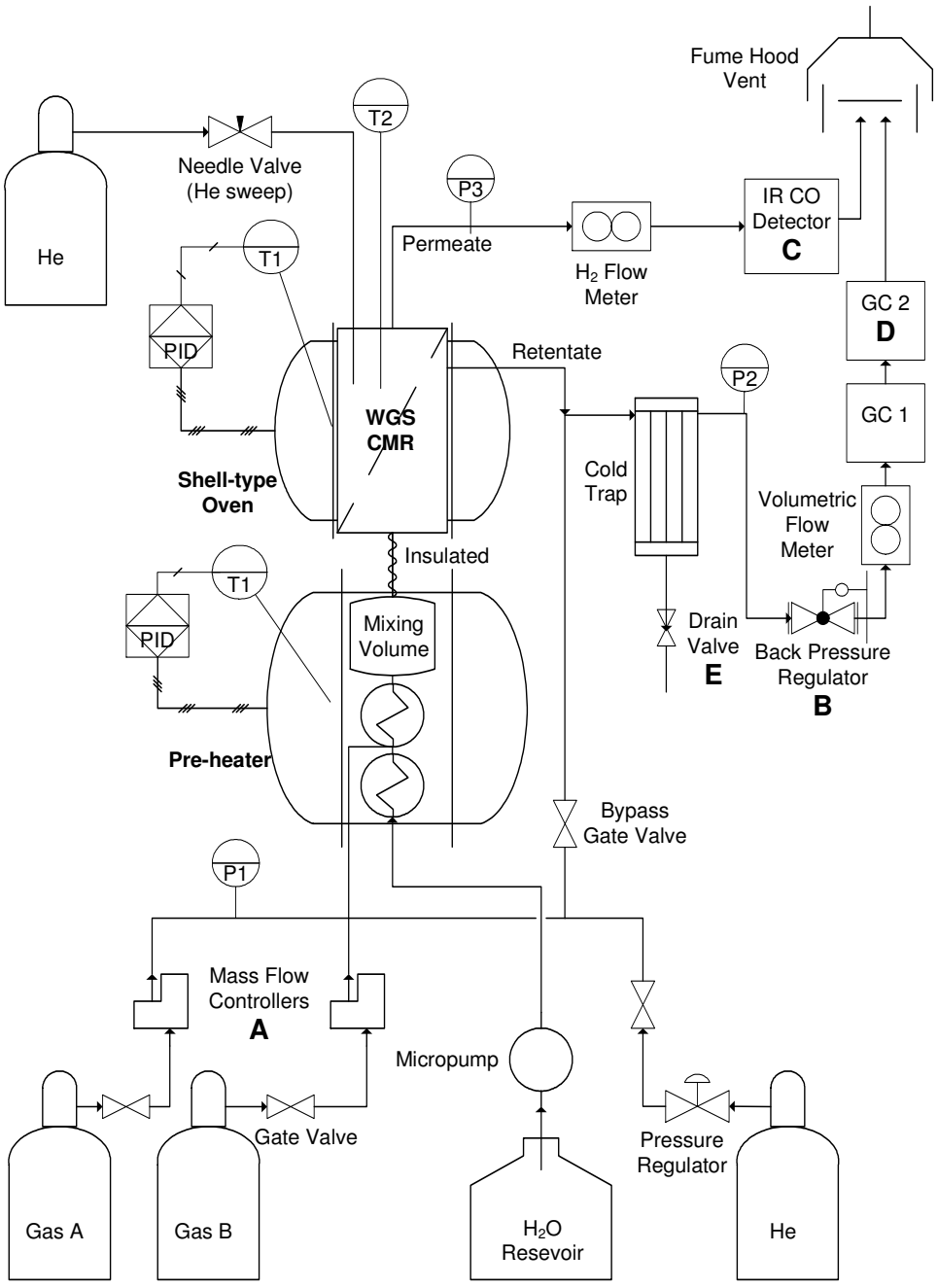

Figure 3.4. Schematic of the WGS CMR system.

The WGS CMR, shown in Figure 3.5, consisted of a 2.54 cm OD and 25.4 cm long (1" x 10") SS tube with a 1.3 cm OD and 25.4 cm long (1/2" x 10") membrane tube assembly mounted inside. The membrane tube assembly was mounted at the approximate center of the reactor and held in place with a Swagelok® stainless steel ferrule-nut assembly. The reactor was packed with 40 - 48 mesh (297 - 400 μm) iron-chrome-oxide catalyst (HiFUEL W210) in the annular space around the membrane. A one-time reduction in catalyst particle size of 5 – 10% was observed during high temperature testing and/or calcinations, if this size reduction occured for the first time in the loaded membrane reactor, 5 – 10% of empty space will be available for the catalyst to move around and create channels. To prevent channeling, the catalyst was calcined at 500℃ for 12 hours prior to use in the reactor. Inert packing, 50 - 70 mesh white quartz sand, was packed above and below the membrane. Quartz wool was used to separate the sand and the catalyst. SS porous disks were used to plug the ends of the reactor.

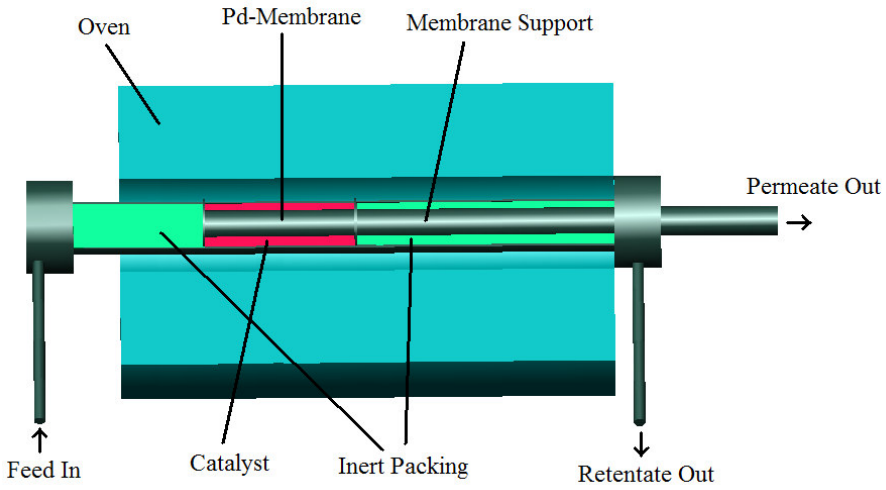

Figure 3.5. WGS CMR scale rendering.

3.5.2. WGS CMR loading procedure

The WGS CMR was assembled and loaded by first mounting the membrane vertically with one end cap (2.54 cm to 1.27 cm reducing union, modified with an additional 0.32 cm tube) and a porous SS washer (2.22 cm OD, 1.27 cm ID) in place. Sand

(approximately 15 g) was then added until the proper depth was reached (a foam-tipped plunger was used to measure the depth). The SS tube was tapped hard with a hammer several times to settle the sand. The plunger was then used again to measure the proper depth (more sand was added if needed). A plug of quartz wool (approximately 0.2 – 0.3 cm thick when compressed) was inserted and pushed down on top of the sand and surrounding the welded interface between the membrane and the support. Iron-chrome-oxide catalyst (approximately 13 g) was then added until the plunger indicated the proper depth (the top end of the membrane). The reactor was tapped again with a hammer to settle/pack the catalyst bed and the depth was measured. A second plug of quartz wool was inserted and pushed down to the top of the catalyst bed. Sand (approximately 75 g) was then added to the top of the reactor tube and the reactor was tapped hard repeatedly until all the packing material in the tube was settled and no change in depth was observed. A porous disk was placed on top of the reactor tube and a reducing union (2.54 to 0.32 cm [1" to 1/8"]) was secured. The reactor assembly was leak tested by pressurizing to 4 atma of helium and applying soap water to all pipe connections (while looking for bubbles).

3.5.3. WGS experimental procedure

In a typical WGS experiment the following procedure was used. The reactor was purged with inert gas (N_2, 200 sccm) for 1 hour prior to the start of the steam feed. The catalyst was oxidized with the steam feed (260 µL/min of H_2O to the preheater, 14.4 mmol/min) for 15 minutes prior to the introduction of other feed gases. During this 15 minute period steam began to condense in the cold-trap and the pressure was ramped up to 14.5 atma at 1 atm/min with the back pressure regulator. Pre-mixed feed gas (42% CO, 40% H_2, 18% CO_2; Middlesex Gases & Tech. Inc., Everett, MA) was fed to the system and at the same time the inert sweep (He, 10 sccm) to the permeate side of the membrane was shut off, as was the N_2 flow to the retentate side. The permeate flow, CO level in the permeate, system pressure, and tube-side temperature were recorded at 4 min intervals by the data acquisition software (LabVIEW 7.1, National Instruments). Samples of the retentate stream were analyzed via the HP 5890 Series GC at 30 minute intervals for short reactions (less than 20 hour) and at 3 hour intervals for long

reactions (greater than 20 hour). Volumetric flow measurements were manually recorded every time a GC analysis was started. Samples of the retentate stream were also analyzed by the SRI 8610C GC at 10 minute intervals when H_2S was present in the feed mixture. The condensed water was drained from the cold-trap every 12 hours by the drain valve **E** (Figure 3.4) and measured. At the end of an experiment the mixed gas was shut off and the inert purge (N_2, 200 sccm) was resumed. When retentate side was purged with N_2, an inert sweep (He, 20 sccm) to the permeate side was necessary to prevent back-flow of H_2 through the membrane. Flow of H_2 from the permeate-side to the retentate-side could draw air through the system tubing and into the membrane, potentially damaging the support and/or Pd-layer by oxidation. 15 minutes after the mixed gas was shut off, the H_2O feed was also shut off. Shortly after the H_2O feed was shut off, the volume of water in the cold trap was drained and measured.

3.6. Post-testing characterization

3.6.1. Leak characterization

The membrane inert gas leak was characterized during high temperature testing by flushing the system with He at 1.5 atma for at least 3 hours, then pressurizing the shell-side of the membrane to 4 atma, and measuring the He flow through the membrane with a bubble flow meter (1.0 mL pipette). When the leak was large (greater than 0.1 sccm at a ΔP of 1 atm) the leak was measured at several pressure differences.

After high temperature testing, an IPA bubble test was usually conducted to determine if any defects had formed due to the testing. If any significant defects were apparent, a 'rising water leak test' was conducted to determine what fraction of the He leak was due to the defective area (Guazzone and Ma, 2008). The rising water leak test was conducted by first measuring the leak at a pressure difference of 1 atm in a vertically mounted, clear plastic shell. Water was then added into the shell so that increments of 0.5 cm of the membrane length were progressively blocked and the leak was measured again.

3.6.2. SEM and EDS analysis

After testing, some membranes were cut and examined by SEM (Amray Model 1610, equipped with a Si(Li) x-ray detector {PGT}) to develop a better understanding of the grading, intermediate, and dense Pd-layers. The samples prepared for this type of analysis were of two types: surface samples and cross-section samples. Surface samples were prepared by cutting the membrane into 1 cm long, 1 cm wide pieces (90° segments of the round tube). The membrane pieces were then affixed to aluminum sample holders by carbon paint (SPI Supplies, Structure Probe Inc.), care was taken not to touch the Pd-surface while the sample was being prepared. Cross-section samples were prepared by first cutting an 1 cm long round section of the membrane, then mounting in a polymer matrix (EpoMet-F Molding Compound, Buehler Ltd.) by heating under pressure to 140℃ via an automatic mounting press (SimpliMet Inc.). The membrane section was mounted vertically such that the circular cross-section of the membrane was visible at the top of the polymer cylinder. The polymer mounted membrane sample was then polished sequentially with 240, 320, and 600 grit SiC-paper on a water-cooled spinning table. The sample was then polished sequentially on spinning felt tables with 1.0, 0.3, and 0.05 μm alumina slurries. At each step of polishing the sample was polished at multiple orientations with respect to the direction of the spinning table. After the first polishing with 1.0 μm alumina particles the surface had a completely smooth appearance to the naked eye, with no directional polishing marks. The polished sample was affixed to an aluminum sample holder with carbon paint.

During operation of the SEM, electrons could build up on non-conductive surfaces or conductive pieces that were not grounded in a phenomenon known as “charging”, resulting in an excessively bright or glowing appearance to the acquired images. To prevent charging a line of carbon paint was made from the sample holder on the bottom, around the side of the polymer cylinder, and extending to touch one edge of the membrane cross-section. The carbon paint conducted charge from the membrane piece to the grounded sample holder. The whole sample was also sputter-deposited (Denton Desk II) with approximately 10 nm of Pd to prevent charging on the polymer surface.

The SEM was operated with two different setting configurations depending on whether the objective was to acquire high quality images or to detect X-ray emissions for Energy-Dispersive Spectroscopy (EDS). The settings for both modes of operation are given in Table 3.1. Images and EDS were recorded with the SEM instrument software Spirit 1.04.02 (PGT Inc.).

Table 3.1. SEM settings for two different modes of operation.

Optimized for image quality	Energy	15 keV
	Spot size	9
	Working distance	15
	Tilt	0°
Optimized for EDS analysis	Energy	20 keV
	Spot size	6
	Working distance	45
	Tilt	33°

3.6.3. XRD analysis

After testing, some membranes were cut and analyzed by X-Ray Diffraction (XRD, Rigaku equipped with a Cu-source) to determine if alloying had occurred as expected or if sulfur or carbon had been incorporated into the Pd-lattice. Surface samples were prepared by cutting the membrane into 1 cm long, 1 cm wide pieces (90° segments of the round tube). The sample pieces were positioned on an adjustable Teflon mount in the XRD such that the top of the sample (flat or curved surface) was at the same level as where the x-ray beam crossed the incident plane of the machine. The x-ray source was excited with a current of 25 mA at 37.5 kV. X-ray diffraction scans were taken between 2θ values of 20 – 100°, with a resolution of 0.2° for broad scans, and a resolution of 0.05° for high definition scans. Scans were recorded with the XRD software DataScan 4.5 (MDI). The XRD software Jade 8.5.4 (MDI) was utilized to check sample spectra against a database of known materials.

3.7. Summary

Methods were described for the synthesis and testing of PSS supported Pd-membranes. The experimental apparatus for mixed gas and WGS testing were explicitly described. Lastly, the characterization methods for the Pd-membranes were described. In Chapter 4 the membrane synthesis methods delineated in Section 3.2 are discussed based on their ability to reproducibly fabricate Pd-membranes, with high H_2 permeance and high selectivity, from low cost PSS supports. In Chapters 6 and 9 membranes are tested under mixed gas conditions in the apparatus and by the procedure described in Section 3.4. In Chapters 7, 9, and 10 membranes are tested under WGS conditions in the apparatus and by the procedure described in Section 3.5. In Chapter 8 coupons are utilized which were prepared by the procedure delineated in Section 3.3. In Chapters 4, 8, 9, and 10 characterization techniques (described in Section 3.6) are utilized after membranes and coupons have been exposed to mixed gas and reaction conditions. In some cases aberrations to the methods described here were made; they are detailed in the Experimental subsections of each chapter.

4. PURE GAS TESTING OF Pd-MEMBRANES

4.1. Introduction

The application of Pd-membranes to the WGS CMR in a commercial setting is dependent on their being fabricated by a simple, reproducible method which is at least somewhat independent of the support quality. To address this, grading methods have been devised to smooth the support surface and fill pores near the surface with particles (Ma *et al.,* 2007; Nam *et al.,* 1999; Tong *et al.,* 2004), intermediate layers have been devised to further reduce the surface pore size and prevent intermetallic diffusion, and dense Pd-plating techniques have been demonstrated which result in uniform deposition (Ayturk *et al*., 2007; Keuler and Lorenzen, 2002; Ma *et al*., 2007; Mardilovich *et al*., 2006; Roa *et al.,* 2002; 2003a; 2003b). Of these three methodologies the dense Pd-plating has often been highlighted as the cardinal process upon which successful synthesis depends, overlooking the grading and intermediate layer functions. If low quality supports with large surface features (contours, bumps, or pores greater than 1 μm in size) are to be utilized, grading may be the most important aspect of membrane synthesis. If supports are produced from low cost metals such as 310-stainless steel, intermediate layer integrity may also be crucial.

It was important to develop a solid understanding of grading methodology, intermediate layer treatment, and surface modification techniques which would lead to highly H_2 permeable, selective, and stable membranes. The objective of this chapter was therefore to develop a better understanding of synthesis methodology, which synthesis steps led to which membrane properties. A focus was also made on those aspects of membrane synthesis which allowed for high reproducibility, an aspect not widely discussed in the literature. An important aspect of synthesis efficacy was the characterization methods by which completed membranes could be evaluated: H_2 flux and inert gas leak stability. As an additional objective for this chapter, a better understanding of the mechanisms of H_2 permeation and leak growth in supported membranes should be developed.

4.2. Background

4.2.1. Grading

The preferred support material for commercial application is porous stainless steel (PSS) due to its low cost, thermal and chemical stability, and mechanical strength. Mardilovich *et al.* (2002) demonstrated that a Pd-layer at least three times thicker than the diameter of the largest pore mouth was necessary to achieve a dense membrane. Highly permeable PSS, with a maximum surface pore size of greater than 10 μm thus required significant support modification to achieve thin (less than 10 μm) and highly H_2 permeable membranes. In order to utilize PSS supports with moderately inconsistent features (pore size distribution, surface roughness, and randomly distributed defects), as well as prohibitively large pore sizes, grading techniques were typically employed (Ma *et al.,* 2007; 2010). Grading consists of anchoring particles either onto the support surface or into the surface pores in order to smooth the surface, reduce the surface pore size, and narrow the pore size distribution. Grading materials which have been used in the literature are α and γ-Al_2O_3, $Al(OH)_3$, $Ce(OH)_4$, Ni, Ag, and W (Ma *et al.,* 2007; Nam *et al.,* 1999; Tong *et al.,* 2004).

Table 4.1 lists several different grading materials and methods reported in the literature for porous metal supports. Nam *et al.* (1999) produced an exceptionally thin dense Pd-layer by grading with nickel powder applied over 5 hours by vacuum and sonication. The use of electroplating probably also aided in the formation of the thin and uniform Pd-layer. Ma *et al.* (2010) also produced an exceptionally thin Pd-membrane by sequential deposition of three different sizes of Al_2O_3-particles (3, 0.3, and 0.01 μm). While it was difficult to compare grading methods from different studies due to the different support qualities and different Pd deposition methods, it was somewhat intuitive and apparent from Table 4.1 that a longer and more intense application of grading material resulted in a better graded layer, which allowed for the fabrication of a thinner Pd-layer.

Table 4.1. Summary of grading methods used on porous metal supports and resulting Pd-thickness.

Grading Material	Application Method	Pd, Pd/Alloy-thickness (μm)	Reference
Ni	5 h, vacuum, sonication	1	Nam *et al.,* 1999
$Ce(OH)_4$	1 h, vacuum, sonication	6	Tong *et al.,* 2004
W	2 x 90 sec, vacuum	33.6	Ma *et al.,* 2007
W + Ag	2 x 30 sec, vacuum	13.1	
Al_2O_3	30 sec, vacuum	14.8	Ma *et al.,* 2010
Al_2O_3	Sequential, 3 x 30 sec, vacuum	3.9	

4.2.2. Porous intermediate layers

An alternative method to improve the support surface was the application of a thin (1 - 20 μm) layer of porous material which had more preferable surface properties than the PSS (i.e. smooth with nano-size pores). An additional function of the intermediate layer was to prevent diffusion of the support metals into the palladium layer, which can result in significant loss of H_2 permeance at temperatures above 400°C (Ayturk *et al.,* 2006). The three primary types of porous intermediate layers which have been reported in the literature were metal-oxides, porous metals, and sol gels. Ma *et al.* (2000; 2007) formed an intermediate layer of iron and chromium oxides to prevent intermetallic diffusion of the support metals into the Pd-layer and, more recently, to anchor alumina grading particles to the surface of the support (Koc, 2012). The oxide layer was formed by heating in air at 500 – 600°C for high chromium content stainless steels, and 700 - 800°C for high nickel content steels such as Hastelloy or Inconel. Ma *et al.* (2007; Ayturk *et al.,* 2006) produced a Pd/Ag intermetallic diffusion barrier by sequential electroless deposition of those two metals. The layer prevented intermetallic diffusion by the extremely low solubility of iron in Pd/Ag-alloys. Additionally, since the silver deposited in a dendritic manor, the surface pore size was significantly reduced so that a thin dense Pd-layer could be formed. An alternative intermediate layer was formed by sputtering titanium in a N_2 atmosphere to deposit TiN on the support (Shu *et al.,* 1996). They demonstrated that the TiN-layer prevented intermetallic diffusion of iron from the PSS support up to a temperature of 700°C.

The final category of intermediate layers which have been utilized to prevent intermetallic diffusion, anchor grading particles, and smooth porous surfaces were sol gels. Sol gels are suspensions of colloid particles produced from the partial hydrolysis and polymerization of transition metal salts (Brinker and Scherer, 1990). When the gel is dried on a surface it forms a solid polymer structure, further drying by calcination at 300 - 600°C drives off more water and results in a nano-porous glass structure. Li *et al.* (2007a) showed that the application of an alumina sol gel with suspended alumina particles (0.3 – 2.5 μm) to a PSS_{316L} support reduced the surface pore size from 20 down to 1 μm with only a 50% loss of support permeance. Nam and Lee (2001) utilized a silica sol gel on a nickel graded SS disk to support a 2 μm $Pd_{63}Cu_{37}$-membrane prepared by electrodeposition. After the sol gel application they observed a drop in inert gas flux of two orders of magnitude, suggesting that the sol gel layer was causing significant mass transfer resistance, however, in the completed membrane they measured a high H_2 permeance of 54.7 m^3/m^2-h-atm at 450°C.

The use of intermediate layers has generally resulted in membranes which remained stable at high (500 – 700°C) temperatures. Unfortunately, the application of both grading and intermediate layers can significantly increase the mass transfer resistance. If the layers are applied in an inefficient manor, the deposition of particles and material can occur deep inside the porous support, resulting in significant loss of permeance. What is instead desired is an ordered layer which is confined completely to the surface but still has strong adhesion to that surface, an aspect which very few literature studies have discussed.

4.2.3. Dense, H_2 permeable Pd-layer

The primary methods of Pd and Pd-alloy dense layer synthesis including electroplating, magnetron sputtering, chemical vapor deposition, and electroless plating were reviewed in Chapter 2, Section 2.2.3. The primary method of interest in this study was electroless plating due to its scalability, inherent safety, and proven efficacy (Ayturk *et al.*, 2007; Keuler and Lorenzen, 2002; Ma *et al.*, 2007; Mardilovich *et al.*, 2006; Roa *et al.,* 2002; 2003a; 2003b). Examples in the literature of Pd-membranes prepared by electroless plating were also given in detail in Chapter 2, Section 2.2.3.e.

4.3. Experimental

4.3.1. Porous supports

The membrane supports used in this study were PSS_{316L}, PSS_{310}, porous Hastelloy (PH), and porous Inconel (PI) tubes (6.5 cm length, 1.3 cm OD, Media Grade 0.2 μm), capped at one end, and welded to a stainless steel tube at the other, purchased from either Mott Metallurgical Corp. (Farmington, CT) or Chand Eisenmann Metallurgical (Burlington, CT). A total of seven different types of porous metal supports were utilized which are detailed in Table 4.2. The supports varied considerably in terms of their mass transfer resistance and surface features. The PH supports, for instance, had a very low mass transfer resistance such that a He permeance of 3000 m^3/m^2-h-atm was initially measured. While a very low mass transfer resistance was desired, it was offset by the very large surface pores, up to 50 μm, observed on those same supports, potentially complicating the membrane synthesis.

Table 4.2. Specifications of the porous metal supports used in this study.

Provider	Designation	Material	Nominal grade (μm)	Surface pore size (μm)	He permeance (m^3/m^2-h-atm)
Mott Corporation (Farmington, CT)	M-$PI_{0.1}$	Inconel	0.1	5	390 – 410
	M-$PSS_{316,\ 0.2}$	316L SS	0.2	10	480 – 650
Chand Eisenmann Metallurgical (Caribou, ME)	C-$PH_{0.1}$	Hastelloy	0.1	50	2900 – 3100
	C-$PSS_{316,\ 0.1}$	316L SS	0.1	10	350 – 440
	C-$PSS_{316,\ 0.2A}$	316L SS	0.2	20	460 – 500
	C-$PSS_{316,\ 0.2B}$	316L SS	0.2	10	270 – 370
	C-$PSS_{310,\ 0.2}$	310 SS	0.2	Unknown	220 – 240

4.3.2. Synthesis methodology

Two specific methods of membrane synthesis were used and described in detail in Section 3.1 and Appendix B. The general method of membrane synthesis was as follows: Initial support treatments (cleaning and oxidation) were conducted first. Grading material (α-Al_2O_3, γ-Al_2O_3, or $Al(OH)_3$) was applied second and repeated if deemed

necessary. Intermediate layers (Pd/Ag barrier or sol-gel) were applied third, and dense Pd-plating was conducted last. Specific aberrations from published synthesis procedures and their perceived effects on membrane properties will be detailed in the Results and Discussion (Section 4.4).

Up until the dense Pd-plating step, the only diagnostic tests considered relevant to synthesis quality were visual inspection and gravimetric thickness (Section 3.1.1). If the color and texture of the membrane were not uniform after a certain treatment, a light mechanical polishing (Section 3.1.3) was conducted and the treatment was repeated. If the change in gravimetric thickness was too low for a certain step, that step was also repeated, typically without mechanical polishing. The He permeance of the membranes was also measured after each synthesis step, but was considered irrelevant up until the dense Pd-plating since the grading and intermediate layers were not expected to cause a significant change in He permeance due to their very slight thickness and porous nature. The IPA bubble test (Section 3.1.2), which was capable of identifying defects and non-uniform regions of the deposited layers, was not conducted until at least 1 μm of dense Pd was applied. The application of a slightly higher pressure in the tube-side (0.2 – 1 atmg) during the test was considered potentially damaging to the grading and intermediate layers due to their fragile nature.

During dense Pd-plating all four characterization tests were considered relevant. The gravimetric thickness was used to confirm that Pd-plating was proceeding at the expected rate, 3 μm/h for a well activated surface (Ayturk and Ma, 2009). By visual inspection if a blotchy or non-uniform surface was observed, mechanical polishing was conducted to smooth the surface prior to further Pd-plating. The IPA bubble test was conducted to identify defects such that spot plating could be done. Lastly the He permeance was measured to determine if a dense layer had been achieved, or to estimate how much more plating was likely to be required.

After dense Pd-plating, membranes were generally annealed in He or H_2 for 12 hours at a temperature of greater than the anticipated testing temperature in order to release microstrains and stresses inherent in the electroless deposited layers (Guazzone *et al.,* 2006). Following annealing the He leak of the membrane typically increased by up to

one order of magnitude, and so the membrane was mechanically polished and plated with additional Pd.

4.3.3. H_2 characterization

An initial characterization in pure H_2 was conducted to judge both the suitability of the support and the synthesis method efficacy. Since the primary focus of this thesis was the operation of the WGS CMR incorporating a Pd-membrane, the initial characterization was also conducted to establish the viability of the Pd-membrane for use in the WGS CMR.

After installation of the membrane into the system, the system was first flushed with He and the tube-side He sweep was turned on. The temperature was increased at 0.5°C/min to 400 or 450°C. The system was transitioned to H_2 by shutting off the He feed and setting the H_2 feed pressure to 1.5 atma. After H_2 permeation flux was observed (less than 1 hour), the tube-side He sweep was turned off. The membrane was allowed to come to steady state in H_2 for approximately 48 hours. The membrane was typically tested for 3 - 5 days at 450°C, then 400°C, then 350°C, all in H_2 and taking Sieverts' law data and He leak measurements at each temperature.

Sieverts' law data were taken by measuring the H_2 permeate flux for at least 8 different shell-side pressures, ranging from 1.5 - 4.0 atma. At least 5 minutes at each pressure was given for the steady state flux to be reached. The Sieverts' law permeance, F_{H2} [m^3/m^2h-$atm^{0.5}$], was calculated by a linear regression analysis of the data based on equation **4.2**.

$$J_{H_2} = F_{H_2}\left(\sqrt{P_{H2,s}} - \sqrt{P_{H2,t}}\right) \qquad \textbf{4.2}$$

where J_{H2} [m^3/m^2-h] was the measured H_2 flux, $P_{H2,s}$ [atma] was the shell-side pressure, and $P_{H2,t}$ [atma] was the tube-side pressure (note that the unit of absolute pressure, atma, was used throughout this document except for situations in which pressure terms were subtracted, divided, etc such that relative pressure, atm, was used). Equation **4.2** was identical to equation **2.31** with $F_{H2} = Q_H/\delta_{Pd}$, for a Pd-foil, but could not be used directly to determine the permeability of palladium because of the uncertainty in the

gravimetric thickness measurement. Where the mass transfer in the support was significant, or the leak was considerable, or the membrane was very thin, the Sieverts' law data was also fitted to the empirical equation **4.3** (similar to equation **2.32**, discussed in Chapter 2) by the Newtonian iterative method via Microsoft Excel ®.

$$J_{H_2} = {}^{n}F_{H_2}\left(P_{H2,s}^{n} - P_{H2,t}^{n}\right) \qquad \textbf{4.3}$$

where ${}^{n}F_{H2}$ [m^3/m^2-h-atm^n] is the *n*-dependent permeance and *n* is the exponent of the absolute pressure difference.

The He leak measurements were typically taken every three days and before and after any changes in temperature so that the rate of leak growth could be estimated. The He leak measurements were taken by first switching the system to helium and switching on the tube-side He sweep. After the system was purged with He for several hours the He pressure was increased, typically to 4 atma. The tube-side sweep was shut off and the He flow was measured with a 1-mL bubble flow meter (minimum detection limit = 0.05 sccm). If the leak at 4 atma was greater than 1.0 sccm, subsequent leak measurements were also taken at 3 and 2 atma shell-side pressures and a linear regression analysis was conducted to determine the He permeance, F_{He} [m^3/m^2h-atm], via equation **4.4**.

$$J_{He} = F_{He}\left(P_{He,s} - P_{He,t}\right) \qquad \textbf{4.4}$$

The ideal selectivity, $\alpha^{i}_{H2\text{-}He}$, was determined for a pressure difference of 1 atm (P_t = 1 atma) via equation **2.34**.

$$\boldsymbol{\alpha}^{i}_{H2-He} = \frac{\boldsymbol{J_{H2}}}{\boldsymbol{J_{He}}} = \frac{\boldsymbol{F_{H2}}*(\sqrt{2atm}-\sqrt{1atm})}{\boldsymbol{F_{He}}*(2atm-1atm)} \qquad \textbf{2.34}$$

If the H_2 permeance at 400℃ was at least 20 m^3/m^2-h-$atm^{0.5}$ and the ideal H_2/He selectivity was greater than 1,000 after the H_2 characterization the membrane was deemed acceptable for use in further experiments. If the selectivity was too low a light mechanical polishing was conducted, followed by Pd-plating. If the H_2 permeance was too low, an aggressive mechanical polishing was conducted followed by Pd-plating, resulting in a net loss of gravimetric thickness.

4.4. Results and discussion

4.4.1. Attainment of a dense Pd-layer

A membrane synthesis was deemed successful if no He leak was detectable by the 1-mL bubble flow meter (less than 0.05 sccm/atm, 0.001 m^3/m^2-h-atm). A membrane synthesis was aborted or deemed a failure if a dense layer could not be achieved with less than 20 μm of dense Pd-plating, or if there was indication from the He permeance changes (less than one-order of magnitude decrease after 5 μm of Pd-plating) that a dense layer would not be possible in that thickness range. A successful membrane synthesis by Method A (described in Section 3.1) is diagramed by a plot of He permeance versus gravimetric thickness as shown in Figure 4.1[a]. A failed membrane synthesis, also by Method A, is diagrammed in Figure 4.1[b]. In the course of this work 41 syntheses were attempted by the author and a further five membranes were contributed from colleagues in the Center for Inorganic Membrane Studies and tested by the author. All of the membranes utilized in this study as well as failed synthesis attempts are listed in Table 4.3 along with the relevant synthesis details.

It should be reiterated that the primary objectives of this research thesis were the investigation of the WGS CMR so the preparation of many of these membranes were conducted with that goal in mind. Nevertheless, some trends among synthesis attempts were observed and are discussed in the following sections of this chapter.

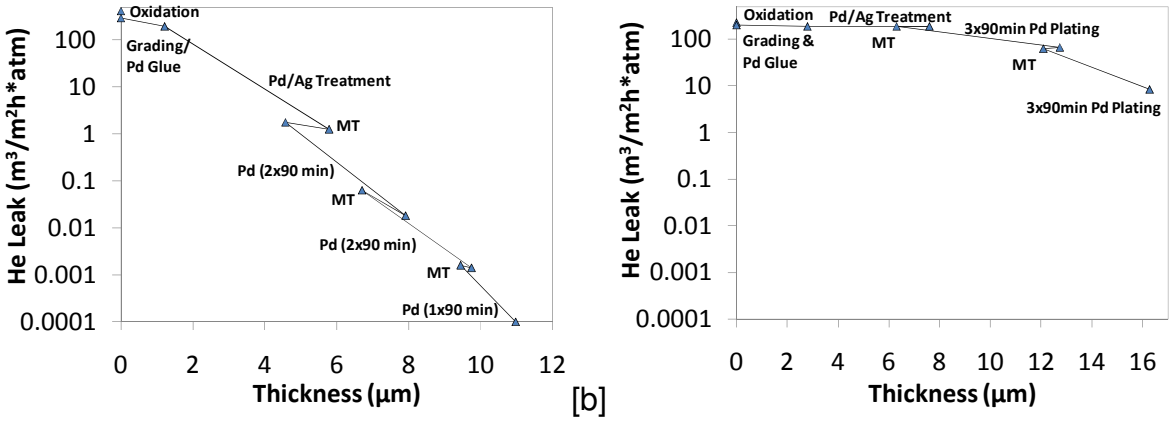

Figure 4.1. Membrane synthesis diagrams [a] Successful synthesis of AA-8 [b] Failed synthesis of AA-9.

Table 4.3. Membranes synthesized and/or tested in this study.

	Support	Grading (μm)	Intermediate Layer (μm)	Pd μm	Notes
AA-1	M-$PI_{0.1}$	-	-	10.8	
AA-2	M-$PI_{0.1}$	Al_2O_3 (0.01 – 1.0)	Pd/Ag (3.3)	9.0	
AA-3	M-$PI_{0.1}$	Al_2O_3 (0.01 – 1.0)	-	-	Aborted (support defect)
AA-4	M-$PI_{0.1}$	Al_2O_3 (0.01 – 1.0)	Pd/Ag (4.5)	7.3	
AA-5	M-$PI_{0.1}$	Al_2O_3 (0.01 – 1.0)	Pd/Ag (2.7)	9.7	
AA-6	M-$PI_{0.1}$	Al_2O_3 (0.01 – 1.0)	Pd/Ag (2.4)	10.3	
AA-7	M-$PI_{0.1}$	Al_2O_3 (0.01 – 1.0)	Pd/Ag (2.5)	9.1	
AA-8	M-$PI_{0.1}$	Al_2O_3 (0.01 – 1.0)	Pd/Ag (3.4)	6.4	
AA-9	C-$PSS_{310,\ 0.2}$	Al_2O_3 (0.01 – 1.0)	Pd/Ag (3.5)	10.0	Aborted (weld defects)
AA-10	C-$PSS_{310,\ 0.2}$	Al_2O_3 (0.01 – 1.0)	Pd/Ag (4.5)	5.8	Aborted (weld defects)
AA-11	C-$PSS_{310,\ 0.2}$	Al_2O_3 (0.01 – 1.0)	Pd/Ag (5.7)	5.8	Aborted (non-uniform surface)
AA-12	C-$PSS_{316,\ 0.2B}$	Al_2O_3 (0.01 – 1.0)	Pd/Ag (<1)	9.9	Support corrosion
AA-13	C-$PSS_{316,\ 0.2B}$	Al_2O_3 (0.01 – 1.0)	Pd/Ag (<1)	8.7	Aborted (support corrosion)
AA-14	C-$PSS_{316,\ 0.2B}$	$Al(OH)_3$	-	11.4	3x pre-annealing and polishing
AA-15	C-$PSS_{316,\ 0.2B}$	$Al(OH)_3$	-	8.3	Ruined by H_2 embrittlement
AA-16	C-$PH_{0.1}$	Al_2O_3 (0.01 – 1.0)	Pd/Ag (10.0)	-	Aborted (large surface pores)
AA-17	C-$PH_{0.1}$	$Al(OH)_3$	-	4.7	Aborted (large surface pores)
AA-18	C-$PSS_{316,\ 0.1}$	Al_2O_3 (0.01 – 1.0)	Pd/Ag (6.0)	12.6	Pre-annealing and polishing
AA-19	C-$PSS_{316,\ 0.1}$	Al_2O_3 (0.01 – 1.0)	Pd/Ag (6.1)	-	Aborted (high He flux)
AA-20	C-$PSS_{316,\ 0.2B}$	Al_2O_3 (0.01 – 1.0)	Pd/Ag (6.8)	13.3	Cu electroplating
AA-21	C-$PSS_{316,\ 0.2B}$	Al_2O_3 (0.01 – 1.0)	Pd/Ag (4.8)	15.7	Pre-annealing and polishing
AA-22	C-$PH_{0.1}$	Al_2O_3 (0.01 – 5.0)	Pd/Ag (<1)	10.6	Support corrosion
AA-23	C-$PSS_{316,\ 0.1}$	Al_2O_3 (0.01 – 3.0)	Pd/Ag (<1)	3.1	Aborted (support corrosion)
AA-24	C-$PSS_{316,\ 0.1}$	Al_2O_3 (0.01 – 1.0)	Pd/Ag (6.2)	6.9	Pre-annealing and polishing
AA-25	C-$PSS_{316,\ 0.1}$	Al_2O_3 (0.01 – 1.0)	Pd/Ag (9.0)	8.5	Pre-annealing and polishing
AA-26	C-$PH_{0.1}$	Al_2O_3	Sol Gel	12.8	Sol-gel peeling
AA-27	C-$PSS_{316,\ 0.2A}$	Al_2O_3	Sol Gel	4.2	Aborted (sol-gel peeling)
AA-28	C-$PSS_{316,\ 0.2A}$	Al_2O_3	Sol Gel	-	Aborted (sol-gel peeling)
AA-29	C-$PSS_{316,\ 0.2A}$	Al_2O_3 (0.01 – 5.0)	Pd/Ag (<1)	9.3	2x grading
AA-30	C-$PSS_{316,\ 0.2A}$	Al_2O_3 (0.01 – 5.0)	Pd/Ag (<1)	9.5	2x grading, single weld defect
AA-31	C-$PSS_{316,\ 0.2A}$	Al_2O_3 (0.01 – 5.0)	Pd/Ag (1.8)	6.8	2x Pd/Ag, weld defects
AA-32	C-$PSS_{316,\ 0.2A}$	Al_2O_3 (0.01 – 5.0)	Pd/Ag (6.2)	8.4	Aborted (weld defects)
AA-33	C-$PSS_{316,\ 0.2A}$	Al_2O_3 (0.01 – 5.0)	Pd/Ag (3.0)	3.8	Aborted, Cr weld plating
AA-34	C-$PSS_{316,\ 0.2A}$	Al_2O_3 (0.01 – 5.0)	Pd/Ag (2.7)	4.1	Aborted (weld defects)
AA-35	C-$PSS_{316,\ 0.2A}$	Al_2O_3 (0.01 – 10)	Pd/Ag (2.3)	4.8	Aborted (general defects)
AA-36	C-$PSS_{316,\ 0.2A}$	Al_2O_3 (0.01 – 10)	Pd/Ag (2.7)	4.7	Aborted (general defects)
AA-37	M-$PSS_{316,\ 0.2}$	Al_2O_3 (0.3 – 3.0)	-	3.9	Aborted (peeling from polishing)
AA-38	M-$PSS_{316,\ 0.2}$	Al_2O_3 (0.01 – 50)	-	1.5	Heavy polishing treatment
AA-39	M-$PSS_{316,\ 0.2}$	Al_2O_3 (0.01 – 10)	-	2.7	Ni weld plating, 0.6 μm Ag-layer
AA-40	M-$PSS_{316,\ 0.2}$	Al_2O_3 (0.01 – 10)	-	1.5	
AA-41	M-$PSS_{316,\ 0.2}$	Al_2O_3 (0.01 – 10)	-	7.7	Aborted (weld defects)
EA-054*	C-$PSS_{316,\ 0.2B}$	$Al(OH)_3$	-	9.3	Aborted (high He flux)
IM-79†	C-$PSS_{316,\ 0.2A}$	Al_2O_3 (0.01 – 1.0)	Pd/Ag (12.2)	10.2	
IM-76C†	C-$PSS_{316,\ 0.2A}$	Al_2O_3 (0.01 – 1.0)	Pd/Ag (5.6)	17.3	
IM-86b†	C-$PSS_{316,\ 0.2A}$	Al_2O_3 (0.01 – 1.0)	Pd/Ag (1.0)	7.5	
RK-16R‡	M-$PSS_{316,\ 0.2}$	Al_2O_3 (0.01 – 10)	-	8.3	Plated with additional 3.2 μm Pd

*Prepared by M. Engin Ayturk
†Prepared by Ivan P. Mardilovich
‡Prepared by Reyyan Koc

The synthesis details of all the membranes synthesized in this study are tabulated in Appendix D. Out of the 41 attempted syntheses, 19 ended in failure due, for the most part, to defects inherent to the lower cost stainless steel supports. The two membranes AA-8 and 9, diagramed in Figure 4.1 were fabricated on porous Inconel and porous SS respectively, with the SS costing $1/3^{rd}$ - $1/6^{th}$ as much. As was clear from Figure 4.1[b], the grading and intermediate layers fabricated by Synthesis Method A were inadequate for the preparation of a dense Pd-layer on the C-$PSS_{310,\ 0.2}$ support for the membrane AA-9.

SEM images (shown in Figure 4.2) of cut cross sections of several membranes fabricated on different supports revealed that, although the supports were all rated nearly identically with regards to the fineness of the pore structure, some had significantly larger pores on the surface. The support ratings of 0.1 or 0.2 μm indicated that the support was capable of filtering particles of that size out from a solution with 95% effectiveness (5% of 0.1 or 0.2 μm particles pass through). The most important aspects of the support, for ease of membrane synthesis, were surface pore size and surface roughness, neither of which were captured in the support rating. For instance the supports used for membranes AA-22, AA-27, and RK-16R all had surface pores larger than 15 μm as shown in Figure 4.2[b], [c], and [d] respectively. In order to effectively synthesize membranes on supports with larger surface pores, more intense grading was necessary such as the Synthesis Method B based on work by Koc (2012) and Ma and Guazzone (2010). Koc (2012) demonstrated effective membrane syntheses on the C-$PH_{0.1}$ supports with surface features as large as 50 μm, by 5 grading steps, beginning with 50 μm, and ending with 0.01 μm alumina particles. Her synthesis methodology was repeated in this study for the four membranes AA-38, AA-39, AA-40, and AA-41 prepared on M-$PSS_{316,\ 0.2}$ supports. Out of those four membranes, one synthesis was still aborted due to defects at the welded regions which were presumably larger than the largest grading particle size (10 μm).

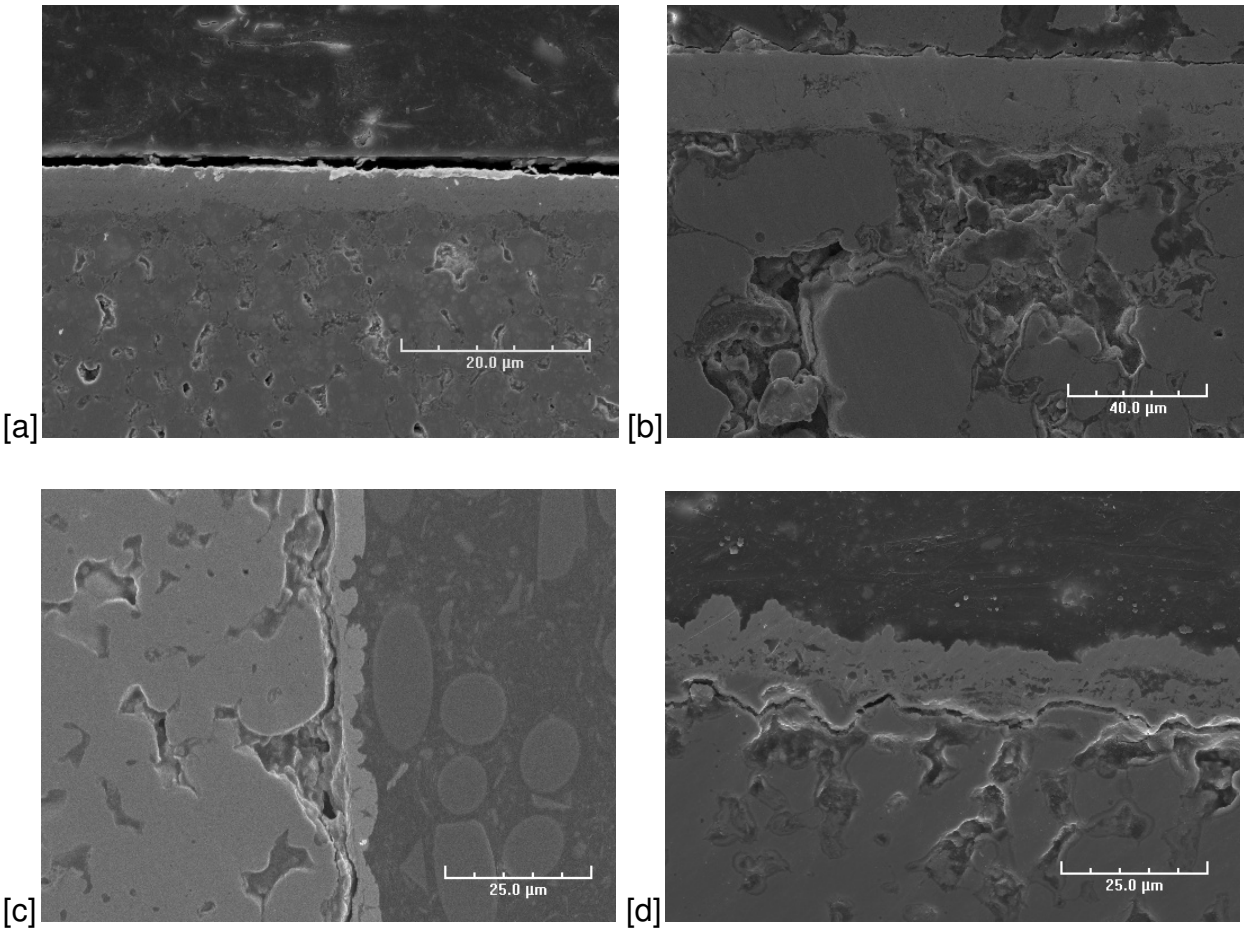

Figure 4.2. SEM cross-section images of fabricated membranes [a] AA-2 (M-$PI_{0.1}$), 1,500X [b] AA-22 (C-$PH_{0.1}$), 500X [c] AA-27 (C-$PSS_{316,0.2B}$), 1,000X [d] RK-16R (M-$PSS_{316,0.2}$), 1,000X.

In many cases defects were observed by the IPA bubble test at the intersection where the porous and non-porous tubes were welded together. When the welding was done (by the support manufacturer) the high temperature could have caused non-uniform sintering in the PSS immediately adjacent to the weld. Excess sintering in the weld regions resulted in rough surface morphology and/or pores much larger (greater than 10 µm) than the expected maximum pore size. In some cases such as the synthesis of AA-30, diagrammed in Figure 4.3[a], additional weld plating was sufficient to block the leaks in those areas. In other cases such as AA-33, diagramed in Figure 4.3[b], a total of 12 + 22 µm of Pd-plating on the defective region was not sufficient to block the defects,

indicating that those defects were initially larger than 10 µm in size (Mardilovich *et al.,* 2002).

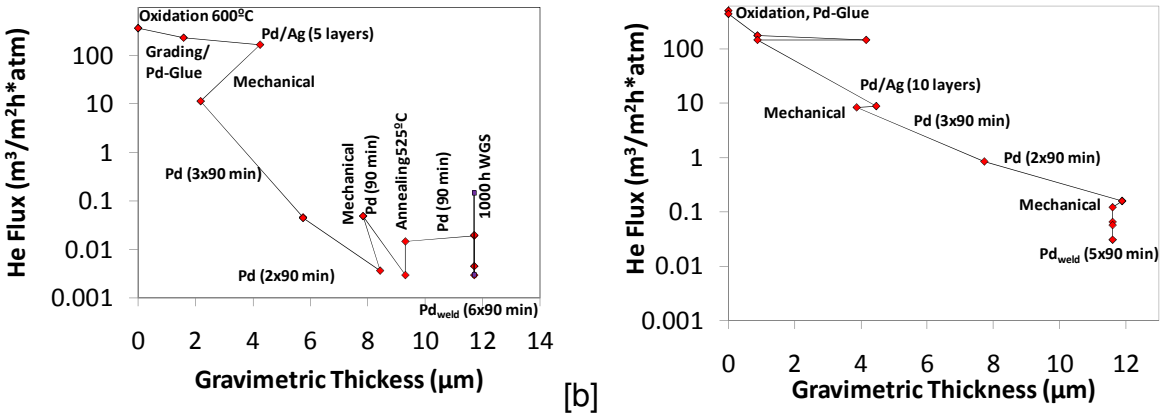

Figure 4.3. Membrane synthesis diagrams [a] Successful weld plating of AA-30 [b] Failed weld plating of AA-33.

Three further attempts were made to block the defective regions of the membranes AA-20, AA-33, and AA-39 by electro-deposition of copper, chromium, and nickel. The electro-plating procedures were described in Chapter 3 (Sections 3.2.5). The rationale for these attempts was that the defective regions could be completely covered by greater than 100 µm of non-permeable dense metal. Electro-deposition was used since much higher plating rates (20 – 100 µm/h) were possible. Figure 4.4 shows the synthesis diagrams of the three membranes AA-20, AA-33, and AA-39. The final step shown in each of the membrane syntheses was electro-deposition of the metal on the regions where defects were observed by IPA bubble test (described in the Chapter 3, Section 3.2.2). For the membrane AA-20, defects were observed on 50% of the surface and including the lower weld. For the membranes AA-33 and AA-39, defects were observed only on the welded regions.

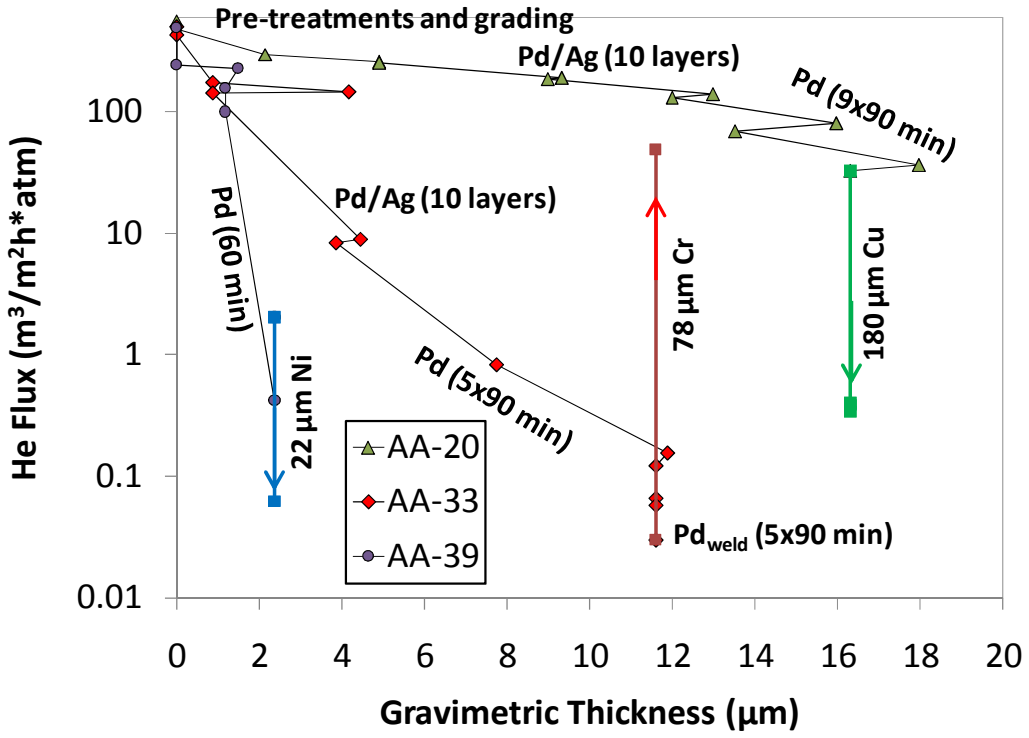

Figure 4.4. Synthesis diagrams of AA-20, AA-33, and AA-39, featuring the electro-plating of defective regions.

The 180 µm Cu-plating conducted on AA-20 significantly lowered the He permeance of the membrane by blocking many of the defects, however, the IPA bubble test showed small leaks still existed in the copper layer indicating that the layer was not completely dense or that the defects were initially larger than 60 µm (significantly greater than previously suspected defect size). The Cr-plating of AA-33 was a complete failure since the Pd-layer warped and cracked where the deposition was occurring due to hydrogen embrittlement. For Cr-plating a higher electric potential of 6.0 volts was required, which, along with the acidic solution, resulted in the evolution of H_2 on the anode (observed as small bubbles) along with the chromium deposition. The deposition of 22 µm of nickel on the welded regions of AA-39 resulted in a significant drop in He flux by masking the surface defects, but was not completely effective as evidenced by IPA bubble test. It was considered possible that a thicker layer of nickel could have effectively blocked the

the surface defects. Koc (2012) achieved limited success at blocking weld defects by repeatedly (up to three times) grading the defective regions with 5 – 0.01 μm α-alumina particles, followed by Pd weld-plating.

Even if grading and additional weld plating could be made effective, an issue still existed with non-weld defects, or defects located randomly on the support surface. These defects could not be dealt with in a specific region by weld-plating but could only be fixed by a treatment applied to the whole membrane surface without significantly increase the membrane thickness. There is not yet a proven method to accomplish this.

The most relevant criterion by which different membrane synthesis methods could be compared was the dense Pd thickness. There seemed to be a correlation between the number of grading layer applications and the final Pd-thickness for the completed membranes as shown in Figure 4.5. The membranes prepared with zero to two grading steps required significantly more Pd-plating to achieve a dense layer. The membranes prepared with four to six grading steps (large particles first, followed by smaller particles as detailed in Synthesis Method B, Experimental, Section 3.1) required as little as 1.5 μm of additional Pd to become dense. The membranes prepared by Guazzone *et al.* (2008), which were also graded with alumina, followed the same trend. It was clear that sequential cycles of grading improved the quality of the grading layer resulting in finer surface features, for at least up to four grading treatments. The membranes prepared by Nam and Lee (1999; 2001) were graded for an extended period (5 hours) suggesting that the quality of grading also improved over time, although that conclusion was not supported by the similar work of Tong et al. (2004; 2006) who required 8 μm of Pd-plating to achieve a dense layer even after 10 hours of grading.

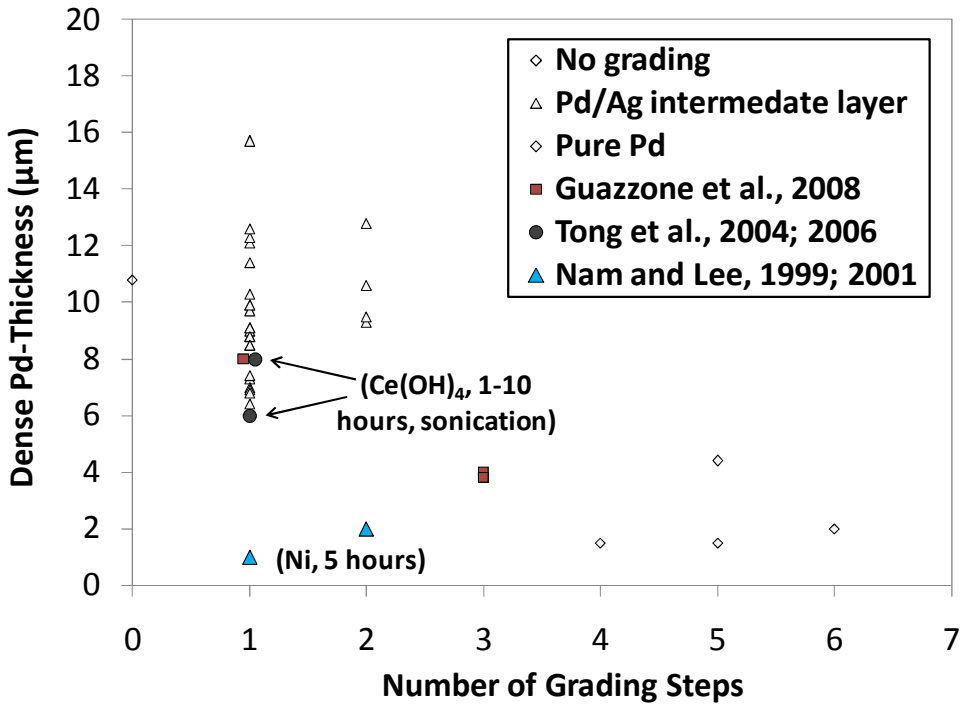

Figure 4.5. Dense Pd thickness versus number of grading steps.

The application of the Pd/Ag intermediate layer was also believed to play the same role as grading (Ma *et al.,* 2007; Ayturk *et al.,* 2006), however, there did not seem to be any correlation between the Pd/Ag thickness and the required dense Pd thickness. In some cases such as AA-31 and AA-34 a second application of the Pd/Ag intermediate layer seemed to decrease the required Pd-thickness as compared to similarly prepared membranes with only one Pd/Ag layer such as AA-29 and AA-30. In other cases such as IM-79 and IM-86b, up to four intermediate Pd/Ag layers did not reduce the required dense Pd-thickness even though the same C-$PSS_{316,0.2A}$ supports were used. Some of the C-$PSS_{316,\ 0.2A}$ supports had extensive defects and some were defect free. The use of a thicker Pd/Ag intermediate layer for the membranes IM-79 and IM-86b would suggest that the supports utilized had small defects (3 – 7 µm in size), which were not big enough to prevent membrane fabrication. The number of Pd/Ag intermediate layers and the estimated Pd/Ag gravimetric thickness for each membrane can be found in Appendix D.

Some membranes developed leaks rapidly upon H_2 testing or, after having been tested for many hundreds of hours, developed a great enough leak so that further testing was not useful, and so those membranes were mechanically polished and re-plated. The membranes which were re-plated in this way are summarized in Table 4.4 and designated by the same name, with a suffix "R". All of the membranes in Table 4.4 were subsequently tested in H_2 and are considered in this study as different membranes.

Table 4.4. Membranes which have been tested then mechanically polished and re-plated.

Membrane	Reason for re-plating	Polishing depth (μm)	Pd-Plating (μm)	Comments
AA-4R	Low selectivity	0.6	3.2	
AA-6R	Long testing period	3.0	1.5	Heavy polishing treatment
AA-8R	Long testing period	0.9	1.5	
AA-8RR	Low selectivity	0.6	2.1	
AA-8RRR	Low selectivity	1.8	2.1	Heavy polishing treatment
AA-12R	Annealing required	1.2	2.4	Mechanical, plating, annealing, mechanical, and plating
		1.2	2.1	
AA-14R	Low selectivity	1.3	2.2	Polishing and buffing
AA-24R	Low selectivity	0.5	1.0	
AA-38R	Higher leak stability	0	2.9	No polishing
AA-40R	Low selectivity	2.1	4.0	Heavy polishing treatment, additional fine grading, 0.8 μm Au
RK-16R	Thicker dense layer	0	3.2	No polishing, plated to obtain similar permeance to AA-40R

4.4.2. H_2 permeance characterization

The H_2 permeance characterization of the membrane AA-5, shown in Figure 4.6, was representative of most of the initial H_2 testing conducted on the membranes described in this study. Upon admitting hydrogen into the system at time = 5 hours, H_2 very quickly (within 1 hour) began permeating the membrane and reached a stable rate. He leak tests were conducted before changing temperatures and are labeled in the figure, the selectivity stability of the membranes will be discussed at length in a following section (Section 4.4.4). When the temperature was changed at 28, 53, and 73 hours, the

membrane permeance changed immediately and stabilized quickly. At each temperature Sieverts' law data were collected.

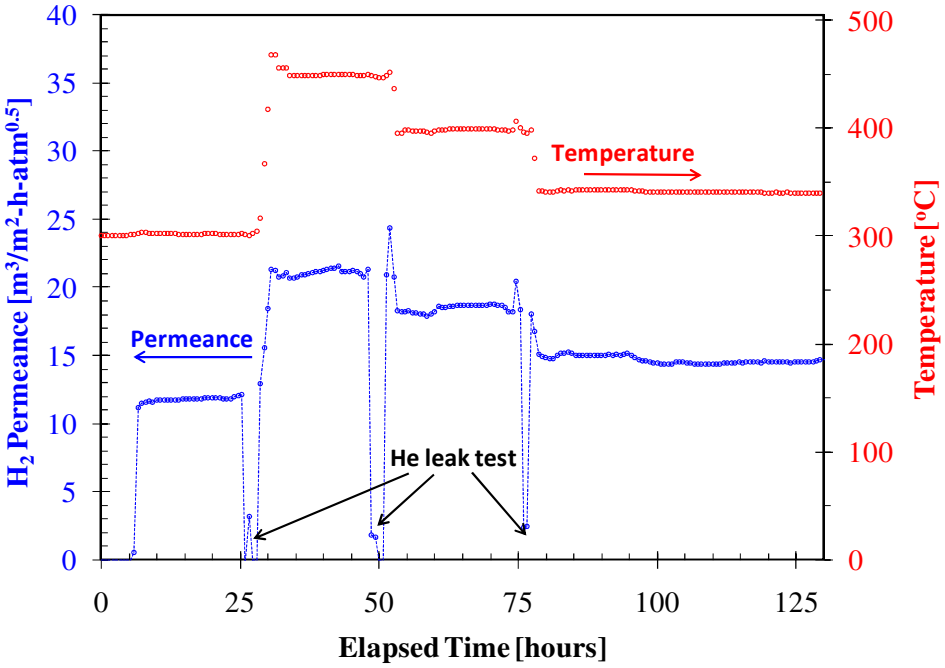

Figure 4.6. H_2 permeance characterization of the membrane AA-5.

Typical Sieverts' plots for the membrane AA-5 at 350, 400, and 450℃ are shown in Figure 4.7 and are also representative of the initial testing conducted on all the membranes. The linear relation shown in the figure confirmed that the H_2 permeation was mainly controlled by the hydrogen diffusion through the bulk Pd-layer.

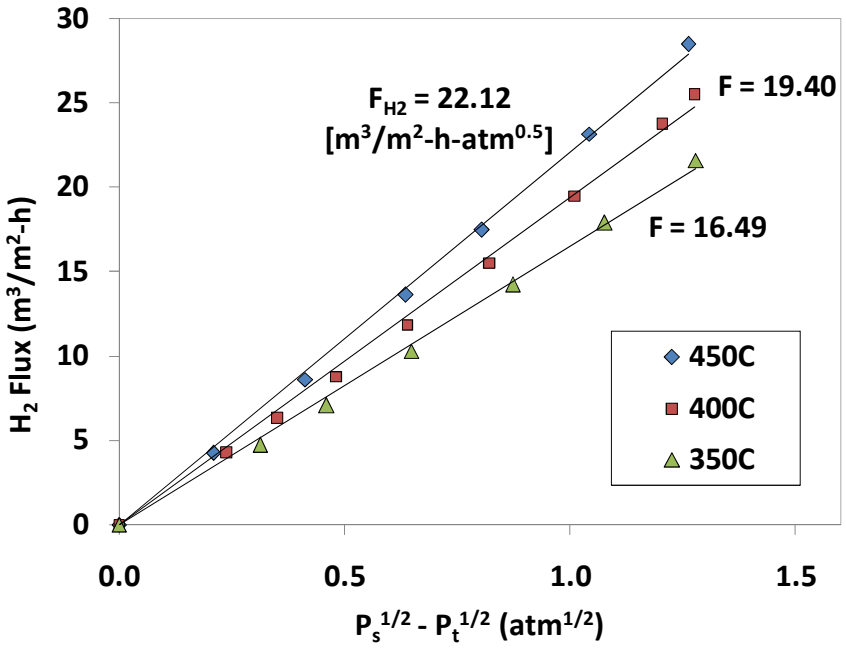

Figure 4.7. Sieverts' law plots for membrane AA-5 at 350, 400, and 450°C.

The activation energy, E_A [kJ/mol], for H-atom diffusion through the Pd-lattice was related to the membrane permeance via equation **4.5**.

$$\boldsymbol{F_{H2} = \frac{Q_0}{\delta_{Pd}} \exp\left(-E_A/RT\right)} \qquad \textbf{4.5}$$

Taking the natural log of equation **4.5** and simplifying resulted in equation **4.6**, known as an Arrhenius relation.

$$\boldsymbol{\ln(F_{H2}) = \ln\left(\frac{Q_0}{\delta_{Pd}}\right) - \frac{E_A}{RT}} \qquad \textbf{4.6}$$

The natural log of the permeance was plotted versus the inverse temperature and a linear regression was conducted. The Arrhrenius relation was plotted for several membranes in Figure 4.8. The slope of the regression was equal to $-E_A/R$ and the y-intercept was equal to the natural log of Q_0/δ_{Pd}.

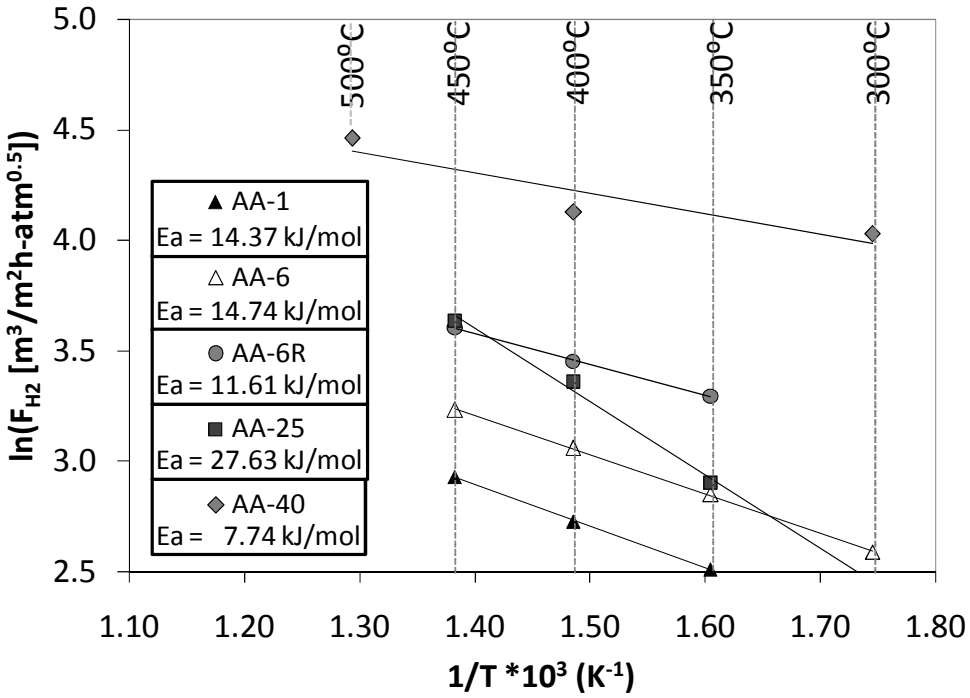

Figure 4.8. Arrhenius plots for the membranes AA-1, AA-6, AA-6R, AA-25, and AA-40.

For every membrane tested at three or more temperatures the activation energy was calculated and can be found in Appendix D. As shown in Figure 4.8 and listed in Appendix D, the activation energy for H_2 permeation in approximately half of the membranes tested was found to be between 11.6 (AA-6R) and 14.7 kJ/mol (AA-6), which was close to the literature value of 13.81 kJ/mol for a Pd-foil (Morreale *et al.,* 2003). The activation energy of higher than the literature value might suggest that some intermetallic diffusion of support metals had occurred. Since the membrane AA-25 incorporated a Pd/Ag barrier, it was unclear why intermetallic diffusion would have occurred. An activation energy lower than the literature value might suggest that mass transfer resistance from the support was partially rate limiting (such as with the thinner membrane AA-40, which had a dense Pd thickness of only 1.5 µm). Mass transfer by Knudsen diffusion was weakly dependant on temperature (to the ½ power) so that the combined activation energy for transport through the composite layer would be low if Knudsen diffusion was the rate limiting step.

The H_2 permeance of the Pd-membranes should be proportional to the inverse thickness of the dense membrane layer (Shu *et al.,* 1991), however, the structure of the intermediate layers, as well as the grain structure of the dense Pd-layer could also have significant effects which could be difficult to isolate and identify. The H_2 permeance of each membrane at 400°C is plotted versus the inverse gravimetric Pd-thickness and versus the inverse overall gravimetric thickness (including the Pd-glue and Pd/Ag barrier) in Figure 4.9[a] and [b] respectively. Note that the gravimetric thickness estimate included significant error due to the slight weight changes being measured on significantly heavier supports (0.01 g weight change on a 160 g support). Thickness estimates were also inaccurate if support corrosion had occurred during plating and/or if plating salts were not adequately rinsed from the support after plating. Only the outlier membranes were specifically labeled in the figure so that they could be discussed; the H_2 permeance of all membranes tested and at every testing temperature can be found tabulated in Appendix D.

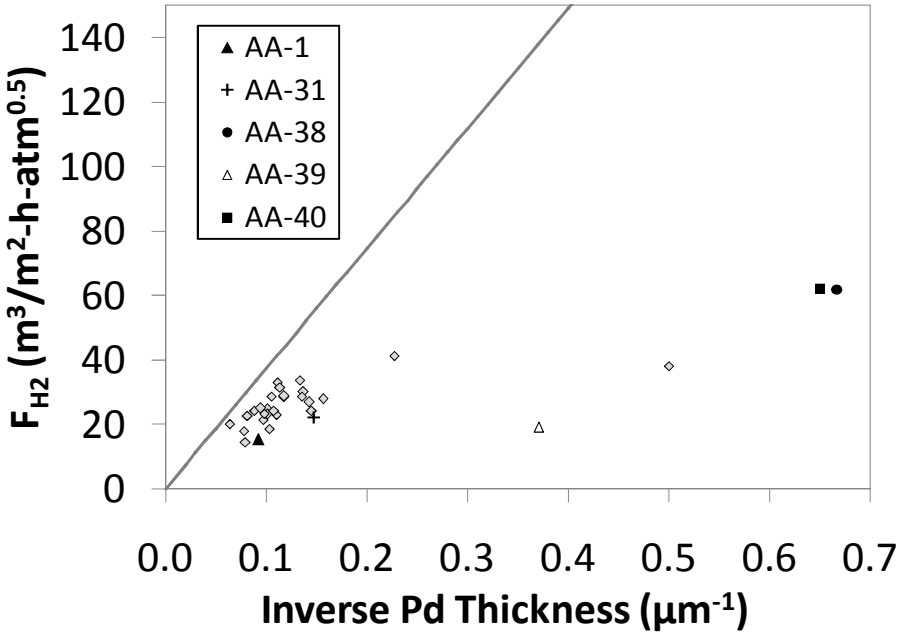

[a]

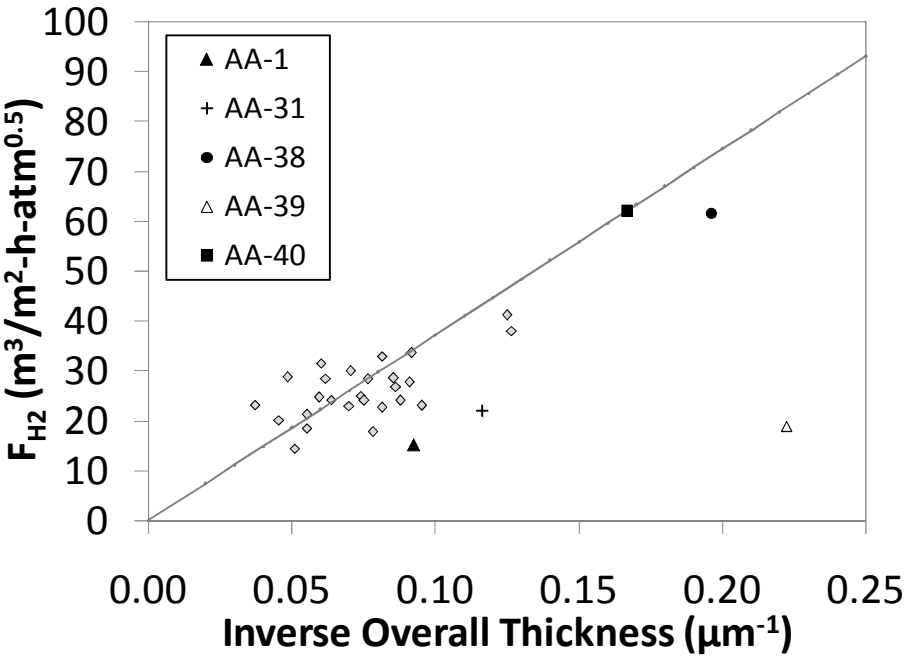

[b]

Figure 4.9. H_2 permeance versus inverse gravimetric thickness at 400°C [a] Considering dense Pd thickness [b] Considering overall gravimetric thickness (Solid lines indicate free-standing Pd-foil {Morreale *et al.,* 2003}).

Generally, when the Synthesis Method A (described in the Experimental, Section 3.1) was adhered to (as was the case with the majority of membranes in Figure 4.9) the H_2 permeance at 400°C was between 15 – 35 m^3/m^2-h-$atm^{0.5}$ and was most closely proportional to the inverse overall thickness.

The H_2 permeance of most of the membranes was 10 – 35% lower than that calculated based on the dense Pd-layer due to the moderate influence of the mass transfer resistance in the PSS support, potentially increased by the alumina grading and Pd/Ag layers. Some membranes such as AA-1, AA-31, and AA-39 had even lower permeance for other reasons. The low H_2 permeance of membrane AA-1 was the result of intermetallic diffusion since that membrane had no oxide or Pd/Ag intermediate layers. The membrane AA-31 was fabricated with significant additional weld plating, effectively blocking about $1/6^{th}$ of the membrane area, reducing the average permeance. If an area of only 19.6 cm^2 (instead of 23.5 cm^2) was used for the H_2 permeance calculation, then

a permeance value of 26.4 m^3/m^2-h-$atm^{0.5}$ was obtained, which was in line with the other membranes shown in Figure 4.9[a] and [b]. The membrane AA-39 was plated with 0.6 μm of Ag as the final step in an attempt to fabricate a Pd/Ag-alloy membrane. The membrane was then annealed at 550°C for 70 hours. It was possible that complete alloying did not occur in the membrane AA-39 since the permeance was very low relative to its thickness.

The membranes AA-38 and AA-40 were fabricated by Synthesis Method B (described in the Experimental, Section 3.1) such that the alumina grading was much more extensive, and no Pd/Ag intermediate layer was applied. When considering just the dense Pd-thickness, both of these membranes fell significantly below the expected H_2 permeance (75% below) due to mass transfer resistance in the support and grading layers. Since both membranes were very thin and the H_2 permeance was high, mass transport in the support potentially became rate limiting. The trend seen in Figure 4.9[a] suggested that membranes with thinner Pd-layers had a smaller fraction of the theoretical foil H_2 permeance, indicating that the fabrication of a thinner Pd-layer would not necessarily result in higher H_2 flux. Further improvement in H_2 permeance should be achieved via better supports and/or intermediate layer modification to obtain lower mass transfer resistance.

4.4.3. H_2 flux behavior at high pressures

The membranes AA-4R, 6R, and 8R were all tested in H_2 at shell-side pressures of up to 16.8 atma as shown by the Sieverts' law plots in Figure 4.10. It was clear from the figure that there was a systemic deviation of the Sieverts' law equation **4.2**, from the data for the membranes AA-6R and 8R as the H_2 flux exceeded the fitting by as much as 4% at high pressure (16.8 atma) and fell short of the fitting by as much as 20% at low pressure (1.2 – 2.3 atma). The accuracy for the mass flow meters was 2% of the full-scale value (5 L/min) and that of the pressure sensors was 0.5% (full-scale: 17.0 atma). The inadequate fitting for those two membranes was potentially due to the solubility of hydrogen in the Pd-lattice deviating from the ½ power in terms of partial pressure. The inadequate fitting may also have been due to mass transfer resistance in the support which also could not be fitted to the ½ power in terms of pressure difference. The flux

data for membrane AA-4R fit the Sieverts' law equation better since the pressure range was not so great (P_s = 1.4 – 9.1 atma) as that applied to the other two membranes.

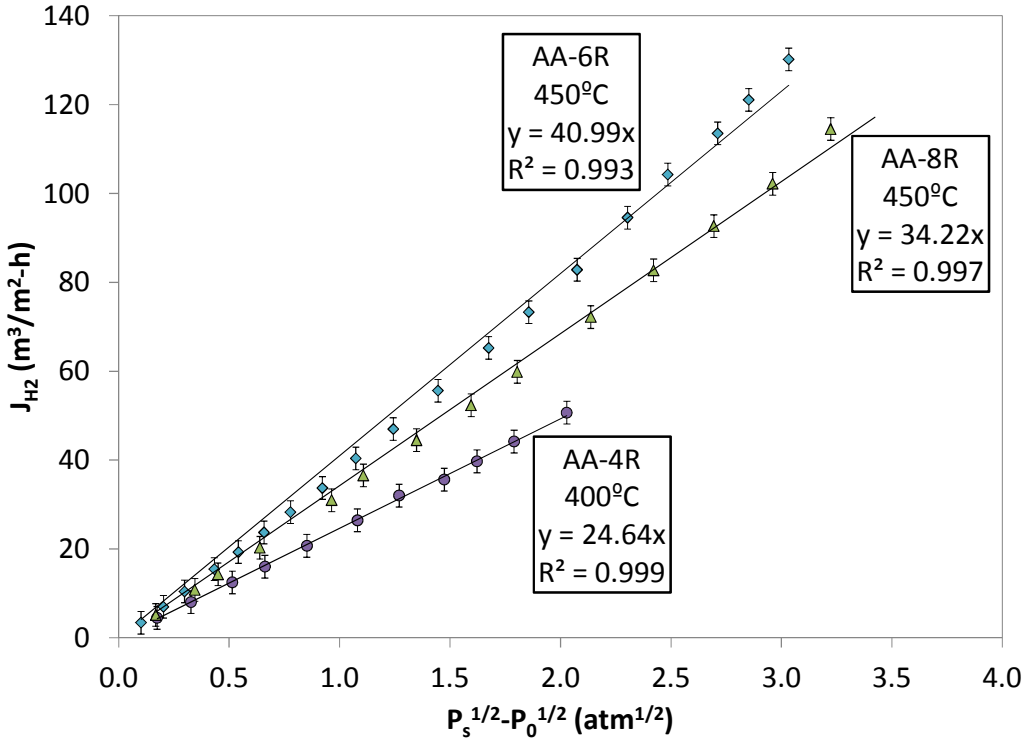

Figure 4.10. Sieverts' law plots over large pressure range (1 – 16.8 atma) for the membranes AA-4R, AA-6R, and AA-8R.

The data sets shown in Figure 4.10 were each fitted to equation **4.3** by the method of least squares and the results are plotted in Figure 4.11 with the calculated *n*-values labeled in the figure. The addition of the adjustable parameter, *n*, allowed for a very good fitting to equation **4.3**, and resulted in a highly linear relationship under the range of conditions tested.

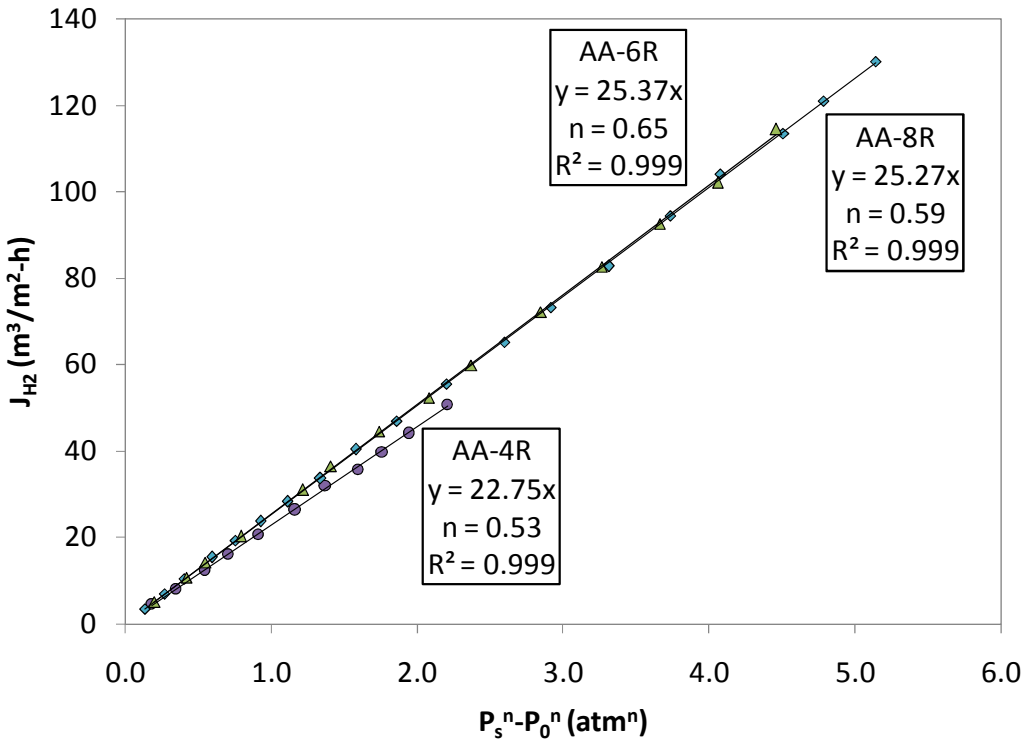

Figure 4.11. Data fitting to equation **4.3** for the membranes AA-4R, AA-6R, and AA-8R, best-fit *n*-values for each series are included in the trend line labels.

The higher *n*-values of 0.65 and 0.59 calculated for AA-6R and AA-8R respectively, indicated several potential phenomena could have been occurring: rate limiting desorption on the downstream Pd-surface, significant leak through defects, a change in solubility of H-atoms in the Pd-lattice at elevated pressures, or significant resistance from the porous support (Ward and Dao, 1999; Catalano *et al.,* 2010; Guazzone *et al.,* 2006; Morreale *et al.,* 2003). The potential existence of each of these phenomena will be discussed below. The *n*-value of 0.53 for AA-4R suggested that the diffusion of hydrogen in the Pd-lattice was the rate limiting transport step and that no assumptions inherent in the derivation of Sieverts' law were violated.

A more comprehensive set of flux data was collected by also changing the tube-side pressure. The membrane AA-12R was comprehensively tested in H_2 at 450℃ with the shell-side pressure varied from 0.97 – 21.5 atma and the tube-side pressure varied from

0.97– 13.7 atma. The shell and tube-side pressure ranges for each series of experiments conducted both in the ascending and descending order of the pressure settings are reported in Table 4.5. Sieverts' law plots of the flux data collected from the experiment series 1-4 and 5-8 are presented in Figure 4.12[a] and [b] respectively. The *n*-value of 0.5 was used to plot the data in each figure so that a clear comparison and discussion could be made of the membrane permeance.

Table 4.5. List of conditions for the experiments conducted with the membrane AA-12R.

Series #	Method	P_s [atma]	P_t [atma]
1	Fixed P_t (baseline)	1.5 - 21.5 (ascending)	0.97
2	Fixed P_s	21.5	0.97 - 13.6 (ascending)
3	Fixed P_s	14.4	13.1 - 0.97 (descending)
4	Fixed P_t	14.4 - 1.5 (descending)	0.97
5	Fixed P_t	4.8 - 21.5 (ascending)	4.3
6	Fixed P_t	7.9 - 21.3 (ascending)	7.1
7	Fixed P_t	11.2 - 21.4 (ascending)	10.3
8	Fixed P_t	14.2 - 21.5 (ascending)	13.6

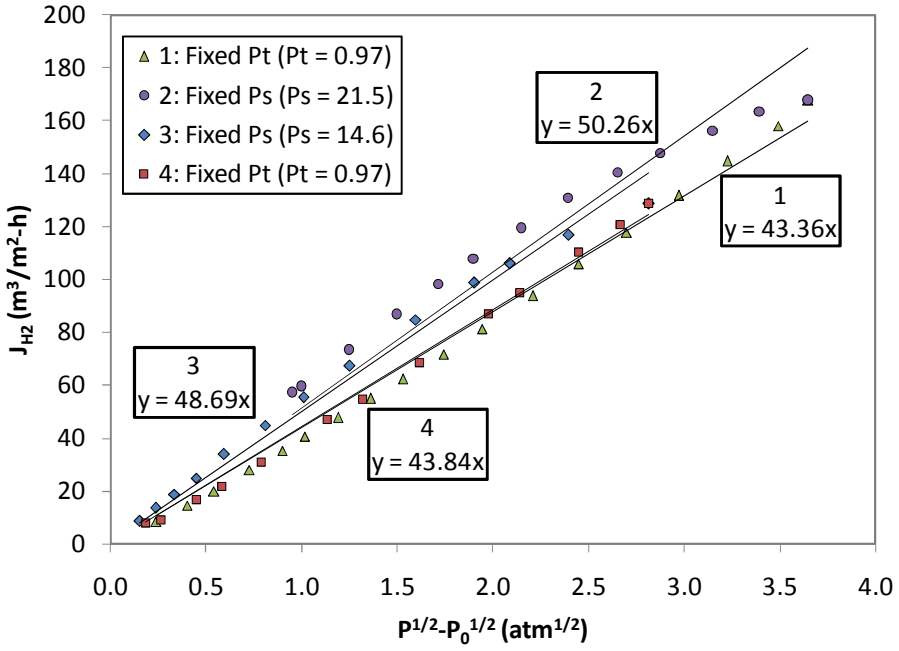

[a]

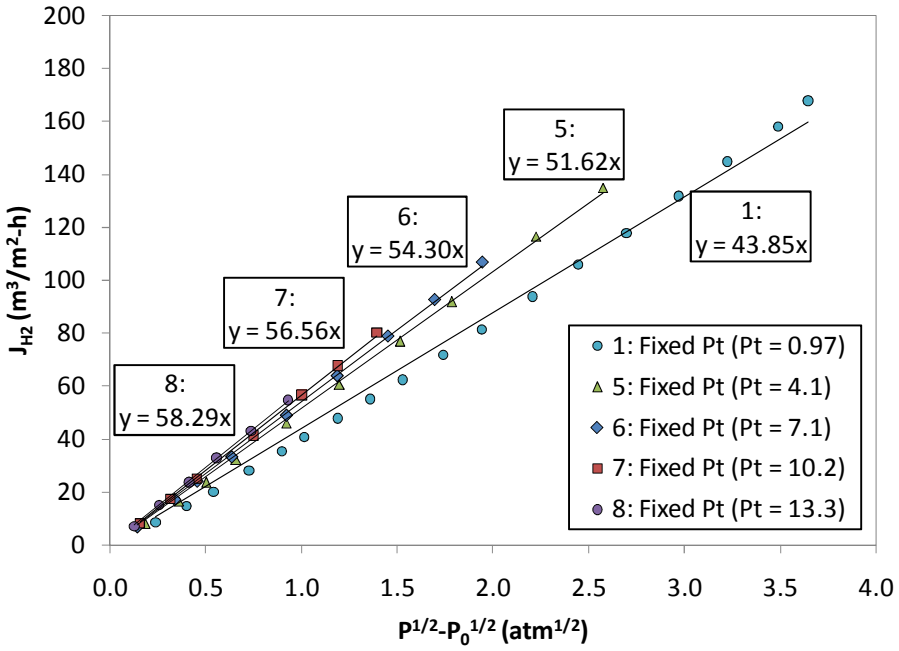

[b]

Figure 4.12. Sieverts' law plots of the high pressure H_2 experiments conducted with the membrane AA-12R [a] Series 1-4 [b] Series 1, 5-8.

While the square root relationship was used to plot the data in Figure 4.12, the best-fit *n*-value for each series of measurements was also calculated by fitting to equation **4.3** using Newton's iterative method, and is listed in Table 4.6.

Table 4.6. Optimal n-values derived by fitting to equation **4.3**.

Series #	n-value	${}^nF_{H2}$ [m^3/m^2-h-atm^n]
1	0.63	28.2
2	0.83	14.6
3	0.77	19.2
4	0.64	28.3
5	0.62	32.1
6	0.62	32.0
7	0.72	22.2
8	0.67	27.4

Series 1 in Figure 4.12, which was the baseline case and the typical method of H_2 permeance measurement (a fixed P_t equal to the atmospheric pressure and an incrementally increasing P_s), yielded a H_2 permeance of 43.9 m^3/m^2-h-$atm^{0.5}$, 17% higher than the H_2 permeance measured at low pressure (P_s = 2.0 and P_t = 0.97 atma). The deviation from Sieverts' law for this series, which corresponded to an *n*-value of 0.63, was similar to the behavior observed for membranes AA-6R and AA-8R.

Series 2 and 3 (Figure 4.12[a]) were conducted by fixing the shell-side pressure and increasing (or decreasing) incrementally P_t. Both series resulted in a significantly higher H_2 permeance (up to 17% higher) for the membrane than the baseline case of Series 1 and significantly higher *n*-values. Series 3 and 4 (Figure 4.12[a]) were conducted in the reverse order of Series 1 and 2 to verify that the order of measurements would not affect the results; indeed Series 1 and 4 matched to within 1.1% despite being measured in ascending and descending order respectively. Series 2 and 3 would be expected to overlap if Sieverts' law was applicable, but they did not because fixed shell-side pressures were not the same.

Series 5-8 (Figure 4.12[b]) were conducted with fixed P_t > 1 atma, such that the P_t for each series was higher than the previous; $P_{t,5} < P_{t,6} <$ etc. At each higher P_t, the estimated H_2 permeance also increased, up to 58.3 m^3/m^2-h-$atm^{0.5}$ (P_t = 13.3 atma), the calculated *n*-values, however, were all very close to 0.62, deviating by less than 4%. The H_2 permeance calculated from Series 8 was 56% higher than the H_2 permeance measured at low pressure. All the series conducted with a fixed P_t yielded low *n*-values (less than 0.64), while the series conducted with a fixed P_s yielded high *n*-values (greater than 0.77). It was clear that over the large range of pressures neither Sieverts' law (equation **4.2**) nor the generalization of Sieverts' law (equation **4.3**) were adequate to fit the experimental data and a more complex model would have to be utilized.

It was expected that the *n*-value would differ slightly from 0.5 due to the inherent uncertainty in the data, however, significantly higher *n*-values could indicate that another transport step was partially rate limiting or that the solubililty relationship assumed in Seiverts' law was invalid at the higher pressure. For data fit to equation **4.3**, an *n*-value in excess of 0.5 could indicate one or more potential phenomena: rate

limiting desorption on the downstream Pd-surface at low temperatures or due to surface impurities, significant leak through defects (a H_2/inert selectivity of less than 400), a change in solubility of H-atoms in the Pd-lattice at elevated pressures partial, or significant resistance from the porous support (Ward and Dao, 1999; Catalano *et al.,* 2010; Guazzone *et al.,* 2006; Morreale *et al.,* 2003). Considering that the selectivity of all three membranes was in excess of 1,000 at the time of testing it was unlikely that flow through defects altered the *n*-value (Guazzone *et al.,* 2006). Ward and Dao (1999) showed that for a 10 μm Pd-layer, desorption limited flux only occurred at temperatures below 300°C, so it was very unlikely that such a limitation existed in our case.

It was possible that the high *n*-values were an indication that the Pd-lattice was becoming saturated with hydrogen such that Sieverts' law was no longer valid at the high pressure. At 450°C and a H_2 pressure of 21.5 atma the approximate solubility of hydrogen atoms in the Pd lattice was 0.040 H/Pd (Magnouche and Fromageau, 1984). If the assumption of low H/Pd ratio was relaxed, the H_2 flux would be governed by equation **2.30** (derived in Section 2.2.1 and in more detail in Appendix A.2).

$$\boldsymbol{J = \frac{D_H \kappa}{\delta_{Pd}} \left(\frac{\sqrt{P_1}}{K_S + \sqrt{P_1}} - \frac{\sqrt{P_2}}{K_S + \sqrt{P_2}} \right)} \qquad \textbf{2.30}$$

Magnouche and Fromageau (1984) estimated the Sieverts' constant, K_S, to be 1.032×10^5 $atm^{0.5}$-mol_{Pd}/m^3_{H2} at 450°C, which was much greater than the square-root of the highest pressure (4.63 $atm^{0.5}$), so saturation of the Pd-lattice was unlikely. The possibility still existed that the square-root dependence of the dissolved H-atom concentration was not legitimate such that equation **4.7** (algebraically rearranged from equation **2.28** in the Literature Review) could not be used.

$$\boldsymbol{\sqrt{P_x} = \frac{K_S v_x}{(1 - v_x)}} \qquad \textbf{4.7}$$

Magnouche and Fromageau (1984) investigated the solubility of H-atoms in the Pd-lattice at high pressure and found the equation **4.8** to better fit the experimental data.

$$\boldsymbol{\ln\left(\sqrt{P_x}\right) = \ln\left(\frac{K_S v_x}{1 - v_x}\right) + \frac{v_x E_H}{RT}} \qquad \textbf{4.8}$$

Where E_H [kJ/mol] was the energy of interaction between dissolved H-atoms which was approximately -52.8 + 0.0257*T kJ/mol$_H$. The interaction term, $v_x E_H$/RT, accounted for increased solubility at higher pressures due to a partial attraction between dissolved H-atoms. At temperatures below 298°C, the interaction term manifested as plateau of pressure versus H/Pd ratio (such as those seen in Figure 2.3 in the Literature Review), corresponding to the α/β-phase transition. Isotherms of the hydrogen solubility (in H/Pd atomic ratio) versus the square-root pressure are plotted in Figure 4.13 based on both equations **4.7** and **4.8**. The highest pressure utilized in the experimental measurements (21.5 atma) is also indicated in the figure as a solid vertical line.

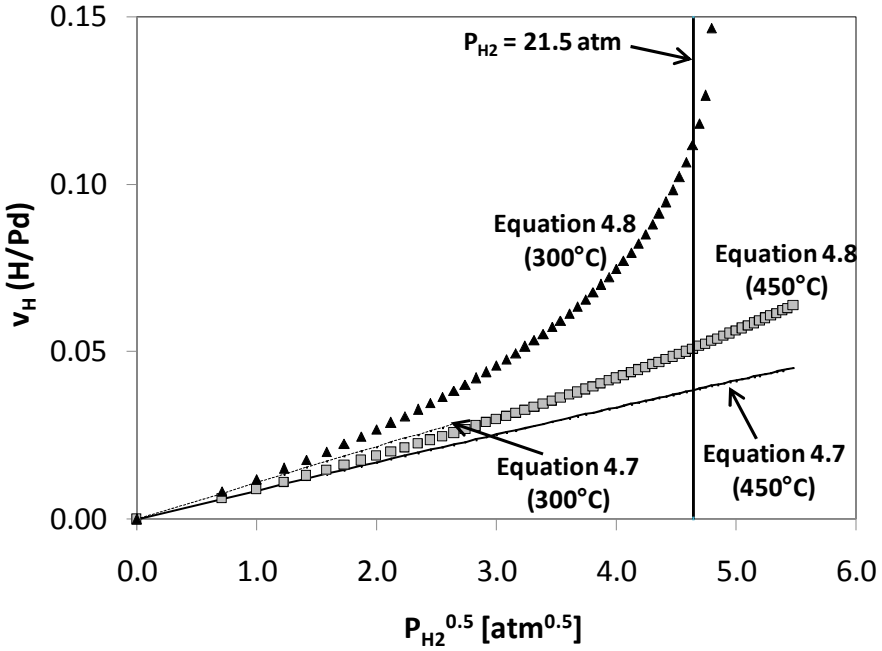

Figure 4.13. Estimation of H-atom solubility in Pd by equations **4.7** and **4.8**.

The deviation of equation **4.8** from the square-root dependence necessary for Seiverts' law was significant at pressures exceeding approximately 4 atma such that equation **4.8** exceeded equation **4.7** by as much as 32% at 450°C. The deviation was much greater at lower temperature (300°C) such that the H/Pd ratio reached a vertical asymptote at a pressure of approximately 23 atma (close to the critical pressure of 19.7 atma determined by Frieske and Wicke {1972} for the limit of the α, β two-phase region).

The equation **4.8** was used to determine v_x, which was then used to calculate the H_2 flux by equation **2.24** (Fick's Law) for the range of pressures tested in Series 1 and 2 with the membrane AA-12R (Table 4.5). The calculation and the experimental results are plotted in Figure 4.14. A Pd-thickness of 12.1 μm (representing the membrane AA-12R) and an H-atom diffusivity of 2.72×10^{-5} m^2/h (Holleck, 1970) were used in the calculation.

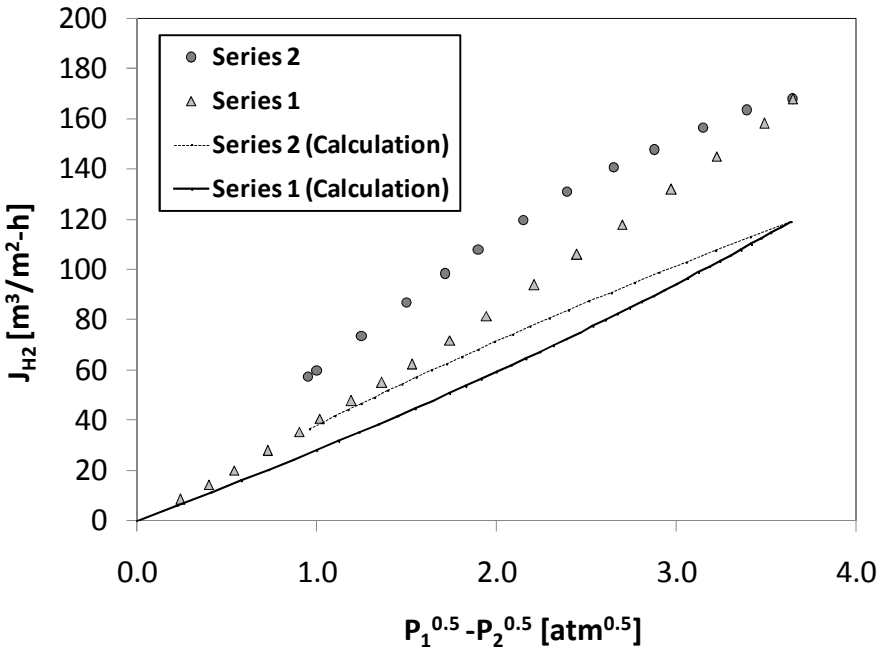

Figure 4.14. Experimental H_2 flux for the membrane AA-12R (Series 1 and 2 from Table 4.5), including the calculated H_2 flux by equations **4.8** and **2.24**.

Since the calculated H_2 flux displayed the same deviation from Sieverts' law as the experimental data (Figure 4.14, positive curvature for Series 1 and negative curvature for Series 2) it seemed likely that the cause could have been the interaction between dissolved H-atoms, expressed by the $v_x E_H$/RT term in equation **4.8** (Magnouche and and Fromageau, 1984). As discussed by Magnouche and Fromageau (1984) the interaction was attractive in nature and resulted in greater hydrogen solubility with increasing pressure. The greater solubility (as shown by Figure 4.13) resulted in H_2 flux exceeding that projected by Sieverts' law at high pressures. In Figure 4.14, the

experimental flux was significantly greater (approximately 45%) than the calculation based on the literature values of solubility and diffusivity. This discrepancy could have been due to the inaccuracy in the gravimetric thickness estimate (the actual Pd-thickness may have been closer to 8 μm) or partial alloying of the Pd/Ag barrier, resulting in a higher H_2 permeability.

The final possible cause for an *n*-value of greater than 0.5 was that the mass transfer resistance in the porous support limited the flux to some extent (Guazzone *et al.,* 2006). Although the He permeance of the bare supports were quite high (220 - 650 m^3/m^2-h-atm), the application of grading and intermediate layers reduced that permeance by up to one-order of magnitude. The mass transfer resistance in the support, $R_{sup.}$ [atm-h/m], was estimated based on the He permeance, F_{He} [m^3/m^2-h-atm], measured during the synthesis as in equation **4.9**. The H_2 mass transfer resistance was adjusted for temperature and gas composition (He to H_2) assuming that the transport in the porous support was primarily Knudsen flow. The mass transfer resistance, R_{Pd} [atm-h/m], for transport through the dense Pd-layer was calculated by equation **4.10**, note that $J_{H2} = \Delta P_{H2}/R_{Pd}$ is algebraically equivalent to Sieverts' law, equation **4.2**. The equation **4.10** is derived in Appendix A.3.

$$R_{sup.} = \frac{1}{F_{He}} * \sqrt{\frac{T_{H2.}}{T_{r.t.}}} * \sqrt{\frac{m_{H2}}{m_{He}}} \qquad \textbf{4.9}$$

$$R_{Pd} = \frac{\delta_{Pd} K_S}{D_H \kappa} \left(\sqrt{P_1} + \sqrt{P_2}\right) \qquad \textbf{4.10}$$

Where T_{H2} [K] was the H_2 testing temperature and m_{H2} [kg/mol] and m_{He} [kg/mol] were the molecular masses of the gas species. Considering the membrane AA-12R, the H_2 mass transfer resistance of the support + grading + intermediate Pd/Ag was 0.0046 atm-h/m, and the mass transfer resistance of H_2 through the 12.1 μm Pd-layer was 0.0135 atm-h/m at the same ΔP (P_s = 2 atma and P_t = 1 atma). Since the mass transfer resistances were within one order of magnitude of each other, the support resistance probably influenced the H_2 flux to some extent and altered the *n*-value. If the dense layer thickness was less than 12.1 μm and/or there was some alloying from the Pd/Ag-layer, the resistance of the dense layer would have been less than the above estimate,

making the support resistance more significant in comparison. A further inaccuracy was introduced by the estimation of the support resistance from the He permeance. It was unclear from the synthesis diagram at what thickness of Pd-plating the mechanism of H_2 transport changed from Knudsen diffusion in the porous media to lattice diffusion in the Pd-layer, leading to only a rough estimate of the true support resistance.

Based on the calculations it seemed likely that both the increased solubility of H-atoms in the Pd-lattice at higher pressure and the contribution of support resistance caused the deviation from Seiverts' law behavior. It was not clear how these two effects could be disentangled and quantified for the composite Pd/PSS membrane.

4.4.4. H_2/inert selectivity and leak stability

A thorough understanding of the leak growth in the PSS supported Pd-membranes under pure H_2 testing was a prerequisite to the more complex issue of leak growth under high pressure, high flow, and reactive conditions. A significant obstacle to understanding the occurrence and mechanisms of leak growth in Pd-membranes was the lack of work in the literature dealing with the subject. Very few studies extensively tested the inert gas leak over extended periods of time in supported Pd-membranes. To more properly explore the phenomenon of leak growth in Pd-membranes, long-term testing (greater than 100 hours) was conducted on over 17 membranes and the results are discussed.

The development of leaks in the dense Pd-layer occurred in several potential stages. An initial high rate stage sometimes occurred upon first heating to a high temperature and switching to H_2. A second stage usually occurred which was characterized by a slow but constant rate of growth. Lastly, a third stage sometimes occurred in which a discontinuous jump in leak was observed. The plot of He leak versus time in Figure 4.15 shows the leak growth for the membrane AA-8 which was primarily second stage. The Figure 4.15 also shows the first stage of leak growth for AA-12R, and the second and third stages for AA-14.

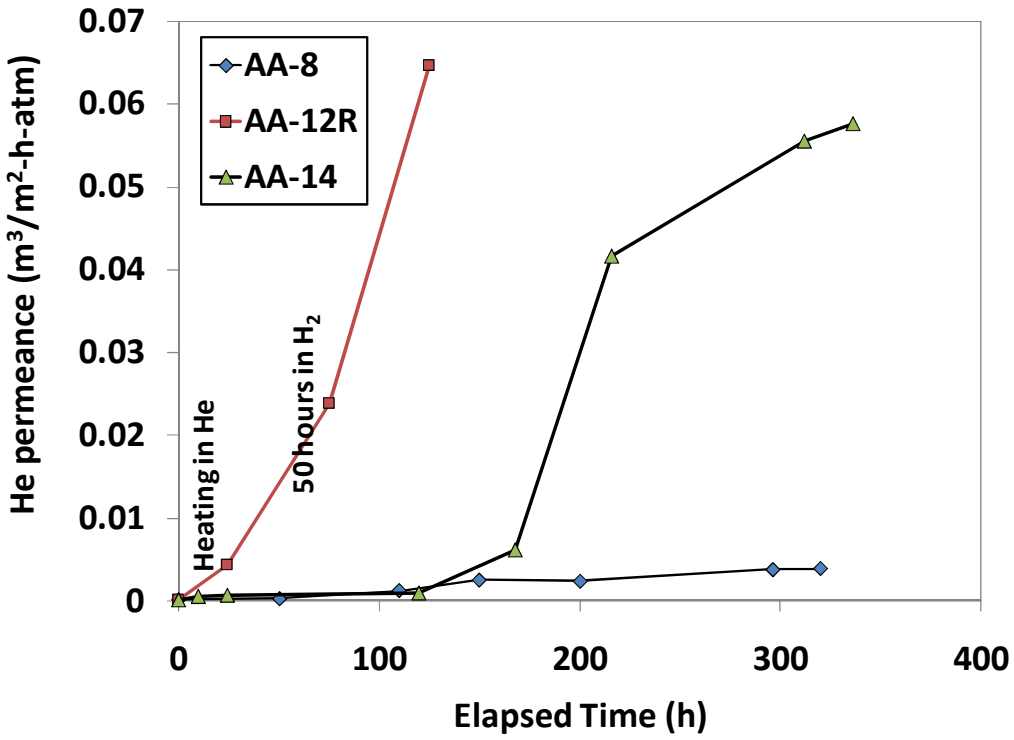

Figure 4.15. He permeance versus time for the membranes AA-8, AA-12R, and AA-14.

The very gradual increase in leak observed for membrane AA-8 in Figure 4.15 typically indicated pinhole formation in the dense Pd-layer, a process which was very slow at temperatures less than 500°C (Guazzone *et al.,* 2006). The immediate jump in leak for the membrane AA-12R, first upon heating, then further upon switching to H_2 was potentially caused by annealing and grain growth of the Pd-layer, resulting in the opening of pre-existing defects or weak areas. The discontinuous jump in leak growth seen in the case of AA-14R also probably resulted from the opening of pre-existing defects. The synthesis step most closely related with this phenomenon was the mechanical treatment since it sometimes resulted in gaps between subsequently plated dense Pd-layers such as those seen in Figure 4.16. The membrane AA-14R was first polished to a depth of 1.3 μm and re-plated by 2.2 μm, between which a gap (labeled 'A' in the figure) was apparent between the Pd-layers. After further testing, the membrane was polished and buffed (labeled 'B' in the figure), followed by further plating, which

resulted in a more extensive line of gaps between the Pd-layers. Gaps between Pd-layers could contain trapped gases or water from the membrane synthesis which could then result in micron-sized defects upon heating to temperature. Based on this hypothesis, membranes fabricated with no polishing or lighter polishing (less than 0.5 μm of Pd removed) would have less initial leak growth and fewer instances of discontinuous leak growth.

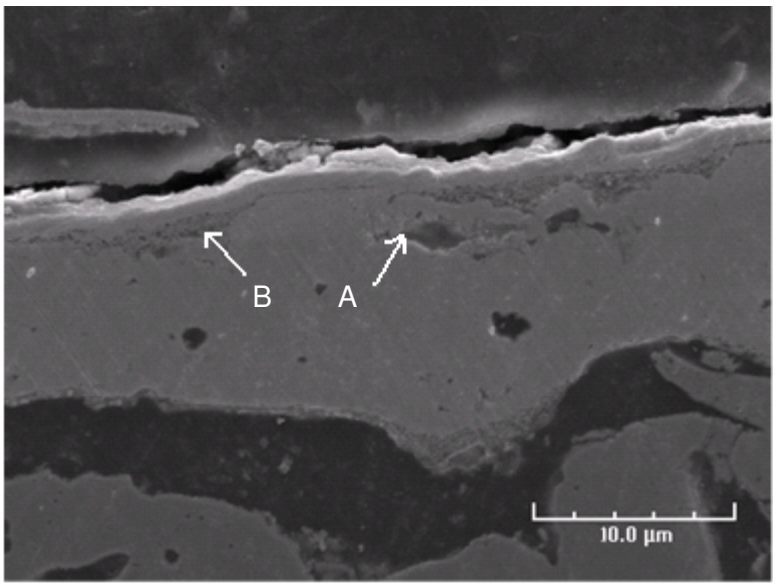

Figure 4.16. SEM image of membrane AA-14R at 2,500X (A: initial Pd-plating and first re-plating, B: polished, buffing, and additional plating).

The membrane AA-21 was synthesized with multiple intermediate polishing treatments (four treatments removing 4.6 μm Pd total). The membrane developed leaks rapidly during H_2 and H_2/H_2O testing at 400°C, after which, specks were observed on the membrane by visual inspection which were not previously visible. Examination by SEM revealed large (100 μm) defects (not to be confused with pinholes, less than 1 μm in size) with clean cut edges as shown in Figure 4.17[a]. The 50 - 100 μm wide defects (numbering approximately 4/cm^2) were randomly distributed across the membrane surface. It was apparent by looking at a cross section of one of these defects Figure 4.17[b], that they extended partially into the Pd-layer but not all the way to the support.

Defects extending several microns into the Pd-surface could certainly cause erratic leak growth during H_2 testing. The cause of these defects, however, was purely speculative. The appearance of the defects gave the impression that a piece of the Pd-layer had flaked or chipped off such as may have occurred due to trapped gases rupturing the membrane at high temperature. This possibility was unusual because electroless Pd-plating has typically resulted in very good adhesion between subsequent Pd-layers.

[a] 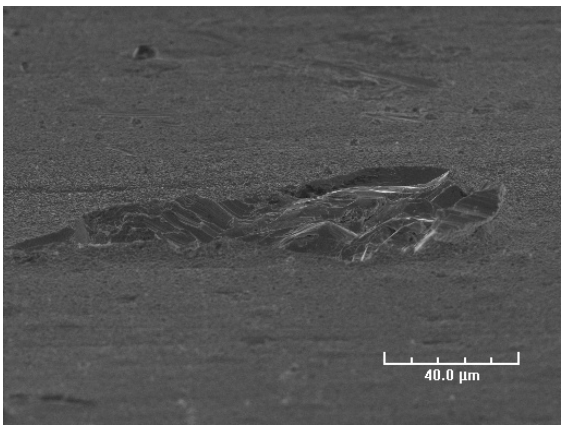

[b] 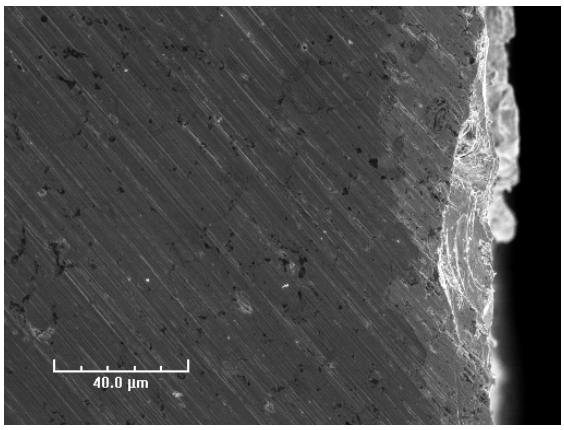

Figure 4.17. SEM images of membrane AA-21 [a] Surface image of large defect viewed at 85° angle (700X) [b] Cross section of a defect (unmounted sample, 700X).

The He permeance of several as-prepared membranes, after heating to temperature, and after 30 – 60 hours of H_2 exposure is shown graphically in Figure 4.18[a] and [b]. In Figure 4.18[a] and [b] an H_2 exposure time of zero indicates the leak after heating to temperature in He (but before introduction of H_2). A shaded region, corresponding to a H_2/He ideal selectivity of 1,000 is also shown in Figure 4.18; the region was roughly defined because membranes with higher H_2 permeance had higher ideal selectivity for an identical He leak (H_2 permeance of 20 – 45 m^3/m^2-h-$atm^{0.5}$ were used in equation **2.34** to define the shaded region). A number of the membranes developed significant leaks during the initial heating in He as shown in Figure 4.18[a]. An additional group of membranes showed significant leak development during the first 30 – 60 hours of H_2 testing as plotted in Figure 4.18[b].

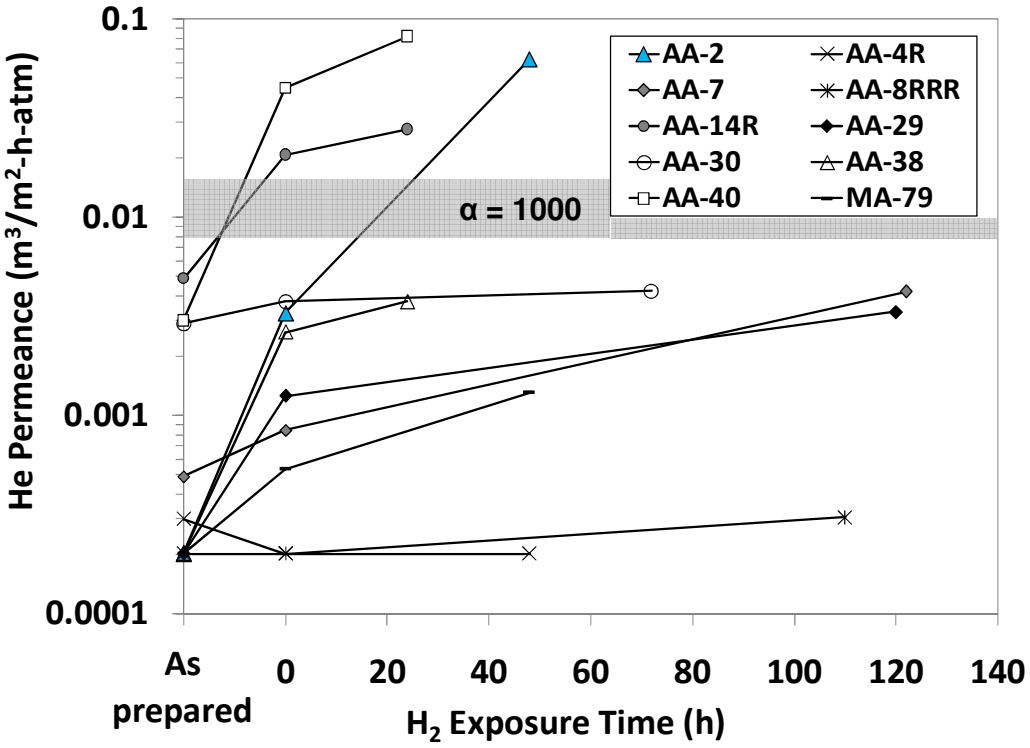

[a]

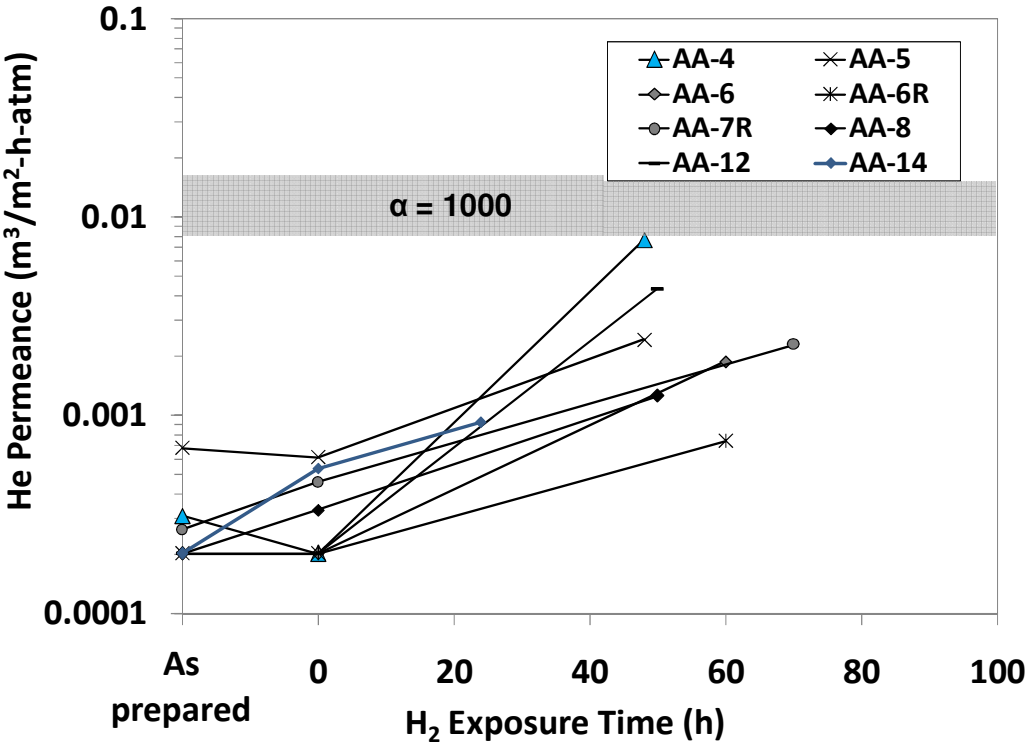

[b]

Figure 4.18. He permeance resulting from first heating in He and initial H_2 testing.

It has been shown that microstrain in the electroless deposited Pd-layer on the order of 100 MPa was irreversibly relaxed at temperatures in excess of 350 - 400℃ due to crystallite growth in the Pd-layer (Guazzone *et al.,* 2006). In the same study Guazzone *et al.* (2006) also concluded that the relaxation of approximately 100 MPa of microstrain did not lead to significant leak growth since the strain was not large enough to cause cracks in the Pd-layer, nor did its relaxation result in pinhole formation. The initial leak development observed in the membranes AA-2, AA-7, AA-14R, AA-29, AA-38, AA-40, and IM-79 (shown in Figure 4.18[a]) was clearly the result of the increase in temperature, suggesting that an alternate mechanism was causing leak growth during heating. In some cases such as AA-4R, AA-8RRR, and AA-30, a pre-annealing step or previous testing and repair (which was similar to a pre-annealing step) seemed to prevent the initial stage of leak growth in helium. However, the membranes AA-14R, AA-29, AA-38, and AA-40 were pre-annealed and re-plated but still had significant initial leak growth.

A subset of the membranes exhibited little or no leak growth upon first heating in He, but then had significant leak development during the first 50 hours of H_2 exposure. At a H_2 pressure of 2 atma the concentration of H-atoms in the Pd-lattice was only 0.019 H/Pd, far less than the approximate 0.1 H/Pd necessary to significantly change the Pd-lattice constant (Magnouche and Fromageau, 1984; Lewis, 1967; Smith, 1948). Guazzone *et al.* (2006), however, investigated the influence of H_2 pressure on the Pd-layer and showed that at P_{H2} = 2 atma a compressive stress of 100 MPa was introduced into the Pd-layer, approximately equal in magnitude to the tensile stress that was first present in the Pd-layer from deposition. Based on several membranes tested at different temperatures, they concluded that stresses of up to 260 MPa did not lead to increased leak growth. It seemed likely that in the above cases of initial leak growth (Figure 4.18), weak spots on the Pd-layer due to support defects or overly aggressive mechanical treatments succumbed to stresses of only 100 MPa, leading to leak growth. Keuler and Lorenzen (2002) observed a similar high rate of leak growth in their α-alumina supported Pd-membranes upon first heating in Ar and upon first admitting H_2, followed by a stabilization of the leak (with a very low rate of leak growth). They

attributed the initial rapid leak growth to the formation of pinhole defects, but did not explain why the leak mostly stabilized after 2 – 5 hours.

The second stage of leak growth was only accurately measureable over longer periods of time (greater than 300 hours). Figure 4.19 shows the long-term H_2 testing results of several membranes in terms of He leak at a constant temperature.

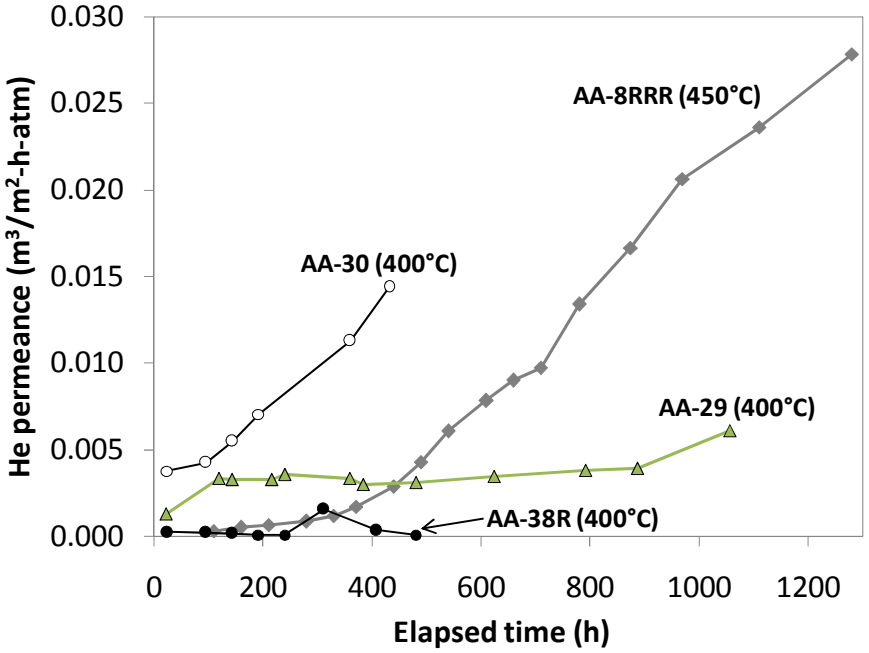

Figure 4.19. He permeance versus time showing the second stage of leak growth.

The membranes AA-8RRR and AA-38R were polished extensively (removing 4.8 and 4.4 µm of Pd for each membrane respectively), the other two membranes, AA-29 and AA-30, were only lightly polished (removing less than 1.2 and 0.6 µm of Pd for each respectively). The pure He leak of membranes AA-29 and AA-38R were remarkably stable over time despite the fact that one membrane was aggressively polished and the other was not. The pure He leak of the membranes AA-8RRR and AA-30 increased steadily over time, again inspite of different polishing treatments. The results of these four membranes showed no correlation between leak development and polishing treatments. SEM analysis was not conducted on the cross-sections of two of these

membranes (AA-8RRR and AA-38R) so a comparison of the composite structure could not be made.

The membrane AA-8RR, replated to AA-8RRR presented an interesting case. During the testing of AA-8RRR, there was a significantly higher He permeance growth rate than during the testing of AA-8RR. Since the membrane AA-8RR was already mechanically treated and plated twice and had very low leak growth, it might be supposed that the mechanical treatment was beneficial to (or at least benign to) the synthesis. It seemed, however, that the gaps between subsequent Pd-layers sometimes occurred, suggesting that the mechanical treatment was difficult to reproduce.

The membrane AA-30 had a considerably higher leak growth rate due to a weld defect. During the synthesis of AA-30, defects were observed on both welds by the IPA bubble test and so weld plating was conducted. While any such defects were completely covered by the 9.5 μm Pd layer plus the 9 μm of extra Pd applied to the welds, the welded regions probably still remained weak and prone to leak growth even though very little leak developed upon initial heating and H_2 exposure. Indeed, upon removal of the membrane from the system, the IPA bubble test showed a single large defect on the welded region at the outlet end of the membrane. Unfortunately, the extent of the leak due to the defect in AA-30 was not estimated until after the WGS testing (discussed in Chapter 10), so the leak growth due to pinhole formation during pure H_2 testing could not be estimated.

The He permeance growth rate during H_2 testing, given in $m^3/m^2\text{-}h^2\text{-}atm$ is plotted in Figure 4.20[a] and [b] for the testing temperatures of 400 and 450°C respectively. For every permeance growth rate plotted in Figure 4.20 at least three leak measurements were taken over a 150 hour period to determine the leak growth rate. All the membranes were tested with a shell-side H_2 pressure of 1.5 atma except for the membranes AA-29 and IM-79. AA-29 was tested with an elevated P_{H2} of 4.9 atma for the final 550 hours of testing. The membrane IM-79 was tested with an elevated P_{H2} of 4.9 and 7.9 atma for 50 hours at 400°C, during which time the He permeance growth rate was in line with the other 800 hours of testing at 400°C, for that same membrane.

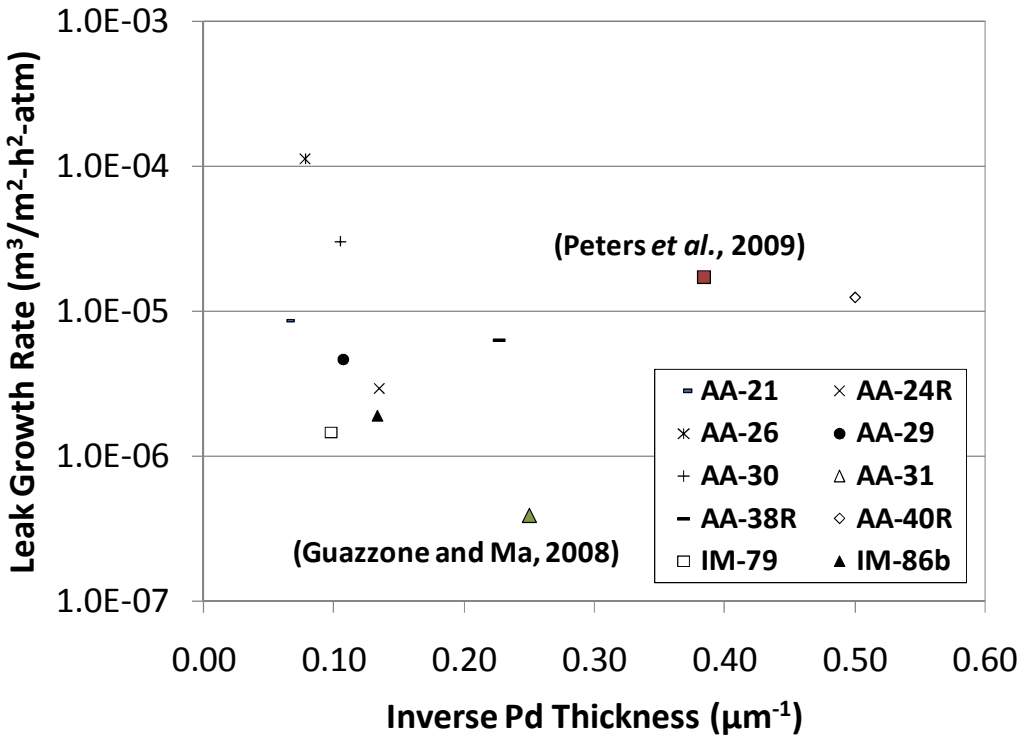

[a]

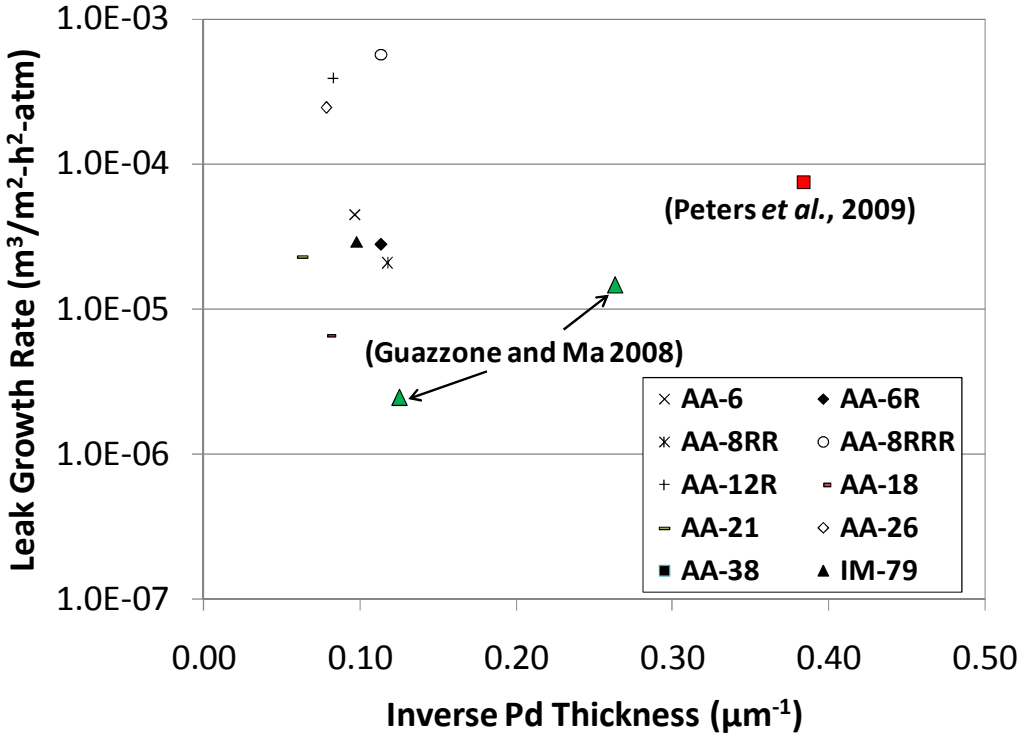

[b]

Figure 4.20. He permeance growth rate during pure H_2 testing [a] 400℃ [b] 450℃.

There is somewhat of a consensus that the leak growth in Pd-membranes was mainly the result of pinhole formation which occurred due to sintering, and began at temperatures in excess of 450℃ (Guazzone and Ma, 2008; Peters *et al.,* 2009; Guazzone *et al.,* 2006; Paglieri *et al.,* 1999). The exceptionally low rate of leak growth observed in the membranes AA-6, AA-6R, AA-8RR, AA-21, AA-29, AA-31, AA-38, AA-38R, AA-40R, IM-79 and IM-86b was in line with previous literature as shown in Figure 4.20[a] and [b], within one order of magnitude of the leak growth rates reported by both Guazzone and Ma (2008) and Peters *et al.* (2009) at the same temperature. The low rate of leak growth of these membranes was thus in line with the pinhole formation mechanism. The low leak growth measured for the membranes AA-29 (tested for 500 hours at P_{H2} = 4.9 atma) and IM-79 (tested for 50 h at P_{H2} = 4.9 and 50 h at P_{H2} = 7.9 atma) confirmed that the leak growth was not accelerated by high H_2 pressure.

There was no clear correlation in Figure 4.20[a] or [b] between the leak growth rate and the inverse Pd-thickness. A correlation was expected because the mass transfer resistance by Knudsen flow through a porous media, given by equation **4.11** (Mardilovich *et al.*, 1998; Guazzone and Ma, 2008), was proportional to the thickness of the media, *L* [m], therefore, pinholes which formed through a thicker Pd-layer would have had a lower He permeance.

$$R_K = \frac{3}{2}\sqrt{\frac{\pi}{8}}\frac{L\sqrt{RTm_i}}{\varepsilon\mu_K d_{pr}} \qquad \textbf{4.11}$$

Where m_i [kg/mol] was the molecular mass of the permeating gas *i*, ε was the porosity of the layer, μ_K [N-s/m^2] was the Knudsen viscosity, and d_{pr} [m] was the pore diameter. It was possible that, since most of the thicker membranes in Figure 4.20 were fabricated with Pd/Ag intermediate layers, gradual annealing resulting in the Kirkendall effect (Smigelskas and Kirkendall, 1947) might have slightly increased He permeance growth in those membranes, masking the correlation with Pd-thickness. Guazzone and Ma (2008) tested only pure Pd-membranes and observed a lower rate of leak growth for thicker membranes (greater than 5 μm).

The vast range of leak growth rates measured in the Pd-membranes suggested that a different leak growth mechanism was occurring besides pinhole formation. The formation of, or opening up of defects has been shown to significantly increase leak growth rates, especially in lower quality SS supports. Methods of mitigating defect formation have not been successfully demonstrated. The lack of a reliable and reproducible method for mitigating defect formation will continue to be a stumbling block for low cost and reproducible membrane synthesis.

4.5. Conclusions

Membrane synthesis attempts have been conducted on economically viable 0.1 and 0.2 μm PSS_{316L} supports with the objective of producing membranes equal in quality (high H_2 permeance and selectivity stability) to those synthesized on higher cost Hastelloy and Inconel supports. The primary problem encountered with these less expensive supports was presence of defects mostly, but not entirely, localized to the welded regions between the porous and non-porous sections of the tubes. Aggressive weld Pd-plating, attempting to block the defects with a very thick (greater than 20 μm) dense layer failed because some of the defects were larger than 10 μm in size. Weld plating with copper, nickel, and chromium also failed due to difficulties in achieving dense layers of those metals. A potential solution to the problem of defect repair was additional alumina grading and Pd-plating of the welded areas.

Multiple grading treatments (up to six) with sequentially smaller particle sizes (ranging from 10 – 0.01 μm) resulted in significantly thinner Pd-layers and much higher membrane H_2 fluxes. Membranes were synthesized by this method on the lower cost support as thin as 1.5 μm, with H_2 permeance of 61.7 m^3/m^2-h-$atm^{0.5}$ and stable selectivity in excess of 3,900.

Membranes which were prepared on high quality supports and membranes which were fabricated with extensive grading treatments exhibited very low leak growth rates, in line with literature values, for periods of up to 1,100 hours in H_2 and at 400 and 450°C. The very low leak growth of these membranes was in line with the pinhole formation mechanism. Other membranes which had some weak spots or defects due to the low

quality supports exhibited significant leak growth upon heating and discontinuous jumps in leak during testing.

A comprehensive set of H_2 flux data was taken by varying both the shell and the tube-side H_2 pressures so that the relationship between flux and partial pressure driving force could be more thoroughly investigated. Neither the Sieverts' law nor the generalization of Sieverts' law with an *n*-dependent driving force was adequate to fit the H_2 flux data obtained at high pressure (greater than 4 atma). The deviation from Sieverts' law was caused by both the mass transfer resistance in the porous support and grading layers and the increased solubility of H-atoms in the Pd-layer at higher pressure (greater than 4 atma).

5. ASSESSMENT OF ONE-DIMENSIONAL MODEL USING LITERATURE DATA

5.1. Introduction

An integral part of the advancement of chemical engineering research is modeling and simulation of chemical engineering processes. The modeling of the WGS CMR can provide important insights into the characteristics and capabilities of the actual system, allowing for improvements and modifications which would not have otherwise been apparent. An accurate model allows for rapid optimization of feed conditions and operating parameters which could take a significant amount of time and money otherwise.

As discussed in the Literature Review (Section 2.3.2), a variety of modeling studies have previously been conducted for CMR's which have achieved good agreement with experimental data. In many studies the use of a 1-D model has provided invaluable insight into membrane reactor function (Ayturk *et al.*, 2009; Barbieri *et al.*, 2001; Basile *et al.*, 2003; Brunetti *et al.*, 2007b; Kumar *et al.*, 2006). In this chapter, a 1-D model was applied to the WGS CMR system incorporating a Pd-membrane and taking into account WGS kinetics, gas phase mass-transfer resistance, and surface adsorption of WGS species on the Pd-membrane. The model was compared to the relevant experimental literature data available for the WGS CMR system. The purpose of this chapter was to evaluate the model such that it can be used in subsequent chapters to aid in the elucidation of experimentally observed phenomena.

5.2. 1-D model details

The use of a 1-D model over a 2-D model was possible since the length of the reactor (6.5 cm) was greater than ten times the characteristic width (0.44 cm) of the catalyst bed (Kumar *et al.*, 2006). A 1-D model was preferred for development simplicity. A steady-state model was chosen over an unsteady-state model since none of the experiments were transitory in nature. Since the catalyst bed was relatively thin (0.44 cm) and the reactor walls were made of stainless steel (with moderate thermal

conductivity, 11 - 45 W/m-K {Perry and Green, 1997}) the simplification of isothermal behavior was made. Also, since an estimation of the pressure drop across the packed bed by the Ergun equation was only 0.12 atm with the specifications of our experimental system (accounting for the maximum expected flow rate of 61 mol/h, $GHSV_{STP}$ = 10,000 h^{-1}), the assumption of constant pressure was also made. The model was developed under the following standard assumptions:

- isothermal and isobaric conditions
- plug flow behavior
- no radial concentration gradient
- no axial dispersion
- infinitely selective Pd-membrane
- one-way transport through the membrane (no back flow)
- no mass transfer resistance around the catalyst particles (effectiveness factor equal to unity)

The model was based on the steady state mass balance equations written in one-dimensional Cartesian coordinates explicitly for all species involved on both the retentate (reaction) side, equation **5.1**, and the permeate side, equation **5.2**, which correspond to the diagram shown in Figure 5.1.

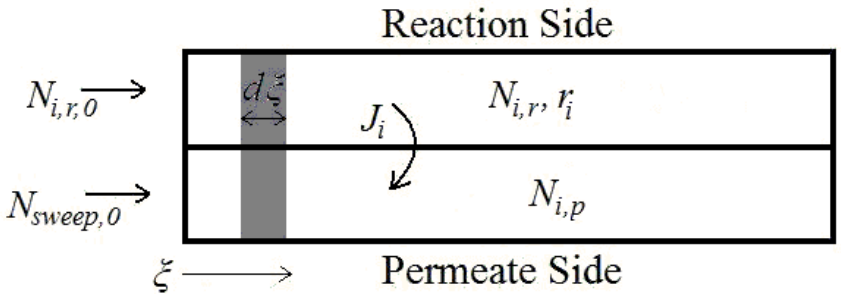

Figure 5.1. Diagram of a 1-D isothermal and isobaric plug flow system.

$$\frac{dN_{i,r}}{d\xi} = \eta(v_i r_{CO})\rho_{cat} A_c L - \frac{J_i A_{Pd} P_0}{RT_0} \quad \textbf{5.1}$$

$$\frac{dN_{i,p}}{d\xi} = \frac{J_i A_{Pd} P_0}{RT_0} \quad \textbf{5.2}$$

where $N_{i,r}$ and $N_{i,p}$ [kmol/h] were the molar flow rates of species *i* in the reaction and permeate sides respectively, ξ was the dimensionless axial coordinate defined as *z/L, z* [m] was the axial position, *L* [m] was the length of the reactor, η was the catalytic effectiveness factor, v_i was the reaction coefficient for each species (-1 for CO and H_2O, +1 for H_2 and CO_2), r_{CO} [kmol/kg-h] was rate of CO consumption, ρ_{cat} [kg/m^3] was the density of the catalyst, A_c [m^2] was the cross sectional area defined as $\pi(R_s^2-R_t^2)$, A_{Pd} [m^2] was the membrane area defined as $2\pi R_t L$, R_s [m] was the inner radius of the reactor shell, R_t [m] was the radius of the membrane, J_i [Nm^3/m^2-h] was the permeating flux, T_0 = 273 K was the standard temperature, P_0 =1.0 atma was the standard pressure, and R = 0.0821 m^3-atm/kmol-K was the gas constant. The factor $P_0/R\text{-}T_0$ accounted for the unit conversion (volume in m^3_{H2} at STP converted to $kmol_{H2}$). Note that, for *i* = CO, CO_2 and H_2O, J_i was zero since hydrogen was assumed to be the only permeating species.

As the reaction occurred and H_2 was separated along the length of the reactor, the pressure of each species changed. The partial pressure profile of each species was given by equation **5.3**.

$$P_{i,r} = P_{T,r}\frac{N_{i,r}}{\sum_j N_{j,r}} \quad \textbf{5.3}$$

The system of steady state differential equations (**5.1** and **5.2**) were simplified by the transformation of the state variables ($N_{i,r}$ and $N_{i,p}$) to two new dimensionless variables: X_{CO} and Y_{H2}, defined by equations **5.4** and **5.5** respectively.

$$X_{CO} \equiv 1 - \frac{N_{CO,r}}{N_{CO,r,0}} \quad \textbf{5.4}$$

$$Y_{H2} \equiv \frac{N_{H2,p}}{N_{CO,r,0}} \quad \textbf{5.5}$$

where X_{CO} was the fraction of CO that was converted to products via the WGS reaction, Y_{H2} was the fraction of H_2 that permeated through the membrane, and $N_{CO,r,0}$ [kmol/h] was the feed rate of CO on the retentate side. The partial pressure of H_2 in the retentate with respect to the variables X_{CO} and Y_{H2} was given by equation **5.6** and that of each other non-permeable species in the retentate was given by equation **5.7**.

$$P_{H2,r} = P_{T,r}\frac{\theta_{H2}+X_{CO}-Y_{H2}}{1+\theta_{H2O}+\theta_{H2}+\theta_{CO2}-Y_{H2}} \qquad \textbf{5.6}$$

$$P_{i\neq H2,r} = P_{T,r}\frac{\theta_i+v_iX_{CO}}{1+\theta_{H2O}+\theta_{H2}+\theta_{CO2}-Y_{H2}} \qquad \textbf{5.7}$$

where $\theta_i = N_{i,r,0}/N_{CO,r,0}$ was the molar ratio of species *i* to CO in the feed.

5.2.1. Reaction rate equation

In the IGCC process and in numerous literature studies two types of WGS catalysts have typically been utilized: iron-chrome oxide catalyst (Klara *et al.,* 2007; Kikuchi *et al.,* 1989; Uemiya *et al.,* 1991a; Damle *et al.,* 2008; Dolan *et al.,* 2010) and copper-zinc oxide catalyst (Basile *et al.,* 1996a; 1996b; Mendes *et al.,* 2010). The 1-D model initially incorporated a rate expression for iron-chrome oxide catalyst reported by Rhodes *et al.* (2002) for temperatures from 360 – 440℃ and given by equation **5.8**. As discussed in Chapter 2 (Section 2.1.2) a number of mechanistic rate expressions for the WGS reaction on iron-chrome oxide catalyst had proven to be inadequate at elevated pressures (greater than 10 atma) and therefore the empirical expression has usually been preferred.

$$r_{CO} = \frac{dC_{CO}}{\rho_{cat}dt} = kP_{CO}(1-\beta) \qquad \textbf{5.8}$$

where C_{CO} [kmol/m^3] was the concentration of CO in the gas phase, $k = 4.34*10^8e^{-Ea/RT}$ [kmol/kg-h-atm], E_a was the activation energy of 112 kJ/mol, and $\beta = P_{CO2}P_{H2}/KP_{CO}P_{H2O}$. Other rate expressions were also utilized in the model as discussed in further sections.

5.2.2. Membrane surface inhibition by CO and *H_2O*

The gas species CO and H_2O are known to reversibly adsorb on the Pd-surface with the net result of lowering the H_2 permeance of the membrane by blocking active surface

sites for H_2 adsorption (Li *et al.,* 2000; Hou *et al.,* 2002; Gallucci *et al.,* 2007). The inhibition by these gas species was approximated by considering the fraction of blocked surface sites as though it were a fraction of the membrane area which was no longer permeable (Scura *et al.,* 2008). The flux of H_2 through the membrane was determined by Sieverts' law, equation **4.2**, incorporating the experimentally determined permeance of the supported Pd-membranes, $F_{H2,0}$ [m^3/m^2-h-$atm^{0.5}$], as well as an inhibition coefficient, γ, defined by equations **5.9**.

$$J_{H2} = \gamma F_{H2,0}\left(\sqrt{P_{H2,s}} - \sqrt{P_{H2,t}}\right) \qquad \textbf{4.2}$$

$$\gamma = \frac{1}{1+\lambda_{CO}P_{CO,s}+\lambda_{H2O}P_{H2O,s}} \qquad \textbf{5.9}$$

where $P_{i,s}$ [atma] was the partial pressure of species *i* at the retentate-side Pd-surface, $P_{H2,t}$ [atma] was the partial pressure of H_2 on the tube-side, and λ_i [atm^{-1}] was the adsorption equilibrium constant for species *i* on the Pd surface. Scura *et al.* (2008) utilized a similar approach to model H_2 permeance inhibition by CO through a Pd membrane. The adsorption equilibrium constants, λ_{CO} and λ_{H2O} were estimated based on literature data for the binding energy of each species to the Pd-surface via the statistical mechanics equation **5.10**. The binding energy (ΔE_i) of each species, which most closely agreed with literature studies of Pd-surface inhibition, is listed in Table 5.1. The adsorption equilibrium constant for each gas at 400℃ are also calculated by equation **5.10** and listed in Table 5.1 for comparison.

$$\lambda_i = \frac{h^3}{T^{5/2}k(2\pi m_i k)^{3/2}}\, e^{\left(\frac{\Delta E_i}{RT}\right)} \qquad \textbf{5.10}$$

Table 5.1. Binding energy and estimated adsorption equilibrium constant for each species at 400℃.

	ΔE_i (kJ/mol)	λ_i@400℃ (atm^{-1})	Reference
CO	-149	0.239	Guo and Yates, 1989
H_2O	-125	0.00691	Catalano *et al.,* 2011

5.2.3. Gas boundary layer mass transfer resistance

For any surface in which a gas phase species interacts and changes (surface reaction, separation, condensation, etc.), a phenomenon known as concentration gas boundary layer formation or concentration polarization will occur. The species being consumed, condensed, or separated will become depleted to some extent at the surface/gas interface and other species will become concentrated. In the WGS CMR the partial pressure of H_2 at the interface becomes somewhat lower than that in the bulk causing a concentration gradient and therefore diffusion of H_2 towards, and non-permeable species away from the membrane surface. The flux of a species through the gas boundary layer was estimated by a corrected average mass transfer coefficient, k_B^* [m/h], as in equation **5.11** (Catalano *et al.,* 2009).

$$J_{H2} = \frac{k_B^* T_0}{P_0 T}\left(P_{H2,b} - P_{H2,s}\right) \qquad \textbf{5.11}$$

where $P_{H2,b}$ [atma] was the partial pressure of H_2 in the bulk gas and $P_{H2,s}$ [atma] was the partial pressure of H_2 at the Pd-surface. Since there was a net flow of gas through the membrane, resulting in a slowing of the axial flow, a correction was needed such that the corrected average mass transfer coefficient, k_B^* [m/h], was given by equation **5.12** (Catalano *et al.,* 2009).

$$k_B^* = k_B ln\left(\frac{P_T - P_{H2,s}}{P_T - P_{H2,b}}\right) \qquad \textbf{5.12}$$

where P_T [atma] was the total shell-side pressure.

The average mass transfer coefficient, k_B [m/h], was calculated by its relationship to the dimensionless Sherwood number, *Sh*, as in equation **5.13**.

$$k_B = \frac{Sh * D_{H2}}{d_h} \qquad \textbf{5.13}$$

where D_{H2} [m^2/h] was the diffusivity of H_2 in the feed mixture estimated by the kinetic theory of gases (Reid *et al.,* 1987) and d_h [m] was the hydraulic diameter of the membrane separator. The hydraulic diameter was the diameter of a hypothetical cylindrical tube in which the fluid flow Reynolds number was the same as the flow

through the real, non-tubular system (defined as $4A_C/Perimeter$, D_1-D_2, for empty tube-in-shell cases, and the particle diameter, d_p [m], for packed bed cases {Caravella *et al.,* 2009}). The Sherwood number was estimated by its relationship with the dimensionless Schmidt number, *Sc* (equation **5.14**), and Reynolds number, *Re* (equation **5.15**), via equation **5.16** (Wakao and Funazkri, 1978; Perry and Green, 1997).

$$Sc = \frac{\mu}{\rho D_{H2}} \qquad \textbf{5.14}$$

$$Re = \frac{\rho v d_h}{\mu} \qquad \textbf{5.15}$$

$$Sh = 1.15 Sc^{0.333} \left(\frac{Re}{\varepsilon}\right)^{0.5} \qquad Re > 1 \qquad \textbf{5.16}$$

where μ [kg/h-m] was the dynamic viscosity (Perry and Green, 1997; Wilke, 1950), ρ [kg/m^3] was the density of the fluid, v [m/h] was the interstitial fluid velocity, and ε was the void fraction of the catalyst bed.

Finally, equation **5.11** was set equal to **4.2** resulting in equation **5.17**, which was solved at each discrete step for the partial pressure of H_2 at the membrane surface, $P_{H2,s}$ [atma]. The quadratic formula, equation **5.18**, was used to determine the $P_{H2,s}{}^{0.5}$ (note that the negative root was discarded since it had no physical significance).

$$J_{H2} = F_{H2}\left(P_{H2,s}^{0.5} - P_t^{0.5}\right) = \frac{k_B^* T_0}{P_0 T}\left(P_{H2,b} - P_{H2,s}\right) \qquad \textbf{5.17}$$

$$\sqrt{P_{H2,s}} = \left(-F_{H2} + \sqrt{F_{H2}^2 - 4\frac{k_B^* T_0}{P_0 T} * \left(-F_{H2}\sqrt{P_{H2,t}} - \frac{k_B^* T_0}{P_0 T} P_{H2,b}\right)}\right) \Big/ \left(2\frac{k_B^* T_0}{P_0 T}\right) \qquad \textbf{5.18}$$

The overall system of equations **5.4 - 18** were simulated and solved numerically via a standard 4th order Runga-Kutta algorithm using the Matlab® software package, utilizing the boundary conditions: $\xi = \frac{z}{L} = 0 \rightarrow N_{i,r} = N_{i,r,0}$ & $N_{i,p} = N_{sweep,0} = 0$. The basic annotated Matlab® code can be found in Appendix E.

When the model was solved a profile was generated of the state variables (X_{CO} and Y_{H2}) with regard to the axial position in the reactor; only the final value of each variable (corresponding to ξ = 1) was retained for comparison to the experimental data. The

partial pressure profile of each species with regard to the axial position in the reactor could be determined algebraically from the state variables by equations **5.6** and **5.7**. An example of the full simulation output and subsequent algebraic transformations can be found in Appendix A.4.

5.3. Model evaluation

The model was used to simulate several experimental WGS CMR studies in order to evaluate its capabilities and weaknesses. Studies which were amenable to the model had the following specifications: iron-chrome oxide catalyst, 350 – 500℃, co-current sweep gas or no sweep gas, and a high aspect ratio (reactor length at least ten times greater than the characteristic width). The modeling parameters of all the simulated studies (Dolan *et al.,* 2010; Damle *et al.,* 2008; Kikuchi *et al.,* 1989; Uemiya *et al.,* 1991a) are tabulated in Table 5.2.

The model results were overlaid with two sets of experimental results from Dolan *et al.* (2010) and one set from Damle *et al.* (2008) for both CO conversion and H_2 recovery in Figure 5.2 and 5.3 respectively. The experimental results by Kikuchi *et al.* (1989) and Uemiya *et al.* (1991a) were simulated using the kinetic rate expression given by Uemiya *et al.* (1991a) on their particular iron-chrome oxide catalyst. The rate constant which they estimated was on the same order as that of Rhodes *et al.* (2002). A much lower rate constant, given by Hla *et al.* (2009), was utilized for the simulation of Dolan *et al.* (2010) since the results could not be fit by the kinetic expression of Rhodes *et al.* (2002). While the activation energy was approximately the same (111 and 112 kJ/mol), the difference in the pre-exponential factor was approximately two orders of magnitude, for which no explanation was given in the more recent rate study (Hla *et al.*, 2009). The comparison between the experimental results and those generated by the model are shown in terms of CO conversion and H_2 recovery in Figure 5.4[a] and [b] respectively for all the data from four experimental studies.

Table 5.2. Modeling parameters of the experimental WGS CMR studies found in the literature.

Research Study	**Damle *et al.*, 2008**	**Dolan *et al.*, 2010**		**Kikuchi *et al.*, 1989**	**Uemiya *et al.*, 1991a**
Catalyst Properties	Fe/Cr-oxide				
Catalyst density, ρ_{cat} [kg/m^3]	1.19*10^3 (1)	1.19*10^3		4.78*10^2	
Catalyst void fraction, ε	NR(1) 0.47 assumed	NR(2) 0.47 assumed		0.68	
Particle size, d_p [m]	7.0*10^{-4}	3.5*10^{-4}		3.0*10^{-4}	
Rate expression, $r_{CO}/(1-\beta)$ [kmol/kg-h]	$4.34 \times 10^8 e^{-112/RT} P_{CO}$ (Equation **5.19**, Rhodes *et al.,* 2002)	$2.52 \times 10^6 e^{-\frac{111}{RT}} P_{CO} P_{CO2}^{-0.36} P_{H2}^{-0.09}$ (Equation **5.20**, Hla *et al.,* 2009)		$8.22 \frac{P_{CO} P_{H2O}}{(1 + 4.4 P_{H2O} + 13.0 P_{CO2})}$ (Equation **5.21**, Uemiya *et al.,* 1991a)	
Effectiveness factor, η	1.0 (no mass transfer resistance around catalyst particles assumed)				
Reactor Dimensions	3-tubes-in-tube	Planar		Tubular (catalyst inside)	Tube-in-tube
Reactor Length, L [m]	0.3	0.07		0.08	
		Case 1:	Case 2:		
Cross-sectional area, A_c [m^2]	2.95*10^{-3}	4.80*10^{-5}	1.36*10^{-4}	5.54*10^{-5}	1.76*10^{-5}
Aspect ratio	12 - 16 estimated (3)	10.3	29.2	8	10
Membrane Properties	3-tubes	Planar		Tubular	
Membrane area, A_{Pd} [m^2]	3.0*10^{-2}	1.4*10^{-3}		2.51*10^{-3}	
Permeance, $F_{H2,0}$ [m^3/m^2-h-atm$^{0.5}$]	23, 34	6.2	15.4	10.5	
Binding energy, ΔE_i [kJ/mol]	CO: -149 (Guo and Yates, 1989), H_2O: -125 (Catalano *et al.,* 2011)				
Feed Properties*	Simulated syngas	Enriched feed		CO + H_2O	CO + H_2O
Feed composition, θ_i	θ_{H2O} = 1.2, θ_{H2} = 4.8, θ_{CO2} = 0.46, θ_{CH4} = 0.15	θ_{H2O} = 3, θ_{H2} = 0.55		θ_{H2O} = 1	θ_{H2O} = 1, 2, 3
Feed rate, $N_{CO,r,0}$ [kmol/h]	2.82*10^{-3} – 5.14*10^{-3}	2.48*10^{-4} – 9.98*10^{-4}		1.35*10^{-4} - 1.09*10^{-3}	1.35*10^{-4} - 3.89*10^{-3}
Inert sweep, $N_{i,p,0}$ [kmol/h]	None	None		Ar: 1.07*10^{-3}	
Temperature, T [°C]	375, 550	400		400	
Reaction pressure, P_s [atma]	7.8, 11.2	20		1.0 – 5.0	1.0
Tube-side pressure, P_t [atma]	1.0	1.0 (0.0 for Case 3 and 4)		1.0	1.0
Dynamic viscosity, μ [kg/h-m]	0.063	0.077		0.091	0.083 - 0.091
Diffusivity of H_2, D_{H2} [m^2/h]	0.0835, 0.126	0.0914		0.0817	
Sherwood number approximation, *Sh*	$1.15 Sc^{0.333} \left(\frac{Re}{\varepsilon}\right)^{0.5}$ (Equation **5.16**, Perry and Green, 1997)				

(1) Catalyst weight not reported, typical void fraction and bulk density assumed
(2) Catalyst was diluted with an unspecified quantity of alumina, typical void fraction assumed
(3) Estimated graphically for three equidistant tubes centered in a larger tube
*Calculated fluid properties such as average velocity, dimensionless Reynolds, and Schmidt numbers are not listed

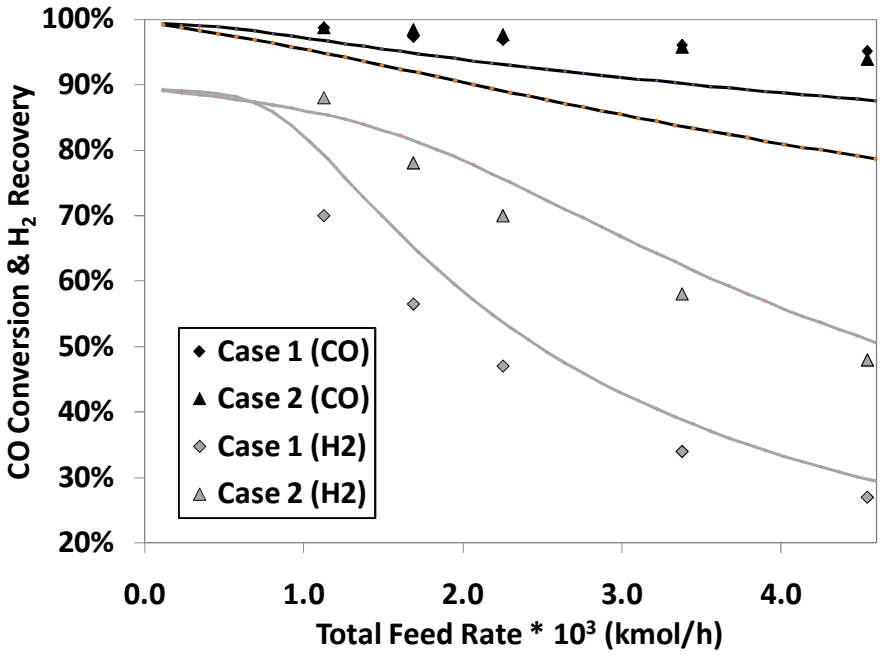

Figure 5.2. Simulation of CO conversion and H_2 recovery data from Dolan *et al.* (2010) Case 1: F_{H2} = 6.2 m^3/m^2-h-$atm^{0.5}$, A_c = 1.36*10^{-4} m^2; Case 2: F_{H2} = 15.4 m^3/m^2-h-$atm^{0.5}$, A_c = 4.80*10^{-5} m^2).

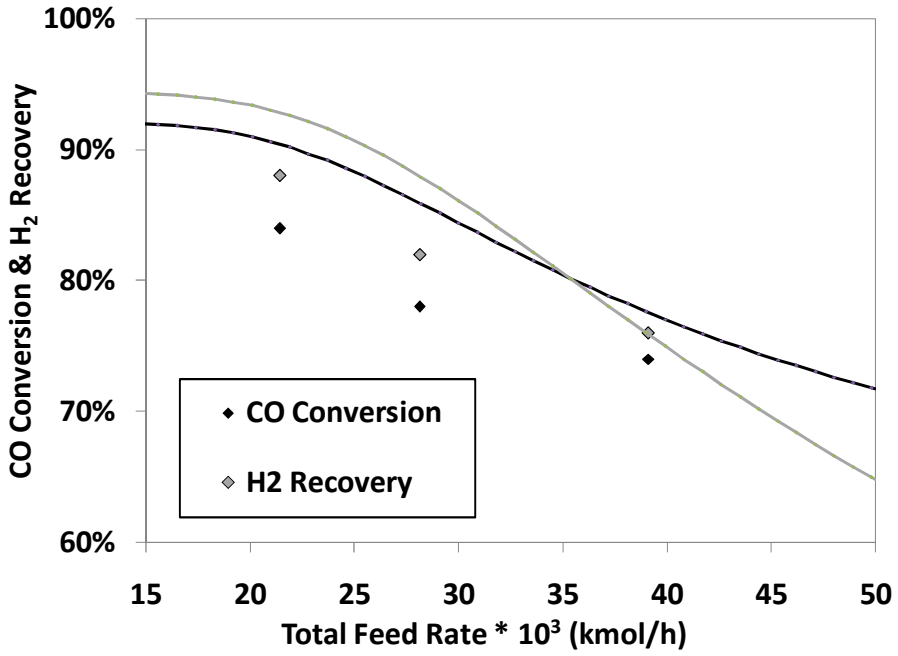

Figure 5.3. Simulation of CO conversion and H_2 recovery data from Damle *et al.* (2008), P_{rxn} = 7.8 atma.

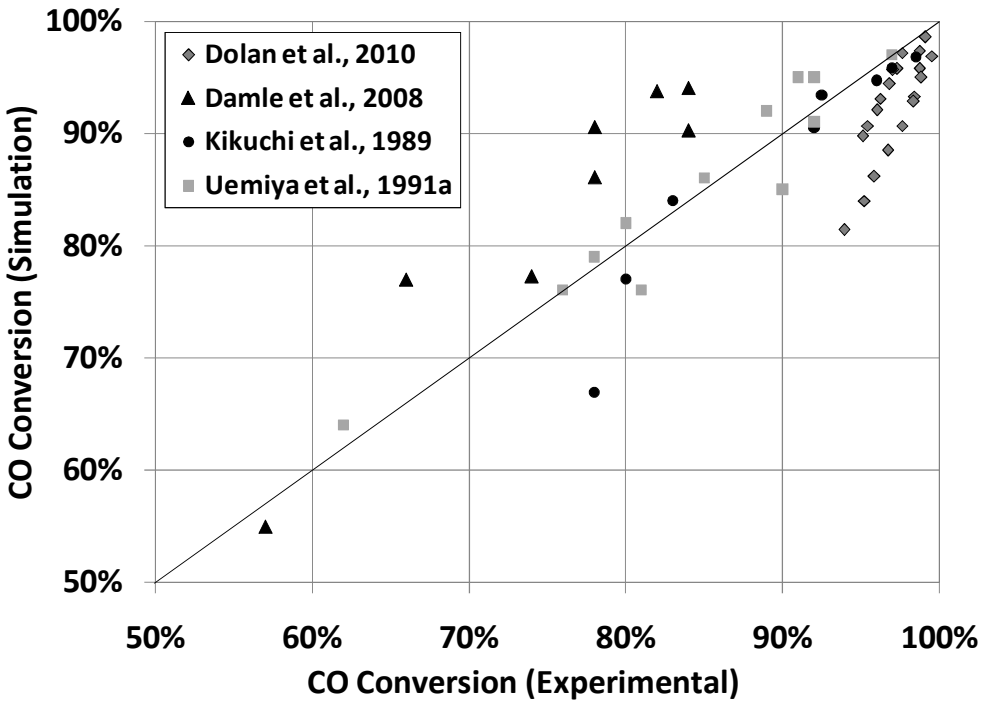

[a]

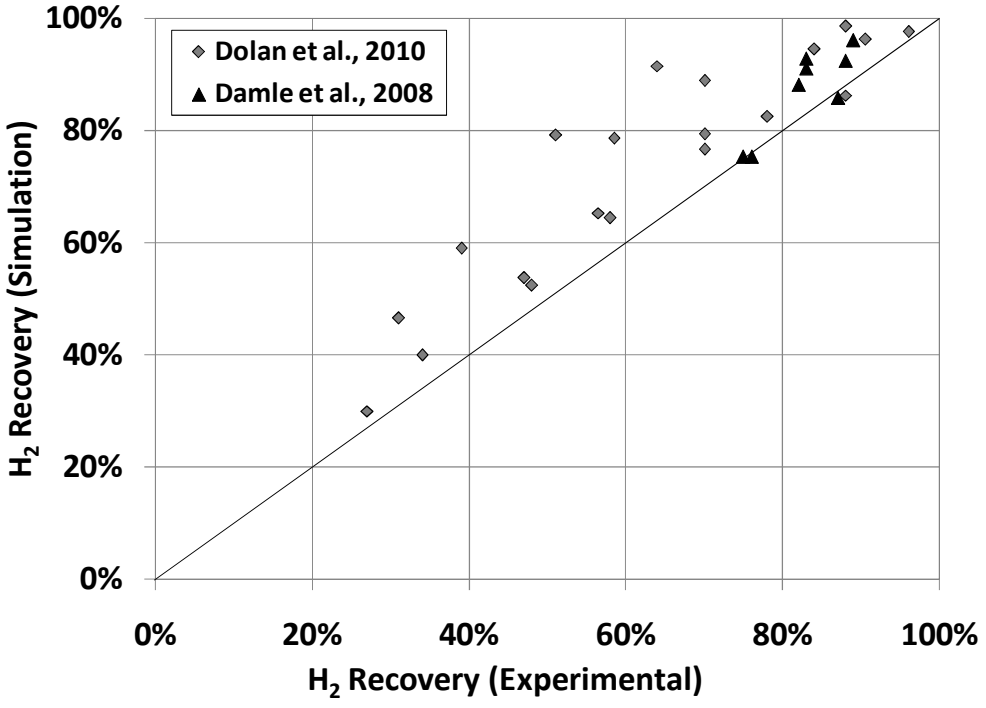

[b]

Figure 5.4. Comparison of the model with WGS CMR experimental studies in the literature [a] CO conversion [b] H_2 recovery.

In terms of CO conversion (Figure 5.4[a]) the model had good agreement (less than 5% difference) with the experimental results accounting for about 70% of the conditions tested. In terms of H_2 recovery (Figure 5.4[a]) the model also had reasonable agreement (less than 10% difference) with the experimental results accounting for about 70% of the conditions tested. The model well captured the trends in some sets of experimental CO conversion and H_2 recovery data as shown in Figure 5.2 (Dolan *et al.*, 2010). The model also partially captured the trend apparent in a further set of experimental data as shown in Figure 5.3 (Damle *et al.,* 2008).

5.4. Discussion

Considering that the primary utility of the model was to aid in the understanding of operational aspects of the WGS CMR, the most important validation test for the model was the comparison of the model to a data set which had a clear trend, to see if the simulation would capture that same trend. In some cases, such as the results simulated in Figure 5.2, the simulation fit the data exceptionally well in terms of H_2 recovery, and captured the trends observed in the data, suggesting that the rate limiting mechanisms (mass transfer in the gas phase and mass transfer in the dense Pd-layer) were appropriately estimated. In other cases such as the results simulated in Figure 5.3, the fit was poor but the trend apparent in the simulation results was in agreement with the data, suggesting that the mechanistic aspects of the model were correct, but that particular constants may have been incorrect, or that some additional mechanistic aspects were unaccounted for.

In cases such as Figure 5.3 and also the other data sets from Damle *et al.* (2008), the simulation diverged from the experimental data by as much as 10% in terms of CO conversion due to an inadequate kinetic rate expression. A significant discrepancy between the sets of literature data in terms of modeling accuracy was the choice of appropriate kinetic rate expression. The four experimental studies which were simulated in Figure 5.4 all used iron-chrome oxide catalyst but displayed results which suggested highly different catalytic activity. The probable explanation for the discrepancy, which was not accounted for in the model, was mass transfer resistance from the bulk reaction mixture to the catalyst particle surface and intraparticle mass transfer resistance.

Depending on the Reynolds number of the gas flow and the size and porosity of the catalyst particles, significantly different coefficients for bulk to catalyst mass transfer could result. The estimated packed-bed Reynolds number of 87 (with d_h equal to d_p) in the kinetic studies by Rhodes *et al.* (2002) was significantly higher than the Reynolds number of 5.0 in the study by Hla *et al.* (2009), suggesting that the gas boundary layer mass transfer resistance from the bulk to the catalyst surface (which was incorporated into the rate constant) was more significant in the later study. A potential correction for this would be to model the bulk-to-catalyst mass transfer with a similar relation to equations **5.11** – **5.13** (bulk to Pd-surface mass transfer). Since Uemiya *et al.* (1991a) and Kikuchi *et al.* (1989) provided a rate expression measured from their own testing setup, which mirrored their WGS CMR setup, a good correlation was observed for both of their data sets in Figure 5.4[a].

Unfortunately neither Uemiya *et al.* (1991a) nor Kikuchi *et al.* (1989) reported H_2 recovery for their experiments, so the model results could not be compared (and are not shown). For both of the studies which reported H_2 recovery (Dolan *et al.,* 2010; Damle *et al.,* 2008), the simulation overshot the experimental data by as much as 20%, due to inadequate characterization of the membrane permeance. Dolan *et al.* (2010) utilized 50 μm Pd and 40 μm $Pd_{75}Ag_{25}$-foils supported on porous ceramic, but did not first test the pure H_2 permeance of those composite membranes. In the simulation the permeance was assumed to be equal to that of the foils only (7.74 and 11.6 m^3/m^2-h-$atm^{0.5}$ respectively at 400°C) and did not consider additional resistance from the ceramic support. If the ceramic support was thick (as would be necessary for operation at 20 atma) then the support resistance might have been high, resulting in a composite membrane permeance significantly less than that of the foil.

The model also might have been inaccurate for the prediction of H_2 flux due to the simplification of modeling surface inhibition by equation **5.9**. The extent to which the flux was inhibited by a surface species was dependent upon the temperature (resulting in a higher or lower adsorption coefficient) and the membrane thickness (with a thicker dense layer having a lattice diffusion limited flux {Catalano *et al.,* 2011}). The most accurate way to calculate the H_2 flux in the presence of reversible surface adsorption by

non-permeable species was through a five step transport model such as that utilized by Ward and Dao (1999) and Catalano *et al.* (2011). The five step model considered the adsorption of H_2 on the upstream surface (equation **2.26** from Chapter 2) the solution of H-atoms into the Pd-lattice from the upstream surface (equation **2.27**), the diffusion of H-atoms from the upstream to the downstream surface (equation **2.24**), the dissolution of H-atoms from the Pd-lattice to the downstream surface (equation **2.27**), and the desorption of H_2 from the downstream surface (equation **2.26**), such that each step had the potential to be rate limiting. A practical assumption was made that fractional surface coverage by a non-permeable gas species would block an equal fraction of the membrane area, resulting in equation **5.9** and simplifying the calculation of the H_2 flux considerably (Scura *et al.,* 2008). In the experimental Pd-membrane system, as the surface coverage by CO (for instance) gradually increased, there was a transition between diffusion limited flux and adsorption limited flux. The equation **5.9** was the most inaccurate for surface coverages in the transitionary region where the surface adsorption step (equation **2.26**) became partially rate limiting.

5.5. Conclusions

A 1-D model was defined to enable a better understanding of the dynamics of the mixed gas separation and WGS CMR systems. The model was applied to simulate several experimental WGS CMR literature studies. The model accurately portrayed trends apparent in the experimental data, indicating that the mechanistic aspects of the system (mass transfer in the gas phase, mass transfer in the dense Pd-layer, and reaction rate) were reasonably estimated. A compact model such as the one presented in this chapter is essential for process modeling in order to design the overall IGCC process incorporating a WGS CMR.

The application of the model to some sets of literature data was impaired by inadequate membrane characterizations reported in those studies. Additionally, the choice of reaction rate expression was complicated by the significant variance in pre-exponential factors reported for various rate studies of iron-chrome oxide catalyst. The simplifying assumption that the reduction in membrane flux was proportional to surface coverage by WGS species also introduced inaccuracy into the model. Lastly, it was possible that

radial concentration gradients existed in the experimental WGS CMR studies which were not accounted for by the model.

The model is able to show relationships between various feed properties (temperature, pressure, GHSV, and composition) and the resultant CO conversion and H_2 recovery. In the following chapters the model will be utilized to aid in the elucidation of mixed gas separation and WGS CMR behavior.

6. H_2 SEPARATION FROM SYNGAS BY Pd-MEMBRANES

6.1. Introduction

In the relevant literature it has been apparent that H_2 separation under conditions approaching a commercial setting can be considerably more hindered and less efficient than a first order approximation would suggest (Abdollahi *et al.,* 2010; Damle *et al.,* 2008; Scura *et al.,* 2008; Ma and Lund, 2003). In order to prepare such a technology as the supported Pd-membrane for introduction into the IGCC process, a more thorough understanding of H_2 separation under complex conditions must be developed.

The separation effectiveness of the Pd-membrane may be impaired by several effects: depletion, resistance of the membrane (1/permeance), gas phase mass transfer resistance, reversible inhibition by adsorbed species, and irreversible inhibition due to surface reactions. Depending on the membrane characteristics as well as the feed conditions, any one of the above effects can significantly limit the H_2 recovery and/or the rate of H_2 separation. The interplay of depletion, membrane resistance, and gas phase mass transfer resistance under low Reynolds number (less than 100) conditions has not been well explored in the literature. Additionally, although several studies have investigated the surface inhibition phenomenon, there are significant discrepancies as to the relative effects of H_2O, CO, and CO_2 on the membrane surface, and the temperature at which those effects are significant. The objective of this chapter was thus to develop a better understanding of each of the above effects so that the improvement and optimization of a membrane separator system could be achieved.

6.2. Background

6.2.1. Gas phase mass transfer resistance

As the mixture is separated by the membrane, H_2 will become depleted to some extent at the surface/gas interface in a phenomenon known as a gas boundary layer formation or concentration polarization. The partial pressure of H_2 at the interface becomes lower than that in the bulk causing a concentration gradient. The concentration gradient

causes H_2 to diffuse towards the membrane surface and non-permeable species to diffuse away. The transport of a species through the gas boundary layer can be estimated by a mass transfer coefficient, k_B [m/h], which is related to the dimensionless Sherwood number, *Sh*, as in equation **6.1**.

$$k_B = \frac{Sh * D_{H2}}{d_h} \qquad \textbf{6.1}$$

Where D_{H2} [m^2/h] is the diffusivity of H_2 in the gas mixture and d_h [m] is the hydraulic diameter of the membrane separator ($4A_C/Perimeter$, $4\pi(D_1^2-D_2^2)/(4\pi(D_1+D_2)$ for empty shell-in-tube cases, and the particle diameter, d_p [m], for PBR cases {Caravella *et al.,* 2009; Perry and Green, 1997}). The flux through the gas boundary layer is then given by equation **6.2**.

$$J_{H2} = k_B\left(P_{H2,b} - P_{H2,s}\right) \qquad \textbf{6.2}$$

Where $P_{H2,b}$ [atma] and $P_{H2,s}$ [atma] are the partial pressures of H_2 in the bulk gas on the retentate side and at the membrane surface (also on the retentate side) respectively. The Sherwood number could be estimated by its relationship with the dimensionless Schmidt number ($Sc = \mu/\rho * D_{H2}$) and the dimensionless Reynolds number ($Re = \rho * v * d_h/\mu$), where μ [kg/m-h] is the dynamic viscosity (Wilke, 1950), ρ [kg/m^3] is the density of the fluid, and *v* [m/h] is the average velocity of the fluid. The Sherwood number could be estimated by the relationships given in Table 6.1.

Table 6.1. Estimation of the Sherwood number from different literature sources.

Sherwood number	Qualifiers	Equation	Reference
$Sh^* = 1.15Sc^{0.333}\left(\frac{Re}{\varepsilon}\right)^{0.5}$	$Re > 1$	**6.3**	Perry and Green, 1997
$Sh = 2 + 1.1Sc^{0.333}Re^{0.5}$	$3 < Re < 10{,}000$	**6.4**	Wakao and Funaskri, 1978
$Sh = 1.61(Sc * Re * d_h)^{0.333}$		**6.5**	Ludtke *et al.,* 1998
$Sh = 0.662Sc^{0.333}Re^{0.5}$	$Sc > 1$	**6.6**	Coulson *et al.,* 1999
$Sh = 1.62\left(Sc * Re\frac{d_h}{L}\right)^{0.333}$	$Re < 2100$	**6.7**	Cussler, 1997

*For packed bed systems

At steady state, equation **6.2** can be set equal to the Sieverts' law expression (equation **4.2**) such that the flux through the boundary layer is equal to the flux through the dense Pd-layer as in equation **6.8**.

$$J_{H2} = F_{H2}\left(P_{H2,s}^{0.5} - P_{H2,perm}^{0.5}\right) = k_B\left(P_{H2,b} - P_{H2,s}\right) \qquad \textbf{6.8}$$

Since the resistance of the dense Pd-layer, ($P_{H2,perm}^{0.5}$+$P_{H2,s}^{0.5}$)/F_{H2} [h/m], was non-linear it could not simply be added to the resistance of the gas boundary layer, $1/k_B$ [h/m], as resistances in series. In practicality, the H_2 partial pressure at the membrane surface, $P_{H2,s}$ [atma], could be solved by either the quadratic formula or a numerical method such as the Newtonian iterative method (Caravella *et al.*, 2009; Catalano *et al.*, 2009) in order to then estimate the H_2 flux by equation **6.2**.

When the flux through the boundary layer was high, such that the flow velocity changed significantly over the length of the membrane, the use of a corrected mass transfer coefficient, k_B* [m/h], was necessary. The corrected mass transfer coefficient was estimated at each point along the membrane by equation **6.9** (Catalano *et al.,* 2009) and then used in equation **6.10**.

$$k_B^* = k_B ln\left(\frac{P_T - P_{H2,s}}{P_T - P_{H2,b}}\right) \qquad \textbf{6.9}$$

Where P_T [atma] was the total pressure on the retentate side.

$$F_{H2}\left(P_{H2,s}^{0.5} - P_{H2,perm}^{0.5}\right) = k_B^*\left(P_{H2,b} - P_{H2,s}\right) \qquad \textbf{6.10}$$

$P_{H2,s}$ could not be determined from equation **6.10** by the quadratic formula since $P_{H2,s}$ appeared in the logarithm equation for k_B*, equation **6.9**, so a numerical method had to be used (Caravella *et al.*, 2009; Catalano *et al.*, 2009).

6.2.2. Reversible surface inhibition

The WGS species CO and H_2O are known to reversibly adsorb onto the Pd-surface with the result of lowering the overall H_2 permeance of the membrane by blocking surface sites for H_2 adsorption (Li *et al.,* 2000; Gallucci *et al.,* 2007; Hou and Hughes, 2002; Peters *et al.,* 2008; Gielens *et al.,* 2006). There is also some indication that CO_2 has an

effect on the Pd-surface (Hou and Huges, 2002). The reversible surface inhibitions by CO and H_2O were shown to be temperature dependent with more inhibition at lower temperatures as was consistent with physical adsorption (Li *et al.,* 2000; Hou and Hughes, 2002).

There was significant discrepancy in the literature as to the relative extents of surface adsorption by H_2O, CO, and CO_2. Both Li *et al.* (2000) and Hou and Hughes (2002) agreed that inhibition by H_2O was greater than CO, but several other papers (Catalano *et al.,* 2011; Alfonso, 2006) indicated the opposite. The comparison of surface inhibitions between gas species was complicated by the potential non-ideal behavior of CO adsorption. Dulaurent *et al.* (1999) showed with infrared spectroscopy that the enthalpy of adsorption for CO on the surface gradually increased from -92 kJ/mol at zero surface coverage to -54 kJ/mol at full surface coverage, and therefore the Temkin model (equation **6.11**) was best for estimating surface coverage (Kul'kova and Temkin, 1949).

$$\theta_{CO} = \frac{RT}{\Delta H_{ads,0} - \Delta H_{ads,1}} * \ln\left(\frac{1+\lambda_0 * P_{CO}}{1+\lambda_1 * P_{CO}}\right) \qquad \textbf{6.11}$$

where $\lambda_i = \frac{h^3}{T^{5/2} k (2\pi m k)^{3/2}} e^{\left(\frac{\Delta E}{RT}\right)}$ was the adsorption equilibrium constant given in the previous chapter as equation **5.10**, $\Delta H_{ads,0}$ [kJ/mol] was the enthalpy of adsorption at zero surface coverage ($\theta_{CO} = 0$), and $\Delta H_{ads,1}$ [kJ/mol] was the enthalpy of adsorption at full surface coverage ($\theta_{CO} = 1$), *h* [J-s] was Planck's constant, *k* [J/K] was Boltzmann's constant, and *m* [kg/mol] was the molecular mass of CO.

Based on the estimated binding energy and equation **5.10**, adsorption equilibrium constants were estimated from several literature studies and listed in Table 6.2.

Table 6.2. Estimated values of λ_{CO}, λ_{H2O}, and λ_{CO2} (atm^{-1}).

	350℃	400℃	450℃	Reference
CO ($\theta_{CO} = 0$)	1.40	0.31	0.083	Dulaurent *et al.,* 1999
CO ($\theta_{CO} = 1$)	0.00091	0.00035	0.00015	Dulaurent *et al.,* 1999
CO ($\theta_{CO} = 0$)	2.44	0.24	0.032	Guo and Yates, 1989
CO ($\theta_{CO} = 1$)	$1.0x10^{-6}$	$2.9x10^{-7}$	$1.0x10^{-7}$	Guo and Yates, 1989
CO	0.95	0.094	0.013	Behm *et al.,* 1980
CO	55,500	2,580	181	Alfonso, 2006
CO	2,800	165	14.0	Rogal *et al.,* 2008
H_2O	0.050	0.0069	0.0012	Catalano *et al.,* 2011
H_2O	$1.4x10^{-10}$	$8.5x10^{-11}$	$5.4x10^{-11}$	Alfonso, 2006
CO_2	0.091	0.011	0.0017	Guo and Yates, 1989

The estimated binding energy of CO varied greatly between different literature studies, resulting in extreme values differing by up to four orders of magnitude. The adsorption of H_2O also varied greatly between theoretical (Alfonso, 2006) and experimental studies (Catalano *et al.,* 2011). Alfonso (2006) showed a surface binding energy of only 23.1 kJ/mol indicating that adsorption should be undetectable over the temperature range of 350 – 450℃ (see Table 6.2), but the experimental study by Catalano *et al.* (2011) showed a distinct inhibition in that range. Alfonso (2006) pointed out that the dissociation of H_2O to adsorbed OH and H, followed by further dissociation to O and H species could result in greater overall surface coverage by oxygen containing species. Guo and Yates (1989) pointed out that CO_2 would also dissociate to some extent on the Pd-surface, resulting in an effective surface coverage that could have been orders of magnitude greater than initial theoretical studies indicated.

6.2.3. Irreversible surface inhibition

Coke formation was likely to occur when the steam to CO ratio was low; it was promoted by the presence of H_2 and suppressed by the presence of H_2O or CO_2 (Li *et al.,* 2007b; 2008c). The formation of coke on the membrane surface can be considered 'irreversible' since the reaction for steam reforming of coke, equation **6.12** proceeds very slowly in the temperature range considered (200 – 500℃).

$$\mathbf{C(s) + H_2O \rightarrow CO + H_2} \qquad \textbf{6.12}$$

Since the formation of coke on the membrane can block the membrane surface for H_2 permeation, it must be avoided completely. A thorough consideration of coke formation is conducted in Chapter 8.

Another well known contaminant which is likely to be encountered in the IGCC process is H_2S. The exposure of a pure Pd-surface to low ppm levels of H_2S inhibits the Pd-surface against H_2 adsorption. Additionally, as little as 2.8 ppm H_2S in H_2 caused the formation of bulk sulfides at 400°C via equation **6.13** (Mundschau *et al.,* 2006).

$$\mathbf{Pd + H_2S \rightarrow Pd_4S + H_2} \qquad \textbf{6.13}$$

A consideration of H_2S poisoning is presented in Chapter 9.

6.3. Experimental

The relevant synthesis details and initial H_2 testing results of the membranes utilized in this chapter are listed in Table 6.3. The preparation and initial testing of those membranes was discussed in Chapter 4.

Table 6.3. Membranes tested in this chapter, comprehensive details are given in Appendix D.

	Pd/Ag [µm]	Dense layer [µm]	H_2 permeance* [m^3/m^2-h-$atm^{0.5}$]	Final select.† [F_{H2}/F_{He}]	Other details
AA-5	2.7	9.7	18.5	2,800	
AA-6	2.4	10.3	21.3	1,100	
AA-21	4.8	15.7	20.2	175	

*at 400°C

†selectivity after final mixed gas experiment described here

The experimental setup for the mixed gas experiments was described in the Experimental, Section 3.4.1. Several gas mixtures were used in this study with the compositions listed in Table 6.4. The Gases A, B, C, and D were prepared mixtures received from Middlesex Gases & Technologies Inc (Everett, MA). The Gas E was

prepared from pure H_2 gas and H_2O added via HPLC pump (Harvard Apparatus Series I), also as described in the Experimental, Section 3.4.1. Pure H_2 was received from ABCO Welding Supply (Waterford, CT).

Table 6.4. Composition of gas mixtures used in this study.

	H_2	He	CO_2	CO	H_2O
Gas A	80%	-	20%	-	-
Gas B	61.7%	-	37.1%	1.2%	-
Gas C	61.7%	38.3%	-	-	-
Gas D	61.7%	-	38.3%	-	-
Gas E	61.7%	-	-	-	38.3%

The experimental H_2 recovery, Y_{H2}, was defined by equation **6.14**.

$$Y_{H2} \equiv \frac{N_{H2,p,out}}{N_{H2,r,0}} \qquad \textbf{6.14}$$

Where $N_{H2,p,out}$ [kmol/h] was the permeate flow rate and $N_{H2,r,0}$ [kmol/h] was the feed flow rate of H_2. The Gas Hourly Space Velocity, $GHSV_{STP}$ [h^{-1}] was calculated via equation **6.15**.

$$\mathrm{GHSV} = 3{,}600\,\frac{(\sum_i N_{i,0})V_m}{V_r} \qquad \textbf{6.15}$$

Where $N_{i,0}$ [kmol/h] was the feed flow rate of species *i*, V_m was the molar volume (22.4 m^3/kmol at STP), V_r [m^3] was the reactor volume of $1.32*10^{-5}$ m^3, and 3,600 was the time conversion factor (seconds per hour). Note that the GHSV was calculated at the standard temperature and pressure, and accounting for H_2O as a gas. The residence time, τ [s], was calculated by equation **6.16**.

$$\tau = \frac{V_r * \varepsilon}{(\sum_i N_{i,0})V_m}\frac{T_{STP}}{T_r}\frac{P_r}{P_{STP}} \qquad \textbf{6.16}$$

Where ε was the void fraction of the catalyst bed, P_r [atma] was the reaction pressure and T_r [K] was the reaction temperature. Note that the residence time was calculated for the gas mixture at system conditions. Also note that the void fraction was unity for the

membrane separator (with no catalyst present) as will be applicable for all of Chapter 6. In the Chapters 7 - 10 a void fraction of 0.47 was estimated for the WGS CMR loaded with iron-chrome oxide catalyst.

The 1-D model described in Chapter 5 was utilized to generate simulation results overlaid onto the experimental results. The model was altered by elimination of the state variable X_{CO} and $Y_{H2} \equiv \frac{N_{H2,p}}{N_{H2,r,0}}$. The simulation parameters for the experimental system are listed in Table 6.5. The membrane permeance was that measured by pure H_2 testing of each membrane listed in Appendix D. The reversible surface adsorption by CO and H_2O was accounted for as described in Section 5.2.2. The gas boundary layer mass transfer coefficient was estimated by the Sherwood number empirical correlation given by Coulson *et al.* (1999). No adjustable parameters were utilized.

Table 6.5. 1-D model parameters for simulation results shown in this chapter.

	Simplified 1-D model, used in Section 6.4.1	Full 1-D model, used in Section 6.4.2
Separator Dimensions	Tube-in-tube	
Length, L [m]	0.065	
Cross-sectional area, A_c [m^2]	$2.33*10^{-4}$	
Aspect ratio	14.8	
Membrane Properties	Tubular	
Membrane area, A_{Pd} [m^2]	$2.5*10^{-3}$ m^2	
Permeance, $F_{H2,0}$ [m^3/m^2-h-$atm^{0.5}$]	AA-5, 18.5	AA-6 and AA-21 (see Appendix D)
Binding energy, ΔE_i [kJ/mol]	None	CO: -149 (Guo and Yates, 1989) H_2O: -125 (Catalano *et al.,* 2011)
Feed Properties		
Feed composition, θ_i	Gas A (Table 6.4)	Gases B, C, D, and E (Table 6.4)
Feed rate, $N_{H2,r,0}$ [kmol/h]	$2.4*10^{-4}$ – $3.1*10^{-2}$	$2.4*10^{-4}$ – $2.0*10^{-2}$
Inert sweep, $N_{i,p,0}$ [kmol/h]	None	
Temperature, T [°C]	400°C	350 - 450°C
Reaction pressure, P_s [atma]	14.5	
Tube-side pressure, P_t [atma]	0.98	
Dynamic viscosity, μ [kg/h-m]	None*	0.060 - 0.066
Diffusivity of H_2, D_{H2} [m^2/h]	None*	0.0724 – 0.225
Sherwood number approximation, *Sh*	None*	$Sh = 0.662Sc^{0.333}Re^{0.5}$ (Equation **6.6**, Coulson *et al.*, 1999)

*Simplifed model assumed no gas boundary layer mass transfer resistance

6.4. Results and discussion

6.4.1. Gas boundary layer resistance and depletion

A better understanding of gas boundary layer resistance and depletion was important to provide a basis for the WGS CMR experiments. Both of the effects were present to the greatest extent under low flow conditions where a low H_2 flux was expected.

Initially, an experiment was conducted by varying the total feed flow rate at a fixed pressure, and utilizing the membrane AA-5 (described in Table 6.3), and Gas A (specified in Table 6.4) to gain a preliminary understanding of the separation dynamics in the system. The results of that experiment in terms of permeate flux and H_2 recovery versus feed flow rate are shown in Figure 6.1. Overlaid on the data are the flux and H_2 recovery calculated by 1-D model described in Chapter 5 (with the parameters listed in Table 6.5, incorporating resistance of the dense Pd-layer and discounting gas boundary layer resistance).

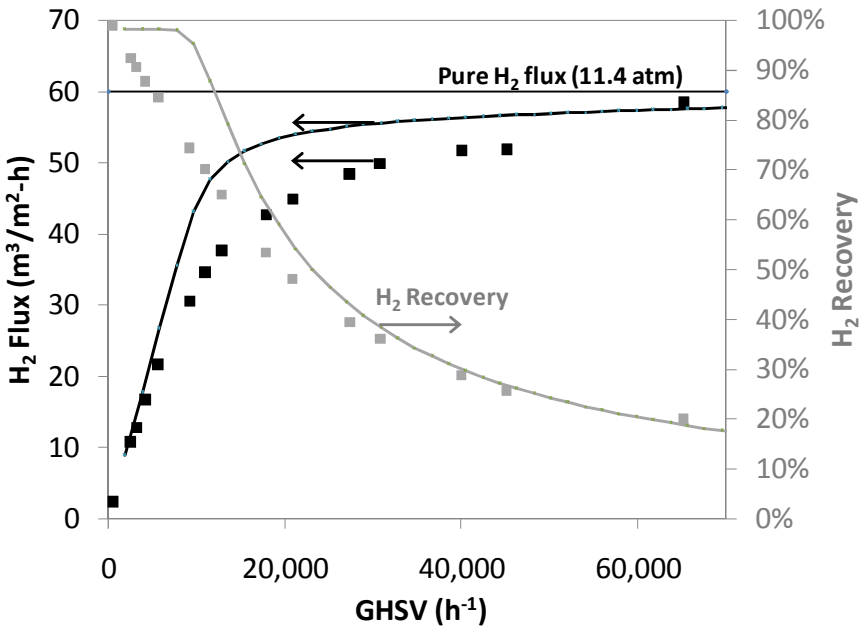

Figure 6.1. Permeate flux and H_2 recovery versus $GHSV_{STP}$ for membrane AA-5, 400℃, 14.5 atma, and Gas A (Overlaid curves represent solutions of a simplified 1-D model, horizontal line indicates pure H_2 flux at equal H_2 partial pressure).

The difference between the experimental data points and the calculated flux and recovery from the 1-D model was due to mass transfer resistance of the gas boundary layer, an important phenomenon that was not accounted for in the calculation. It was clear from the figure that this effect was significant over almost the entire flow range, up to a $GHSV_{STP}$ of approximately 50,000 h^{-1}. At very low total feed rates of less than 1,000 h^{-1}, the H_2 recovery was as high as 98% due to the high residence time of the gas in contact with the membrane (approximately 21.0 seconds by equation **6.16**). At the low feed rates, the partial pressure of hydrogen on the shell-side was reduced by depletion to very close to that of the tube-side (note that the total shell-side pressure did not change detectably over the length of the membrane). As a consequence, at low total feed rates the hydrogen recovery was high (although the permeate H_2 flux was low). In the WGS CMR, a high degree of H_2 removal from the reaction zone was necessary to achieve CO conversion in excess of the thermodynamic equilibrium (Damle *et al.*, 2008; Dolan *et al.*, 2010; Mendes *et al.*, 2010).

There is a heat transfer analogy to the Pd-membrane separator consisting of a hot fluid being cooled by heat exchange with a constant temperature heat sink (analogous to the constant tube-side pressure of 0.98 atma). When the heat exchanger had a high contact area or a high heat transfer coefficient, the Number of Transfer Units (NTU) became large, resulting in an outlet temperature very close to that of the heat sink. The heat transfer effectiveness was similar to the H_2 recovery in so far as it was defined as the ratio of the permeated H_2 to the maximum amount of H_2 present in the feed (equation **6.14**). The analogy was less suitable when one considered the comparison of the partial pressure driving force of H_2 across the membrane with the temperature difference across a heat exchanger. In the case of the constant temperature heat sink with very large contact area, the outlet temperature approached the heat sink temperature and the effectiveness approached 100%. For the membrane separator with infinite selectivity and very large area, the partial pressure of H_2 in the retentate approached that in the permeate, but the H_2 recovery (defined by equation **6.14**) approached a value of less than unity (bounded by the 0.98 atma partial pressure of H_2 which remained in the retentate). In Figure 6.1, when the feed rate was less than 1,000 h^{-1}, the partial

pressure of H_2 in the retentate was approximately 0.99 atma (such that the partial pressure driving force was almost zero), and the H_2 recovery was approximately 98%.

Since the Pd-membranes had extraordinarily high selectivity (greater than 2,800 for the membrane AA-5) the separation was fundamentally different than that of microporous or polymeric membranes. In polymeric membranes with H_2/CO_2 selectivities of up to 100 (Robeson, 2008) a low stage cut, $N_p/(N_p + N_r)$, must be used to achieve reasonable purity of the separated product. In those membrane systems, an increase in membrane area (or a decrease in feed rate) resulted in a higher stage cut and therefore a lower permeate purity. In the dense Pd-membrane system (assuming infinite selectivity) the stage cut could not exceed the mol fraction of H_2 in the feed since the non-permeable species could not cross the membrane, even if the membrane area was increased to infinity. For the series of experiments shown in Figure 6.1, the stage cut was approximately 0.16 at the highest feed rate (65,000 h^{-1}) and approximately 0.79 at the lowest feed rate, 500 h^{-1} (note that the mol fraction of H_2 in Gas A was 0.80). Since the Pd-membrane had a slight leak, the H_2 purity was likely dependent on the stage cut. However, that dependence could not be determined since the level of CO_2 in the permeate was less than the 0.5% detection limit of the GC over the whole range of feed conditions.

At high total feed rates, greater than 50,000 h^{-1}, the permeate flux reached the upper bound of the membrane permeance (shown as a solid horizontal line in Figure 6.1). At high feed rates the velocity of the gas was high, resulting in a low gas phase mass transfer resistance and a high Sherwood number given by equation **6.3 – 6.7**. The flux of H_2 through the boundary layer was dependent upon two mechanisms: bulk flow of gases to and from the surface (convection), and molecular diffusion of gaseous components. The Sherwood number is the ratio of the convection mass transfer rate to the diffusion mass transfer rate. It has been experimentally shown in a number of studies (listed in Table 6.1) that the average Sherwood number can be estimated by an empirical correlation with the Reynolds number and the Schmidt number. The Reynolds number is the ratio of inertial to viscous forces in a flowing fluid and can be thought of as a measure of the convective mixability of that fluid in a particular system. The

Schmidt number is the ratio of the viscous transport to the molecular diffusion transport and remains invariant to the fluid velocity and flow channel dimensions.

In order to overcome the boundary layer mass transfer resistance, the Reynolds number of the flow should be increased (Caravella *et al.,* 2009). Unfortunately, in the experimental system it was virtually impossible to exceed a Reynolds number of 200 due to the convective cooling caused by the flow of greater than 9,000 sccm of room temperature gas into the hot membrane module (higher flow rates and therefore a higher Reynolds number would have been possible with better heat transfer in the preheater module). In a commercial system with larger dimensions, a characteristic length of 4 cm for instance (as opposed to 4.4 mm in our case), a turbulent flow with a Reynolds number of 2,000 – 4,000 could be established with the same feed space velocity (and considering appropriate feed pre-heating via a heat exchanger).

6.4.2. Surface inhibition

In addition to the gas phase mass transfer resistance, it was also likely that the presence of CO and H_2O caused some decrease in the permeance by reversible binding to the surface (Hou and Hughes, 2002; Arstad *et al.,* 2006; Li *et al.,* 2000). The inhibition effects of CO and H_2O were further investigated with a series of experiments conducted with the membranes AA-6 and AA-21 (described in Table 6.3) and using the Gases B, C, D, and E (specified in Table 6.4). The gas mixtures chosen all had the same mol fraction of H_2 present (62%) and therefore it was expected that differences in H_2 flux would be due to either the interaction of the other gas species (CO and H_2O) with the Pd-surface or the differences in the molecular size and mass of those species (He, CO_2, CO, and H_2O). The results from the experiments are shown in Figure 6.2 in terms of J/J_0, where J [m^3/m^2-h] was the measured H_2 flux and J_0 [m^3/m^2-h] was the flux of pure H_2 at 7.9 atma (equivalent to the partial pressure of H_2 in the gas mixtures), which was extrapolated from the Seiverts' law permeance (see Table 6.3). Neither membrane AA-6 nor AA-21 was tested in pure H_2 at a pressure of greater than 5 atma. Results from the 1-D model (described in Chapter 5, and with parameters listed in Table 6.5) are also plotted in Figure 6.2.

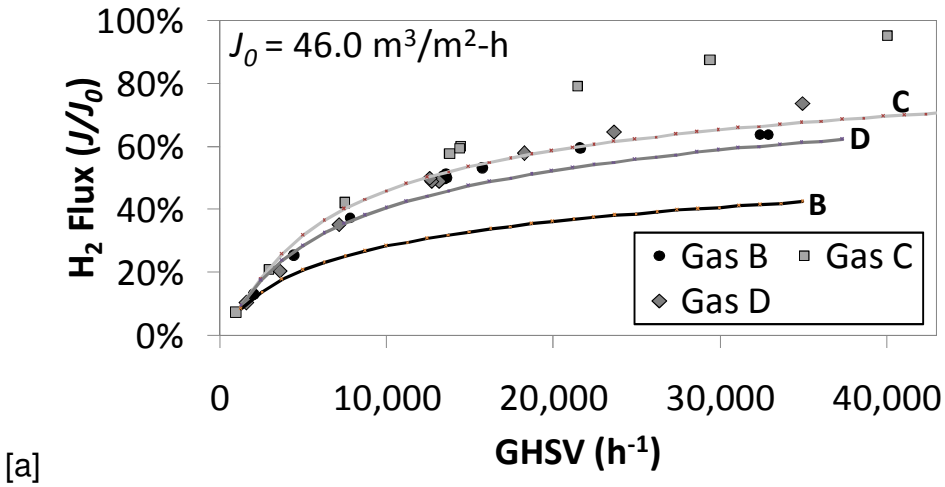

[a]

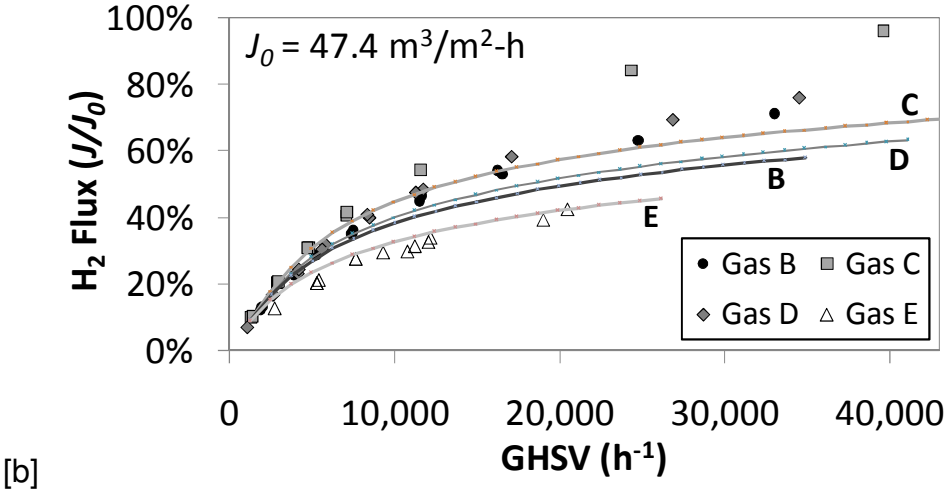

[b]

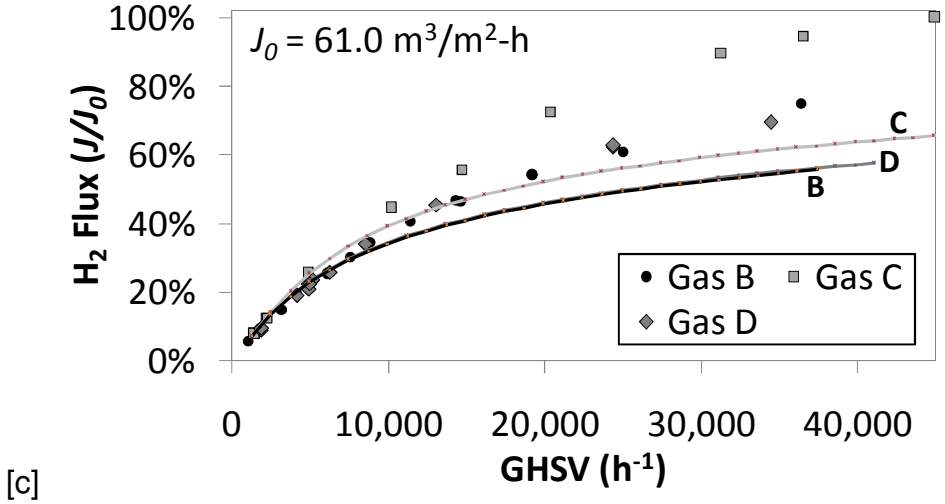

[c]

Figure 6.2. Permeate flux over J_0 versus $GHSV_{STP}$ with membrane AA-6 and three gas mixtures at 14.5 atma [a] 350℃ [b] 400℃ (membrane AA-21 used for Gas E only) and [c] 450℃.

Figure 6.2[a], [b], and [c] show the relationships between the permeating H_2 flux and the total feed space velocity of the four mixed gases at three different temperatures: 350, 400, and 450°C. Since the concentration of H_2 in each mixture was the same, discrepancies between them must have been caused by either the different diffusivity of H_2 in the gas mixtures or differing interactions between the additive gases and the Pd-membrane. The qualification of these effects will lead to a better understanding of the permeation inhibition caused by the additive gases.

There has been some discrepancy in the literature regarding the potential surface inhibition by CO_2, with Hou and Hughes (2002) observing slight inhibition of the Pd-surface and Arstad *et al.* (2006) observing no effect. The results presented in Section 6.4.1, namely the final flux measurement in Figure 6.1 which was very near to the flux measured under pure H_2 testing, suggested that there was not significant inhibition by CO_2 at 400°C. It was therefore expected that the difference in H_2 flux behavior between the Gases C and D would be due entirely to the mass transfer resistance which was greater for the H_2/CO_2 mixture (Gas D) because the diffusivity of H_2 was lower in that mixture. The diffusivity of H_2 in each binary mixture, calculated by the kinetic theory of gases, is listed in Table 6.6.

Table 6.6. Diffusivity of H_2 in each binary H_2/i mixture (Reid *et al.,* 1987).

	350°C	400°C	450°C
H_2/He (m^2/h)	0.176	0.201	0.2254
H_2/CO_2 (m^2/h)	0.0724	0.0824	0.0929
H_2/CO (m^2/h)	0.0785	0.0892	0.0958
H_2/H_2O (m^2/h)	0.0803	0.0918	0.104

The diffusivity of H_2 in the H_2/He mixture was approximately 2.5 times greater than that of the H_2/CO_2 mixture, which allowed for considerably better mass transfer. For the Gas C, at feed rates of greater than 35,000 h^{-1}, the permeating flux approached asymptotically (within 5%) to that of the flux at the equivalent partial pressure of pure H_2 (Figure 6.2[a-c]), suggesting that the only limitation was the permeance of the

membrane. With the exception of Gas C, the flux measured for all of the gases over the whole range of feed rates was significantly affected by gas phase mass transfer resistance. For Gas D, the lower diffusivity of H_2 in the H_2/CO_2 mixture resulted in a reduction in H_2 flux of about 23% for the feed rate range of 5,000 – 35,000 h^{-1} due to greater mass transfer resistance. These results were in agreement with the set of experiments described in Section 6.4.1, which indicated that for the H_2/CO_2 mixture, a feed space velocity of over 50,000 h^{-1} would be necessary to overcome the gas boundary layer resistance.

At total flows of less than 1,000 h^{-1}, the H_2 recovery for all of the gas mixtures was very high (approximately 90%) due to the high residence time of the gas mixtures in contact with the membrane (21.0 seconds at 1,000 h^{-1} compared to 0.6 seconds at 35,000 h^{-1} at 400°C and 14.5 atma via equation **6.16**). This result indicated that there was very little driving force for H_2 separation towards the outlet end of the membrane. Over the whole range of feed rates two effects limited the permeating H_2 flux, the gas boundary layer resistance and the resistance through the dense Pd-layer. Even though these resistances both factored into the data presented in Figure 6.2, information could still be extracted as to the relative extent of surface inhibition by CO and H_2O, resulting in a lower H_2 flux when those species were present. The diffusivity of the H_2 in the H_2/CO and H_2/H_2O mixtures was slightly higher than that of the H_2/CO_2 mixture (indicating lower gas phase resistance), yet the H_2 flux from those two mixtures was lower than that of the H_2/CO_2 mixture due to reversible surface inhibition.

At 350°C Gas B, containing 1.2% CO, showed an 11% lower flux than Gas D due to the reversible adsorption of CO on the Pd-surface. At 450°C Gas B showed an H_2 flux that was approximately equal to Gas D, indicating that CO inhibition was not occurring to a detectable extent at that temperature. The permeation inhibition by CO was significantly less at 400°C than at 350°C, and undetectable at 450°C; this was in good agreement with the literature (Hou and Hughes, 2002; Arstad *et al.,* 2006; Li *et al.,* 2000).

At 400°C Gas E, containing 37% H_2O, showed a 32% lower H_2 flux than Gas D at the highest feed rate, 20,500 h^{-1}, due to inhibition by the high concentration of H_2O, which has also been previously reported in the literature (Li *et al.,* 2000). Even though the

surface interaction of the steam was significant, a high H_2 flux of 27.9 m^3/m^2-h-atm (with 40% H_2 recovery) was achieved at the highest feed rate (20,500 h^{-1}). At the lowest feed rate (2,700 h^{-1}) a high H_2 recovery of 90% was achieved along with an H_2 flux of 8.3 m^3/m^2-h.

The lack of agreement by the 1-D model with the experimental data was disappointing and indicated significant shortcomings of the model. The possible reasons for this lack of agreement were the assumptions of no radial concentration gradient and an average mass transfer coefficient (instead of a local mass transfer coefficient). Regardless, it should be pointed out that at feed rates of less than 10,000 h^{-1}, reasonable agreement was observed in some cases such that the model may still be relevant for WGS CMR experiments (which were conducted with feed rates of less than 6,000 h^{-1}). Additionally, the model did predict the lower H_2 flux measured for the $H_2/CO/CO_2$ (Gas B in Table 6.4) mixture at 350 and 400°C, as well as that of the H_2/H_2O mixture (Gas E in Table 6.4) at 400°C, suggesting a reasonable estimation of the surface inhibition phenomenon for those two gas species.

Since the mass transfer resistance was significant over the whole range of feed conditions, a quantitative analysis of the surface inhibition could not be achieved. Experiments should be conducted with a higher flow velocity such that the Reynolds number of the flow would be higher, and gas phase mass transfer resistance would be lower. In conjunction with the inhibition experiments, the surface coverage of CO and H_2O should be directly measured at experimental conditions with infrared spectroscopy (Behm *et al.*, 1980; Dulaurent *et al.*, 1999).

Gielens *et al.* (2006) conducted experiments on a micro-sieve supported Pd-membrane prepared by sputter deposition, with H_2/CO_2 and H_2/H_2O mixtures at 350, 400, and 450°C and 1 atma (P_{tube} = 1 atma, N_2 sweep). The study found that (reversible) inhibition by H_2O was much greater than that of CO_2, but that coke was gradually being deposited by the H_2/CO_2 mixture, resulting in a gradual decline in the membrane permeance over several hours. Li *et al.* (2000) conducted mixed gas permeation experiments on PSS supported Pd-membranes with H_2/N_2, H_2/CO, and H_2/H_2O mixtures at 380°C and 3 atma (P_{tube} = 1 atma). At a composition of 1.8% CO in 98% H_2 there

was almost no discernible inhibition by CO (when compared to N_2), but there was a 16% lower H_2 flux for the H_2O mixture indicating much more significant inhibition (H_2O > CO). Unfortunately, Li *et al.* (2000) did not describe their system and conditions in enough detail to calculate the Reynolds number of their flow, so it was unclear if significant gas phase mass transfer resistance was present. Hou and Hughes (2002) conducted experiments with H_2/CO_2, H_2/CO, and H_2/H_2O mixtures at 275°C and 2 atma (P_{tube} = 1 atma). The study concluded that the extent of inhibition by each species was ordered as H_2O > CO > CO_2. Hou and Hughes (2002) also conducted experiments with an H_2/H_2O mixture (20% H_2O in H_2) over the temperature range of 275 - 350°C, observing that the inhibition by H_2O was greater at lower temperatures. Due to the discrepancy between these literature studies, further experiments should be conducted with several H_2/CO and H_2/H_2O mixtures, at temperatures of 350, 400, and 450°C, and with high Reynolds number (greater than 2,000) fluid flows. A complication in conducting these experiments is the tendency of H_2/CO mixtures to form coke on the membrane surface when little or no H_2O is present.

6.5. Conclusions

Mixed gas separation experiments were conducted with simulated syngas at 350 – 450°C, and over a range of total flow rates to investigate the effects of gas boundary layer mass transfer resistance and Pd-surface inhibition by CO, CO_2, and H_2O. In all cases, at low feed rates (less than 1,000 h^{-1}), H_2 recoveries of over 90% were observed in which the partial pressure driving force of H_2 was very low at the retentate outlet. At high feed rates (up to 40,000 h^{-1}) the permeate flux for H_2/He mixtures was observed to closely approach that of pure H_2 such that gas boundary layer resistance was negligible. For the H_2/CO_2 mixture, the gas phase mass transfer resistance was significant for feed rates of up to 50,000 h^{-1}. For other gas mixtures containing CO, H_2O, and CO_2, the permeate flux was significantly lower than that for pure H_2 such that gas phase mass transfer resistance was significant.

For the gas mixtures containing H_2O and CO, the permeate flux was lower than the mixture containing CO_2, due to reversible surface inhibition. The inhibition by CO was inversely dependent on temperature such that there was a significant effect at 350°C

and no observable effect at 450°C. The inhibition by H_2O was significant at 400°C, resulting in approximately 34% lower H_2 flux than that of the H_2/CO_2 mixture over the feed rate range of 5,000 – 20,000 h^{-1}.

7. WATER-GAS SHIFT CATALYTIC MEMBRANE REACTOR INCORPORATING A Pd-MEMBRANE

7.1. Introduction

As was discussed in the Literature Review, Section 2.3.1, it has been established that by utilizing elevated reaction pressure in a membrane reactor, both CO conversion and H_2 recovery can be increased significantly. A high reaction pressure can also allow for cost savings during CO_2 capture as the retained CO_2 will already be at an elevated pressure. Operating at low pressure has severely limited the majority of previous studies by requiring the use of a sweep gas to establish the driving force for H_2, resulting in a highly dilute H_2 product. A sweep gas is impractical in the IGCC process because a subsequent separation step would then be necessary. Utilizing steam as a sweep gas would simplify the separation step but would increase the energy demand of the process. When a high H_2 recovery is achieved (by way of high reaction pressure) CO conversion in significant excess of the PBR equilibrium can be achieved so that higher reaction temperatures can be used. At higher temperatures commercial WGS catalysts have significantly higher catalytic activity, which would enable higher throughput compared to an equivalently sized PBR. Additionally, the H_2 permeance of Pd-membranes is greater at higher temperatures and the surface inhibition phenomena are less, which would allow for greater H_2 recovery.

Few studies have explored the characteristics of the WGS CMR at pressures exceeding 6 atma since robust, highly permeable, PSS supported membranes were not available. High pressure operation is essential to achieving high CO conversion and H_2 recovery at high through-put. The aim of this chapter was therefore to utilize PSS and PI supported Pd-membranes for the WGS CMR in order to characterize and assess the effects of the operating conditions (H_2O/CO ratio, temperature, and feed flow rate) on the CO conversion and H_2 recovery achieved by the reactor at high temperature (350 - 500°C) and high reaction pressure (14.4 atma). By way of this characterization, a better fundamental understanding of the WGS CMR system was developed.

7.2. Experimental

The relevant synthesis details and initial H_2 testing results of the membranes utilized in this chapter are listed in Table 7.1. The preparation and initial testing of those membranes was discussed in Chapter 4.

Table 7.1. Membranes tested in this chapter, comprehensive details are given in Appendix D.

	Pd/Ag [μm]	Dense layer [μm]	H_2 permeance* [m^3/m^2-h-$atm^{0.5}$]	Final select.† [F_{H2}/F_{He}]	Other details
AA-5	2.7	9.7	18.5	2,800	
AA-6	2.4	10.3	21.3	1,100	
AA-8R	3.4	6.4	26.9	174	
AA-24R	6.2	7.4	28.5	365	High temp. annealing
AA-30	<1.0	9.3	28.6	240	

*at 400°C
†selectivity after final WGS testing

The system configuration was shown in Figure 3.4 (Chapter 3, Section 3.5.1). The loading procedure for the membrane reactor including quartz sand, plugs of quartz wool, and iron-chrome oxide catalyst was described in Section 3.5.2. The operating procedure for a typical WGS experiment was described in Section 3.5.3.

The syngas mixture used for the experiments in Sections 7.3.3 and 7.3.4 was chosen based on the composition of syngas produced by a GE Energy coal gasification plant (Klara *et al.,* 2007). The feed gas on a dry basis was composed of 41.6% CO, 40.3% H_2, and 18.1% CO_2 and was prepared by Middlesex Gases & Technologies Inc (Everett, MA). Water was purified by a MilliQ deionization system, then allowed to degas for at least 24 hours in air so that no bubbles would form in the pump lines. Pure CO gas was received from ABCO Welding Supply (Waterford, CT).

The experimental CO conversion, X_{CO}, was calculated by equation **7.1** and the experimental H_2 recovery, Y_{H2}, was calculated by equation **7.2**.

$$X_{CO} = \frac{N_{CO,feed} - N_{CO,ret,out} - N_{CO,perm,out}}{N_{CO,feed}} \quad \textbf{7.1}$$

$$Y_{H2} = \frac{N_{H2,perm,out}}{N_{H2,feed} + N_{CO,feed}} \quad \textbf{7.2}$$

The equilibrium conversion, $X_{CO,EQ}$, for a given set of feed conditions was calculated by solving the equation **7.3** via the quadratic formula. Note that the quadratic formula yielded two solutions; the negative solution was discarded since it had no physical significance.

$$\boldsymbol{K} = \frac{(x_{CO2} + X_{CO,EQ})(x_{H2} + X_{CO,EQ})}{(x_{CO} - X_{CO,EQ})(x_{H2O} - X_{CO,EQ})} \quad \textbf{7.3}$$

where $\boldsymbol{K} = \boldsymbol{e}^{\frac{4577.8}{T} - 4.33}$ (Moe 1962) and x_i [mol/mol] was the mol fraction of species *i* in the feed.

The 'dynamic' equilibrium conversion, $X_{CO,d}$, (Basile *et al.*, 2001; Damle *et al.*, 2008) was determined by assuming that the removal of H_2 occurred until there was zero driving force for H_2 across the membrane at the outlet; $P_{H2,ret,out} = P_{H2,perm,out}$. The mol fraction of H_2 in the retentate, $x_{H2,ret}$, was then given by equation **7.4** and the 'dynamic' equilibrium expression by equation **7.5**.

$$x_{H2,ret} = \frac{P_{H2,perm,out}}{P_T} \quad \textbf{7.4}$$

$$\boldsymbol{K} = \frac{(x_{CO2} - X_{CO,d})\left(\frac{P_{H2,perm,out}}{P_T}\right)}{(x_{CO} - X_{CO,d})(x_{H2O} - X_{CO,d})} \quad \textbf{7.5}$$

where P_T was the total reaction pressure.

The 1-D model described in Chapter 5 was utilized to generate simulation results overlaid onto the experimental results presented in this chapter. The simulation parameters for the experimental system are listed in Table 7.2. The membrane permeance used in the simulation was that measured by pure H_2 testing of each membrane listed in Appendix D. The reversible surface adsorption by CO and H_2O was incorporated into the simulation as described in Section 5.2.2. The gas boundary layer

mass transfer coefficient was estimated by the Sherwood number empirical correlation, equations **5.12, 5.13** and **5.16**, discussed in Section 5.2.3. No adjustable parameters were utilized.

Table 7.2. 1-D model parameters for simulation results shown in this chapter.

Catalyst Properties	Fe/Cr-oxide
Catalyst density, ρ_{cat} [kg/m^3]	1.06*10^3
Catalyst void fraction, ε	0.47
Particle size, d_p [m]	3.5*10^{-4} (average particle size)
Rate expression, $r_{CO}/(1-\beta)$ [kmol/kg-h]	$2.52 \times 10^6 e^{-111/RT} P_{CO} P_{CO2}^{-0.36} P_{H2}^{-0.09}$ (Equation **5.20**, Hla *et al.,* 2009)
Effectiveness factor, η	1.0 (assumed)
Reactor Dimensions	Tube-in-tube
Reactor Length, L [m]	0.065
Cross-sectional area, A_c [m^2]	2.33*10^{-4} m^2
Aspect ratio	14.8
Membrane Properties	Tubular
Membrane area, A_{Pd} [m^2]	2.5*10^{-3} m^2
Permeance, $F_{H2,0}$ [m^3/m^2-h-atm$^{0.5}$]	Specified for each membrane in Appendix D
Binding energy, ΔE_i [kJ/mol]	CO: -149 (Guo and Yates, 1989) H_2O: -125 (Catalano *et al.,* 2011)
Feed Properties	
Feed composition, θ_i	Specified in figure captions
Feed rate, $N_{CO,r,0}$ [kmol/h]	1.47*10^{-4} – 7.22*10^{-4} (specified in figure captions)
Inert sweep, $N_{i,p,0}$ [kmol/h]	None
Temperature, T [°C]	350 - 500 (specified in figure captions)
Reaction pressure, P_s [atma]	5 – 14.6 (specified in figure captions)
Tube-side pressure, P_t [atma]	0.98
Dynamic viscosity, μ [kg/h-m]	0.074 - 0.090
Diffusivity of H_2, D_{H2} [m^2/h]	0.0785 – 0.114
Sherwood number approximation, *Sh*	$1.15Sc^{0.333}\left(\frac{Re}{\varepsilon}\right)^{0.5}$ (Equation **5.16**, Perry and Green, 1997)

7.3. Results and Discussion

A series of four WGS PBR experiments were conducted at a pressure of 14.4 atma and with a feed composed of CO and H_2O (1.1:1 steam to CO ratio) to validate the equilibrium calculation for the WGS reaction as shown in Figure 7.1. Four WGS CMR experiments were also conducted at the same pressure, feed composition, and feed rate with the membrane AA-5 and the results of those experiments are also plotted in Figure 7.1. In all of the WGS CMR experiments a gradual decrease in H_2 recovery and CO conversion over time was observed; an example of which is shown in Figure 7.2. The WGS PBR data did not show similar drifting over time indicating that a steady state was reached within the first 60 minutes of each experiment; in all cases experiments were continued for at least four hours.

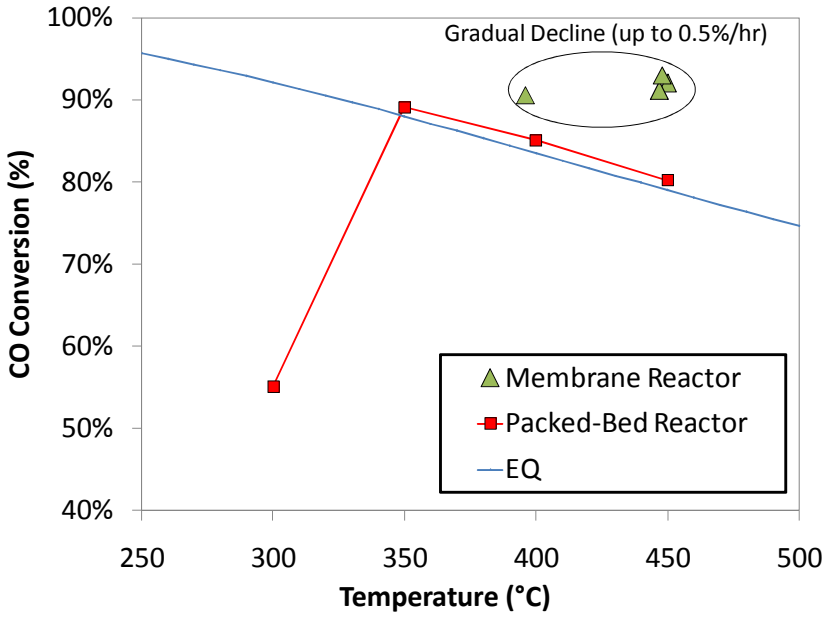

Figure 7.1. CO conversion versus temperature (Membrane: AA-5, 14.4 atma, H_2O/CO = 1.1, $GHSV_{STP}$ = 1,600 h^{-1}).

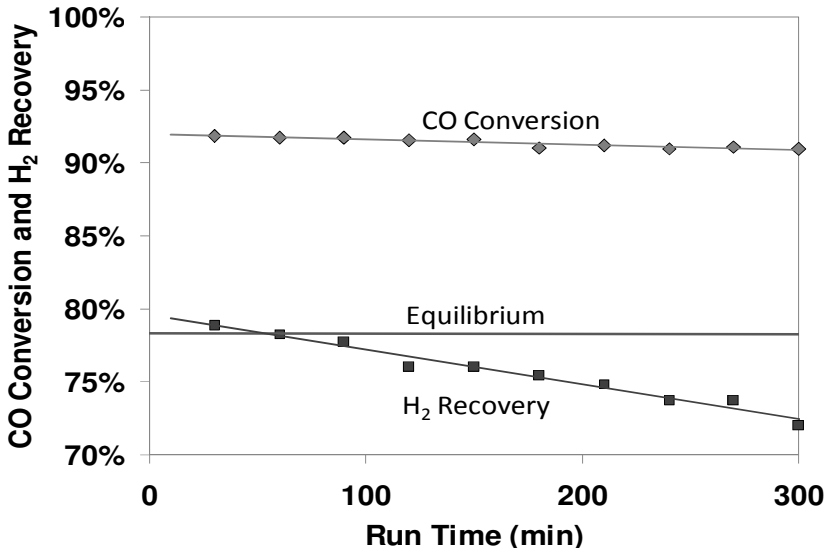

Figure 7.2. CO conversion and H_2 recovery versus time (Membrane: AA-5, 450℃, 14.4 atma, H_2O/CO = 1.1, and $GHSV_{STP}$ = 1,600 h^{-1}).

For the PBR experiment at 300℃ the CO conversion was only 55.1%, 37% below the equilibrium conversion for that temperature. The iron-chrome oxide catalyst (HiFUEL 210, Alfa Aesar), had optimal activity above approximately 400℃, and therefore could not achieve equilibrium conversion with respect to the feed rate at 300℃. At 350, 400, and 450℃ the CO conversion was within 1.6% of the expected equilibrium value. The carbon balances for the reactions were 94.6, 96.9, 100.1, and 100.6% respectively. For all four CMR experiments, higher CO conversions were achieved than for the PBR experiments conducted at the same temperature and pressure, despite the gradual decrease in H_2 recovery and CO conversion over time. CO conversion in excess of the equilibrium conversion resulted from the removal of H_2 from the system causing the reaction mixture to shift further towards the products as per Le Chatelier's principle (Basile *et al.,* 1996b; Barbieri *et al.,* 2008).

Figure 7.2 shows the CO conversion and H_2 recovery over time for a reaction carried out at 450℃, with a steam to CO ratio of 1.1, and a $GHSV_{STP}$ of 1,600 h^{-1}. After 300 minutes the hydrogen recovery had decreased by 8.7% from its initial value of 79% and the CO conversion had decreased by 0.9% from 92%. The permeance of the

membrane was incrementally decreased after each experiment as shown in Figure 7.3. The CMR was dismantled without attempting experiments at different feed and temperature conditions due to the decreased membrane permeance. A picture of the membrane after use in the WGS experiments is shown in Figure 7.4. The membrane was observed to have coke deposits embedded on the surface, mainly towards the inlet end of the reactor. The deposits were very thin and tightly bound to the surface. The weight change of the membrane due to the coke deposites could not be determined since the membrane tube had to be cut in order to remove it from the system.

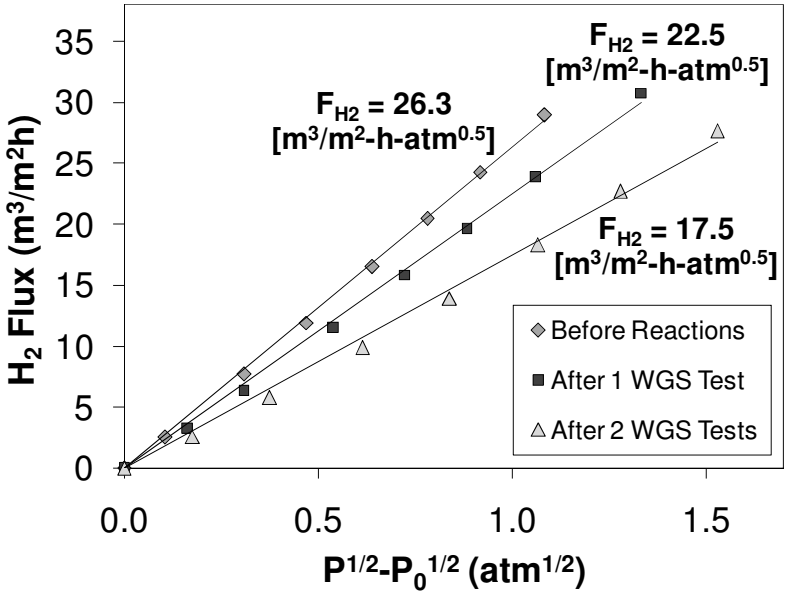

Figure 7.3. Sieverts' law permeance of the membrane AA-5 at 450℃.

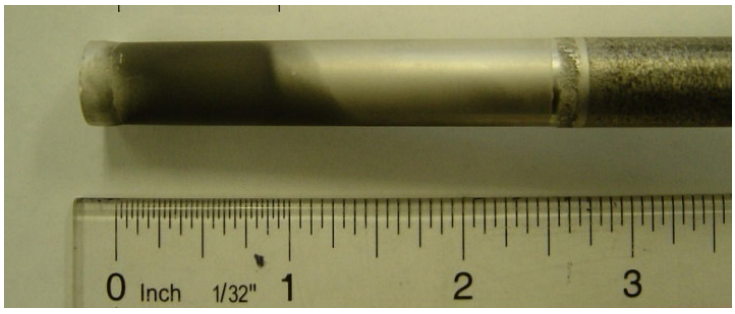

Figure 7.4. Image of the membrane AA-5 after use in WGS experiments.

The low H_2O/CO ratio of 1.1 allowed for carbon formation to gradually occur on the membrane surface. The deposition of carbon reduced the membrane permeance over time by blocking the Pd-surface for H_2 permeation, resulting in the gradual reduction of H_2 recovery seen in Figure 7.2, as well as the incremental decreases in the Sieverts' law permeance shown in Figure 7.3. The carbon balances for the reaction experiments were all within 4% of unity, and any weight gain by the catalyst due to coking was undetectable, it was therefore unlikely that any significant amount of coke was deposited on the catalyst. Furthermore, the four PBR experiments shown in Figure 7.1 had constant CO conversion over time suggesting that there was no loss of catalytic activity due to coking.

While it is generally known that the iron-chrome oxide catalyst is resistant to coke formation under WGS conditions (Newsome, 1980), there is some literature evidence that the Pd-surface has a propensity towards coke formation in the presence of CO by equation **7.7** (Li *et al.,* 2007b; 2008b). Since it was unlikely that the activity of the catalyst was decreased by coking, the gradual decline in CO conversion observed in all four CMR experiments was probably the result of lower H_2 removal, and therefore a lesser shift in the WGS reaction.

$$\mathbf{2CO \rightarrow C(s) + CO_2} \qquad \mathbf{7.7}$$

A further set of WGS CMR experiments was conducted with the membrane AA-6 over the temperature range of 350 - 500℃ and with H_2O/CO ratios of 1.6 and 2.6. Higher H_2O/CO ratios were utilized in an attempt to avoid coke formation on the membrane surface. The results of all the experiments in terms of CO conversion and H_2 recovery versus temperature are shown in Figure 7.5[a] and [b] respectively. The results in Figure 7.5[a] are also overlaid with the equilibrium conversion at the experimental conditions and the 1-D simulation results from the WGS CMR model (described in Chapter 5, and by Augustine *et al.,* 2011). The results in Figure 7.5[b] are also overlaid with the 1-D simulation results. The parameters of the 1-D simulation are listed in Table 7.2.

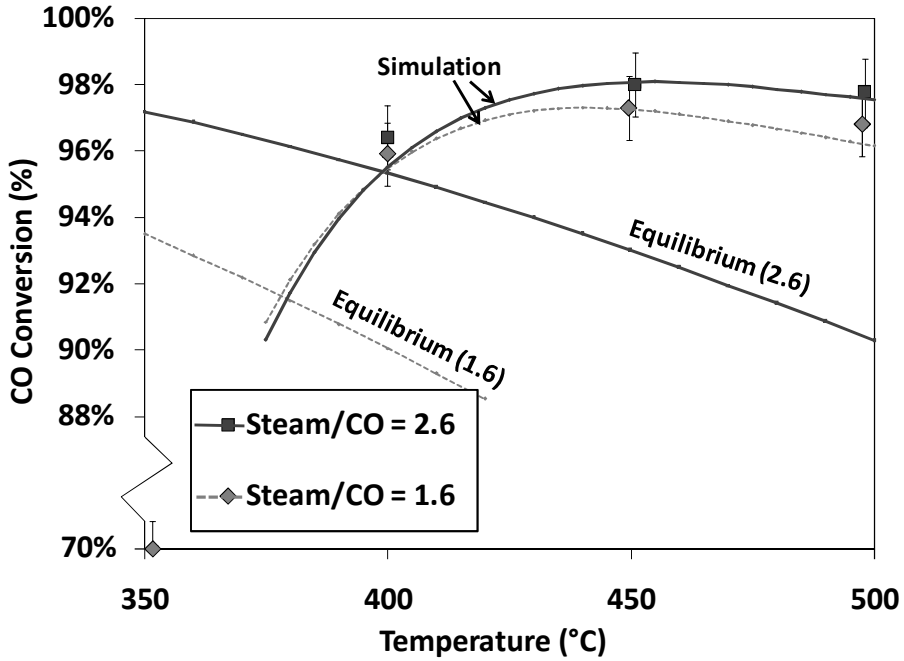

[a]

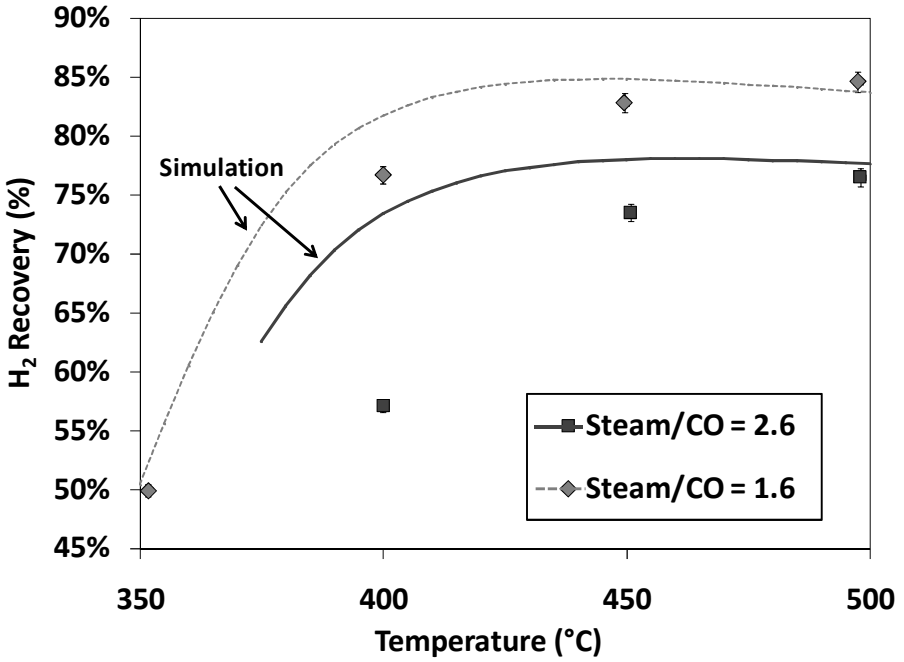

[b]

Figure 7.5. CO conversion [a] and H_2 recovery [b] as a function of temperature for a constant CO feed rate of 7.95 mmol/min (Membrane: AA-6, 14.4 atma, ◊: H_2O/CO = 1.6, $GHSV_{STP}$ = 2,100 h^{-1}, □: H_2O/CO = 2.6, $GHSV_{STP}$ = 2,900 h^{-1}).

At the temperatures of 350 and 400℃, with a H_2O/CO ratio of 1.6, the CO conversion and the H_2 recovery decreased gradually over the testing period. Figure 7.6[a] shows the CO conversion and the H_2 recovery over time for the experiment performed at 400℃. The gradual decline observed was similar to that seen in the experiments performed previously with a steam to CO ratio of approximately 1.1, indicating that similar coke formation was probably occurring. At the temperatures of 450 and 500℃ the reactions reached a steady state, with very little change after the first hour of testing. Figure 7.6[b] shows the CO conversion and the H_2 recovery over time for the experiment performed at 450℃. At the highest steam to CO ratio of 2.6, no evidence of coke formation was observed at any temperature tested (400, 450, and 500℃).

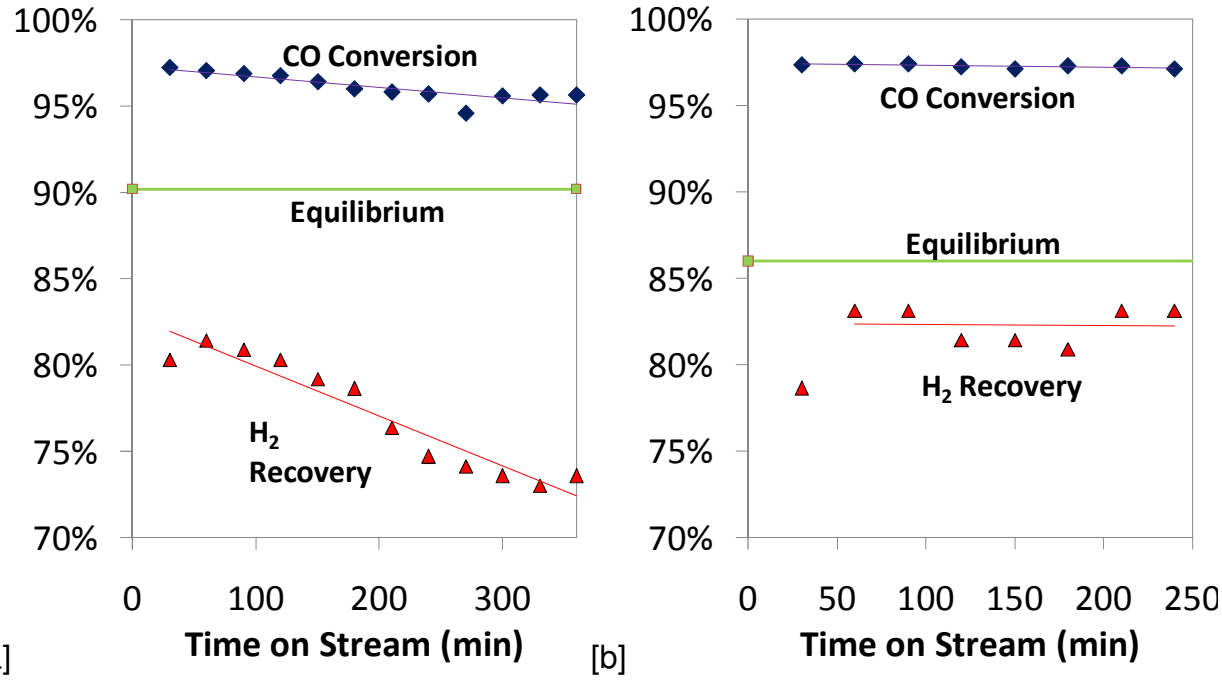

Figure 7.6. CO conversion and H_2 recovery versus time on stream [a] 400℃ [b] 450℃ (Membrane: AA-6, 14.4 atma, H_2O/CO = 1.6, and $GHSV_{STP}$ = 2,100 h^{-1}).

7.3.1. Effect of H_2O/CO ratio

When comparing the CO conversion from Figure 7.1 and Figure 7.5[a] for a set temperature (400 or 450℃), it was clear that a higher H_2O/CO ratio led to a higher CO

conversion for all three sets of experiments, as expected and consistent with WGS PBR cases (Damle *et al.,* 2008; Bi *et al.,* 2009). The equilibrium conversion for the H_2O/CO ratio of 2.6 was significantly higher than for the H_2O/CO ratio of 1.6 over the whole temperature range shown in Figure 7.5[a]. The H_2 recovery was dependent on the membrane permeance and the CO conversion, while the CO conversion increased as the H_2O/CO ratio increased. However, when the H_2O/CO ratio was too high (such as with excess steam), the dilution of H_2 caused the H_2 recovery to decrease, as seen when comparing the H_2 recoveries at the same temperature in Figure 7.5[b]. The best H_2 recovery, observed at the H_2O/CO ratio of 1.6 and 450℃, resulted from the high CO conversion of 97.3% in addition to lower dilution by the steam. A lower H_2O/CO ratio was therefore preferable for high H_2 recovery, but limited by the deposition of coke which occurred at or below the H_2O/CO ratio of 1.6.

7.3.2. Effect of temperature

Figure 7.5[a] shows the CO conversion profile as a function of temperature for experiments conducted with H_2O/CO ratios of 1.6 and 2.6. CO conversions of 97.3 and 98.2% were observed for H_2O/CO ratios of 1.6 and 2.6 respectively, both at 450℃. At temperatures of 400℃ and above the CO conversion in all experiments exceeded the equilibrium conversion, with greater advantage being gained under conditions where the equilibrium conversion was much lower, such as at high temperatures and low H_2O/CO ratios. At 350℃ the CO conversion was 68.4%, significantly less than the equilibrium conversion, indicating that the system was reaction rate limited at that temperature; 350℃ was below the optimal temperature range of the iron-chrome oxide catalyst.

Several factors influenced the relationship between the CO conversion and the temperature in the WGS CMR. At lower temperatures the equilibrium constant was higher but the reaction rate was lower, and the permeance of the Pd-membrane was lower. At higher temperatures the reaction rate was higher and the permeance of the Pd-membrane was also higher, but the equilibrium constant was lower. Since H_2 recovery was not 100%, the equilibrium expression still applied and limited the conversion to what could be called the dynamic equilibrium (Augustine *et al.,* 2011; Basile *et al.*, 2001; Damle *et al.*, 2008). The dynamic equilibrium conversion could be

calculated by evaluating equation **7.5** with the quadratic formula. The presence of the opposing factors (reaction rate, membrane permeance, and equilibrium constant) suggested the possibility of a maximum in the CO conversion at some intermediate temperature as was observed in Figure 7.5[a].

Figure 7.5[b] shows the H_2 recovery as a function of temperature for both sets of experiments conducted with H_2O/CO ratios of 1.6 and 2.6. The H_2 recovery increased with increasing temperature up to 500°C (with higher H_2 recovery corresponding to a H_2O/CO ratio of 1.6) because the permeance of the Pd-membrane increased with temperature. Since the H_2 recovery was dependent on the H_2 production via the WGS reaction, it was possible that there would be a temperature-dependent maximum in H_2 recovery as well, but not necessarily at the same temperature as the maximum in CO conversion; this result occurred in the 1-D simulation results in Figure 7.5[b]. A maximum in the H_2 recovery versus temperature was not observed in the experimental data (Figure 7.5[b]), possibly because experiments were not conducted at a high enough temperature (greater than 500°C) for it to be observed.

Basile *et al.* (1996b) performed a series of six WGS CMR experiments in the temperature range of 250 - 360°C and observed a temperature dependent maximum in the CO conversion of approximately 93% at 323°C, 1 atma, a H_2O/CO ratio of 0.96, and GHSV's of 210 and 420 h^{-1}, utilizing an alumina supported 0.2 µm Pd-membrane. They attributed the CO conversion maximum to a compromise between the kinetic reaction rate and the thermodynamic equilibrium of the reaction. Barbieri *et al.* (2008) also observed a temperature dependent maximum in the CO conversion of approximately 94% at 300°C, 6.0 atma, a H_2O/CO ratio of 1.0, and a $GHSV_{STP}$ of 2,070 h^{-1}, utilizing a 60 µm unsupported Pd/Ag foil. They conducted three WGS CMR experiments at each of three different GHSV's in the temperature range of 280 - 320°C and observed maxima for each set of data at 300°C. Both Basile *et al.* (1996b) and Barbieri *et al.* (2008) utilized a low-temperature shift copper-zinc oxide catalyst. Bi *et al.* (2009) conducted a series of experiments at four different temperatures in the range of 325 - 400°C, 12.0 atma, a H_2O/CO ratio of 3.0, and a $GHSV_{STP}$ of 6,300 h^{-1}, with a ceramic supported 1.4 µm Pd-membrane, and utilizing a custom catalyst with much higher

activity at intermediate temperatures. They reported a maximum CO conversion of 98.0% at 375°C, 1.3% higher than at 400°C, which they attributed to a balance between the H_2 permeance of the membrane increasing with temperature and the methane formation side-reaction which occurred on their catalyst at temperatures exceeding 375°C. Additionally, although Basile *et al.* (1996b) utilized an ultra-thin membrane with the low H_2/N_2 ideal selectivity of 8, which could have influenced their results, Barbieri *et al.* (2008) employed a much thicker membrane with a nearly infinite ideal selectivity and obtained a very similar maximum CO conversion temperature. The results of the three studies (Basile *et al.,* 1996b; Barbieri *et al.,* 2008; Bi *et al.,* 2009) in terms of CO conversion as a function of temperature are compared to our results in Figure 7.7.

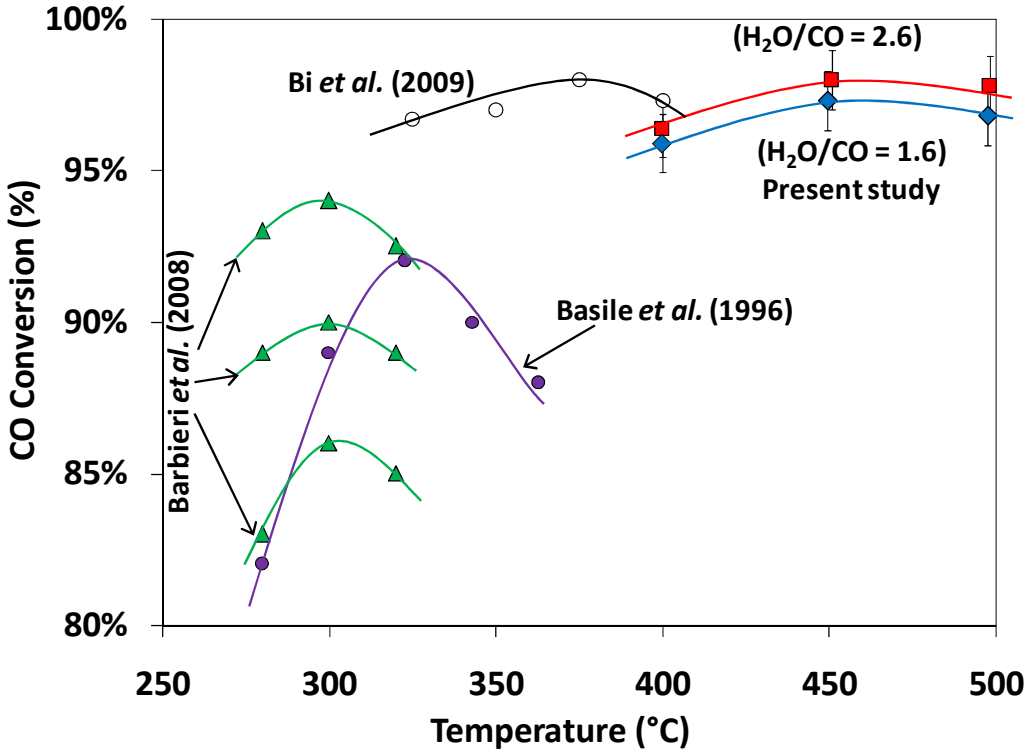

Figure 7.7. CO conversion as a function of temperature for WGS CMR results from several studies.

As seen in Figure 7.7, the conditions and catalyst utilized in the present study resulted in a significantly higher optimal temperature than those found in the literature. The

temperature of the maximum CO conversion correlated to the optimal operating range of the catalysts used. Low-temperature shift catalyst was used by Barbieri *et al.* (2008) and Basile *et al.* (2006) and their results showed optimal temperatures of 300 – 325°C while the present study utilized a high-temperature shift catalyst and observed an optimal temperature of approximately 450°C. Bi *et al.* (2009) suggested that their custom catalyst was superior to iron-chrome oxide over the whole temperature range, but observed lower H_2 yeild (H_2 generated from the WGS devided by the CO feed rate) at temperatures exceeding 400°C due to CH_4 formation. Two unrelated studies (Uemiya *et al.,* 1991a; Ma and Lund, 2003) both concluded that the WGS CMR system utilizing a Pd membrane thinner than 10 μm and with temperatures less than 400°C would be kinetically limited so that no advantage would be gained by the use of a better membrane. While the WGS reaction was traditionally conducted at low temperatures, with a low GHSV, to take advantage of the equilibrium constant, the CMR allowed for the use of a much higher temperature, to take advantage of the higher catalytic activity for greater throughput. The advantages of the WGS CMR operated at high pressure and high temperature have not been previously elucidated in the literature. Finally, it should be also pointed out that operating at a higher temperature would be preferable in terms of energy efficiency in the IGCC process as the WGS operating temperature would be closer to the coal gasifier effluent temperature.

7.3.3. Effect of reaction pressure

Experiments were conducted with a simulated syngas mixture (19% CO, 18% H_2, 8% CO_2, and 55% H_2O), at 400°C, and a $GHSV_{STP}$ of 4,500 h^{-1}, over a range of pressures, utilizing the membranes AA-24R and AA-30. The CO conversion and H_2 recovery for the set of experiments were plotted versus pressure in Figure 7.8. Since the membranes AA-24R and AA-30 had nearly identical permeance of 28.5 and 28.6 m^3/m^2-h-$atm^{0.5}$ respectively at 400°C the results were compared as a single set of data. The 1-D simulation (with the parameters listed in Table 7.2) was utilized to generate the curves overlaid in the figure.

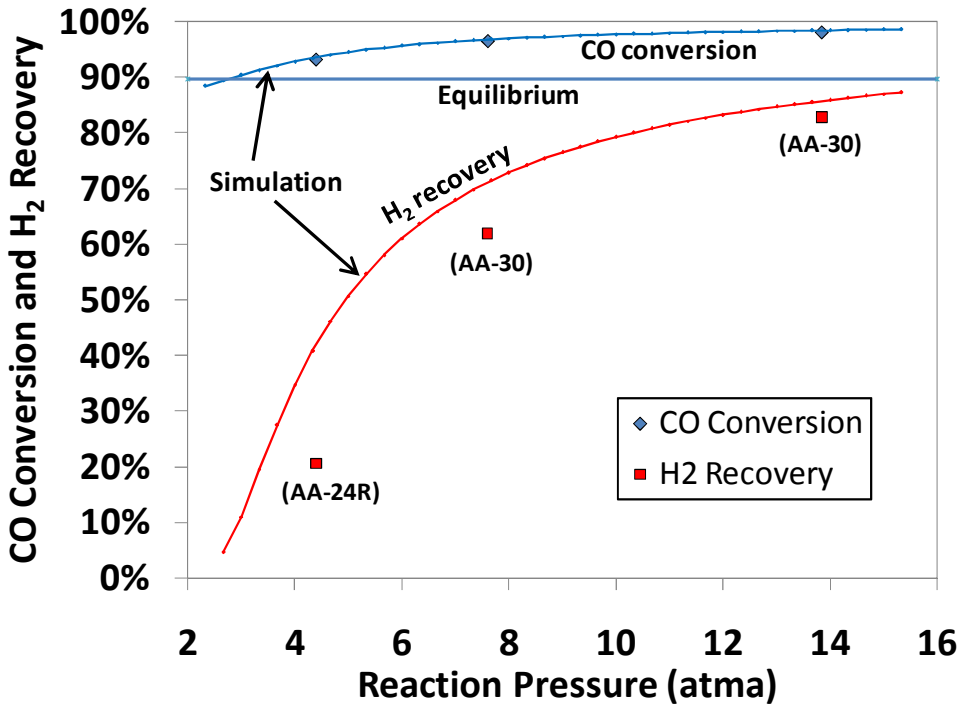

Figure 7.8. CO conversion and H_2 recovery versus reaction pressure (Membranes: AA-24R and AA-30; 19% CO, 18% H_2, 8% CO_2, and 55% H_2O; 400°C; 4,500 h^{-1}).

At total pressures in excess of 2.8 atma H_2 was recovered from the system and the CO conversion was in excess of the thermodynamic equilibrium. The H_2 recovery asymptotically approached 100% with increasing pressure, reaching 83% at a pressure of 13.9 atma. The CO conversion also asymptotically approached 100% from the equilibrium conversion of 89.6%. Since the CO conversion was in excess of equilibrium for all of the experiments, there was probably no reaction rate limitation. At the temperature of 400°C and moderate feed space velocity, the system was limited by the gas boundary layer resistance and the H_2 permeance of the supported membrane. As the reaction pressure was increased, the driving force for H_2 separation was increased, resulting in higher H_2 recovery. Additionally, with the higher reaction pressure, the residence time, τ, calculated by equation **6.16**, was increased from approximately 1.4 sec at 4.4 atma to 4.5 sec at 13.9 atma, allowing higher H_2 recovery due to the longer contact time between the gas mixture and the membrane.

The use of the high reaction pressure also negated the use of a sweep gas, allowing for the direct production of high purity H_2 at significant economic advantage (Criscuoli *et al.*, 2001; Damle *et al.*, 2008).

7.3.4. Effect of feed space velocity

A series of WGS CMR experiments were conducted with the simulated syngas mixture composed of 23% CO, 22% H_2, 10% CO_2, and 45% H_2O, at 14.4 atma, and 350, 400, and 450°C, and GHSV's of 1,100 – 5,400 h^{-1}, utilizing the membrane AA-8R. A plot of CO conversion versus GHSV for the experiments with temperatures of 400 and 450°C, overlaid with the 1-D simulation results, is shown in Figure 7.9[a]. The parameters used in the 1-D simulation are listed in Table 7.2. A plot of H_2 recovery versus GHSV for those same experiments is shown in Figure 7.9[b]. A plot of retentate gas composition on a dry basis versus time for three of the experiments performed at 400°C with GHSV's of 1,100, 3,400, and 5,400 h^{-1} is shown in Figure 7.9[c].

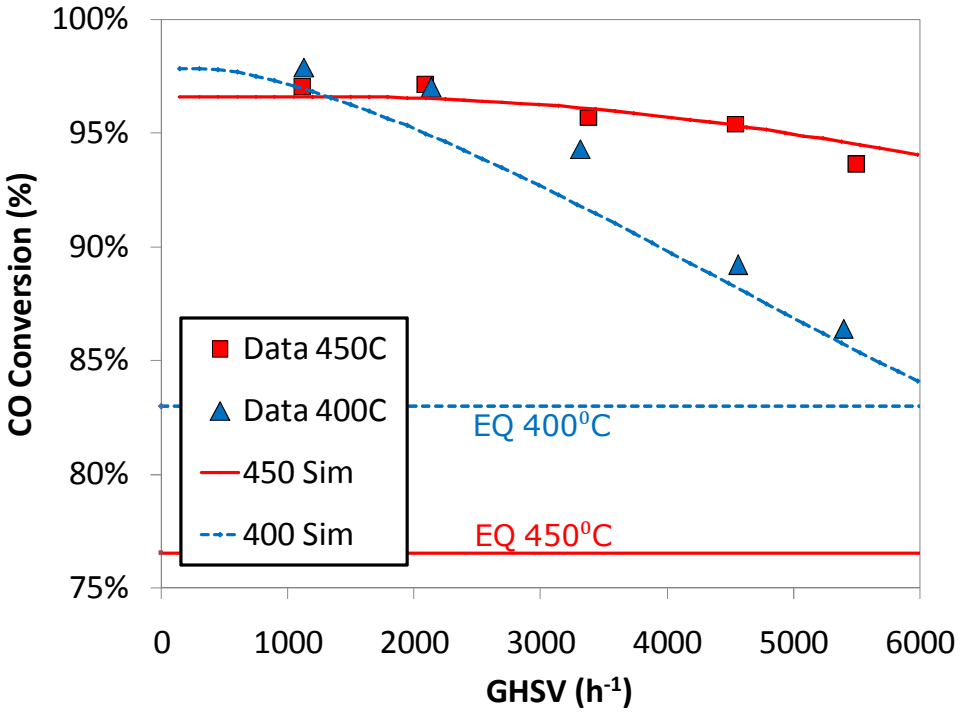

[a]

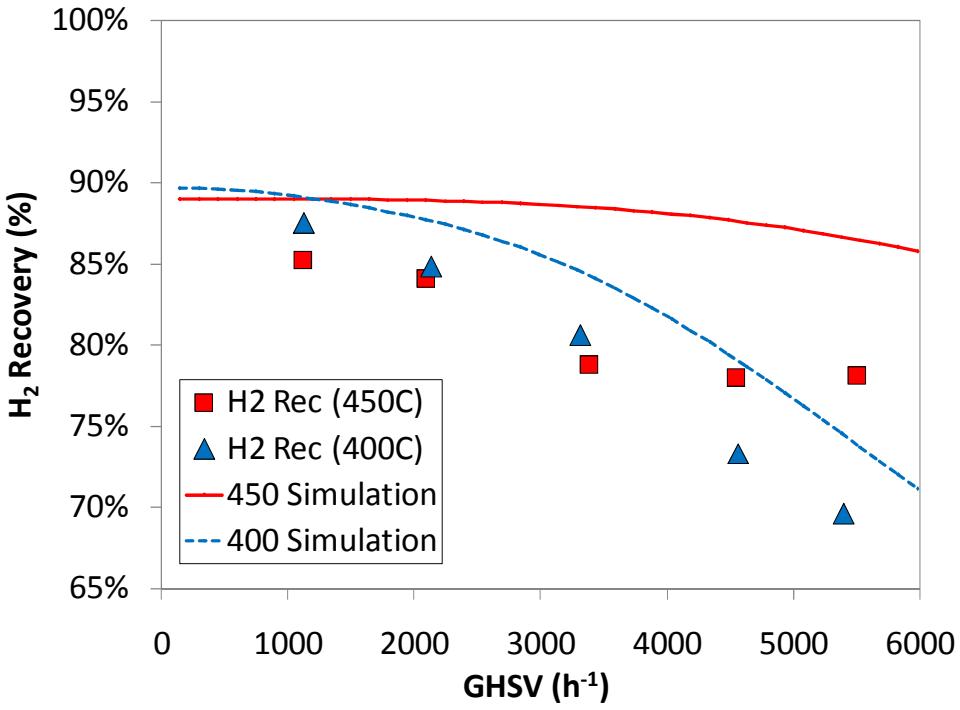

[b]

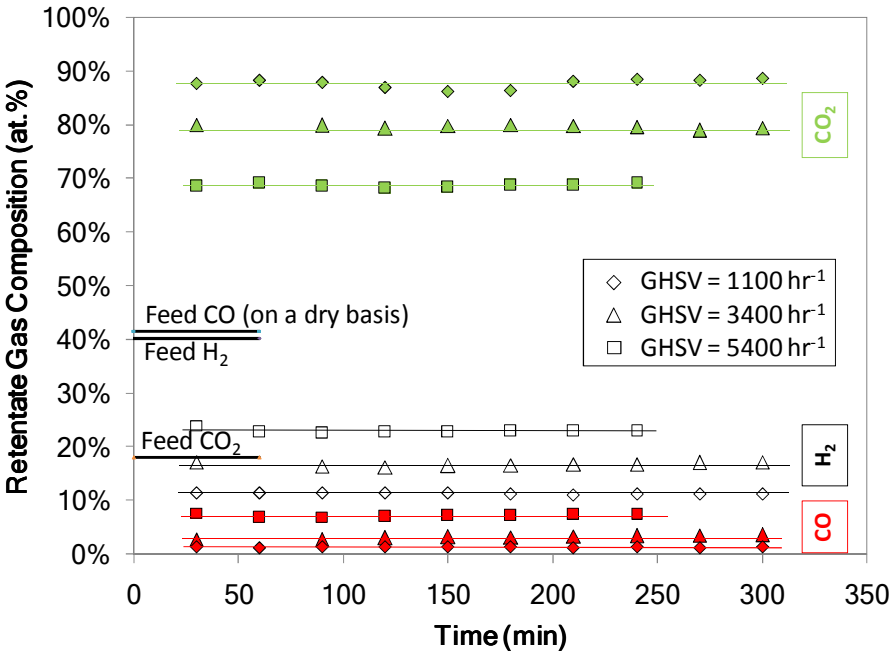

[c]

Figure 7.9 [a] CO conversion versus $GHSV_{STP}$ [b] H_2 recovery versus $GHSV_{STP}$ [c] Retentate composition (dry basis) versus time for three experiments at 400℃ (Membrane: AA-8R, Feed: 22.7% CO, 22.0% H_2, 9.9% CO_2, 45.4% H_2O, 14.4 atma).

For GHSV's below approximately 2,200 h^{-1} the CO conversion results at 400°C appeared constant, at higher GHSV's (3,400 – 5,400 h^{-1}) the CO conversion decreased in a linear fashion. At 400°C and a $GHSV_{STP}$ of 1,100 h^{-1} a CO conversion of 97.9% (15% in excess of equilibrium) was achieved with a hydrogen recovery of 87.5%. At 450°C the CO conversion appeared to be constant at GHSV's below approximately 4,500 h^{-1}, then declined at the highest GHSV (5,400 h^{-1}). The maximum conversion achieved at 450°C was 97.0% (21% in excess of equilibrium) with a hydrogen recovery of 85.2% at a $GHSV_{STP}$ of 1,100 h^{-1}. The H_2 recovery versus GHSV data, Figure 7.9[b], displayed the same crossing as that was observed in the CO conversion versus GHSV data, Figure 7.9[a], but occurring at a slightly higher GHSV (approximately between 2,100 – 3,400 h^{-1}). Oddly however, at high GHSV and 450°C the H_2 recovery did not appear to decrease linearly, instead it seemed to remain level at approximately 78% up to a $GHSV_{STP}$ of 5,400 h^{-1}. The steady state behavior of the reactor was evident from the plot of retentate composition over time in Figure 7.9[c]. Measurements of the retentate composition, the retentate flow, and the permeate H_2 flow all varied by less than 5% over the course of 5 hours.

At GHSV's below approximately 1,700 h^{-1} a higher CO conversion was achieved at the lower temperature (400°C) while at GHSV's above approximately 1,700 h^{-1}, higher CO conversion was achieved at the higher temperature (450°C). The reason for the crossing of these two curves, between approximately 1,100 – 2,100 h^{-1}, was the balance of temperature dependent factors which influenced the CO conversion in the WGS CMR: kinetic reaction rate, H_2 permeance of the membrane, gas phase mass transfer, and the thermodynamic equilibrium. At a low GHSV the CO conversion was limited by the driving force of H_2 across the membrane, such that the system was very close to the dynamic equilibrium as defined by equation **7.5** (Iyoha *et al.,* 2007a). The equilibrium constant, which was higher at 400°C, allowed for a higher CO conversion. At a high GHSV the CO conversion was limited by the kinetic reaction rate, the membrane permeance, and the gas phase mass transfer resistance, with both the membrane permeance and kinetic reaction rate being higher at higher temperatures. Some qualitative discussion can be made about these factors based on the data presented. Since the H_2 recoveries were very high at low GHSV's (below approximately 1,700 h^{-1} at

400°C and below approximately 4,500 h^{-1} at 450°C) the limiting factor was most likely the driving force of H_2 across the membrane; higher conversion being prevented by a minimal 1 atma of H_2 pressure in the reaction mixture. At the lowest GHSV's, if vacuum was applied or a sweep gas admitted to the permeate side, further H_2 would be removed/recovered and CO conversions of very close to 100% would be observed. The experiments performed at high GHSV's (above 1,700 h^{-1} at 400°C and above 4,500 h^{-1} at 450°C) were probably limited by the gas phase mass transfer resistance since the experiments exceeded equilibrium conversion, but still had H_2 recoveries of significantly less than 90%.

It should be pointed out that even though the H_2 recovery was lower at high GHSV, the H_2 flux through the membrane was higher; at 450°C the H_2 flux was 2.4 and 10.5 m^3/m^2-h at 1,100 and 5,400 h^{-1} respectively. Process modeling software should be utilized during the design phase of an IGCC plant to determine the optimal GHSV considering the trade-off between H_2 recovery and H_2 flux. In order to achieve a higher H_2 recovery while still achieving a high H_2 flux at high throughput, a longer reactor should be employed with a higher flow velocity such that the Reynolds number of the flow would be higher for an equivalent GHSV. This would result in a lower gas phase mass transfer resistance.

An anomaly was observed in the characterization of the membrane after the reaction experiment conducted at 450°C and a $GHSV_{STP}$ of 3,300 h^{-1}. The H_2 permeance of the membrane, tested immediately after the reaction was found to be 26% lower than before the experiment. The H_2 permeance was observed to slowly recover over the next 48 hours. It was possible that a short disruption in the H_2O feed pump (an air bubble potentially) caused a significantly lower H_2O/CO ratio and therefore coke formation on the membrane. The coke would then slowly be reformed by steam during the remainder of the reaction, and would slowly be converted to CH_4 after the re-introduction of pure H_2. Evidence of methane presence was not sought after the reaction, and no coke was observed on the membrane after the series of reactions were completed. It seems likely that the lower permeance of the membrane during that particular reaction experiment

caused the apparent discontinuity in the experimental H_2 recovery data at 450°C and a $GHSV_{STP}$ of 2,200 – 3,400 h^{-1} in Figure 7.9[b].

The high mol fraction of CO_2 in the retentate stream, already at the elevated pressure of 14.4 atma makes the WGS CMR very attractive for the potential IGCC process with CO_2 sequestration. The ability of the WGS CMR to deliver a CO_2 enriched stream, already at elevated pressure has the potential to reduce the compression cost for sequestration by over 50% (2.4% net power savings over acid gas removal followed by compression {Klara *et al.,* 2007; Gray *et al.,* 2009}).

The simulation results correlated well with the CO conversion results at all temperatures and GHSV's in Figure 7.9[a], differing by only as little as 1.7% at 450°C and high GHSV. There was, however, a discrepancy of up to 13% with the two sets of H_2 recovery results in Figure 7.9[b]. The discrepancy between the H_2 recovery simulation and experimental data was the greatest at high GHSV's. The discrepancy was not so great (approximately 4%) at the lowest GHSV's, but still significant. Since the aspect ratio (reactor length divided by characteristic width) was only slightly greater than ten, the radial concentration gradient may have had an impact on the H_2 recovery (Tiemersma *et al.,* 2006). Unfortunately the only way to correct that error would be to utilize a 2-D model. Significantly, the qualitative comparison of the model to the experimental data showed the same trend with regard to each aspect of the CMR operating parameters: temperature, pressure, and feed rate.

At a $GHSV_{STP}$ of 4,500 h^{-1} an additional experiment was conducted at a temperature of 350°C. Further experiments at 350°C were not conducted due to the declining selectivity of the membrane. The results of the three experiments with a $GHSV_{STP}$ of 4,500 h^{-1} as well as the results of the 1-D simulation (parameters listed in Table 7.2) for those same conditions are shown in Figure 7.10.

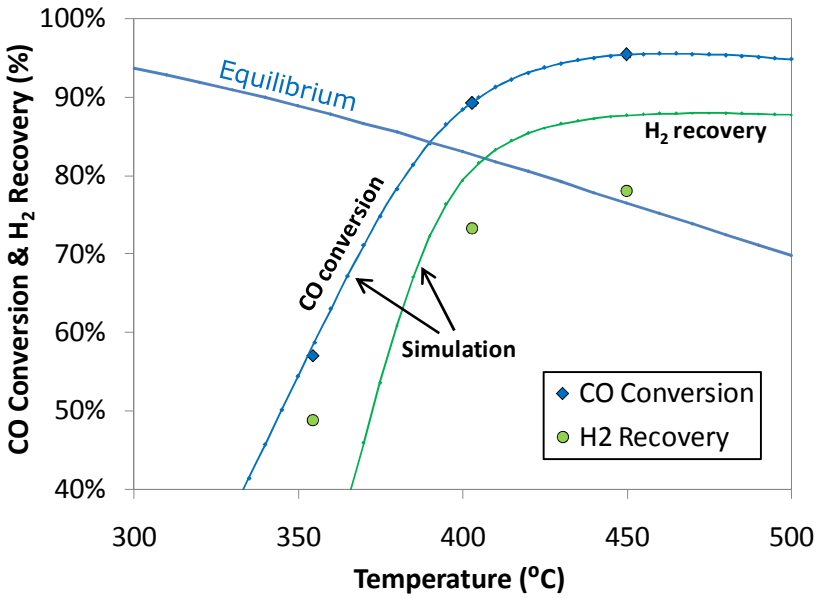

Figure 7.10. CO conversion and H_2 recovery versus temperature (Membrane: AA-8R, Feed: 22.7% CO, 22.0% H_2, 9.9% CO_2, 45.4% H_2O, 14.4 atma, $GHSV_{STP}$ = 4,500 h^{-1}).

The CO conversion of 57.1% at 350℃ was significantly below the equilibrium conversion due to the low reaction rate at that temperature. At 400 and 450℃, however, the conversion increased to 89.2 and 95.4%, 6.2 and 18.9% in excess of the equilibrium conversion respectively. The simulation results correlated well with the experimental results at 400 and 450℃ but deviated by as much as 20% at 350℃ in terms of H_2 recovery. The simulation results indicated the likelihood of a maximum for both CO conversion and H_2 recovery with regard to the temperature at approximately 460 and 470℃ respectively, although neither maximum was observed experimentally (as experiments in this series were not conducted above 450℃).

The H_2 recovery of 49% was considerably lower at 350℃ since much less H_2 was produced. The definition of experimental H_2 recovery, equation **7.2**, considered both the H_2 and the CO in the feed to be potential sources of H_2, so that if CO conversion was low, H_2 recovery must also be low. Additionally, a higher partial pressure of H_2 remained in the retentate at 350℃ (2.3 atma) than for 400 or 450℃ (1.8 and 1.6 atma respectively) suggesting that the permeance of the membrane was considerably lower

at 350°C. As was discussed in Chapter 6, reversible adsorption by the WGS species significantly lowered the membrane permeance at temperatures of less than 400°C, accentuating the need to operate at higher temperatures.

7.4. Conclusions

The advantages of the WGS CMR incorporating a supported Pd-membrane and operating at high temperatures and high pressures have been investigated. Utilizing both a CO/steam feed and a synthetic syngas feed, CO conversions as high as 98% were achieved while simultaneously recovering up to 88% of the H_2 at the relatively high temperature of 450°C.

A lower H_2O/CO ratio of 1.6 was desirable for the sake of higher H_2 recovery; however, gradual coke formation occurred on the membrane surface, lowering the H_2 recovery over time for many experiments with H_2O/CO ratios of less than 2.6. The effect of the reaction pressure was investigated and it was found that both CO conversion and H_2 recovery were strongly dependent on reaction pressure in the range of 3 - 10 atma, and reaching 98 and 83% respectively at 13.9 atma. The effect of the operating temperature on the CO conversion was investigated and it was found that the optimal operating temperature for high CO conversion was dependent on the GHSV and the activity range of the catalyst, high GHSV and a high-temperature shift catalyst leading to a high optimal operating temperature. The effect of the feed rate on the CO conversion was also considered with a synthetic syngas feed. While at the lower temperature of 400°C a high CO conversion could only be achieved at the low $GHSV_{STP}$ of 1,100 h^{-1} due to the combination of low reaction rate and gas boundary layer mass transfer resistance. At the higher temperature of 450°C, a CO conversion as high as 94% was achieved with a $GHSV_{STP}$ of 5,400 h^{-1}, indicating that with a higher operating temperature, significantly higher throughput could be achieved with a minimal reduction in CO conversion.

8. COKE FORMATION IN THE WGS CMR

8.1. Introduction

While coke formation is not typically a concern in the WGS PBR due to the high H_2O/CO ratios employed as well as the coking resistance of both iron-chrome oxide and copper-zinc oxide catalysts (Newsome, 1980), coke formation can be a significant problem in the WGS Pd-CMR since a lower H_2O/CO ratio is preferred (as discussed in Chapter 7, Section 7.3.1) and since the Pd-surface most likely has some catalytic propensity for coke formation (Li *et al.,* 2007b; 2008b). Coke formation can block active sites on the Pd-surface resulting in significant H_2 permeance inhibition. Additionally, several studies have suggested that carbon may dissolve in the Pd-lattice to some extent, causing increased strain and therefore leak growth in Pd-membranes (Selman *et al.,* 1970; Li *et al.,* 2007b).

The objective of this chapter was therefore to investigate the set of conditions which favored coking in order to develop a better understanding of the formation mechanisms occurring in the WGS CMR system.

8.2. Background

8.2.1. Thermodynamics of coke formation

Two potential routes of coke formation may occur under WGS conditions; CO cracking (equation **8.1**, also known as the Boudouard reaction, also known as CO disproportionation) and CO reduction by H_2 (equation **8.2**).

$$\mathbf{2CO \rightarrow C(s) + CO_2} \qquad \Delta H = \text{-125.2 kJ/mol} \qquad \mathbf{8.1}$$

$$\mathbf{CO + H_2 \rightarrow C(s) + H_2O} \qquad \Delta H = \text{-84.0 kJ/mol} \qquad \mathbf{8.2}$$

The equilibrium expressions for these reactions are given by equations **8.3** and **8.4** respectively.

$$K_1 = \frac{P_{CO2}}{P_{CO}^2} \qquad \mathbf{8.3}$$

$$K_2 = \frac{P_{H2O}}{P_{H_2} P_{CO}} \qquad \textbf{8.4}$$

where P_i [atma] is the partial pressure of each gas species, and K_1 [atm^{-1}] and K_2 [atm^{-1}] are the equilibrium constants relating to equations **8.1** and **8.2** respectively. Note that the equations were simplified by assuming the activity of solid carbon to be one.

Carbon formation is thermodynamically favored by these reactions for a given gas composition when either of the ratios P_{CO2}/P^2_{CO} or P_{H2O}/P_{H2}-P_{CO} exceed their respective equilibrium constants. The equilibrium constants can be calculated by their relationship with the change in Gibbs free energy of the reaction, given by equation **8.5**.

$$K_x = e^{-\Delta G_x / RT} \qquad \textbf{8.5}$$

where ΔG_x [kJ/mol] is the change in Gibbs free energy for reaction x and can be found listed for each species in Appendix A.

The structure of equations **8.3** and **8.4** indicates the relationship between the gas composition and the propensity towards coke formation. Coke formation will be favored by higher partial pressures of CO and/or H_2. Coke formation will be slowed or reversed by increased partial pressure of H_2O (due to steam reforming of coke) or CO_2 (due to dry reforming of coke). Since the Gibbs free energies for reactions **8.1** and **8.2** (-52.7 and -39.0 kJ/mol respectively) at 400℃ were negative, coke formation will be more thermodynamically favored at lower temperatures.

It should be noted that when equation **8.2** is subtracted from **8.1** (or vice versa) the result is the WGS reaction, therefore $\Delta G_{WGS} = \Delta G_1 - \Delta G_2$ and $K_{WGS} = K_1/K_2$, and for a system at WGS equilibrium, both reactions **8.1** and **8.2** will proceed in the same direction. When a given gas composition is not at WGS equilibrium the potential exists that coke could be simultaneously deposited by one reaction and reformed by the other, with the net rate being dependent on which process is dominant. Jorgensen *et al.* (1995) suggested that net carbon formation should be expected if favored by equations **8.3** or **8.4**, assuming both the reforming and shift reactions had reached equilibrium, even for gas mixtures not at equilibrium (such as at the reactor inlet).

8.2.2. Kinetics of coke formation

Even when thermodynamically favored, coke does not readily form from the WGS mixture at 100 - 500℃ without the presence of a catalyst. Additionally, iron-chrome oxide and copper-zinc oxide catalysts are known to be inactive towards the coke formation reactions (Newsome, 1980). There is a significant body of literature, however, suggesting that the palladium surface is catalytically active towards coke formation (Doering *et al*., 1982; Malciejewski and Baiker, 1994; Krishnankutty and Vannice, 1995; Albers *et al.,* 2001; Li *et al.,* 2007b). Doering *et al*. (1982) first observed that the surface activity (for reversible adsorption of CO) of nanometer-sized Pd-particles supported on mica, decreased gradually over time at 200℃. They utilized core-electron-energy-loss spectroscopy to demonstrate that carbon had deposited onto the Pd surface indicating that the Pd surface was catalyzing carbon formation via equation **8.1**. Note that the surface area available from nano-meter sized particles was very large (approximately 100 m^2/g for 5 nm spherical particles) so the carbon formation rate was probably several orders of magnitude greater than that which might occur on a Pd-membrane surface. Malciejewski and Baiker (1994) prepared a zirconia supported Pd-catalyst by oxidation of a glassy $PdZr_2$ alloy and exposed it to CO in a thermoanalytical balance and monitored the effluent gas by mass spectroscopy. They observed a weight gain of 23%, occurring between 375 and 475℃ and a corresponding release of CO_2, indicating that CO disproportionation, **8.1**, was occurring. The authors further showed that coke formation from CO was detectable at a temperature as low as 101℃.

Based on the Langmuir adsorption model, the formation of coke from CO could occur via the mechanistic pathway given by equations **8.6** - **8.9**:

1) $\mathbf{CO(g) + * \leftrightarrow CO*}$ **8.6**

2) $\mathbf{CO* \leftrightarrow O* + C*}$ **8.7**

3) $\mathbf{CO* + O* \leftrightarrow CO_2*}$ **8.8**

4) $\mathbf{CO_2* \leftrightarrow CO_2(g) + *}$ **8.9**

Neurock (1999) demonstrated that the rate limiting step was Step 2 (equation **8.7**, CO dissociation) with an activation energy of 264 kJ/mol. The overall reaction rate based on

Step 2 was given by equation **8.10**. The forward rate constant, k_2 [s^{-1}], could then be estimated by equation **8.11**.

$$r_2 = k_2\theta_{CO}\theta_* - k_{-2}\theta_C\theta_O = k_2\left(\frac{1-K_4P_{CO2}/K_3K_1P_{CO}-\theta_C}{1+K_1P_{CO}+K_4P_{CO2}}\right)^2 K_1P_{CO} - k_{-2}\theta_C\frac{K_4P_{CO2}}{K_3K_1P_{CO}} \quad \textbf{8.10}$$

$$k_2 = A\mathrm{e}^{-E_A/RT} \quad \textbf{8.11}$$

where θ_i was the fractional coverage of each species (CO, CO_2, O, and C), θ_* was the fraction of unoccupied sites, K_j was the equilibrium constant for the steps 1, 3, and 4, and A [s^{-1}] was the frequency factor. The frequency factor was estimated as $9.77*10^{12}$ s^{-1} based on the vibrational frequency of the Pd-C-O bending mode (330 cm^{-1}) because the CO molecule would have to bend to mostly flat on the Pd-surface in order to reach the transition state (Alfonso *et al.,* 2006). At 400°C the forward rate constant, k_2, was $3.15*10^{-8}$ s^{-1} or 0.000114 h^{-1} which was exceedingly low, resulting in approximately 50% surface coverage of carbon after 4,400 hours.

Given that the several literature studies discussed above have shown coke formation at even lower temperatures, there is probably a further catalytic aspect to the coke formation that is yet uninvestigated such as Pd-support interaction. Johanek *et al.* (2000) demonstrated that CO disproportionation occurred on alumina supported Pd-clusters, but not on pure Pd or pure alumina samples indicating that the interface between the Pd and the support was more catalytically active than the Pd-surface. Since the Pd-clusters were approximately 6 nm in size, there was certainly several orders of magnitude more contact area between Pd-clusters and support material than would be possible for a Pd-membrane surface.

Alternatively, Rupprechter *et al.* (2004) conducted an XPS study of coke formation on Pd(111) and roughened Pd surfaces, and found that coke formation only occurred on the roughened surface and when H_2 was present, suggesting that reaction **8.2** (reduction of CO) was the dominant coke formation pathway at low temperatures (25°C). They proposed that coke formation occurred through a formyl intermediate pathway, resulting in CH_3OH and CH_X-C bond formation.

8.2.3. Solubility of carbon in palladium

Several papers have reported on the formation of a Pd/C-phase when palladium samples have been exposed to gas phase carbon species (CO, ethylene, and acetylene) and/or solid samples of graphitic carbon. Several studies are in agreement that for temperatures exceeding approximately 550°C a relatively low concentration (0.3 - 8 at%) of carbon is soluble in the palladium lattice, increasing with temperature, as shown in the phase diagram in Figure 8.1 (Siller *et al.,* 1968; Selman *et al.,* 1970; Yang *et al*., 1990; Yokoyama *et al.,* 1997; Okamoto, 2007). Additionally, several studies have reportedly synthesized a Pd/C-phase with 10 – 15 at% carbon at temperatures from 100 – 500°C depending on the source of carbon (Stachurski and Frackiewicz, 1985; Ziemecki *et al.,* 1985; 1987; Lamber *et al.,* 1990; Maciejewski and Baiker, 1994; Hsiung *et al.,* 1999; Li *et al.,* 2007b). Unfortunately, no studies have found evidence of carbon solubility in both temperature regimes or even attempted to apply the same analytical techniques to both regimes to resolve this discrepancy.

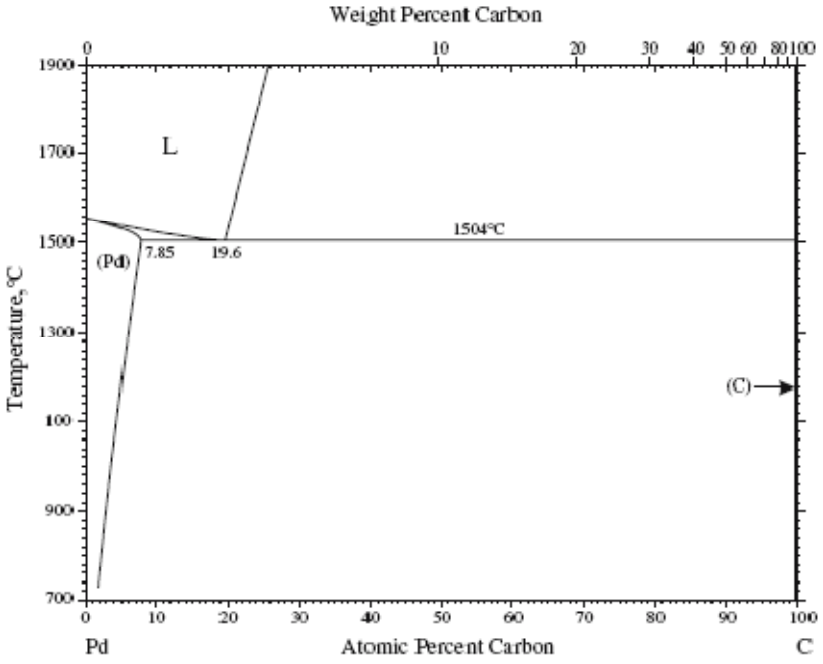

Figure 8.1. Pd/C phase diagram (Okamoto, 2007).

Additionally, the carbon atoms are mobile to some extent in the palladium lattice as demonstrated by several studies. Selman *et al.* (1970) sealed graphite into palladium capsules (with a wall thickness of 500 μm), then heated them *in vacuo* to 1,400°C; they observed 'rapid' formation of a black surface coating which they identified as carbon. Ziemecki *et al.* (1988) constructed a type of membrane reactor with a 25 μm thick palladium foil, exposing the upstream side of the membrane to ethylene and the downstream side to H_2O. They found that H_2, CO and CO_2 were generated on the downstream side of the membrane at temperatures between 150 - 375°C indicating that ethylene was catalytically decomposed on the upstream side of the membrane, carbon atoms (and possibly H atoms) diffused through the membrane, and were then catalytically reformed by H_2O on the downstream side of the membrane. Based on the flow rates of CO and CO_2 on the downstream side of the membrane, they calculated the diffusion coefficient of carbon in palladium as $5.0*10^{-12}$ cm^2/s at 310°C (approximately 6 orders of magnitude lower than that of hydrogen at the same temperature). Hsiung *et al.* (1999) challenged a commercial Johnson Matthey H_2 purifier (incorporating a 120 μm thick Pd/Ag-alloy membrane of unknown composition and operating at 375°C) with feed mixtures composed of H_2 and 5 – 60 ppmv CO, CO_2, and CH_4. When the H_2/CO and H_2/CO_2 feed mixtures were admitted they observed up to 50 ppbv of CH_4 in the purified H_2 stream after 90 minutes indicating that both the CO and CO_2 were dissociating on the membrane surface, and that carbon was diffusing through the dense alloy. When they supplied H_2/CH_4 feed mixtures to the purifier, less than 4 ppbv of CH_4 was measured in the purified H_2 stream indicating that the membrane had nearly infinite selectivity. The concentration versus time profile in their study was similar to a breakthrough curve, leading to an estimated diffusion coefficient for carbon in the Pd/Ag-alloy of $6.7*10^{-9}$ cm^2/s. Yang *et al.* (1990) used thermogravimetric analysis to simultaneously estimate the solubility and diffusivity of carbon in palladium at 550 - 700°C. They found relatively low solubility (0.32 – 0.71 at% at 550 and 700°C respectively) and diffusivity ranging from $5.0*10^{-9}$ to $6.5*10^{-8}$ cm^2/s at 550 and 700°C respectively. Yokoyama *et al.* (1998) determined the diffusivity of carbon in palladium in the high temperature regime (810 – 1,200°C) to be given by equation **8.12**.

$$D\left(\frac{cm^2}{s}\right) = D_0 e^{-E_A/RT} \qquad \textbf{8.12}$$

where D_0 = 0.1995 cm^2/s and E_A = 132.0 kJ/mol.

The diffusivity of carbon in palladium is plotted in Figure 8.2 on a logarithmic scale versus the inverse absolute temperature for the four studies in which it was estimated. The diffusivity value calculated from Ziemecki *et al.* (1988) falls surprisingly close to (approximately 1-order of magnitude greater than) that projected by Yokoyama *et al.* (1988). The large discrepancy with the diffusivity derived from Hsiung *et al*. (1999) cannot be rightly compared since the commercial membrane utilized was of an unspecified composition and could therefore have had a much different diffusivity of carbon.

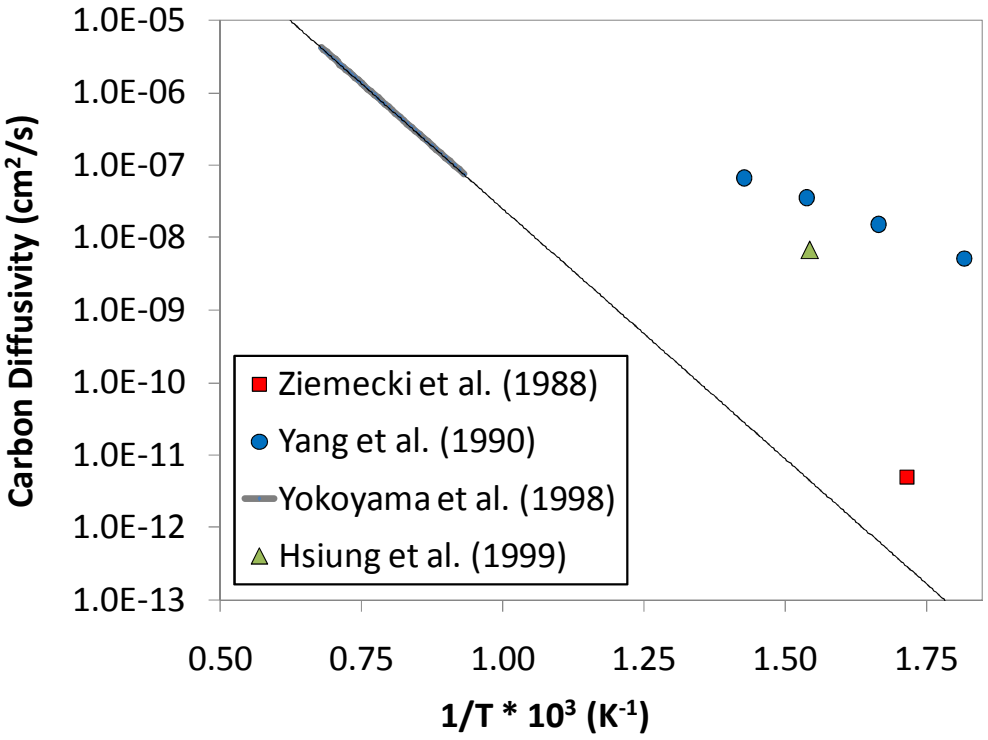

Figure 8.2. Diffusivity of carbon in palladium obtained from experimental studies.

By x-ray diffraction it has been established by several authors that the Pd/C-phase (with 10 – 15 at% C) has a lattice parameter of 3.99 Å, significantly greater than the lattice

parameter of pure Pd (3.89 Å), and close to that of the *β*-H/Pd phase (4.02 Å). Similarly to the *α/β* H/Pd phase transition, the formation of the Pd/C-phase has been associated with surface distortions and leak growth in thin Pd-layers (Selman *et al.,* 1970; Galuszka *et al.,* 1998; Li *et al.,* 2007b). Li *et al.* (2007b) reported on the formation of the Pd/C-phase (10 at% C) from exposure to 33% CO in H_2 at 500°C. They found that the deposition of carbon reduced the N_2 leak, but that after repeated cycles of carbon deposition and removal, the N_2 leak increased significantly. Galuszka *et al.* (1998) tested alumina supported Pd-membranes under methane partial oxidation and methane dry reforming conditions, and observed significant deposition of carbon on the Pd-surface at 550 – 650°C. They also observed swelling and development of porosity in the Pd-layer resulting in membrane failure which they associated with the carbon formation.

Lamber *et al.* (1990) deposited a thin film of Pd on an amorphous carbon by vacuum condensation at 50°C. They measured the Pd-lattice constant to be 2.8% higher than the literature value. Upon heating to 425°C under vacuum they observed the lattice constant change to the expected 0.390 nm and a film of carbon appear by TEM on the Pd-particle surfaces which they interpreted as the decomposition of the Pd/C-phase.

8.3. Experimental

8.3.1. Thermodynamic calculations

The propensity for carbon formation was determined by the minimization of Gibbs free energy for the system including the species CO, H_2O, CO_2, H_2, C(s), O_2, CH_4, C_2H_6, C_2H_4, C_2H_2, CH_3OH, CH_2O, CHOOH, and $CO(OH)_2$ and following the method described by Ma and Shipman (1972) and more recently by Lwin (2000). Starting conditions such as those described in Table 8.1 were utilized and the above compounds were allowed to form via any stoichiometric pathway. For conditions in which coke formation was thermodynamically favored, the final moles of carbon in the system would greater than zero, indicating net carbon formation. For conditions in which coke formation was thermodynamically disfavored, the final moles of carbon would remain equal to zero.

Table 8.1. Starting composition for the determination of coke formation.

	C(s) [mol]	CO [mol]	H_2O [mol]	CO_2 [mol]	H_2 [mol]
CO + H_2O	0	1.0	1.0	0	0
Syngas	0	1.0	1.0	0.435	0.969

The syngas described in Table 8.1 was the same dry gas composition (41.6% CO, 40.3% H_2, and 18.1% CO_2) as that used for experiments in Chapter 7, discussed in Section 7.2, prepared by Middlesex Gases & Technologies Inc (Everett, MA).

The attainment of equilibrium was also confirmed by the calculation of the change in chemical potential, $\triangle\mu$ [kJ/mol], equal to zero for each reaction: **8.1**, **8.2**, and the WGS. The Excel spreadsheet for the minimization of Gibbs free energy is included in Appendix E.

8.3.2. Pd-coupon coking

The coupons tested in this chapter were prepared according to the procedure described in Chapter 3, Section 3.3. The coupons were approximately 11 μm Pd on non-porous Hastelloy. The coupons were exposed to gas mixtures in which coke formation was thermodynamically favored. The coking conditions are summarized in Table 8.2 for all of the coupons tested. An annealed and polished Pd-foil sample was also exposed to coking conditions as detailed in Table 8.2.

Table 8.2. Coupon coking conditions (P = 14.4 atma).

Coupon	Feed	Temp (°C)	Time (h)	Catalyst
C-1, C-2	100% H_2	400	100	Quartz sand only
C-3, C-4	10% CO, 90% H_2	450	100	Quartz sand only
C-5, C-6	66% CO, 33% H_2O	400	100	Quartz sand only
C-7, C-8	66% CO, 33% H_2O	400	50	Fe/Cr-oxide
Pd-Foil	42% CO, 40% H_2, 18% CO_2	400	48	No packing material

After coking, the coupons were first analyzed by visual inspection, then by XRD to determine if any changes in the lattice constant had occurred.

8.4. Results and discussion

Evidence of coke formation was first observed in the WGS CMR due to the gradual decrease in H_2 recovery over time for several reaction experiments with the membrane AA-5 as was discussed in Chapter 7 and seen in Figure 8.3. Coke formation was not expected to be problematic since several packed-bed experiments were conducted with similar feed conditions and no indications of coke formation on the catalyst were observed. After the series of experiments was completed, the membrane was removed from the system and coke was observed on the membrane surface by visual inspection as seen in Figure 8.4.

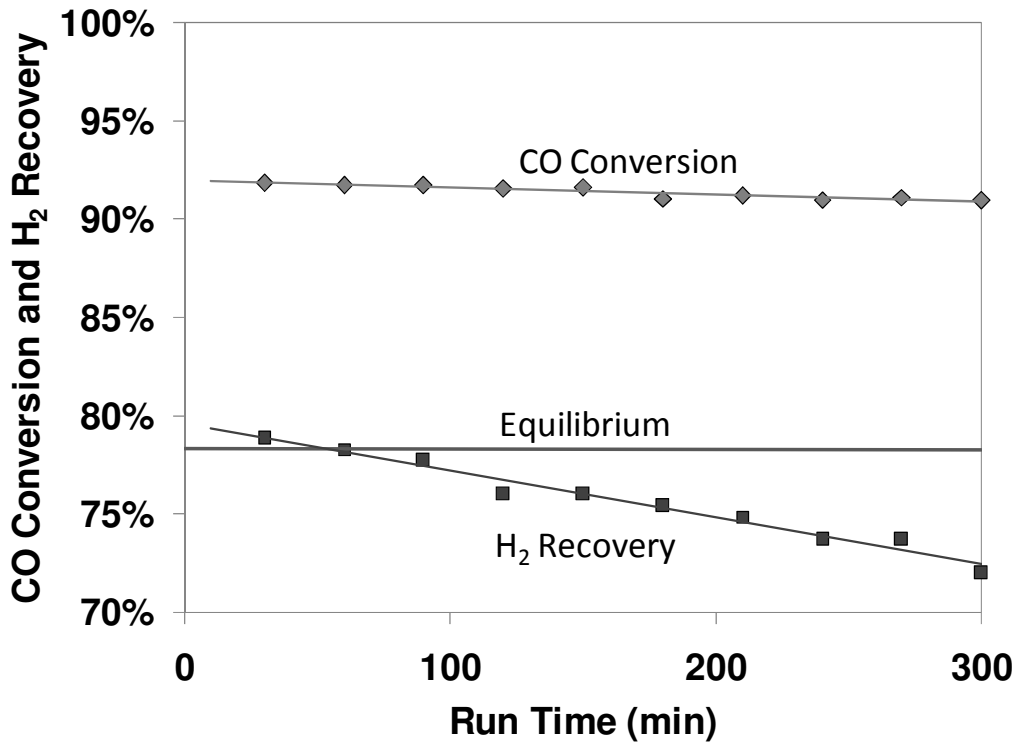

Figure 8.3. CO conversion and H_2 recovery versus time (Membrane: AA-5, 450°C, 14.4 atma, H_2O/CO = 1.1, and $GHSV_{STP}$ = 1,600 h^{-1}).

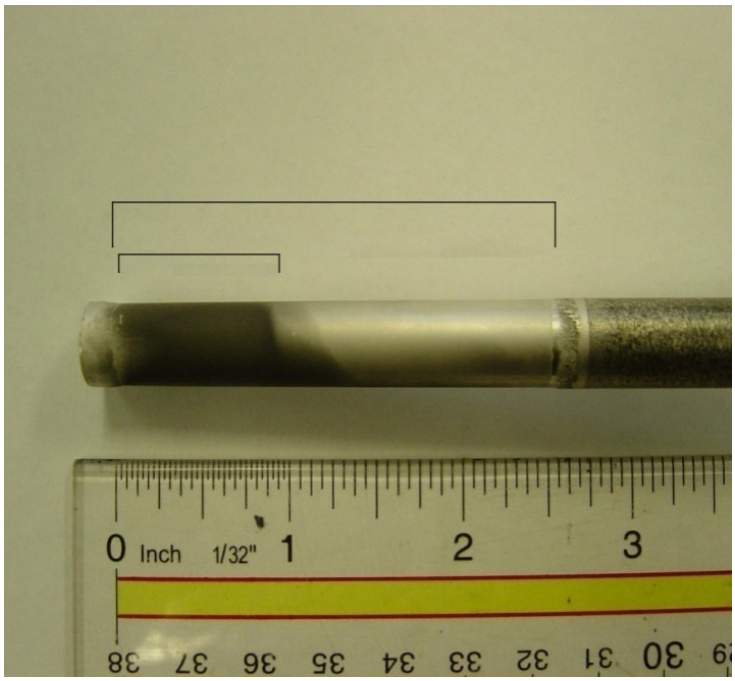

Figure 8.4. Membrane AA-5 appearance after use in WGS experiments.

Over the course of WGS CMR testing, several experiments displayed the same gradual decline as was observed in Figure 8.3 suggesting that coke formation was also occurring on the membrane surfaces in those experiments. In the WGS CMR experiments where coke formation was observed on the membrane, none was observed on the catalyst by visual inspection. In almost all of the experiments where evidence of coking was observed, CH_4 was also observed up to 1% in the dry retentate gas (CH_4 was not observed in the other cases), suggesting that reverse methane cracking, equation **8.13**, was occurring.

$$\mathbf{C(s)} + \mathbf{2H_2} \rightarrow \mathbf{CH_4} \qquad \Delta H = \text{-122 kJ/mol} \qquad \textbf{8.13}$$

In one instance, coke formation was also observed to cause a much slower decline in H_2 recovery as is shown in Figure 8.5[a]. In that case, a short-term (5 hours) experiment indicated apparently stable behavior and so a longer experiment was conducted for the purposes of leak growth measurement (to be discussed in Chapter 10), but significant reductions in H_2 recovery and CO conversion were observed. After the reaction, H_2 was

sent to the membrane at 400°C and the H_2 permeance was observed to gradually increase from 15 m^3/m^2-h-$atm^{0.5}$ to its previous level (21 m^3/m^2-h-$atm^{0.5}$) over 100 hours, as shown in Figure 8.5[b], due most likely to the gradual reduction of coke to methane by equation **8.13**.

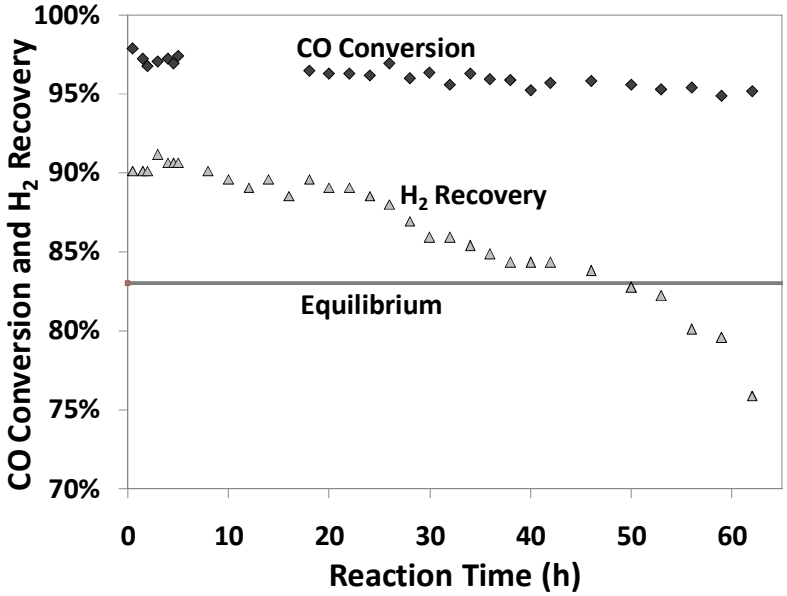

[a]

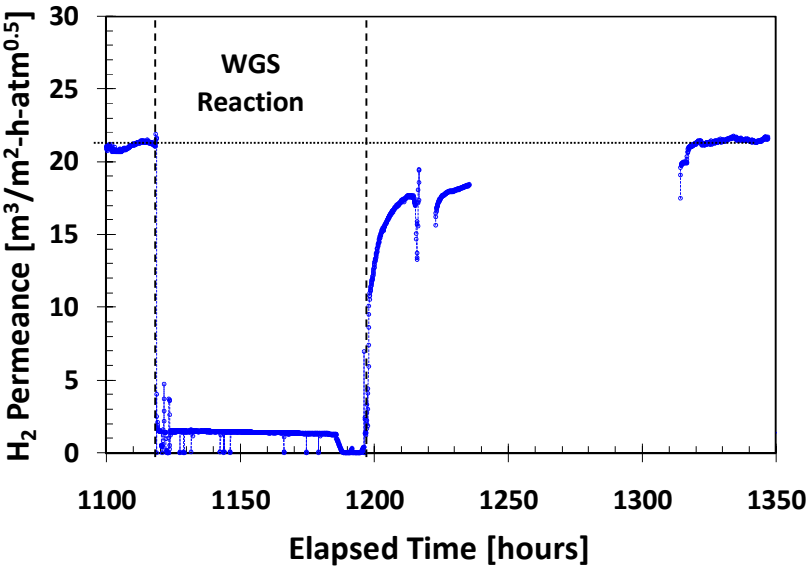

[b]

Figure 8.5. Evidence of coking for the long-term experiment with membrane IM-79 [a] WGS CMR results (23% CO, 22% H_2, 10% CO_2, 45% H_2O; 400°C; 14.6 atma; $GHSV_{STP}$ = 2,100 h^{-1}) [b] Pure H_2 permeance at 400°C before and after the reaction experiment.

The feed conditions for all of the WGS CMR experiments are plotted in Figure 8.6 indicating where evidence of coke formation was observed. Three of the experiments are labeled in Figure 8.6 as long-term (greater than 50 hours) and the rest were short-term (less than 10 hours).

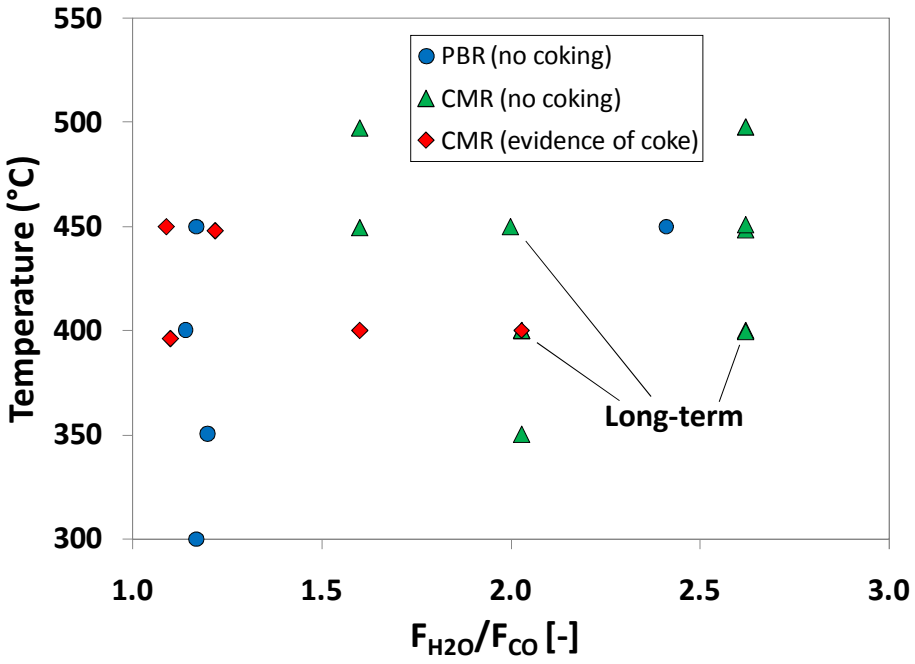

Figure 8.6. PBR and CMR experimental results indicating evidence of coke formation.

As can be seen in the Figure 8.6, coke formation occurred on the membranes at temperatures of 450°C and below, and with H_2O/CO ratios of 2.0 and below. In the WGS system, the removal/recovery of H_2 from the reaction mixture should have had the effect of reducing coke formation by consuming the reactants (CO and H_2) in both equations **8.1** and **8.2**. In contrast, for the MSR system, the removal/recovery of H_2 from the reaction mixture increased the propensity for carbon formation necessitating a higher H_2O/CH_4 ratio when compared to the conventional PBR (Galuszka *et al.,* 1998; Jorgensen *et al.,* 1995; Pedernera *et al.,* 2007). In that system the methane cracking reaction, given by equation **8.14** (the reverse of equation **8.13**), was prevalent, which was thermodynamically favored at higher temperatures.

$$\mathbf{CH_4 \rightarrow 2H_2 + C(s)} \qquad \mathbf{8.14}$$

The removal of H_2 in the MSR system pushed the reaction **8.14** towards coke formation because H_2 was a side-product in that reaction. While the WGS equilibrium was also being achieved in the MSR, it was much less significant at the higher temperatures (800°C) at which MSR has typically been conducted (Pedernera *et al.*, 2007). The reverse methane cracking reaction, or hydrogenation of coke (equation **8.13**), potentially explains the CH_4 observed in the retentate which coincided closely with other evidence of coke formation. Unfortunately, CH_4 was not looked for during the gradual recovery of the H_2 permeance for MA-79 (Figure 8.5[b]).

Concentration polarization resulted in depletion of H_2 from the membrane surface, which should have further reduced coke formation in that region. Concentration polarization also resulted in a greater concentration of CO in the region close to the membrane surface, such that a greater propensity towards coke formation might have been expected. Fortunately, the species CO_2 and H_2O were also concentrated in that region, nullifying the effect of increased CO concentration. Since the Pd-surface was catalytically active towards the WGS reaction, it could be assumed that the gas mixture there would be at WGS equilibrium, such that the reactions **8.1** and **8.2** would both proceed in the same direction (Jorgensen *et al.,* 1995).

8.4.1. Thermodynamic analysis of coke formation in the WGS CMR

For the CO/H_2O and syngas mixtures in the PBR, no coke formation was predicted by the minimization of Gibbs free energy over the entire range of experimental conditions. The equilibrium compositions of the CO/H_2O and syngas mixtures for both low and high steam to CO ratios and at both the minimum and maximum temperatures (300 and 500°C) for the range of experiments conducted are listed in Table 8.3.

Table 8.3. Equilibrium mixtures of syngas determined by the minimization of Gibbs free energy.

Initial	H_2O/CO	Temp(℃)	C(s)	CO	H_2O	H_2	CO_2	CH_4
CO + H_2O	1.0	300	0	0.007%	33.3%	0.12%	50.0%	16.6%
CO + H_2O	1.0	500	0	0.28%	32.8%	0.90%	49.7%	16.2%
CO + H_2O	3.0	300	0	0.003%	71.3%	0.18%	21.5%	7.1%
CO + H_2O	3.0	500	0	0.082%	70.3%	1.3%	21.5%	6.7%
Syngas	1.0	300	0	0.004%	40.6%	0.15%	39.0%	20.3%
Syngas	1.0	500	0	0.22%	40.0%	1.1%	38.8%	19.9%
Syngas	3.0	300	0	0.002%	67.4%	0.20%	21.4%	11.1%
Syngas	3.0	500	0	0.094%	66.4%	1.4%	21.5%	10.7%

The concentration of the species O_2, C_2H_6, C_2H_4, C_2H_2, CH_3OH, CH_2O, CHOOH, and $CO(OH)_2$ were found to drop below 0.01% in the gas phase for all sets of starting conditions listed in Table 8.3. A significant amount of CH_4 was estimated for the equilibrium mixtures because reverse methane steam reforming, equation **8.15**, was strongly favored at temperatures of less than approximately 600℃. No CH_4 was observed experimentally for the PBR cases because of the high selectivity of iron-chrome oxide catalyst towards the WGS reaction (Newsome, 1980).

$$\mathbf{CO_2 + 4H_2 \rightarrow CH_4 + 2H_2O} \qquad \textbf{8.15}$$

No coke formation was predicted by the Gibbs energy minimization for any of the starting compositions since sufficient H_2 was available in each case to generate CH_4 via equation **8.13**. Based on the thermodynamic analysis, coke formation probably occurred as an intermediate phase which was not at equilibrium considering the reactions **8.13** and **8.15** since the rates of those reactions were very low in the temperature range tested.

8.4.2. Kinetic evaluation of coke formation

As discussed in Section 8.2.2, the kinetic rate for coke formation was almost certainly very low. However, only a very small quantity of coke on the membrane surface had the potential to obstruct the H_2 flux considerably. Unfortunately, the quantity of coke on the membrane AA-5 (pictured in Figure 8.4) was not measureable since the membrane was

irreversibly sealed with a stainless steel ferrule. Several coupons were exposed to coking conditions (as listed in Table 8.2) in an effort to better understand the rate of coke formation. Astonishingly, coke was not observed to a significant extent on any of the coupons by visual inspection. The coupons which had the most coke embedded on the surface were C-7 and C-8, which were loaded with iron-chrome oxide catalyst, and are shown in Figure 8.7. During the coking of C-7 and C-8 significant coke deposition occurred at the inlet of the catalyst bed. A plug of coke weighing approximately 1.1 g was lodged at the inlet of the catalyst bed but not encompassing either of the coupons. The slight discoloration in the middles of the coupons (shown in Figure 8.7) was minor coke formation which was undetectable by the microbalance, indicating that it weighed less than 0.1mg. The coke observed on the Pd-foil was equally slight and the weight could not be measured.

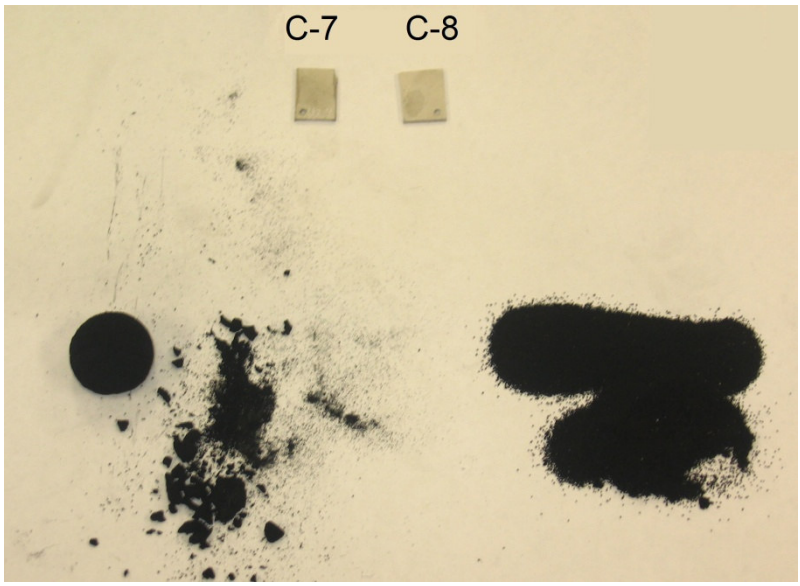

Figure 8.7. Coupons C-7 and C-8 along with coke plug blocking inlet (lower left) and used catalyst (lower right).

The coupons were also examined by XRD to determine if any change in the lattice parameter had occurred due to dissolution of carbon into the Pd-lattice (Ziemecki *et al.,* 1985; 1987). The full XRD spectrum of the coupon C-3 is shown in Figure 8.8[a] and an

overlay of the high definition spectra for the Pd(111) diffraction angle of C-1, C-3, and a green (as prepared) coupon are shown in Figure 8.8[b]. The coking results from all of the coupons in terms of the Pd(111) diffraction angle and visual appearance are listed in Table 8.4.

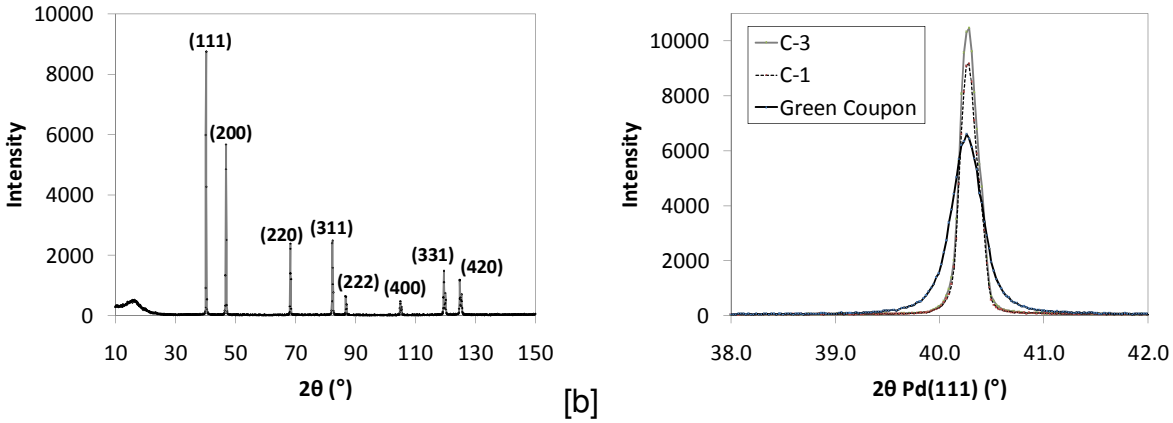

[a] [b]

Figure 8.8. XRD scans of the Pd-coupons [a] C-3: 2θ = 10 – 150° [b] C-1, C-3, and a green (freshly prepared coupon): 2θ = 38 – 42°.

Table 8.4. Coupon coking results.

Coupon	Feed	$2\theta_{Pd\ (111)}$ (°)	Visual appearance
C-1, C-2	100% H_2	40.15	No coke
C-3, C-4	10% CO, 90% H_2	40.27	No coke
C-5, C-6	66% CO, 33% H_2O	40.27	No coke
C-7, C-8	66% CO, 33% H_2O	40.13	Slight coke at middle
Pd-Foil	42% CO, 40% H_2, 18% CO_2	40.11	Slight coke at inlet end

As was clear from the results listed in Table 8.4, the Pd(111) diffraction angle was almost perfectly identical, and in agreement with literature values in all cases tested (Ziemecki *et al.,* 1985), suggesting that no Pd/C-phase had formed. It should be noted that the diffraction peaks observed for the green coupon were considerably broader due to microstrain incorporated into the electroless deposited layer (Guazzone *et al.,* 2006).

The relaxation of that strain at temperatures above 300°C was apparent in the sharper diffraction peaks of all the coupons exposed to higher temperatures.

The lack of coke formation on coupons C-5, C-6, C-7, and C-8 seemed to contradict the results from the membrane AA-5, in which significant deposits were observed. A H_2O/CO ratio of 0.5 was utilized for the coupons (significantly lower than the experiments with the membrane AA-5), which was thought likely to further increase the prevalence of coking. This would seem to suggest that either the separation of H_2 or the presence of the catalyst was responsible for the coke formation. As was discussed in Section 8.4.1, the separation of H_2 probably reduced the extent of coke formation. Also, no evidence of coke formation was observed in the PBR experiments, supporting the literature conclusion that the iron-chrome catalyst was not active towards coke formation (Newsome, 1980). It was also noted that there was no shifting of the Pd-fcc diffraction peaks, indicating no (or very little) dissolution of carbon into the Pd-lattice. The coking conducted by Li *et al.* (2007b) was accomplished with nearly identical conditions to the coking of C-3 and C-4, after which they observed a shift in the Pd(111) to approximately 39.0°, indicating formation of the $Pd_{90}C_{10}$-phase.

The lack of detectable coke formation on the coupons is in agreement with the extremely low rate indicated by the equation **8.11**. A possible explanation for the discrepancy between the coupon experiments and the relevant literature was that the Pd-catalyst interaction or contact allowed for increased catalysis of coking. Johanek *et al.* (2000) demonstrated that CO disproportionation occurred on alumina supported Pd-clusters, but not on pure-Pd or pure alumina samples. Some other literature works also showed coke formation with mica and zirconia supported Pd-clusters at even lower temperatures of 100 and 200°C (Doering *et al*., 1982; Malciejewski and Baiker, 1994). The Pd-clusters in those studies had significantly greater surface area than the Pd-membrane and therefore significantly more contact area between Pd-clusters and support material than would be possible for the Pd-coupon surface. Nevertheless, it was still possible that the Pd-surface/catalyst interface catalyzed coke formation in a similar manner (but with a lower rate). Unfortunately, this theory also seems to be contradicted

by the results of the coupons C-7 and C-8, in which significant coke deposits occurred on the catalyst, but not on the coupon surfaces.

Rupprechter *et al.* (2004) suggested that reaction **8.2** (reduction of CO by H_2) was the dominant coke formation pathway such that coking occurred through a formyl-intermediate, resulting in CH_3OH and CH_x-C bond formation. This alternative mechanism was further supported by the application of supported Pd-catalysts to methanol synthesis from syngas (Gusovius *et al.,* 1999; Gotti and Prins, 1998). The mechanism suggested by those authors involved the adsorption of CO on the basic-metal-oxide-promoted silica support, followed by H-transfer from the Pd at the support-Pd interface to generate a formate-intermediate species. That formate-intermediate was then reduced to methanol by excess H_2 present in the reaction system. CO adsorption was favored on the iron-chrome oxide catalyst, while H_2 adsorption was disfavored as discussed by Podolski *et al.* (1974). In the WGS CMR, for the catalyst in close contact to the Pd-surface, H-atoms could transfer in a similar manner to generate a formate-intermediate at the Pd/catalyst interface. Since H_2 was not present in excess, the formate-intermediate would not be reduced to form methanol, potentially allowing for the condensation of formate-intermediates into more complex carbon species. For the CMR, H_2 was depleted from the Pd-surface by the lower tube-side pressure (0.98 atma), allowing for formate-condensation to coke. For the coupons suspended in the reaction mixture, H_2 was not depleted by the membrane, potentially allowing for CH_3OH formation instead of coke. Further experiments should be conducted to determine if this may have been occuring.

The formation of coke was a highly complex phenomenon, much more so than the mechanism **8.6** – **8.9** would suggest. After atomic carbon was deposited on the surface, some of it would likely be hydrogenated to CH_4 via reverse methane cracking (Pedernera *et al.,* 2007), some of it may dissolve in the Pd-lattice (as discussed in Section 8.2.3), and some of it would form C-C bonds in either a graphitic or amorphous manner which could grow off of the Pd-surface. The thermodynamic partition between these paths is unclear because the energy of dissolution for carbon in Pd is not known and because the resulting allotropes of carbon have not been identified. The relative

rates of these processes are also yet unknown, and are probably highly dependent on the Pd-surface characteristics and Pd-catalyst interaction. Niemantsverdriet and van Langeveld (1986) utilized auger electron spectroscopy in conjunction with secondary ion mass spectroscopy to distinguish between allotropes of carbon deposited on several precious metals (Rh, Ir, and Pt). A similar technique should be applied to analyze the surface of coupons tested under WGS conditions. Siller *et al.* (1968) used a high frequency induction furnace to determine the extent of carbon dissolved in palladium in the high temperature range (900 – 1,200°C), a similar technique should be applied to determine the dissolved carbon in several foil samples after exposure to various WGS conditions.

8.5. Conclusions

Coke was observed to form on the Pd-surface in the WGS CMR in several cases, gradually lowering the H_2 recovery of the reactor by blocking the Pd-surface. Coke was not observed to form on the iron-chrome oxide catalyst, even at the lowest H_2O/CO ratio of 1.1. The thermodynamic calculations indicated that coke formation was disfavored over nearly the entire range of experimental conditions and that methane formation was favored. In WGS experiments where coke formation occurred, methane production was also observed with up to 2% estimated conversion. The formation of methane was likely the result of hydrogenation of coke, also known as reverse methane cracking. Membranes which were coked were observed to have significantly lower H_2 permeance, which gradually recovered over 100 hours in H_2, likely due to the hydrogenation of coke off of the surface.

Several coupons were exposed to coking conditions for which coke was observed in the WGS CMR experiments and also in the literature. No significant coke was observed on any Pd-coupons visually or by XRD, seemingly in contradiction to the WGS CMR results and the previous literature studies. It seemed likely that the coke formation was catalyzed by the Pd-surface in conjunction with the catalyst particles or dust, as has been suggested in the literature. The rate of coke formation was impossible to determine and the mechanism occurring at the Pd/catalyst interface remains speculative.

9. H_2S POISONING OF Pd-MEMBRANES

9.1. Introduction

For Pd-membranes to be utilized in the IGCC process, at least a small degree of tolerance to H_2S is necessary. The exit stream from the coal gasifier typically contains 0.7 mol% of H_2S, which can then be reduced down to 15 ppmv at a reasonable cost by the Selexol AGR process (Klara *et al.,* 2007; Korens *et al.,* 2002). It is known in the literature that pure Pd-membranes cannot tolerate 15 ppmv of H_2S in pure H_2 over the temperature range of 300 – 500°C due to the formation of bulk Pd_4S, leading to loss of permeability and sometimes membrane rupture. Pd/Au and Pd/Cu-membranes are more promising for the IGCC process since they have a higher threshold for bulk Pd_4S formation.

Regardless, exposure of Pd, Pd/Au, and Pd/Cu membranes even to small concentrations (less than 1 ppmv) of H_2S has resulted in significant decreases in the membrane permeance due to surface adsorption of sulfur. What is still undocumented in the literature is the effect that other reversibly adsorbed gases (such CO and H_2O) have on H_2S poisoning of these membranes. The objective of this chapter, therefore, was to develop a better understanding of H_2 permeation behavior of Pd and Pd/Au-membranes in the presence of H_2/H_2O mixed gas, simulated syngas, and under WGS reaction conditions, with 1 - 20 ppmv of H_2S present.

9.2. Background

Pure Pd-membranes are known to lose a significant fraction of their permeance due to as little as 2 ppmv H_2S present in the feed gas (Peters *et al.,* 2012). Furthermore, at higher H_2S concentrations, and depending on temperature, the bulk Pd_4S phase can form, resulting in further H_2 permeance decrease, pinhole formation, and membrane rupture (Chen and Ma, 2010; Pomerantz and Ma, 2009; Morreale *et al.,* 2007; Mundschau *et al.,* 2006; Iyoha *et al.,* 2007b). The reaction expression for H_2S adsorption on Pd, followed by incorporation into the Pd-lattice is given by equation **9.1**,

the surface adsorption equilibrium expression is given by equation **9.2**, and the overall equilibrium expression for Pd_4S formation is given by equation **9.3**.

$$H_2S + Pd^* \leftrightarrow Pd^*S + H_2 \leftrightarrow Pd_4S + H_2 \qquad \textbf{9.1}$$

$$K_1 = \frac{P_{H_2}\theta_S}{P_{H_2S}\theta_*} \qquad \textbf{9.2}$$

$$K_2 = \frac{P_{H_2}}{P_{H_2S}} \qquad \textbf{9.3}$$

where K_1 was the Langmuir adsorption equilibrium constant for sulfur, K_2 was the equilibrium constant for Pd_4S formation, P_x [atma] was the partial pressure of species x at the surface, θ_S was the surface coverage of sulfur, and θ_* was the fraction of free surface sites. Note that the equation **9.3** was simplified such that the activity of each solid species a_{Pd} and a_{Pd4S} was set equaled to one since those species occurred in their pure states. The surface adsorption was thought to occur quickly followed by rapid dissociation (Alfonso, 2008), while the formation of bulk Pd_4S was slower.

It was calculated and observed experimentally that for a pure Pd surface at 400℃, more than 2.8 ppmv H_2S in pure H_2 would form the bulk Pd_4S (Chen and Ma, 2010; Mundschau *et al.,* 2006). The equilibrium expression **9.3** indicated that the partial pressure of H_2 was inversely proportional to the equilibrium constant, meaning that when a gas mixture was used with less than 100% H_2 (with inert gas making up the difference), the threshold concentration of H_2S which resulted in Pd_4S formation would be lower (Iyoha *et al*., 2007b). Another phenomenon which must be considered was the effect that reversibly adsorbed species such as CO and H_2O would have on the formation of Pd_4S. Those gases could potentially compete for active surface sites, resulting in a lower surface coverage by sulfur, and perhaps a lower rate of bulk Pd_4S formation.

The adsorption of H_2S is known to be considerably stronger than that of either H_2O or CO. It has also been proposed that a sulfur coverage of only 0.25 mono-layer (ML) resulted in the complete deactivation of the Pd-surface for H_2 adsorption (Wilke and

Scheffler, 1995). If H_2S is only present at ppmv levels, however, competition for surface sites can still occur since H_2O and CO are present in much higher concentrations (1 – 50% by volume). The energy of desorption or binding energy, ΔE_i [kJ/mol], for each gas species is given in Table 9.1. The binding energy can be utilized to estimate the adsorption equilibrium constant, λ_i [atm^{-1}], for each gas species via equation **5.10** (discussed in Chapter 5). Based on equation **5.10** the adsorption constant at 400℃ for each species is also tabulated in Table 9.1. Even though the adsorption constant for H_2S was many orders of magnitude greater than that of CO and H_2O, the surface coverage of each species was proportional to $\lambda_i P_i$ as shown in equation **9.4**, so values of $\lambda_i P_i$ are listed in Table 9.1 for a syngas mixture (19% CO, 18% H_2, 8% CO_2, 55% H_2O, and 1 ppmv H_2S) at 14.0 atma.

$$\theta_i = \frac{\lambda_i P_i}{1+\lambda_{CO}P_{CO}+\lambda_{H_2O}P_{H_2O}+\lambda_{CO_2}P_{CO_2}+\lambda_{H_2S}P_{H_2S}} \qquad \textbf{9.4}$$

Table 9.1. Proposed binding energies, adsorption constants, and relative surface coverage factors for gas species on the palladium surface at 400℃.

	ΔE_i [kJ/mol]	λ_i [atm^{-1}]	$\lambda_i P_i$	Reference
H_2S	-256 (θ_S=0)	$1.12*10^7$	157	Alfonso, 2005
	-190 (θ_S=0.5)	274.8	0.0038	
	-300 (θ_S=0)	$1.02*10^{11}$	$1.42*10^6$	Gravil and Toulhoat, 1999
	-244 (θ_S=0.33)	$4.27*10^6$	59.8	
CO	-149	0.239	0.64	Guo and Yates, 1989
H_2O	-125	0.00691	0.053	Catalano *et al.,* 2011

The adsorption energy of sulfur was found to be strongly dependent on the surface coverage of sulfur such that the surface coverage was not well represented by equation **9.4** and would be better fit by the Temkin equation, **6.11** (Alfonso, 2005; Gravil and Toulhoat, 1999). As was discussed in Chapter 6, the effective adsorption energy of H_2O was considerably higher than the *ab initio* calculations suggested due most likely to the dissociation on the Pd-surface resulting in bound OH and O species (Alfonso, 2006).

Competative adsorption could only have occurred between the WGS species and H_2S at surface coverages of greater than 0.33 – 0.5 ML of sulfur because that was the surface coverage range at which $\lambda_{CO}P_{CO}$ and $\lambda_{H2O}P_{H2O}$ values (given in Table 9.1) eclipsed the value of $\lambda_{H2S}P_{H2S}$. If the gases CO and H_2O competitively adsorbed with H_2S in an ideal manner such that the Langmuir equation, **9.4**, was valid, the combined effect might be a net increase in blocked surface sites, and therefore a decrease in the H_2 permeance of the Pd-membrane. Alternatively, the adsorption of WGS species along with H_2S may have lowered the binding energy of sulfur such that the Tempkin equation, **6.11**, was valid. If that occurred, then the presence of those gases could potentially reduce the overall fraction of blocked surface sites for H_2 adsorption and prevent a significant loss of H_2 permeance.

To gain some resistance to H_2S poisoning, different Pd-alloys have been fabricated and tested: Pd/Cu (Pomerantz and Ma, 2009; Morreale *et al.,* 2004; McKinley, 1967), Pd/Au (Chen and Ma, 2010; McKinley, 1967; Peters *et al.,* 2012), and Pd/Fe (Bryden and Ying, 2002). All of these alloys have experimentally shown a lower extent of surface coverage by sulfur and a higher thermodynamic threshold for bulk sulfide formation with respect to H_2S concentration. The most preferable alloy among the three in terms of membrane permeance has been the Pd/Au-alloy since it has higher permeability than pure Pd for the gold compositions of 1 – 20 at% (McKinley, 1967). A small range of Pd/Cu-alloy compositions around 40 at% Cu form a body-centered cubic (bcc) phase which has a slightly higher permeability than pure Pd, but also does not have any of the sulfur tolerance that the fcc-Pd/Cu-alloy phase is claimed to have in the composition range of 1 – 35 at% Cu (Knapton, 1977; Howard *et al.,* 2004; Morreale *et al.,* 2004).

Chen and Ma (2010) engineered a more effective H_2S resistant Pd/Au membrane by depositing gold on the surface of a pure Pd-membrane, then partially annealing that gold layer. The resulting asymmetric membrane had a high concentration of gold (20 – 30 at%) on the surface, but which declined to zero several microns into the dense layer. This was preferable to minimize the use of expensive gold and to minimize the thickness of the lower H_2 permeability associated with Pd/Au-alloys containing greater than 20 at% Au.

9.3. Experimental

The relevant synthesis details and initial H_2 testing results of the membranes utilized in this chapter are listed in the Table 9.2. The preparation and initial testing of those membranes was discussed in Chapter 4.

Table 9.2. Membranes tested in this chapter, comprehensive details are given in Appendix D.

	Pd/Ag [µm]	Dense layer [µm]	H_2 permeance* [m^3/m^2-h-$atm^{0.5}$]	Final select.† [F_{H2}/F_{He}]	Other details
AA-31	1.8	6.8	22.0	250	
AA-38R	N/A	4.4	41.2	2500	
AA-40R	N/A	2.7	38.0	340	10 at% Au
RK-16R	N/A	6.0	37.5	675	

*at 400°C
†selectivity after final testing

9.3.1. Pd/Au-membrane synthesis

The Pd/Au asymmetric membrane AA-40R was synthesized by electroplating the pure Pd-membrane AA-40 with 0.8 µm (10 at% overall) of gold by the method described in the Experimental, Section 3.2.4. The membrane was annealed for 100 hours in H_2 at 450°C such that partial alloying would occur. It was desired that a gold gradient would remain with a higher alloy composition (20 – 30 at%) on the surface for increased H_2S resistance (Chen and Ma, 2010; Chen, 2011).

9.3.2. Mixed gas and WGS experimental procedure

H_2S was introduced into the feed stream by the addition of one of the gas mixtures listed in Table 9.3. The H_2/H_2S gas mixtures were obtained from Airgas Inc. The H_2/H_2S mixtures were analyzed by Airgas Inc. and the measured compositions in terms of H_2S concentration are reported in Table 9.3.

Table 9.3. H_2/H_2S mixtures used in this chapter (concentration measured by Airgas Inc).

Mixture designation	Measured H_2S (ppmv)	Balance
5 ppm	5.0	H_2
50 ppm	54.8	
400 ppm	406.3	

Mixed gas experiments were conducted as per the procedure given in the Experimental, Sections 3.4.2 with two exceptions. An unsteady state behavior (H_2 permeate flux varying by ±30% from the mean over an approximately 10 second interval) was observed at intermediate space velocities (3,000 – 6,000 h^{-1}) and 14.6 atma which was found to be dependent on the physical orientation of the system. When the system was operated with reversed flow (counter-current flow in the downward direction) the fluctuations ceased completely, so that orientation was used. Since there was no sweep gas, the direction of the flow along the membrane should not have affected the separation dynamics.

The only other clarification of Section 3.4.2 was that the H_2S feed was switched on last, after all other feed gases, pressure, and stable permeate flows were established. This was done to ensure that no spike in the H_2S concentration could occur upon start-up or shut-down. In some preliminary system testing the stainless steel system components adsorbed H_2S from the feed such that little or no H_2S was detected at the system outlet for several hours. When syngas species were introduced into the feed (with H_2S still present) a significant increase in H_2S concentration, of up to ten times that in the feed, was sometimes measured at the retentate outlet. Upon shutting off the system, the H_2S feed was ceased first. The other feed gases were then shut off within 60 seconds. Chen (2011) observed that the bulk Pd_4S phase on the surface would gradually revert back to pure Pd in an H_2 atmosphere, so when XRD analysis was planned, the system was flushed with helium (1,000 sccm) immediately upon shutting off the feed gases and for 60 minutes before cooling the system at 2°C/min to room temperature.

WGS experiments were conducted as per the experimental procedure given in Sections 3.5.2 – 3.5.3. Again, the only clarifications were that H_2S was turned on last during start-

up and shut off first during shut-down. When XRD analysis was to be conducted, the system was flushed with helium and cooled quickly in the same manor.

9.4. Results and discussion

The results of the H_2S testing are presented in the following manner: experiments conducted with H_2/inert/H_2S mixtures are presented first in Section 9.4.1, followed by experiments conducted with H_2/H_2O/H_2S mixtures in Section 9.4.2 to explore how H_2O could affect the poisoning by H_2S. In Section 9.4.3 separation experiments with a shifted syngas mixture (enriched in H_2 and depleted in CO) were presented which highlighted the performance of the $Pd_{90}Au_{10}$-membrane AA-40R, challenged with up to 20 ppmv H_2S. Finally, in Section 9.4.4 WGS CMR experiments were conducted with a pure Pd-membrane and over extended periods of time (400 hours). At the end of Section 9.4.4 the irreversible poisoning by H_2S (Pd_4S formation) is discussed from a thermodynamic stand point. SEM images are also presented at the end of Section 9.4.4 showing interesting morphology changes which were attributed to the poisoning by H_2S.

9.4.1. H_2/inert/H_2S mixtures

Testing with H_2/N_2/H_2S mixtures was conducted to confirm the equilibrium relationship given by equation **9.2** which expressed that the surface coverage was dependent on the H_2/H_2S ratio in the gas mixture. The initial pure H_2 testing at 400°C and the first three H_2/H_2S experiments are shown in Figure 9.1. The H_2 permeance shown in the figure was determined using the partial pressure of H_2 measured in the retentate stream. The horizontal dashed line labeled 'A' indicated the H_2 permeance during poisoning by 1 ppmv H_2S in H_2. The horizontal line 'B' indicated the 'recovered' permeance upon switching back to pure H_2. The horizontal line 'C' indicated the H_2 permeance during poisoning by 1 ppmv H_2S in 50% H_2 and 50% N_2.

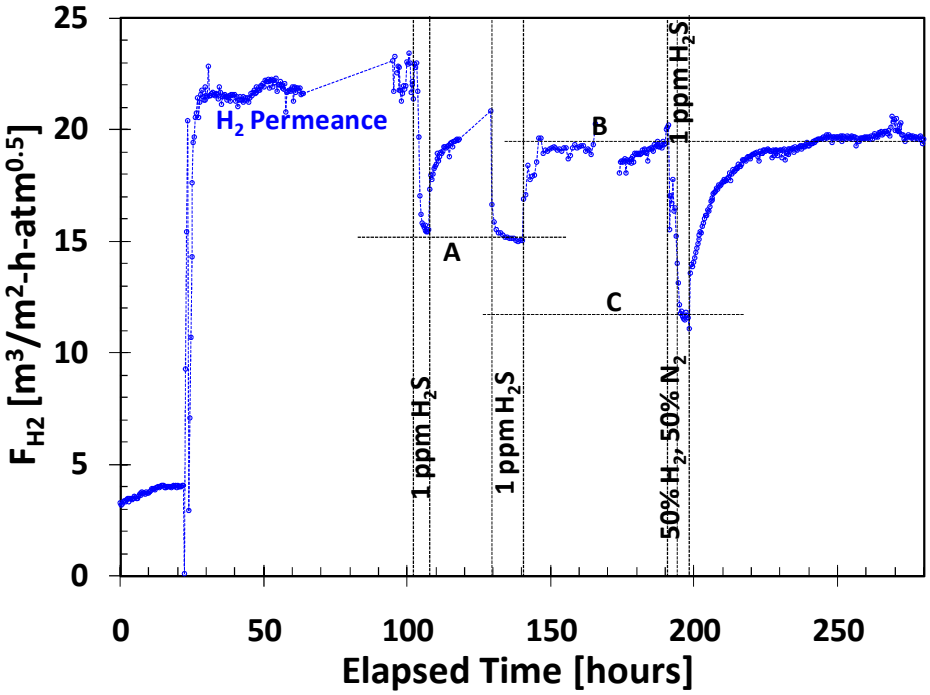

Figure 9.1. Initial H_2 characterization and H_2/H_2S testing at 400℃ (Membrane: AA-31).

Two poisonings with 1 ppmv H_2S in H_2 were conducted consecutively for 5 and 12 hours at a pressure of 2 atma. During both poisonings, the H_2 permeance dropped to 68% of its initial value (horizontal dashed line A). After switching back to pure H_2, the permeance was observed to return to 87% of its initial value (horizontal line B), indicating that there was some irreversible poisoning, perhaps due to trace sulfur remaining on the surface. The membrane AA-31 performed much better than a similar membrane, C-10, reported by Chen (2011) where a permeance of only 22% of the initial value was observed upon 1 ppmv exposure to H_2S at 400℃. Following the H_2S exposure, the membrane C-10 only recovered 67% of its initial permeance upon switching back to pure H_2. The membrane AA-31 performed comparably to a Pd-membrane tested by Peters *et al.* (2012) with 2 ppmv H_2S at 450℃. Their membrane maintained 62% permeance upon poisoning and recovered up to 95% of the initial permeance upon pure H_2. The irreversible poisoning was caused by some surface sites adsorbing H_2S with a very high binding energy, requiring higher temperature (greater

than 500℃) to obtain complete removal (Chen and Ma, 2010). The membranes AA-31 and C-10 were very similarly prepared and the testing conditions were nearly identical so it was unclear why the membrane AA-31 performed better.

The third experiment shown in Figure 9.1 was conducted with 50% N_2 in H_2 mixed gas, first for 2 hours with no H_2S, then for 5 hours with 1 ppmv H_2S, at 5 atma and 4,500 h^{-1} feed rate. During the first two hours, with no H_2S present, a H_2 permeance 15% lower than the 'recovered permeance' (horizontal line B) was observed, due to the moderate influence of gas boundary layer mass transfer resistance. Upon exposure to 1 ppmv H_2S, the H_2 permeance dropped a further 29% (horizontal line C), which was a 32% greater drop than the difference between lines A and B, indicating greater permeance inhibition by H_2S. The inhibition by 1 ppmv H_2S in the 50% H_2/N_2 mixture was significantly greater than the inhibition by 1 ppmv in 100% H_2 since the lower partial pressure of H_2 in the mixture allowed for the shifting of equation **9.1** towards the adsorbed species Pd*S. Once the system was returned to pure H_2, the rate at which the H_2 permeance recovered was considerably slower in the third experiment even though it eventually returned to the same recovered permeance (horizontal line B). The slower permeance recovery was a further indication that the equilibrium was shifted towards adsorbed sulfur in the third experiment. Additionally, the permeance returned to the same level as before suggesting that there was no further irreversible poisoning. The addition of 50% inert gas should have lowered the threshold for Pd_4S formation to 1.4 ppmv and so bulk sulfide formation was not expected (Mundschau *et al.,* 2006).

9.4.2. $H_2/H_2O/H_2S$ mixtures

Experiments were conducted with $H_2/H_2O/H_2S$ mixtures as a precursor to experiments involving the separation of H_2 from syngas with 1 – 20 ppmv H_2S. The primary motivation for this was to determine if H_2O might competitively adsorb with H_2S on the Pd-surface, lessening the extent of sulfur poisoning on the surface, and potentially increasing the threshold for Pd_4S formation. The first series of experiments are shown in Figure 9.2[a], all conducted with 50% H_2 gas mixtures at a total feed rate of 4,550 h^{-1}.

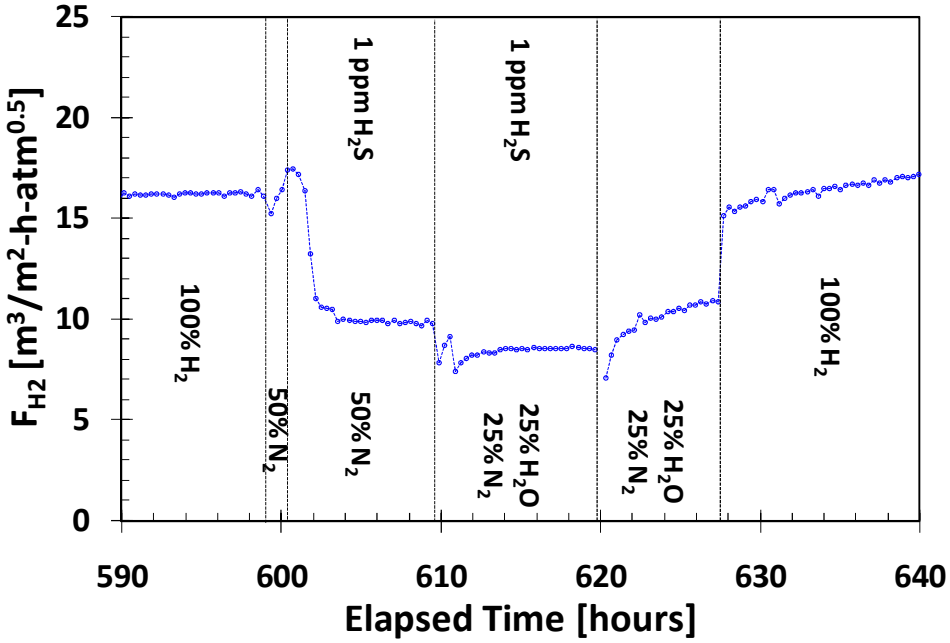

[a]

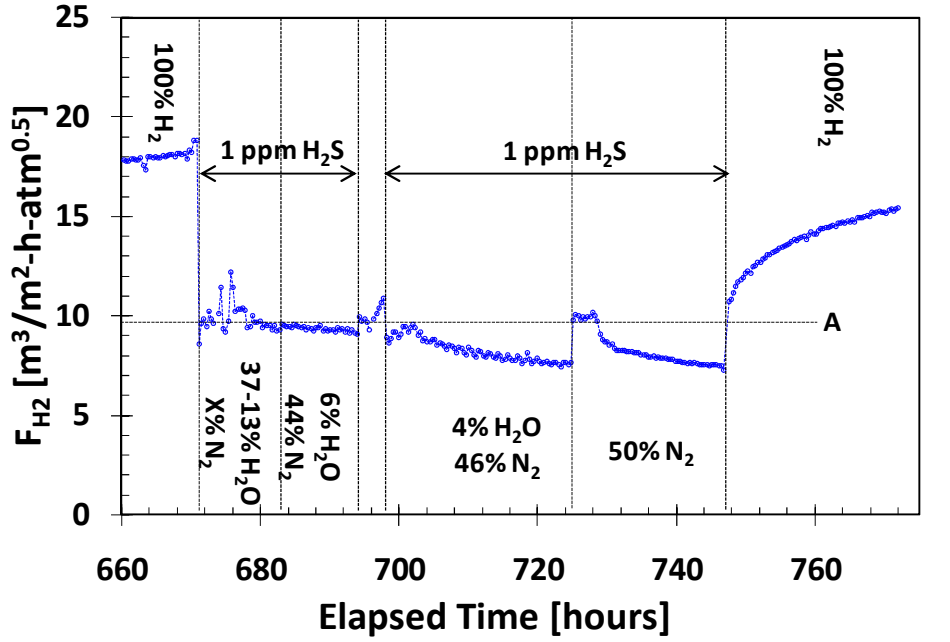

[b]

Figure 9.2. $H_2/H_2O/N_2$ testing of the membrane AA-31 with 1 ppmv of H_2S [a] First series of experiments (25% H_2O) [b] Second series of experiments (4 – 37% H_2O).

The introduction of 1 ppmv H_2S in the 50% H_2/N_2 mixture, reduced the membrane permeance by 39% to 9.9 m^3/m^2-h-$atm^{0.5}$ as shown in Figure 9.2[a], moderately greater than the 29% reduction previously observed under identical conditions. The H_2S measured in the retentate increased to 1.1 ppmv over 8 hours to reach nearly 100% sulfur mass balance. The extended period required to reach H_2S saturation was attributed to the clean (not previously exposed to H_2S) stainless steel pieces of the pre-heater, installed shortly before the experiments. The 50% N_2 was then replaced with 25% H_2O and 25% N_2, resulting in an additional loss of 15% permeance to 8.7 m^3/m^2-h-$atm^{0.5}$ as shown in Figure 9.2[a]. Interestingly, the H_2S measured in the retentate spiked to over 3.3 ppmv upon admission of the H_2O, indicating that the H_2O probably caused desorption of H_2S from the membrane and/or the stainless steel piece of the system. The spike in H_2S concentration was cause for alarm as the threshold for bulk sulfide formation was exceeded for approximately 20 minutes.

When both H_2O and H_2S were admitted to the system, they competitively adsorbed on the membrane surface, blocking active sites for H_2 adsorption and dissociation. The observed decrease in H_2 permeance indicated that the overall extent of surface coverage was probably greater than that due to either species alone. When the H_2S was shut off, the H_2 permeance gradually recovered by about 25% to a level at which only surface blocking by H_2O (and the irreversibly adsorbed S) was occurring.

Experiments were then conducted, as shown in Figure 9.2[b], to determine if there was some H_2O composition under which a higher H_2 permeance would be observed than that measured during 50% H_2/N_2 + 1 ppmv H_2S conditions, suggesting that adsorption of H_2O was lowering the binding energy for sulfur. As the amount of H_2O in the feed flow was decreased (and replaced by inert N_2), the H_2 permeance continued to decrease, eventually to only 43% (7.5 m^3/m^2-h-$atm^{0.5}$) of the recovered permeance when the system was switched to 50% H_2/N_2. The final permeance measured was significantly lower (21%) than the previous experiment with 1 ppmv H_2S in 50% H_2/N_2 (horizontal line **A** in Figure 9.2[b]), indicating that further irreversible poisoning had occurred on the membrane surface, possibly caused by the presence of H_2O; there was no clear explaination as to why this would occur. Based on the experiments shown in Figure

9.2[b], it became obvious that the membrane would have to be recovered at 500°C after every set of conditions in order to collect reliable data.

Following the H_2S exposure the membrane only recovered 67% of his initial permeance upon switching to pure H_2 indicating further irreversible poisoning. The further poisoning could have been caused by the spikes in the H_2S concentration due to the starting and stopping of the H_2O feed.

Even considering the additional irreversible poisoning observed, the membrane AA-31 performed better than the similar membrane, C-10, reported by Chen (2011), where a permeance of only 22% of the initial value was observed upon 1 ppmv exposure to H_2S at 400°C. A key difference in the system configurations utilized here and by Chen (2011) was the temperature control. Since no thermal tape was utilized by Chen (2011) it was possible that a temperature gradient existed in their system such that part of the membrane was as much as 40°C below the operating temperature, allowing for greater poisoning by H_2S.

9.4.3. Syngas/H_2S mixtures

Separation experiments were conducted with a shifted syngas mixture (50% H_2, 30% CO_2, 19% H_2O, and 1% CO) to gain a better understanding of the deleterious effects that H_2S could have on the H_2 permeance and stability of the membrane. A pure Pd-membrane (RK-16R) was utilized as a baseline and a $Pd_{90}Au_{10}$-membrane (AA-40R) was utilized for H_2S resistance. The membrane RK-16R was tested for 25 hours under the shifted syngas with no H_2S present, then for 25 hours with 1 ppmv H_2S, then for 25 hours with 2.5 ppmv H_2S. The H_2 flux over time and sulfur mass balance for the mixed gas testing of RK-16R is shown in Figure 9.3[a]. The membrane AA-40R was tested for 25 hours under the shifted syngas with no H_2S present, then with 1, 2.5, 5, 10, and 20 ppmv H_2S in the feed. The H_2 flux over time for the mixed gas testing of AA-40R is shown in Figure 9.3[b].

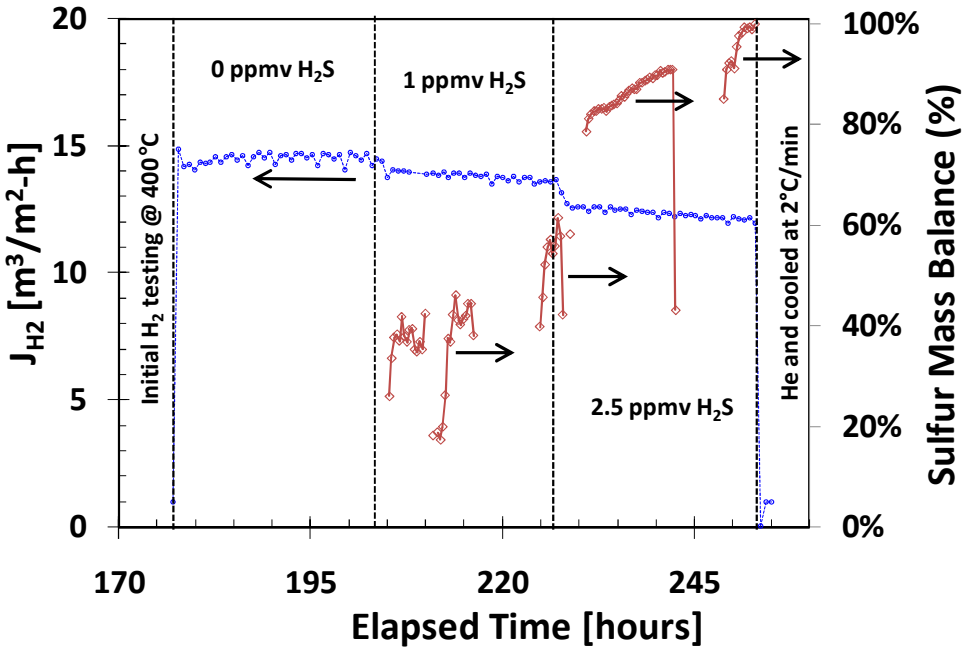

[a]

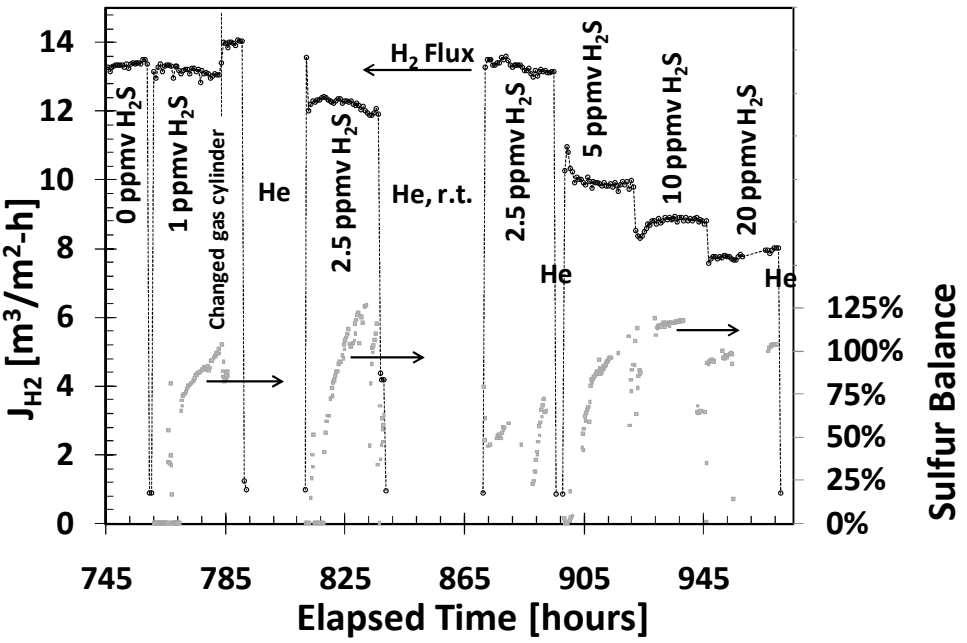

[b]

Figure 9.3. Syngas separation with H_2S in feed stream [a] RK-16R [b] AA-40R (50% H_2, 30% CO_2, 19% H_2O, 1% CO; 14.0 atma; 400℃; 5,600 – 5,800 h^{-1}).

Both membranes maintained a stable H_2 flux of approximately 14 m^3/m^2-h when no H_2S was present, corresponding to a high H_2 recovery of 90 – 92%. When 1 ppmv H_2S was introduced into the feed a gradual drop in H_2 flux of 2% was observed in both cases most likely due to the reversible adsorption of H_2S on the membranes. As shown by the sulfur mass balance in Figure 9.3[a] and [b], the H_2S concentration measured in the retentate gradually increased when 1 ppmv of H_2S was introduced, probably because the stainless steel walls of the system adsorbed H_2S to some extent before becoming saturated. The gradual increase in the H_2S concentration during the initial testing with 1 ppmv resulted in the gradual decline of H_2 flux from membrane RK-16R (Figure 9.3[a]) because of increasing Pd-surface coverage by sulfur. It was unlikely that bulk Pd_4S was forming in either case because the concentration of H_2S at the retentate was still below the thermodynamic formation threshold (Chen, 2011; Mundschau *et al.,* 2006). When 2.5 ppmv H_2S was added to the feed the sulfur mass balance quickly approached 100% in both cases, but the H_2 flux again gradually decreased over 25 hours for both membranes. During the second period of testing at 2.5 ppmv H_2S for the membrane AA-40R (Figure 9.3[b]) a slightly higher feed rate (5,800 h^{-1}) was utilized explaining the apparent discontinuous jump in H_2 flux; for all other testing periods a feed rate of 5,600 h^{-1} was utilized as this was the highest flow rate the flow controllers were capable of accurately delivering for the given syngas concentration.

The H_2 flux for the membrane RK-16R decreased significantly over time (8% over 25 h) when testing with 2.5 ppmv H_2S because bulk Pd_4S was probably forming at the retentate end of the membrane. The H_2S/H_2 ratio in the retentate of $3.4*10^{-5}$ was significantly greater than that at which Pd_4S had been previously been formed in pure H_2/H_2S experiments with Pd-coupons ($1.0*10^{-5}$ mol_{H2S}/mol_{H2}), and even further above the thermodynamic threshold at 400°C, $2.8*10^{-6}$ (Chen, 2011; Mundschau *et al.,* 2006).

The membrane AA-40R was further tested with 5, 10, and 20 ppmv H_2S in the feed. Stable H_2 flux was observed over each 25 hour period indicating that only surface adsorption of sulfur was occurring and was responsible for the incremental drops in H_2 permeance. The transition from 2.5 to 5 ppmv H_2S caused a considerable drop in H_2 flux due to increasing Pd-surface coverage by sulfur. The further exposure, however, to

10 and 20 ppmv did not result in significant drops, suggesting that the surface was nearly saturated with sulfur, but that there were still unoccupied active sites for H_2 adsorption. The Pd/Au-surface can be considered to have multiple types of adsorption sites which have different binding energy for sulfur (Chen, 2011; Alfonso, 2005). It is possible that the addition of Au decreased the binding energy preferentially for some surface sites over others such that a portion of low binding energy sites still existed and would become saturated with sulfur only by significantly higher concentrations of H_2S (greater than 20 ppmv).

The saturation effect can most easily be seen in a plot of H_2 recovery versus H_2S concentration as shown for both membranes in Figure 9.4. Two other studies (Gade *et al.,* 2011; Peters *et al.,* 2012) also tested Pd/Au-membranes in shifted syngas with up to 20 ppmv H_2S present; their H_2 recoveries are also shown for comparison in Figure 9.4.

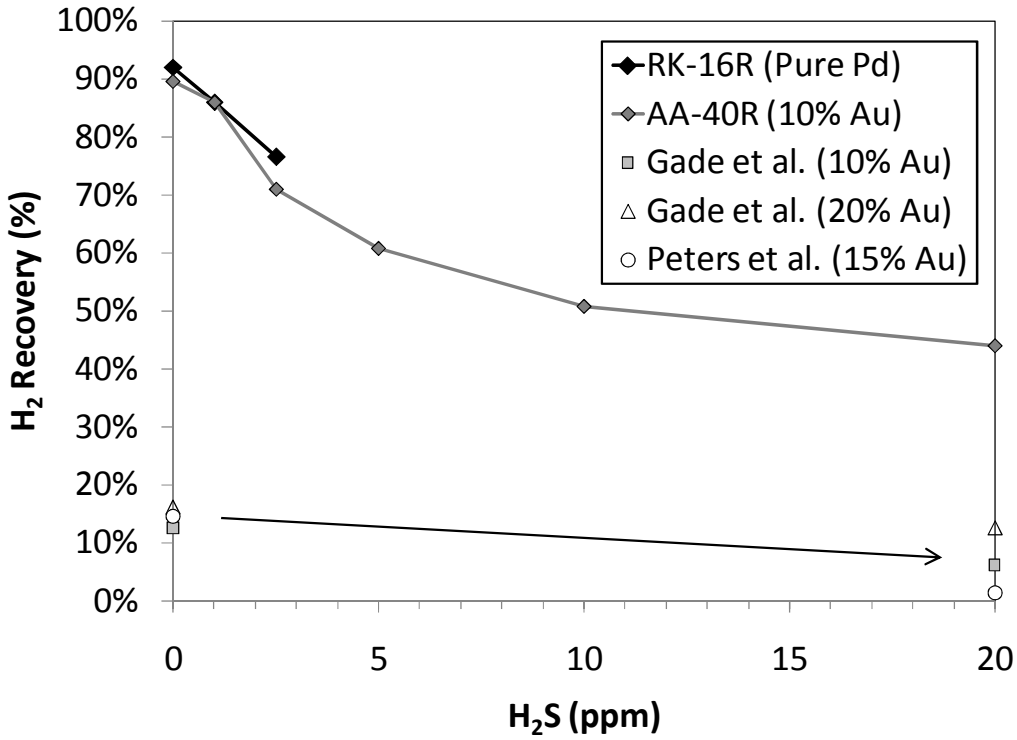

Figure 9.4. H_2 recovery versus H_2S concentration for syngas mixtures containing H_2S (Membranes: RK-16R, AA-40R, and literature data).

As shown in Figure 9.4, a high H_2 recovery of 90% was achieved by both membranes when no H_2S was present since the inhibition by the gas species H_2O, CO, and CO_2 were not significant at 400°C. When 1 and 2.5 ppmv H_2S were added to the feed, the H_2 recovery achieved by both membranes declined to nearly identical extents, suggesting that the surface inhibition by H_2S was nearly equivalent. Since the membranes had similar pure H_2 permeance (37.5 and 38.0 m^3/m^2-h-$atm^{0.5}$ for RK-16R and AA-40R respectively), it was expected that the Pd/Au-membrane would perform better under H_2S poisoning due to its sulfur tolerance. It was previously demonstrated by Chen (2011) and Peters *et al.* (2012) that alloying with 5 – 20% Au allowed for better H_2 permeance tolerance to H_2S by as much as 40% for a given H_2S concentration, yet no significant difference was observed between the two membranes presented (Figure 9.4) when exposed to H_2S in syngas. The key difference between that previous study (Chen, 2011) and the current results was the presence of the syngas species (H_2O, CO, and CO_2) in the gas stream. It was theorized that the H_2S could be reacting on the Pd-surface with one or more of the syngas species to form an alternate sulfur compound such as COS or CH_3SH which had a different interaction with the Pd and Pd/Au-surfaces. Indeed, a new sulfur containing species was visible by GC which may have been COS based on the retention time (1.61 min compared to 1.76 min for H_2S) and information from the GC manufacturer (SRI). The presence of COS was not confirmed since no COS standard mixture was available. Since the poisoning effect of COS on Pd has not been studied in the literature, it is unclear how its formation would affect the membranes.

The stable H_2 flux over time with 20 ppmv of H_2S present (Figure 9.3[b]) suggested that bulk Pd_4S was not forming on the membrane AA-40R. The tolerance of the Pd/Au-membrane to up to 20 ppmv H_2S was unsurprising considering the relevant literature on Pd/Au-alloys (Chen and Ma, 2010; Chen, 2011; Mundschau *et al.,* 2006). Chen and Ma (2010) showed an 83% decline to a stable H_2 permeance when feeding a 50 ppmv H_2S in H_2 mixture. The comparison with the two literature studies (Gade *et al.,* 2011; Peters *et al.,* 2012) at 20 ppmv H_2S was not ideal since both of those studies worked with higher feed rates, resulting in higher H_2 flux but lower H_2 recovery. H_2 fluxes of 8.9 and 16.9 m^3/m^2-h were achieved by Gade *et al.* (2011) for their 10% and 20% Pd/Au-alloys

respectively with 20 ppmv H_2S present, due to the higher space velocity utilized in their study which lowered gas phase mass transfer resistance. At the same time, the lower H_2 recovery achieved by Gade *et al.* (2011) resulted in a better partial pressure driving force for H_2 flux than was achieved in the present study. They observed a significantly greater H_2 flux when a higher gold content of 20% was utilized, suggesting that a gold content of greater than 10% was preferable for both of the situations when H_2S was present, and when only the syngas species were present.

After the extended period of testing under shifted syngas mixtures, the membranes RK-16R and AA-40R were switched directly to helium with a high purge rate and cooled quickly to room temperature as described in Section 9.3.2. The membranes were cut and characterized by SEM. Samples were cut from the inlet, middle, and outlet ends of the membranes as shown in Figure 9.5, so that the extent of Pd_4S formation could be estimated with respect to the position of the sample in the experimental setup.

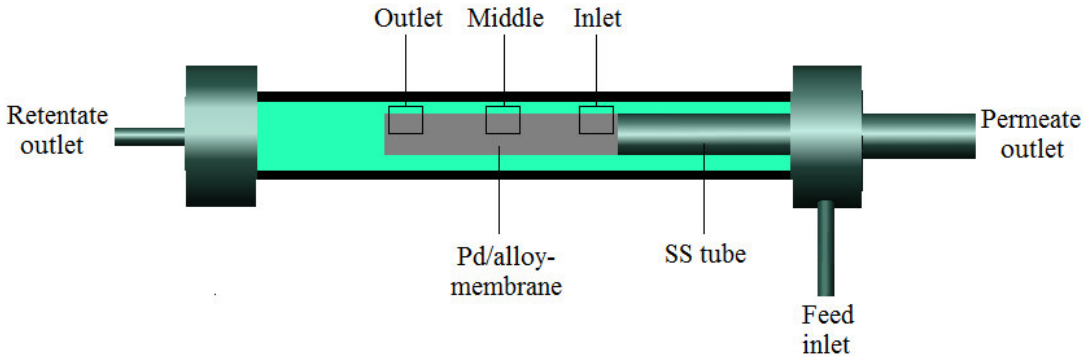

Figure 9.5. Diagram of the experimental membrane module indicating the locations where membrane samples were cut for characterization.

Since low flow, high recovery conditions were used such that the H_2S/H_2 ratio was considerably higher at the outlet end of the membrane, it was expected that the extent of poisoning would be greater there. SEM cross-section images and EDS line scans are shown for the outlet-samples of the two membranes RK-16R and AA-40R in Figure 9.6[a-d]. The results from the outlet-samples were representative for the inlet and middle-samples since no significant differences were observed.

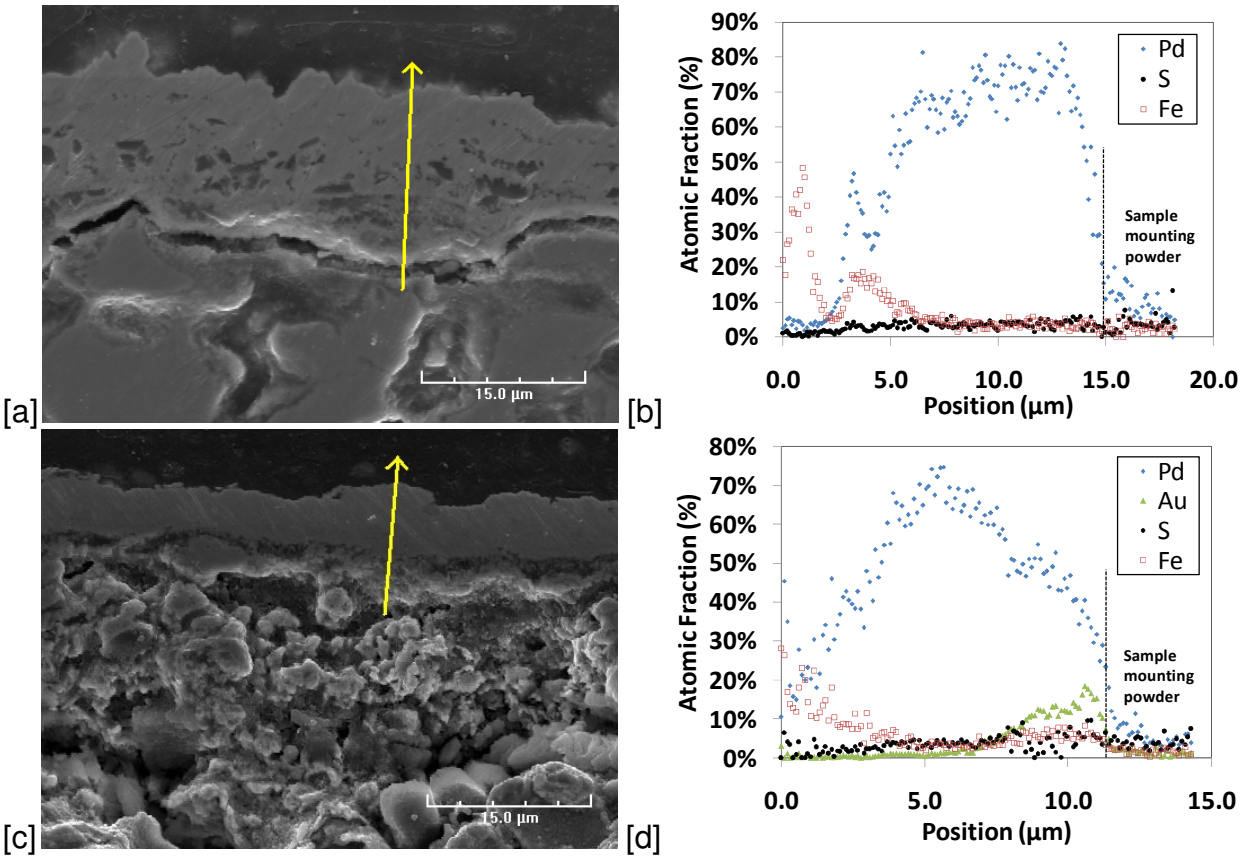

Figure 9.6. SEM images and EDS line scans of membrane cross-sections [a] SEM, RK-16R outlet, 2,500X [b] EDS, RK-16R outlet [c] SEM, AA-40R outlet, 2,500X [d] EDS, AA-40R outlet.

It was apparent from the SEM images shown in Figure 9.6[a] and [c] that the membranes both had similar 5 – 7 µm thick dense Pd and Pd/alloy-layers with substantial (5 – 10 µm) grading layers, which was in line with the measured pure H_2 permeance of 40 m^3/m^2-h-$atm^{0.5}$. In the EDS line scan of AA-40R (Figure 9.6 [d]) a gradient can be seen in the gold concentration, ranging from approximately 16 at% at the surface (Position = 12 µm in the figure) to nearly zero over 5 µm, exactly what was desired from the synthesis methodology.

For the pure Pd-membrane RK-16R less than 5 at% sulfur was detected by EDS over the whole cross section (Figure 9.6[b]), which was below the accuracy level for EDS, suggesting no substantial bulk Pd_4S phase was formed on that membrane. For the

$Pd_{90}Au_{10}$ membrane AA-40R up to 9 at% sulfur was observed in the 7 – 12 μm range at the membrane surface (Figure 9.6[d]). The measurement accuracy for the EDS composition analysis shown in Figure 9.6[d] (specifically considering the position range of 7 – 12 μm where both sulfur and gold were detected) was compromised by the partial overlap of the sulfur $K\alpha^1$ and gold $M\alpha^1$ x-ray emission peaks (at energies of 2.31 and 2.12 keV respectively) that were utilized for the calculation.

The membrane samples were examined by XRD to determine the extent of bulk sulfide formation. XRD spectra (2θ = 20 - 100°) for the inlet and outlet samples from RK-16R are shown in Figure 9.7[a] and [b] respectively. XRD spectra of the inlet and outlet samples from AA-40R are shown in Figure 9.7[c] and [d] respectively.

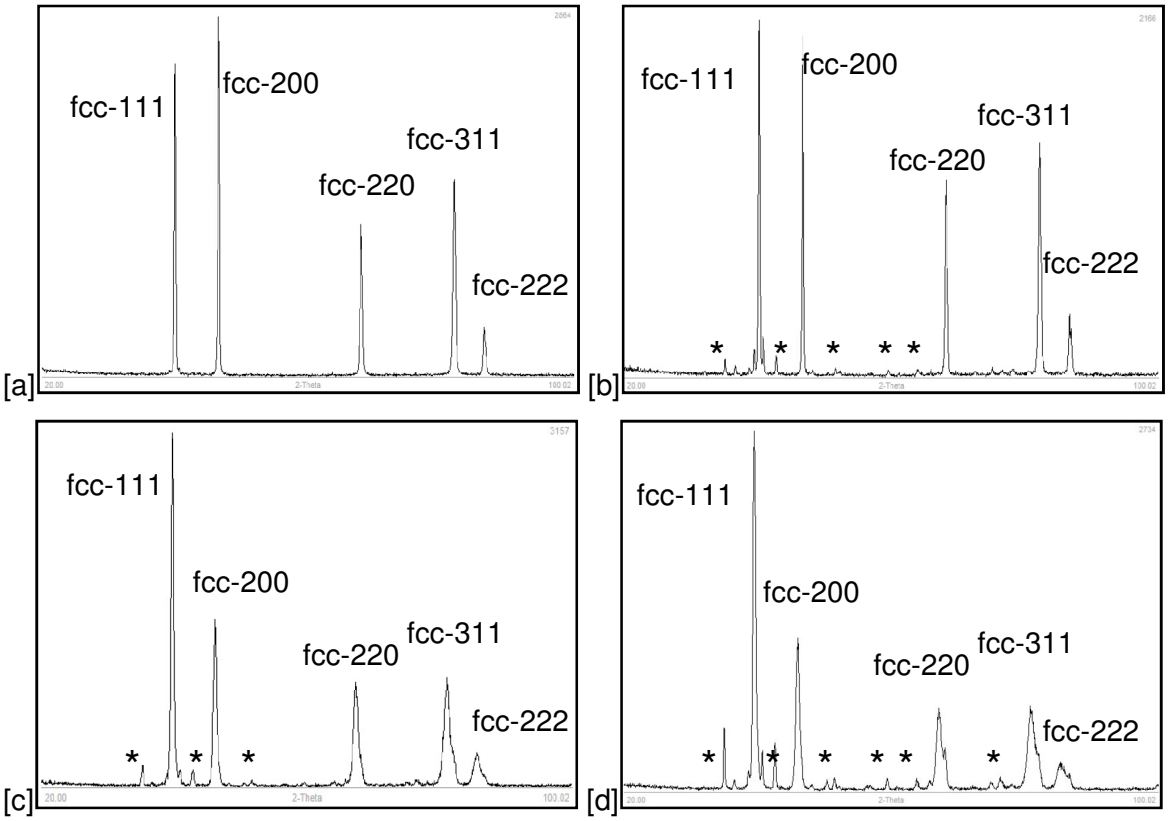

Figure 9.7. XRD analysis, asterisks indicate characteristic peaks of the Pd_4S-tetragonal phase (Gronvold, 1956) [a] RK-16R inlet [b] RK-16R outlet [c] AA-40R inlet [d] AA-40R outlet.

In Figure 9.7[a] and [b] the primary component was identified to be palladium with all characteristic peaks of the fcc-structure falling within 1% of their expected diffraction angles (Swanson and Tatge, 1953). The diffraction angles corresponding to the first five crystal planes of fcc-Pd phase are labeled in Figure 9.7[a] and [b]. For the membrane RK-16R, the bulk Pd_4S phase was observed only very slightly on the outlet sample as evidenced by the characteristic diffraction peaks of the tetragonal-Pd_4S phase seen at 36, 37, 39.5, 43.5, 60, and 64.5°, marked with asterisks in Figure 9.7[b] (Gronvold, 1956). It was expected that a significant amount of bulk sulfide would be observed since the retentate gas composition was in excess of the thermodynamic threshold for Pd_4S formation. It was speculated that the WGS species were reacting with the adsorbed sulfur to form a new, less reactive species (such as COS) and increasing the threshold for Pd_4S formation. Alternatively, the competitive adsorption of the WGS species may have only lowered the rate of bulk sulfide formation so that a longer time frame would be necessary for significant Pd_4S formation.

The characteristic diffraction peaks for the fcc-Pd/Au phase in membrane AA-40R (Figure 9.7[c] and [d]) were shifted to slightly lower angles (40.1 to 39.0° for the fcc-111 peak) with respect to the pure Pd-phase due to the slightly greater lattice constant of the Pd/Au-alloy (Chen, 2011). Bulk Pd_4S phase was observed very slightly on all sections of the membrane AA-40R, marked by asterisks on the XRD spectra (Figure 9.7[c] and [d]). It was also apparent based on the intensity of the Pd_4S peaks that there was a greater extent of Pd_4S formation towards the outlet end, probably because of the depletion of H_2 along the length of the membrane.

The permeation of H_2 through the membrane resulted in a higher H_2S/H_2 ratio of the gas mixture at the outlet end of the membrane (as compared to the inlet composition), and therefore a greater propensity for Pd_4S formation by equation **9.1**. It was surprising to observe Pd_4S formation at the inlet end of the membrane AA-40R (Figure 9.7[c]) since the H_2S/H_2 ratio of $4.0*10^{-5}$ mol_{H2S}/mol_{H2} was less than that utilized by Chen and Ma (2010; Chen, 2011) {$5.5*10^{-5}$ mol_{H2S}/mol_{H2}} in pure H_2/H_2S experiments with $Pd_{90}Au_{10}$ and $Pd_{82}Au_{18}$(surface composition) coupons and membranes, after which no bulk sulfide was observed. Again, the primary difference between this study and that of Chen

and Ma (2010) was the presence of the WGS species, suggesting that a reaction might have occurred to form a new sulfur species with different reactivity to the Pd and Pd/Au-surfaces. It was unreasonable to suggest that the WGS species both raised the threshold for sulfide formation in the pure Pd case and lowered the threshold in the Pd/Au case, so other explainations should be sought after.

EDS spot scans of the surface of AA-40R indicated that the gold concentration was not completely uniform, with some areas having as much as 20 at% and others as little as 11 at% Au. An X-ray image was taken by monitoring the gold $M\alpha^1$, sulfur $K\alpha^1$, and palladium $L\alpha^1$ x-ray emissions. An SEM image of the surface of the AA-40R-outlet sample and the gold $M\alpha^1$ x-ray image are shown in Figure 9.8[a] and [b] respectively. The x-ray image showed that some areas were indeed rich in gold and others mostly absent of gold so spot scans were done on specific locations. The spots labeled 1 and 2 in Figure 9.8[a] had a low gold concentration and the spot 3 had a high gold concentration. The EDS analyses of those spots in terms of Pd, Au, and S are listed in Table 9.4.

[a] 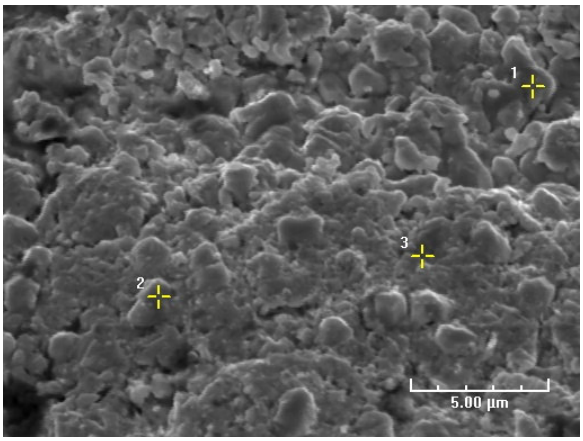

[b] 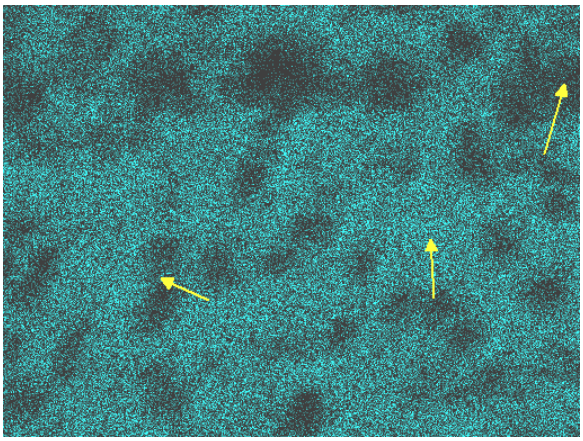

Figure 9.8. Images of AA-40R-outlet at 5,000X [a] SEM image [b] X-ray image of the gold $M\alpha^1$ emission energy.

Table 9.4. Spot scan results corresponding to the locations marked on Figure 9.8[a].

	Pd (at%)	Au (at%)	S (at%)
Spot 1 (low gold)	86.5	3.2	10.2
Spot 2 (low gold)	86.9	3.4	9.8
Spot 3 (high gold)	72.9	22.6	4.5

As suspected, the spots 1 and 2 which were low in gold concentration had significantly increased sulfur contents of 10% whereas the spot 3 which was high in gold concentration had a much lower sulfur content of 4.5%. Locations which were low in gold content adsorbed more sulfur and potentially formed bulk sulfides, while areas which were high in gold content were resistant to bulk sulfide formation. Since the sulfur composition at spots 1 and 2 was only 10 at% it was likely that any Pd_4S was thinner than 200 nm since that was the approximate EDS penetration depth. It was probable that areas low in gold such as spots 1 and 2 were responsible for the observance of bulk Pd_4S by XRD, marked by asterisks in Figure 9.7[c] and [d].

A steady state appeared to have been reached in the mixed gas separation with 20 ppmv H_2S (Figure 9.3[b]), suggesting that the bulk Pd_4S-phase observed could have been in equilibrium with the Pd/Au fcc-phase such that no further formation was occurring over time. As the Pd_4S phase formed, the Au would have become concentrated in the remaining alloy, resulting in greater sulfur tolerance. Additionally, if bulk sulfides were only forming at low gold concentration sites, those areas would have become saturated with sulfur, allowing for equilibrium between the phases present.

9.4.4. WGS CMR with syngas/H_2S feed

The pure Pd-membrane AA-38R was loaded into the WGS CMR with iron-chrome oxide catalyst so that the effect of H_2S on the reactor operation could be quantified. The membrane was first tested in H_2 for 220 hours to determine the H_2 permeance and selectivity stability as shown in Figure 9.9[a]. Reaction experiments were then conducted at 14.6 atma, 400°C, and with simulated syngas (19% CO, 18% H_2, 8% CO_2, 55% H_2O, and with 0 – 2 ppmv H_2S) fed at 2,700 h^{-1}. A lower feed rate was utilized so that experiments could be conducted for extended testing periods, accommodating for

the capacity of the steam trap which had to be emptied every eight hours. The results of the reaction experiments are shown in Figure 9.9[b] in terms of CO conversion, H_2 recovery, and sulfur mass balance for the system.

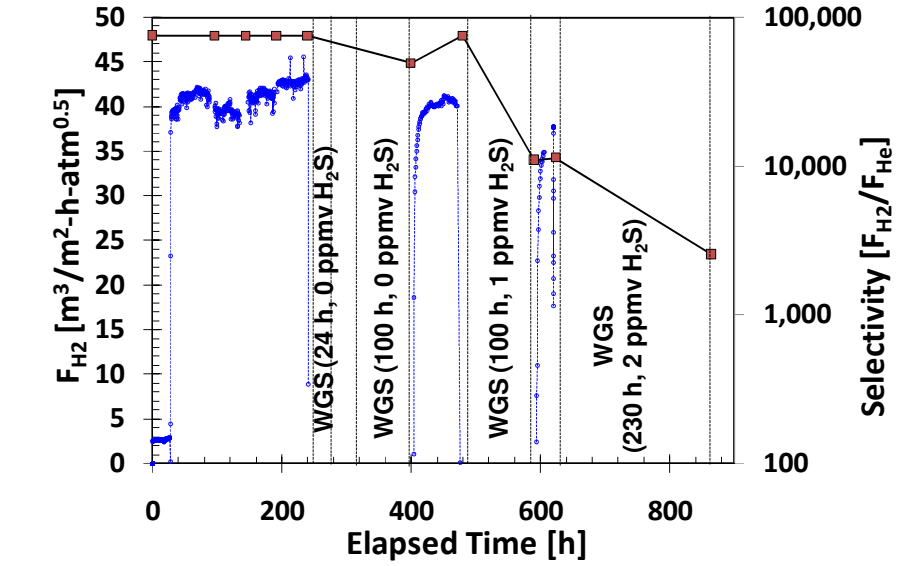

[a]

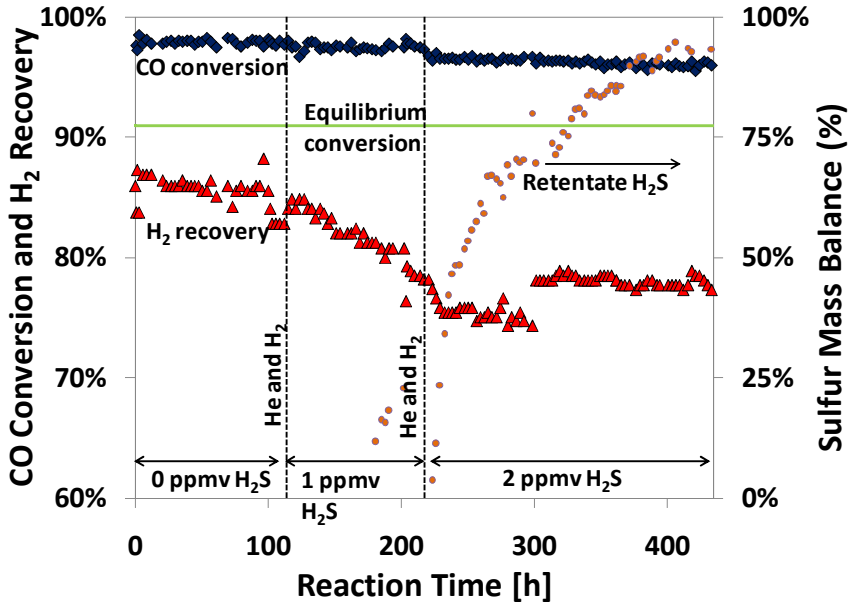

[b]

Figure 9.9. Reaction experiments with H_2S in the feed stream [a] Membrane AA-38R testing history [b] Reaction experiments conducted with membrane AA-38R (19% CO, 18% H_2, 8% CO_2, 55% H_2O; 14.6 atma; 400℃; 2,700 h^{-1}).

The system was first operated with no H_2S present for 100 hours to establish a baseline for comparison, then for 100 hours with 1 ppmv H_2S, then for 230 hours with 2 ppmv H_2S in the feed. Between each period of WGS testing, the system was switched to He for a leak test and then switched to H_2 to test the pure H_2 permeance, as shown in Figure 9.9[a].

During the first 100 hours of WGS reaction testing (shown in Figure 9.9[b]) a stable CO conversion and H_2 recovery of 98 and 86% respectively were observed. The CO conversion and H_2 recovery were both consistent with those measured during similar experiments utilizing the membranes AA-30 (Chapter 7.3.3) and AA-8R (Chapter 7.3.4). Upon the admission of 1 ppmv H_2S to the reactor, the H_2 recovery was observed to gradually decline to 80% over 100 hours due to surface adsorption of H_2S resulting in surface bound S-atoms blocking H_2 adsorption. No H_2S was detectable in the retentate stream until 80 hours had passed, as shown by the sulfur mass balance (plotted on the secondary y-axis in Figure 9.9[b]), since it was being absorbed by the catalyst to form either Fe_2S_3 or Cr_3S_4 (Bohlbro, 1963). The lack of H_2S observed in the retentate indicated that some fraction of the membrane area was not being exposed to the full 1 ppmv of H_2S, and that steady-state conditions had not yet been reached. The rate of increase in the sulfur mass balance suggested that the time frame necessary to achieve steady state was approximately 7.5 additional days, which was prohibitive (considering the cost of the pre-mixed syngas and the potential for instrument disruption leading to experimental failure).

The system was switched back to pure H_2 and the permeance of the membrane, shown in Figure 9.9[a], returned to 89% of its initial permeance, indicating that there was some irreversible surface-poisoning by sulfur. The irreversible poisoning resulted in the 11% loss of pure H_2 permeance, although that could not be compared to the permeance recovery in previous experiments since the system was not fully saturated with H_2S, and therefore the majority of the membrane area was exposed to less than 1 ppmv H_2S. In order to saturate the system with H_2S faster, the higher concentration of 2 ppmv was applied to the reactor.

Upon the admission of 2 ppmv H_2S to the reactor, the H_2 recovery further decreased to 75 – 78% (Figure 9.9[b]) due to increased surface coverage of sulfur on the membrane, which lowered the H_2 permeance. The CO conversion decreased to 96% also as a result of the lower H_2 permeance. Over the final 80 hours the retentate H_2S concentration remained stable at 2.52 ppmv (93% mass balance with respect to the feed), with the H_2 recovery also constant, suggesting that the system was at steady state. The presence of up to 2 ppmv H_2S in the feed stream had a relatively minor effect on the membrane reactor operation in terms of CO conversion and H_2 recovery over 350 hours at 400°C. Since a low feed space velocity was utilized and there was significant gas phase mass transfer resistance, the H_2 recovery was relatively insensitive to the permeance of the membrane, and therefore insensitive to the poisoning effect.

The significant discrepancy in the sulfur balance, observed from a reaction time of 100 - 350 h in Figure 9.9[b], suggested that H_2S was probably forming bulk iron or chromium sulfide species with the catalyst. Bohlbro (1963) reported that iron-chrome oxide catalyst retained 0.5 – 1 wt% sulfur when saturated with 75 ppmv H_2S in syngas. They also showed that the saturation by sulfur did not significantly affect the kinetic rate for the WGS reaction. Since the overall discrepancy in the sulfur mass balance amounted to an estimated 0.014 g sulfur (0.11 wt% on average desposited on the catalyst), the sulfur on the catalyst was not likely detectable by EDS or XRD analysis, and so was not looked for. Since the sulfur mass balance stabilized below 100%, it was possible that some H_2S was also being converted to an alternative sulfur species. A small amount of COS was observed by GC, but was not quantitatively determined due to the lack of a COS standard.

After testing under WGS conditions with 2 ppmv H_2S, the system was switched to helium with a high purge rate and cooled quickly to room temperature as described in Section 9.3.2. After the membrane was removed from the reactor, samples were cut from the inlet, middle, and outlet and analyzed by XRD as shown in Figure 9.10[a] and [b]. The three XRD spectra were virtually identical so the spectrum from the ‘middle’ sample is not shown in the figure.

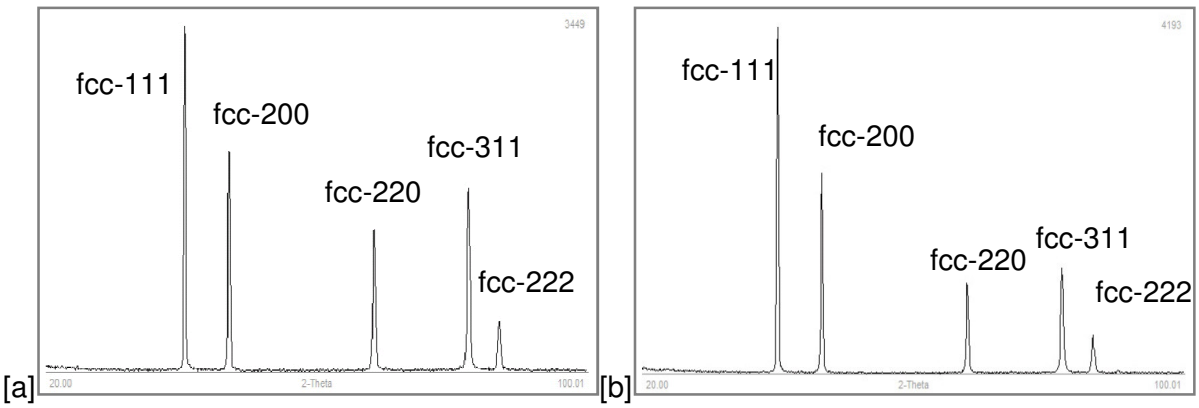

Figure 9.10. Post-testing characterization of AA-38R by XRD (2θ = 20 - 100°) [a] Inlet-sample [b] Outlet-sample.

Only the palladium fcc-phase was observed by XRD as evidenced by the XRD spectra shown in Figure 9.10[a] and [b] of the inlet and outlet samples respectively; the characteristic 111, 200, 220, 311, and 222 diffraction peaks were well resolved and located to within 1% of their expected angles (Swanson and Tatge, 1953). The XRD spectra showed no indication of bulk Pd_4S phase on any of the membrane samples.

The H_2S/H_2 ratio at both the inlet and outlet ($1.1*10^{-5}$ and $1.2*10^{-5}$ mol_{H2S}/mol_{H2}) was significantly in excess of the thermodynamic threshold for bulk Pd_4S formation ($2.8*10^{-6}$ mol_{H2S}/mol_{H2}, Mundschau *et al.*, 2006). The concentration of H_2 at the outlet was only slightly higher than that at the inlet for the membrane AA-38R due to the relatively low concentration of H_2 in the feed mixture (18%); over the length of the membrane H_2 was simultaneously produced by the reaction and removed by the membrane. Chen (2011) conducted coupon poisoning experiments with H_2/H_2S mixtures above and below the thermodynamic threshold as shown in Figure 9.11. The inlet and outlet conditions for the membranes AA-38R, RK-16R, and AA-40R are plotted in the figure with an arrow pointing from the inlet to the outlet conditions. The membrane data was offset slightly from 400°C for ease of viewing the data clearly. The thermodynamic threshold for bulk sulfide formation was also plotted in the figure as a solid curve, calculated by Mundschau *et al.* (2006).

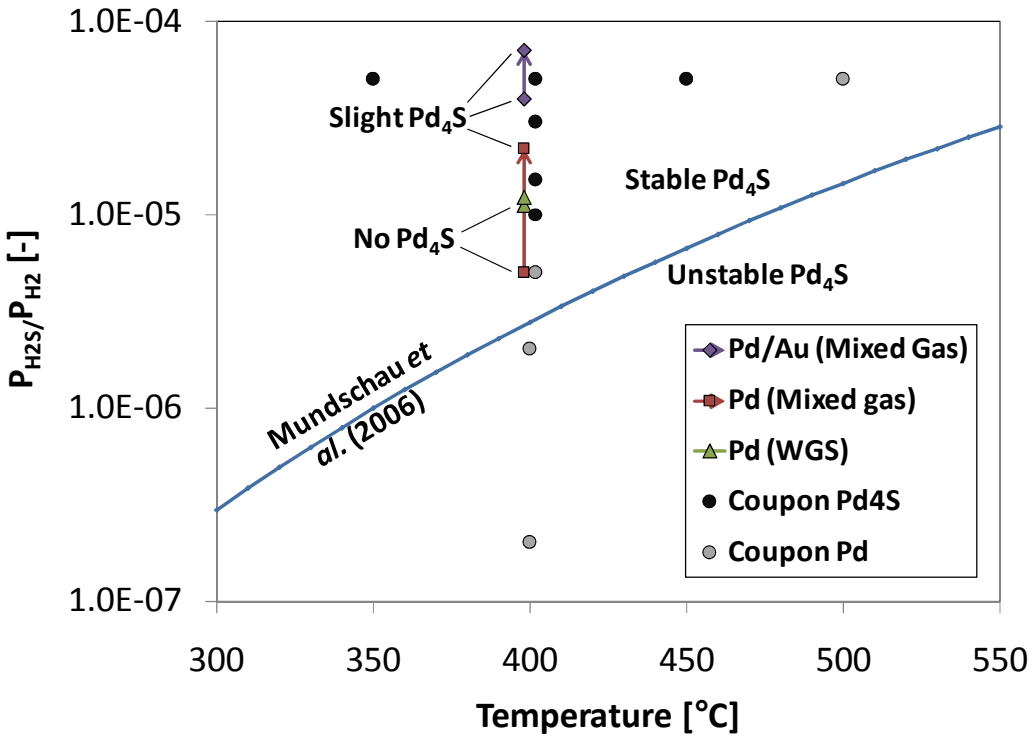

Figure 9.11. H_2S/H_2 ratio versus temperature indicating Pd_4S formation (Membrane data organized as Inlet → Outlet, offset horizontally from 400°C, coupon data from Chen {2011} in circles).

In the study by Chen (2011), Pd_4S formation on Pd-coupons was found to occur about two times above H_2S/H_2 equilibrium ratio proposed by Mundschau *et al.* (2006) due to an insufficient time necessary to reach thermodynamic equilibrium. The pure Pd-membrane AA-38R tested in this work was subjected to higher H_2S/H_2 conditions, and for longer time periods than coupons poisoned by Chen (2011) and yet no bulk Pd_4S was observed. The outlet of the membrane RK-16R was subjected to significantly higher H_2S/H_2 conditions than the coupon poisoned by Chen (2011) where significant sulfide formation had occurred, yet only slight Pd_4S was observed in RK-16R.

It was possible that a reaction was occurring on the Pd-surface, resulting in the conversion of H_2S to a less poisonous species, thereby lowering the effective H_2S/H_2 ratio. Faraji *et al.* (1996) showed that both COS and CH_3SH can be formed from H_2S

and CO mixtures at 350℃. If this reaction were diffusion limited then only a small amount of H_2S conversion would be observed at the outlet, but a significant fraction of the H_2S could have been depleted at the membrane surface. Indeed, a small amount of COS was measured by GC in the retentate as was mentioned above. To study this potential effect, analysis of the retentate gas stream would have to be conducted by mass spectroscopy to determine the other trace sulfur species present in the retentate but not in the feed.

Alternatively, the lower extent of Pd_4S formation in this study as compared to that of Chen (2011) may not have been due to a change in the H_2S concentration near to the Pd-surface, and may instead have resulted from a lower rate of Pd_4S formation. The formation of bulk Pd_4S formation proceeded first by surface adsorption, followed by dissociation, followed by incorporation into the bulk. Competition for surface sites by other adsorbed species (CO and H_2O) could lower the rate of any of those steps. There were no literature studies found to support this possibility.

In previous studies (Chen, 2011; Morreale *et al.,* 2007; Iyoha *et al.,* 2007b) H_2S exposure has been observed to cause significant changes in the Pd-surface morphology so SEM analysis was conducted for several surface samples from each of the membranes tested under H_2S conditions. SEM images of the membrane AA-38R inlet and outlet-samples are shown in Figure 9.12[a] and [b] respectively. Images are shown of the surface of membrane RK-16R inlet and outlet-samples in Figure 9.12[c] and [d] respectively. Images are shown of the surface of membrane AA-40R inlet and outlet-samples in Figure 9.12[e] and [f] respectively.

[a] 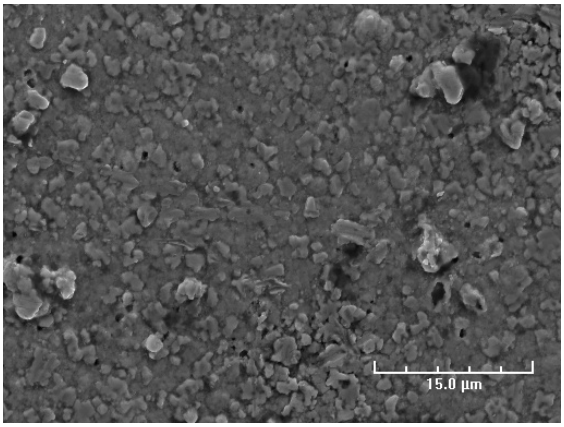

[b] 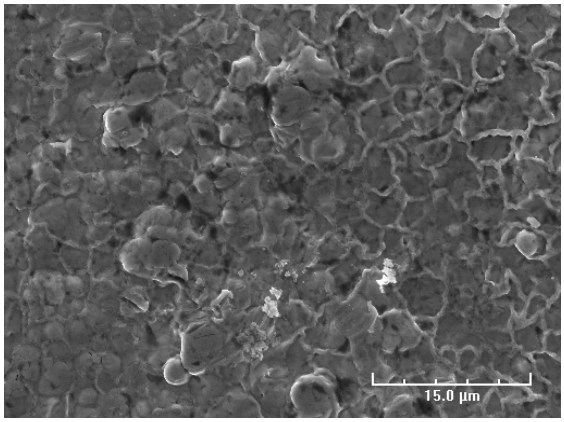

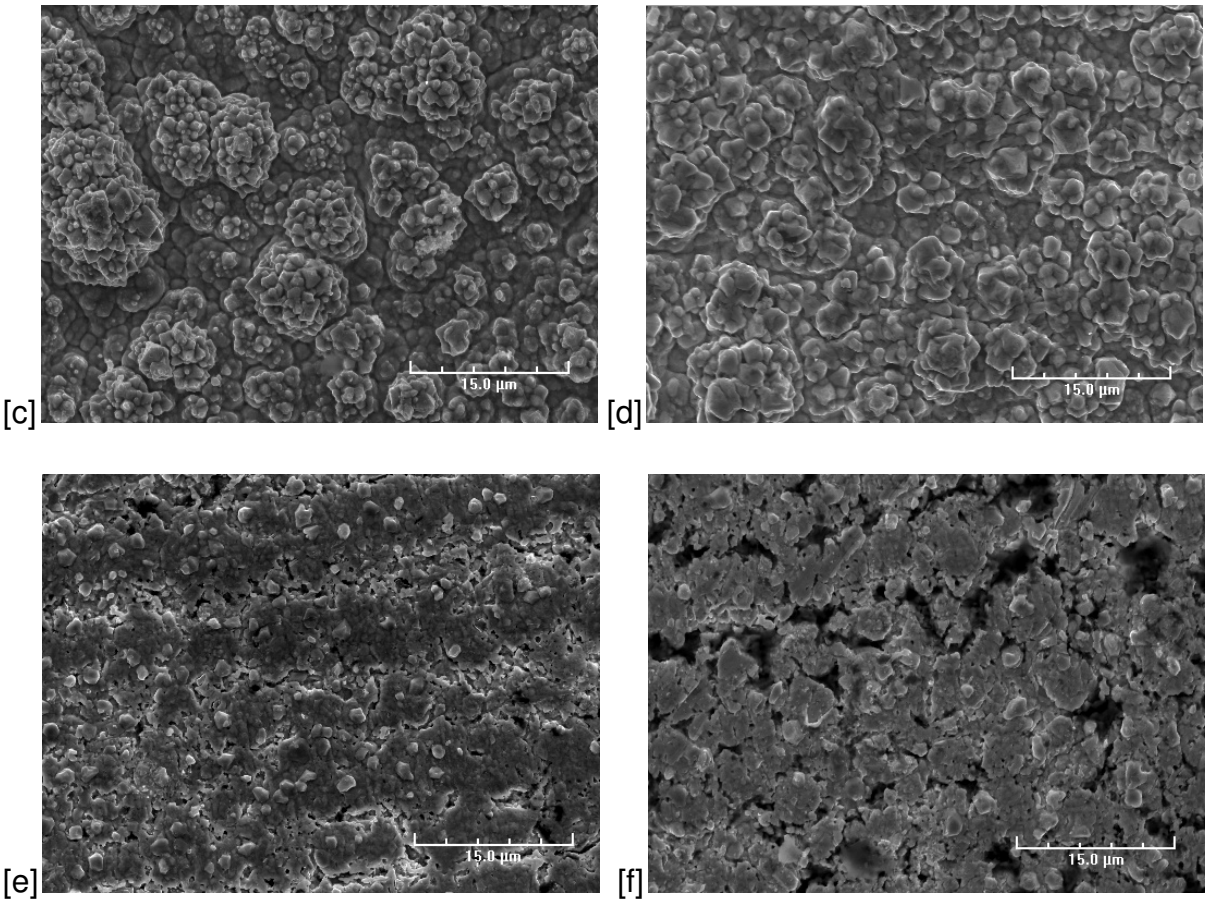

Figure 9.12. Surface morphology images of membranes poisoned with H_2S (2,500X) [a] AA-38R-inlet [b] AA-38R-outlet [c] RK-16R-inlet [d] RK-16R-outlet [e] AA-40R-inlet [f] AA-40R-outlet.

The SEM images of the membrane AA-38R-inlet and outlet showed very different surface morphology, with the inlet sample (Figure 9.12[a]) showing more sharply defined Pd-clusters, and the outlet sample (Figure 9.12[b]) showing smoother Pd-crystallites with peculiar ridges at their boundaries. The surface morphology of AA-38-outlet was somewhat similar to morphology previously observed after Pd poisoning by 5 - 10 ppmv H_2S in H_2 (Chen, 2011; Iyoha *et al.,* 2007b). The morphology change was explained as sulfur segregation to the grain boundaries and the start of bulk Pd_4S formation at those locations (Pomerantz and Ma, 2009; Chen, 2011). Both SEM images

showed some evidence of pinhole formation on the order of 0.5 μm which was surprising given the testing temperature of only 400°C (Guazzone and Ma, 2008).

The images of the membrane RK-16R-inlet and outlet were very similar, showing distinct and sharp Pd-crystallites of 1 – 3 μm in size. Surprisingly, the morphology observed on the RK-16R-outlet (Figure 9.12[d]) was not at all similar to that of the AA-38R-outlet, despite the exposure to a greater H_2S/H_2 ratio, and indications of Pd_4S formation by XRD (Figure 9.7[b]). The membrane RK-16R showed significantly larger grain clusters than AA-38R because no mechanical treatments were conducted on RK-16R to smooth the surface. The membrane AA-38R had a significant mechanical polishing applied after annealing and before initial testing (when the membrane was refered to as AA-38, no "R"), resulting in a much finer surface for Pd-plating. The surface inhibition by H_2S resulted in a rate limitation for the surface adsorption step in the H_2 permeation mechanism (Ward and Dao, 1999). Since the membrane RK-16R had a rough surface (compared to AA-40R), the rate of H_2 adsorption may have been higher due to more surface sites per superficial area, partially compensating for the inhibition by H_2S. The increased surface roughness of RK-16R perhaps explained why its performance under H_2S poisoning was better than expected, and closely in line with the results of the Pd/Au-membrane AA-40R.

The images of the membrane AA-40R-inlet and outlet were similar, showing distinct metal crystallites, but also significant porosity or large pinhole formation on the order of 1 – 3 μm in size. It was unclear whether this unusual porous character resulted from the testing in H_2S or if it resulted from the fabrication. Regardless, it was unlikely that the porosity extended deeply into the Pd/alloy-layer since the selectivity was so high (greater than 2,500). It was possible that during the electroplating some palladium was displaced off of the surface resulting in small cavities. It was also possible that during the annealing at 450°C, the porosity resulted from the Kirkendall effect (Smigelskas and Kirkendall, 1947) as gold diffused into the palladium (and away from the surface) at a higher rate than palladium diffused into gold. Considering the different fabrication methods employed for the membrane AA-40R, it was unsurprising that the surface morphology was different from the other two membranes.

9.5. Conclusions

Experiments conducted with 1 ppmv H_2S in 100% H_2 and in 50% H_2/N_2 showed that the presence of an inert gas (N_2) increased the poisoning effect of the 1 ppmv H_2S due to the nature of the reversible adsorption at low-ppm levels of H_2S. Experiments conducted on a pure Pd-membrane with 1 ppmv H_2S in 50% H_2/N_2 and 4 – 25% H_2O (balance N_2) resulted in gradually decreasing membrane H_2 flux over time, suggesting that the combined effect of H_2S and H_2O was causing more irreversible poisoning to the membrane.

A Pd-membrane was tested under shifted syngas (50% H_2, 30% CO_2, 19% H_2O, 1% CO) with 0, 1, and 2.5 ppmv H_2S present. With no H_2S present, high H_2 flux and recovery (14.0 m^3/m^2-h and 90% respectively) were achieved which were consistent with previous studies. With 2.5 ppmv H_2S present a gradual decline in H_2 flux and recovery was observed over 25 hours and Pd_4S-phase was observed by XRD on the membrane surface at the outlet end. A $Pd_{90}Au_{10}$-membrane was also tested under shifted syngas with 0 - 20 ppmv H_2S in the feed. The H_2 flux decreased significantly with increasing amounts of H_2S up to 5 ppmv, but then only decreased slightly due to the addition of 10 and 20 ppmv H_2S, suggesting a saturation of the Pd-surface by sulfur. A stable H_2 flux of 7.8 m^3/m^2-h (with 44% H_2 recovery) was achieved with 20 ppmv H_2S present for 25 hours. Regardless of the stable H_2 flux, some Pd_4S-phase was still observed by XRD on the membrane surface at the feed and the retentate ends.

The WGS Pd-CMR was operated with 0, 1, and 2 ppmv H_2S for 440 hours; steady-state conditions were achieved only after the system was saturated with H_2S for 360 hours. With 2 ppmv H_2S in the feed, a stable CO conversion and H_2 recovery of 96 and 78% respectively were achieved for the final 80 hours. No bulk Pd_4S was detected anywhere on the membrane surface by XRD and the addition of 2 ppmv H_2S to the WGS mixture did not result in a significant change to the membrane selectivity.

The low level of Pd_4S formation on the Pd-membranes indicated that a reaction was probably occurring between H_2S and the WGS species on the Pd-surface to produce COS, thereby increasing the thermodynamic threshold for Pd_4S formation.

10. DURABILITY OF SUPPORTED Pd-MEMBRANES UNDER MIXED GAS AND WGS CONDITIONS

10.1. Introduction

One of the key performance requirements for PSS supported Pd-membranes to be applied in a commercial setting is long-term permeance and selectivity stability. Relatively few studies have unambiguously demonstrated robust membrane stability over periods on the order of 1,000 hours. In such a context, very thin Pd/alloy-membranes (1.5 – 5.5 μm) have been prepared on porous alumina or porous ceramic supports through electroless deposition and have shown excellent results under pure H_2 testing (Roa and Way, 2003; Hou and Hughes, 2003; Pan *et al.,* 2003). Kulprathipanja *et al.* (2004), on the other hand, tested similar $Pd_{75}Cu_{25}$-membranes in reactive H_2/CO_2 and H_2/CO atmospheres and observed a significant decrease in the ideal H_2/N_2 selectivity. They also observed increased surface roughness by SEM for which they proposed several possible causal roots: lattice stress relaxation, bcc/fcc phase transition in the Pd/Cu-alloy, Pd-grain coalescence, or Pd-grain sintering.

In light of the above considerations, one of the most promising types of membrane for use in a membrane reactor process is the dense Pd-membrane supported on PSS due to their low support resistance and high mechanical strength. The membranes prepared in this study (Chapter 4) as well as several literature examples (Guazzone and Ma, 2008; Peters *et al.,* 2009) have already shown excellent permeance and selectivity stability during pure H_2 testing. Several examples from the literature are summarized in Table 10.1.

Table 10.1. Summary of long-term testing of Pd and Pd/alloy membranes.

Support	Selective layer	Temp [℃]	H_2 permeance	Testing conditions	Testing time [h]	Final selectivity	Reference
ZnO_2/porous alumina	1.5 μm $Pd_{90}Cu_{10}$	450	12.5 m^3/m^2-h-atm	H_2, 2 atma	4,100	7,000 (H_2/N_2)	Roa and Way, 2003
Porous alumina	5.5 μm PdAg*	200 – 400	15.3 m^3/m^2-h-$atm^{0.61}$	H_2, 4 atma	960	4,500 (H_2/N_2)	Hou and Huges, 2003
Porous alumina	3.0 μm Pd	430	16.2 m^3/m^2-h-atm	H_2, 2.5 atma	800	1,300 (H_2/N_2)	Pan *et al.,* 2003
ZnO_2/porous alumina	3.0 μm $Pd_{75}Cu_{25}$	450	8.8 m^3/m^2-h-atm	50% H_2/CO_2, 95% H_2/CO, 3.8 atma	340	11 (H_2/N_2)	Kulprathipanja *et al.,* 2004
Porous Hastelloy	4.0 μm Pd	400	42.6 m^3/m^2-h-$atm^{0.5}$	H_2, 2 atma	2,200	22,000 (H_2/He)	Guazzone and Ma, 2008
PSS	4.0 μm $Pd_{77}Ag_{23}$	350 – 450	24.2 m^3/m^2-h-atm	50% H_2/N_2, 19.8 atma	2,400	500 (H_2/N_2)	Peters *et al.,* 2009
PSS	20 μm Pd	350	5.0 m^3/m^2-h-$atm^{0.5}$	CH_3OH SR, 14.9 atma	900	4,000 (H_2/N_2)	Lin and Rei, 2001
Self supported	2 – 6 μm Pd 380 μm Ta	425	1.74 m^3/m^2-h-$atm^{0.5}$	66% H_2/H_2O, 20.8 atma	70	>17,000 (H_2/He)	Torkelson *et al.,* 2008
		425	1.74 m^3/m^2-h-$atm^{0.5}$	WGS, 15.4 atma	25	>17,000 (H_2/He)	
Porous alumina	10.9 – 13.8 μm Pd	550	17.8 m^3/m^2-h-atm	CH_4 SR, 15 – 35 atma	120	NR*	Li *et al.,* 2011
PSS	<20 μm Pd/rare earth*	495 – 540	NR*	CH_4 SR, 9.1 atma	3,300	>10,000† (H_2/other)	Shirasaki *et al.,* 2009

*further details not reported †estimated separation factor

Examples in the literature of Pd-membranes tested for extended periods under reaction conditions are far fewer, and are also listed in Table 10.1. Lin and Rei (2001) fabricated a 20 μm Pd-membrane on an alumina graded PSS support and tested it under methanol Steam Reforming (SR) conditions for 900 hours at 350°C. They observed a stable H_2 flux and selectivity over the whole testing period, likely due to the thickness of the selective layer. Torkelson *et al.* (2008) electroless plated a 2 - 6 μm Pd-layer onto a dense 380 μm thick Ta-tube. The Pd-layer catalyzed the adsorption and dissociation of H_2, and the Ta-tube acted as the selective layer. They tested one of the membranes in 66% H_2/H_2O, 20.8 atma, and 425°C for 70 hours, observing a stable selectivity and a gradual reduction in the H_2 flux of 20%, which they attributed to the reversible surface adsorption of H_2O. They tested another similar membrane for 25 hours in 4% CO, 90% H_2, and 5% He, then 25 hours in 3% CO, 62% H_2, 31% H_2O, and 3% He, both at 425°C and 15.3 atma, observing a stable H_2 permeance and an undetectable leak. Li *et al.* (2011) tested eight Pd/porous alumina membranes simultaneously in a multi-tube MSR CMR for over 120 hours of reaction conditions: 550°C, 15 – 35 atma, $H_2O/CO = 3$, and 1,000 – 3,100 h^{-1}. They reported stable H_2 recovery and CH_4 conversion, but unfortunately did not report post-testing leak or selectivity data. The Tokyo Gas Company Ltd. has commercialized a membrane MSR capable of 40 m^3/h H_2 production from natural gas, for which they demonstrated 3,300 hours of membrane permeance and selectivity stability for their PSS supported, Pd/rare-earth-metal alloy films. However, since their work was proprietary, the membrane synthesis and characterization details were not clearly reported (Shirasaki *et al.,* 2009).

Considering the studies in the literature that included long-term Pd-membranes tested under reactive conditions, the membranes utilized all had prohibitively low H_2 permeance (Lin and Rei, 2001; Torkelson *et al.,* 2008) or prohibitively low selectivity (Kulprathipanja *et al.,* 2004), rendering those types of membranes unviable for commercial applications (Mendes *et al.,* 2010; Shu *et al.,* 1991). Therefore, in addition to recognizing the paucity of experimental data concerning highly permeable membranes tested for long-term stability under mixed gas and WGS conditions, the objective of this study was to develop a comprehensive framework to assist our understanding of leak growth mechanisms based on several long-term tests, as well as

post-test membrane characterization. In particular, economically viable (lower cost) stainless steel supports were utilized so that the membrane synthesis and subsequent long-term testing closely mirrored that of a commercial process. Effects such as coke formation and surface rearrangement were also discussed in this context since they had the potential to gradually alter the H_2 permeance of the membranes.

10.2. Experimental

The relevant synthesis details and initial H_2 testing results of the membranes utilized in this chapter are listed in the Table 10.2. The preparation and initial testing of those membranes was discussed in Chapter 4.

Table 10.2. Membranes tested in this chapter, comprehensive details are given in Appendix D.

	Pd/Ag [μm]	Dense layer [μm]	H_2 permeance* [m^3/m^2-h-$atm^{0.5}$]	Final select.† [F_{H2}/F_{He}]	Other details
AA-21	4.8	15.7	20.2	175	
AA-24R	6.2	7.4	28.5	365	High temp annealing
AA-29	<1	9.3	24.1	1,700	
AA-30	<1	9.5	28.6	240	
AA-38R	N/A	4.4	41.2	2,600	
AA-40R	N/A	2.7	38.0	340	10 at% Au
RK-16R	N/A	6.0	37.5	675	
IM-79	12.2	10.2	23.2	1,100	
IM-86b	1.0	7.5	33.7	1,200	

*at 400°C

†selectivity after final mixed gas or WGS experiment described here

The rate of leak development or the change in He permeance over time, $\Delta F_{He}/\Delta t$, was determined by dividing the change in He permeance by the time period between leak measurements, equation **10.1**. If the plot of He leak versus time was mostly linear, then equation **10.1** was applied to the first and final leak measurements for a period of uniform testing conditions. Note that the change in He permeance over time is in units of m^3/m^2-h^2-atm.

$$\frac{\Delta F_{He}}{\Delta t} = \frac{F_{He,2} - F_{He,1}}{t_2 - t_1} \quad \textbf{10.1}$$

The H_2/CO separation factor was calculated for some membranes during mixed gas and WGS testing by equation **2.33**.

$$\alpha_{H2-CO} = \frac{y_{H2}/y_{CO}}{x_{H2}/x_{CO}} \quad \textbf{2.33}$$

where y_{H2} is the mole fraction of H_2 in the permeate, y_{CO} is the mole fraction of CO in the permeate, x_{H2} is the mole fraction of H_2 in the retentate, and x_{CO} is the mole fraction of CO in the retentate.

10.3. Results and discussion

10.3.1. Effect of high pressure H_2 on leak growth

In the majority of the long-term mixed gas and WGS CMR experiments conducted, a pressure of 4.4 – 14.6 atma was utilized, with an H_2 partial pressure of up to 7.3 atma. Although some studies have been done in the past to rule out the possibility of membrane degradation due to high H_2 pressure (Guazzone *et al.,* 2006), it was still important to rule out that possibility in the present study. As such, the membrane AA-29 was tested in H_2 at the elevated pressure of 4.9 atma for 550 hours. The membrane IM-79 was also tested with an H_2 pressure of 4.9 and 7.9 atma for 50 hours each. The He leak of both membranes as well as the H_2 permeance (of IM-79 only) is plotted over time in Figure 10.1.

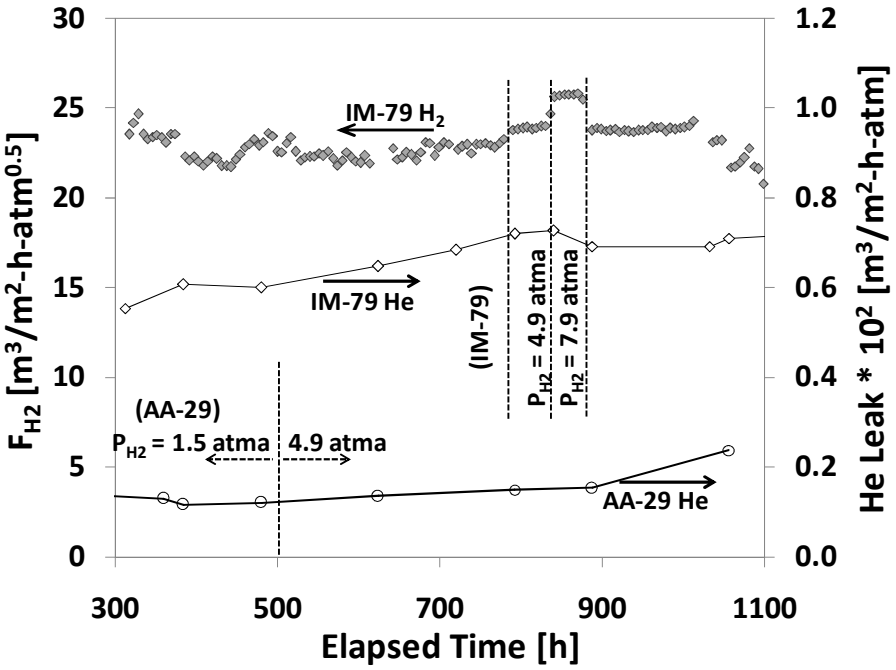

Figure 10.1. He leak development during pure H_2 testing at elevated pressure for AA-29 and IM-79 (H_2 permeance shown for IM-79 only).

As can be seen in Figure 10.1, the slope of the leak over time during high pressure testing did not deviate from that measured beforehand, essentially reducing the possibility that the elevated H_2 pressure adversely affected the dense Pd-layer. As was discussed in Chapter 4, Section 4.4.4, the change in stress/strain of approximately 100 MPa due to 7.9 atma of H_2 was not great enough to cause cracks or pinhole formation in defect free membranes. The rate of leak growth in both of these membranes, $4.60*10^{-6}$ and $3.46*10^{-6}$ m^3/m^2-h^2-atm for AA-29 and IM-79 respectively, was in line with other literature results (Guazzone and Ma, 2008; Peters *et al.,* 2009). The leak growth rates, $\Delta F_{He}/\Delta t$, of all of the membranes tested in this chapter (with regard to the testing conditions, and determined by equation **10.1**) as well as some examples from the literature are listed in Table 10.3.

Table 10.3. Comparison of He leak growth rates under H_2, mixed gas, and WGS conditions.

Membrane	$\Delta F_{He}/\Delta t$ in H_2 at 400°C [m^3/m^2-h^2-atm]	Conditions, Time [h]	$\Delta F_{He}/\Delta t$ under conditions [m^3/m^2-h^2-atm]	α_{final} [F_{H2}/F_{He}]
Guazzone and Ma, 2008	3.88×10^{-7}	H_2, 2,290	N/A	22,000
Peters *et al.,* 2009	6.73×10^{-6} (N_2)	H_2/N_2, 2,400	N/A	500*
AA-29	4.60×10^{-6}	H_2 (4.8 atma)	N/A	1,710
AA-21	2.92×10^{-5}	H_2/H_2O, 40	4.93×10^{-4}	175
IM-86b	1.91×10^{-6}	H_2/H_2O, 190	3.99×10^{-6}	1,230
RK-16R	2.50×10^{-5}	Shifted syngas, 72†	6.31×10^{-5}	675
AA-40R (10%Au)	1.25×10^{-5}	Shifted syngas, 24	3.30×10^{-5}	1,540
		Shifted syngas, 144‡	7.45×10^{-5}	340
AA-24R	2.90×10^{-6}	WGS, 110	2.66×10^{-4}	365
IM-79	3.46×10^{-6}	WGS, 65	9.44×10^{-6}	1,110
AA-30	2.60×10^{-5}	WGS, 500 pt 1	7.52×10^{-7}	2,000
		WGS, 500 pt 2	4.38×10^{-5}	240
AA-38R	$<1\times10^{-7}$	WGS, 124	$<1\times10^{-7}$	11,300
		WGS, 330†	1.98×10^{-5}	2,550

*H_2/N_2 selectivity †With 0 – 2.5 ppmv H_2S present ‡With 0 – 20 ppmv H_2S present

10.3.2. Effect of H_2O on leak growth

The testing under H_2/H_2O mixed gas was conducted in order to isolate the effects of the H_2O on the supported Pd-membrane as a preliminary to long-term WGS tests. In the subsequent sections, experiments were conducted with syngas mixtures in which it may be supposed that the differences in H_2 permeance and He leak stability may be attributed to the presences of CO and/or CO_2 in the gas mixture.

The membranes AA-21 and IM-86b were both tested initially in pure H_2 then in H_2/H_2O mixtures to determine if the presence of H_2O would accelerate the leak growth. The membrane AA-21 was tested in H_2 at 400°C for 280 hours, then in 37% H_2O in H_2 at 14.6 atma and 5,000 – 20,500 h^{-1} feed flow rate for 40 hours. Figure 10.2 shows the H_2 permeance and He leak of the membrane AA-21 for the whole testing period.

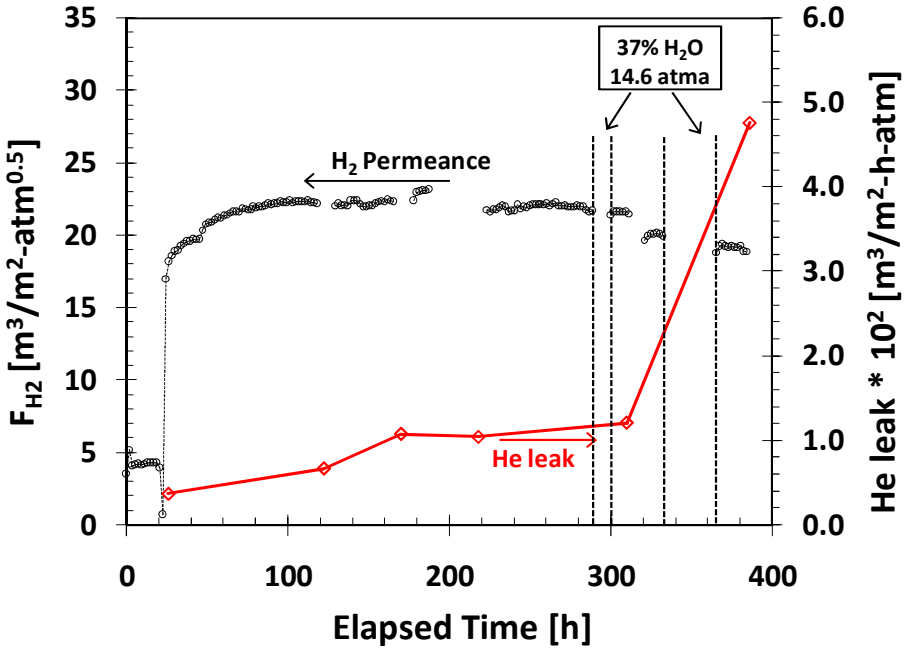

Figure 10.2. Testing history of AA-21 including H_2, He, and H_2/H_2O testing (Pure He leak plotted on the secondary y-axis).

No significant change in He permeance was observed during an initial, short (8 h) period of H_2/H_2O testing. After a longer period of H_2/H_2O testing (time = 335 - 365 h in Figure 10.2) significant He leak growth was observed, probably due to convection cooling of the membrane surface by the high feed rate utilized. In an attempt to characterize the permeation behavior over a range of feed rates (discussed in Chapter 6), a feed rate as high as 4.5 L/min was maintained for one hour during which time the temperature was observed to fluctuate by up to 15℃ over several minutes, which may have been enough to accelerate leak development. It was also possible that incomplete mixing was occurring due to the low residence time (1.1 sec by equation **6.16**) in the pre-heater. The He permeance growth rate is listed in Table 10.3 for the pure H_2 testing and for the H_2/H_2O testing periods of AA-21. To better study the effect of H_2/H_2O mixtures, a new pre-heater was constructed with a significantly larger mixing volume (160 cm^3 instead of 14 cm^3), and experiments were conducted at lower total feed rates with the membrane IM-86b.

The membrane IM-86b was initially tested for 1,000 hours in H_2 and had a very low rate of He leak growth ($1.91*10^{-6}$ m^3/m^2-h^2-atm). After the initial H_2 testing, the membrane was tested under H_2/H_2O mixtures at 2.6 - 6 atma and 400°C for 50 hour periods, between which, the system was switched to He and then back to H_2 for pure gas permeation measurements. The testing history is shown in Figure 10.3 in terms of pure H_2 permeance, H_2 flux during H_2/H_2O testing periods, and pure He leak measurements plotted on the secondary y-axis.

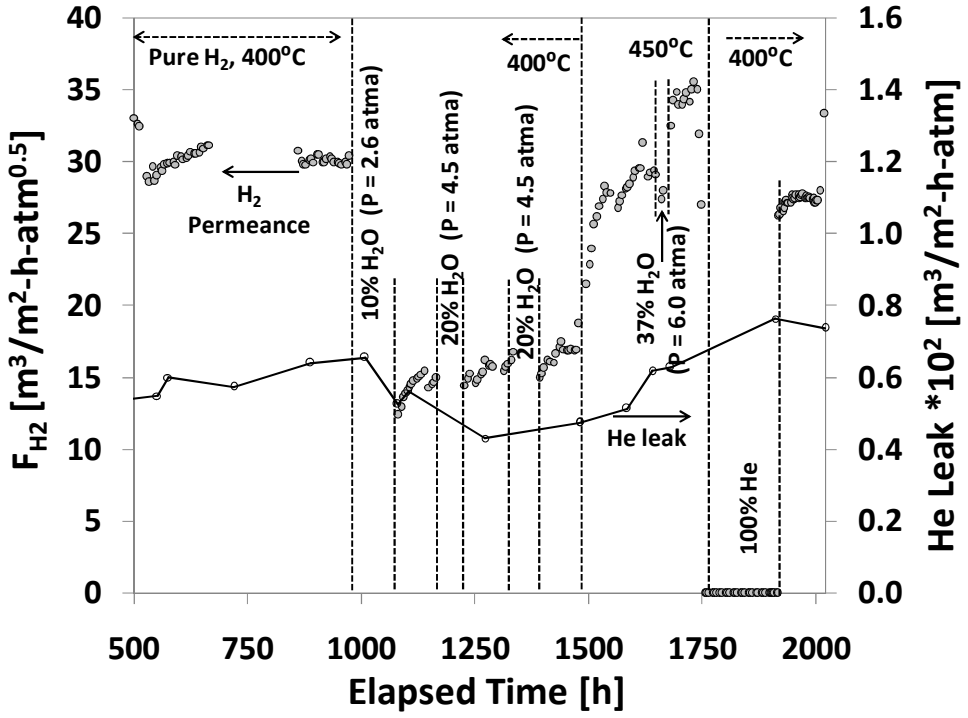

Figure 10.3. Pure H_2 testing of IM-86b, with 50 hour periods of H_2/H_2O mixed gas testing (He leak plotted on the secondary Y-axis).

Following the first 50 hour period of H_2/H_2O exposure (time = 1,050 hours in Figure 10.3) the system was switched back to pure H_2 and the H_2 permeance of the membrane remained at 40% of the initial pure H_2 permeance, possibly due to poisoning from the walls of the newly installed pre-mixer (installed at time = 960 h). After additional H_2/H_2O testing periods the H_2 permeance increased slightly, suggesting that the poisoning effect had ceased; when the temperature was raised to 450°C nearly complete recovery

of the H_2 permeance resulted (as shown at time = 1,500 hours in Figure 10.3). The He leak slightly decreased, apparently as a result of the first two H_2/H_2O testing periods, which was unusual and may have been due to the poisoning from the walls of the newly installed pre-mixer. After the initial decrease in He leak, gradual leak growth occurred at a rate of $3.99*10^{-6}$ m^3/m^2-h^2-atm, almost equivalent to that observed during pure H_2 testing. The leak growth rate of the membrane MA-86b under pure H_2 testing and under H_2/H_2O conditions is listed in Table 10.3.

Several studies have shown that H_2O reversibly adsorbed on the Pd-surface and ceased to affect the H_2 permeance within less than 30 minutes of returning to pure H_2 (Li *et al.,* 2000; Hou and Hughes, 2002; Gielens *et al.,* 2006). There has been no evidence in the literature, during short-term experiments, to suggest that H_2O, in any form, penetrated into the bulk Pd. It was, therefore, unsurprising that over the long-term testing similar rates of leak growth were measured under pure H_2 conditions and H_2/H_2O mixed gas conditions in the membrane MA-86b, such that H_2O did not accelerate the leak growth.

10.3.3. Effect of syngas on leak growth

Membranes were tested in a synthetic syngas mixture to determine if the species CO or CO_2 could have altered the rate of leak growth in the Pd-layer. The pure Pd-membrane RK-16R and the Pd/Au membrane AA-40R were both tested in shifted syngas (50% H_2, 30% CO_2, 19% H_2O, and 1% CO) for extended periods of time, first with no H_2S present, then with 1 – 20 ppmv H_2S for the study conducted in Chapter 9. The leak growth and permeate CO levels over time for the membranes RK-16R and AA-40R are shown in Figure 10.4[a] and [b] respectively. For the membrane RK-16R, the He leak was not measured after initial mixed gas testing and before H_2S was introduced, so changes in the leak growth of that membrane could be attributed to mixed gas exposure and/or H_2S poisoning.

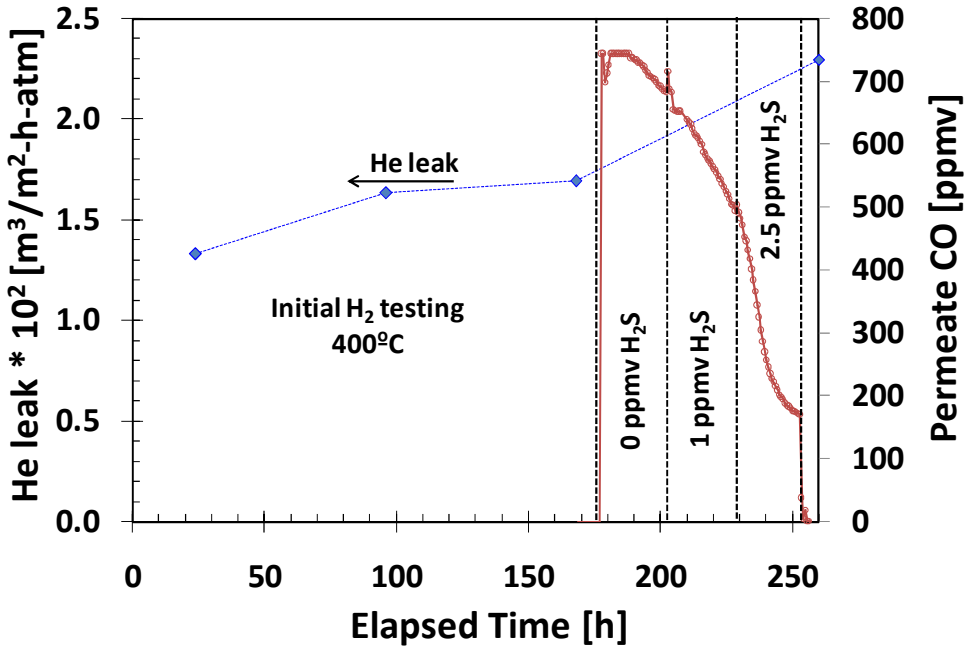

[a]

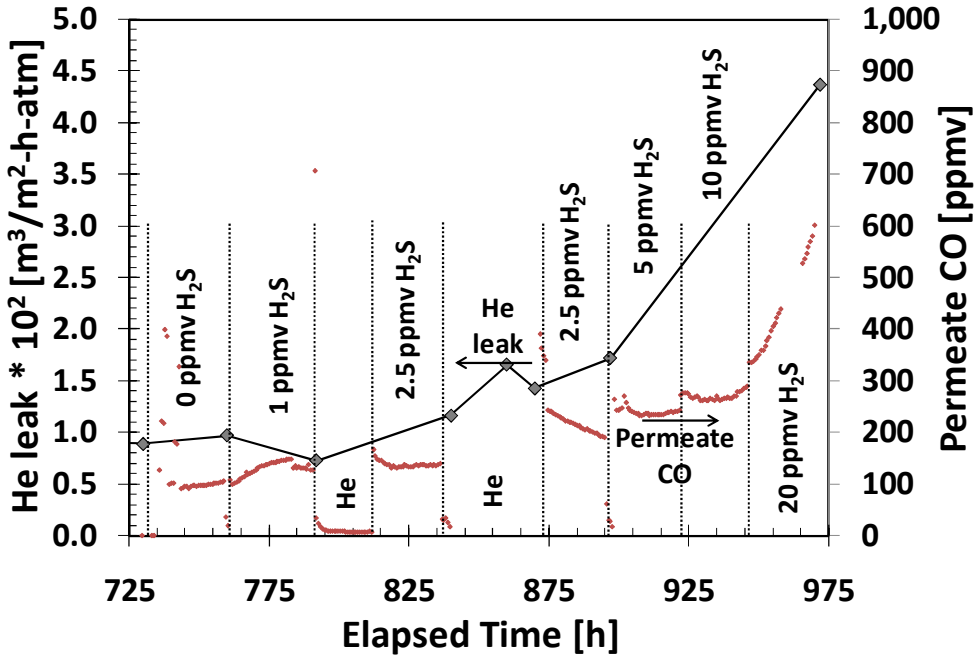

[b]

Figure 10.4. Leak development during shifted syngas testing [a] RK-16R [b] AA-40R (50% H_2, 30% CO_2, 19% H_2O, and 1% CO; 400°C; 13.9 atma; $GHSV_{STP}$ = 5,600 h^{-1}).

The leak growth rate measured for the membrane RK-16R approximately doubled due to mixed gas testing with up to 2 ppmv H_2S present. The leak growth rate measured in the membrane AA-40R also approximately doubled due to mixed gas testing (with no H_2S) then doubled again due to the addition of up to 20 ppmv H_2S (all leak growth rates are listed in Table 10.3). While the results were complicated by the simultaneous mixed gas and H_2S exposure, it was clear that the combination of those factors increased the leak growth in the Pd-membrane, significantly exceeding that measured in pure H_2 (Guazzone and Ma, 2008; Peters *et al.,* 2009). As can be seen in Figure 10.4[b], as greater concentrations of H_2S were added, the leak growth rate increased even more.

In a related study by Gade *et al.* (2011), significant leak growth occurred in both $Pd_{90}Au_{10}$ and $Pd_{80}Au_{20}$-membranes upon exposure to a similar mixed gas composition including 20 ppmv H_2S, which was attributed to a loss of membrane thickness due to corrosion spalling or flaking. Peters *et al.* (2012) did not observe leak growth but did observe a significant surface pitting which they attributed to (intentional) air exposure at 450°C. Surface morphology and cross-section images were shown of both the membranes RK-16R and AA-40R in Chapter 9 (Section 9.4.4). Typical surface morphology features were observed for the membrane RK-16R considering the extended tested at 400°C. It was unclear from those images if significant surface morphology changes occurred with the membrane AA-40R due to the different fabrication methodology, as discussed in Chapter 9. The cross-section images showed a dense Pd thickness in line with the gravimetric thickness suggesting that no corrosion had occurred.

Interestingly, the CO measured in the permeate stream (Figure 10.4[a]) continuously decreased (by about 75%) during the mixed gas testing, seemingly decoupled from the He leak which increased over the testing. Since the PSS supports contained both iron and chromium, they may have had some catalytic activity towards the WGS reaction. The mixture on the support side of the membrane contained greater than 99% H_2 in most cases, so the reverse-WGS reaction may have been occurring to generate CO from the permeating CO_2. If the support gradually lost catalytic activity over the timeframe of the experiment, that could explain the drop in CO measured in the

permeate stream. It should be pointed out that this explaination was purely speculative. Regardless of the reason, the level of CO in the permeate stream was not representative of the membrane leak rate.

10.3.4. Effect of the high-temperature WGS reaction on leak growth

Since it was not thoroughly demonstrated in the previous section whether the syngas species had a significant effect on the He leak growth in the Pd-membrane, a series of experiments were conducted under WGS conditions with iron-chrome oxide catalyst packed in the annular space around the membrane. Several membranes (AA-24R, AA-30, AA-38R, and IM-79) were mounted in the WGS CMR and tested under reaction conditions for extended periods of time. Long-term experiments were also conducted to develop a better understanding of the stability of the WGS CMR operation.

The membrane AA-24R was tested at 400°C, 4.4 atma, and 2,700 h^{-1} $GHSV_{STP}$ of simulated syngas (19% CO, 55% H_2O, 18% H_2, and 8% CO_2). The reaction pressure of 4.4 atma was utilized so that there would be a low H_2 recovery such that the partial pressure of H_2 did not change significantly along the length of the membrane. With the low H_2 recovery, a CO conversion very close to the equilibrium conversion was expected. It was intended that the pressure would be elevated to 7.8 and then 14.4 atma within 100 hours if little or no selectivity decline was observed, followed by increases in the feed flow rate. The H_2 permeance and He leak of the membrane AA-24R over the whole testing period are shown in Figure 10.5[a]. The CO conversion and H_2 recovery are shown in Figure 10.5[b]. The level of CO in the permeate stream and the H_2/CO separation factor (calculated by equation **2.33**) are shown for the first 80 hours of the experiment in Figure 10.4[c]. After 80 hours the level of CO in the permeate exceeded the limits of the detector, and after 110 hours, the experiment was stopped due to condensation of H_2O in the permeate outlet. The condensation of H_2O in the room temperature tubing indicated that greater than 2.3% H_2O was present in the permeate stream (considering the saturated vapor pressure of H_2O at 20°C).

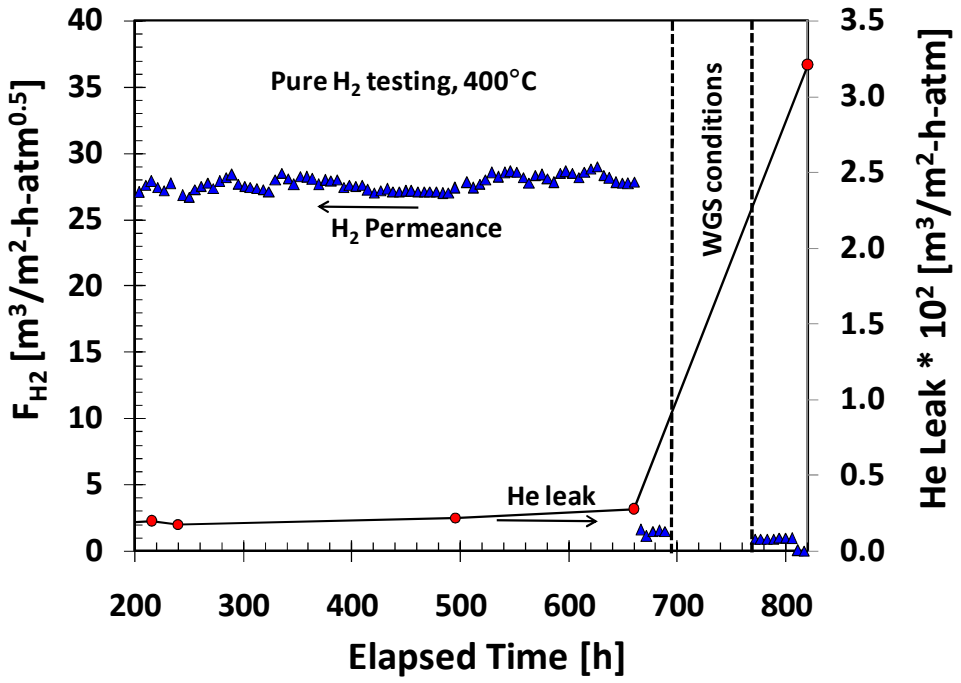
Pure H_2 testing, 400°C
H_2 Permeance
He leak
WGS conditions
F_{H2} [m^3/m^2-h-$atm^{0.5}$]
He Leak * 10^2 [m^3/m^2-h-atm]
Elapsed Time [h]
0
5
10
15
20
25
30
35
40
0.0
0.5
1.0
1.5
2.0
2.5
3.0
3.5
200
300
400
500
600
700
800

[a]

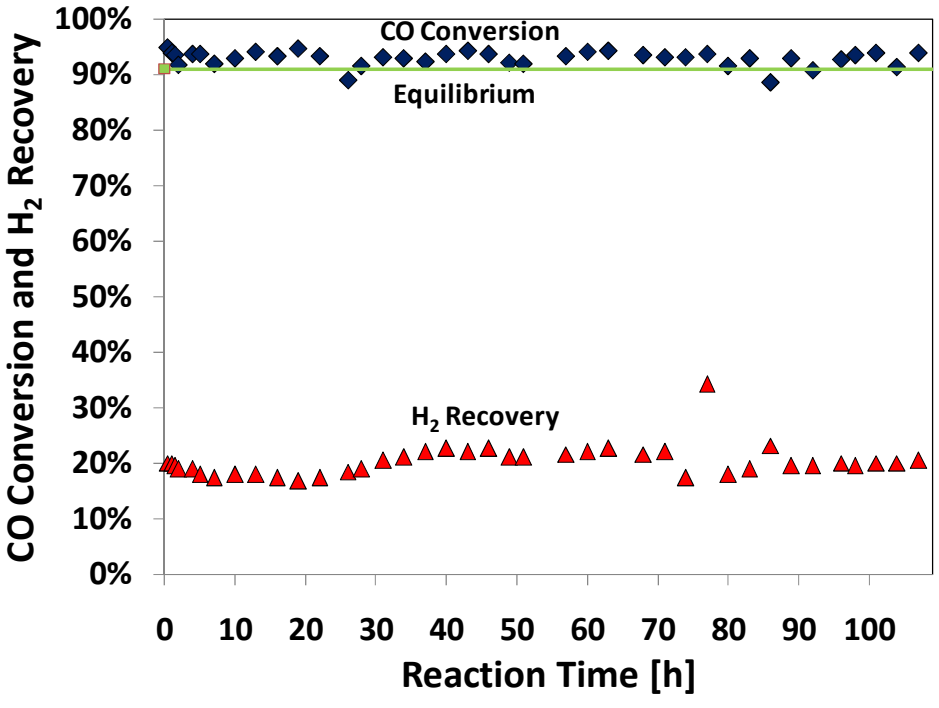
CO Conversion
Equilibrium
H_2 Recovery
CO Conversion and H_2 Recovery
Reaction Time [h]
0%
10%
20%
30%
40%
50%
60%
70%
80%
90%
100%
0
10
20
30
40
50
60
70
80
90
100

[b]

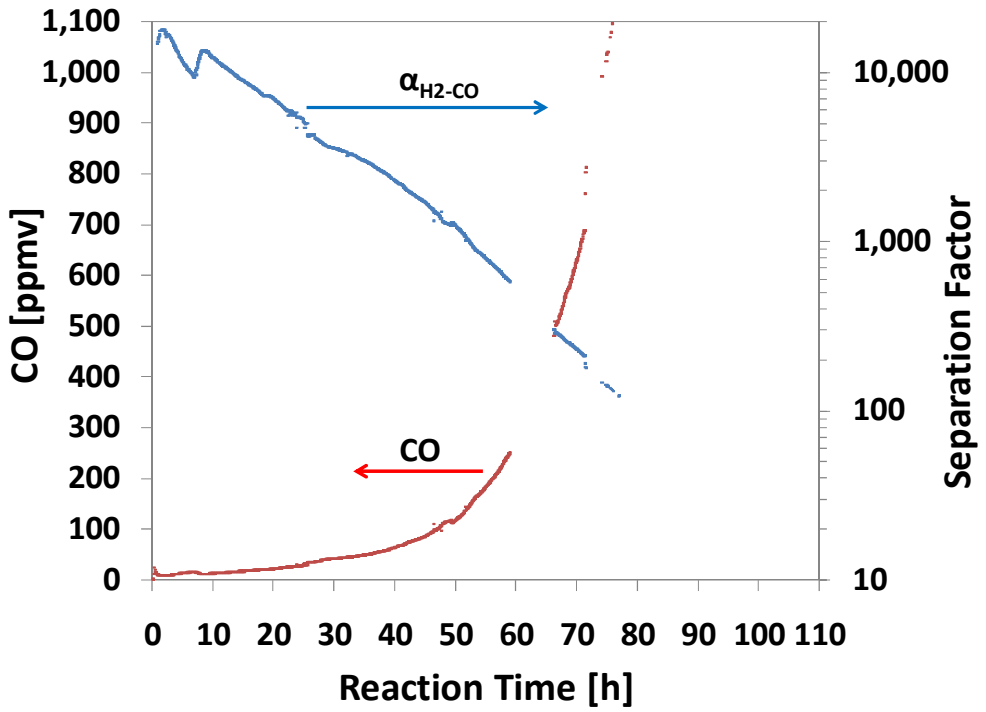

[c]

Figure 10.5. H_2, He, and WGS testing of AA-24R [a] Testing history [b] WGS CMR results [c] CO measured in the permeate and H_2/CO separation factor during WGS test (19% CO, 18% H_2, 8% CO_2, and 55% H_2O; 400°C; 4.4 atma; $GHSV_{STP}$ = 2,700 h^{-1}).

The He leak, which was stable during pure H_2 testing, increased by one-order of magnitude during the 110 hour reaction test as shown in Figure 10.4[a]. The average rate of leak growth during the reaction test was approximately two orders of magnitude greater than during the pure H_2 testing (see Table 10.3). Although the CO conversion and H_2 recovery remained stable over the 110 hour testing period (Figure 10.4[b]), the H_2/CO separation factor of the membrane declined significantly. The decline in H_2/CO separation factor was continuous and exponential (note the logarithmic scale on the secondary y-axis in Figure 10.4[c]) indicating that the leak growth was not due to any particular event such as a loss of pressure or disruption of the H_2O feed pump (as had previously been problematic) but by the reaction conditions. The ideal H_2/He selectivity (measured before and after the reaction) also declined from 4,200 to 360. There was some doubt as to the viability of the results from the membrane AA-24R since it was

annealed at a significantly higher temperature (690℃) before additional Pd-plating, so WGS testing was continued with other membranes.

The membrane IM-79 was tested for 1,100 hours under H_2, then under WGS conditions for 65 hours, with similar feed conditions: 400℃, 14.6 atma, 23% CO, 22% H_2, 10% CO_2, and 45% H_2O at 2,100 h^{-1}). The CO conversion, H_2 recovery, and He leak of before and after the WGS test are shown in Figure 10.6.

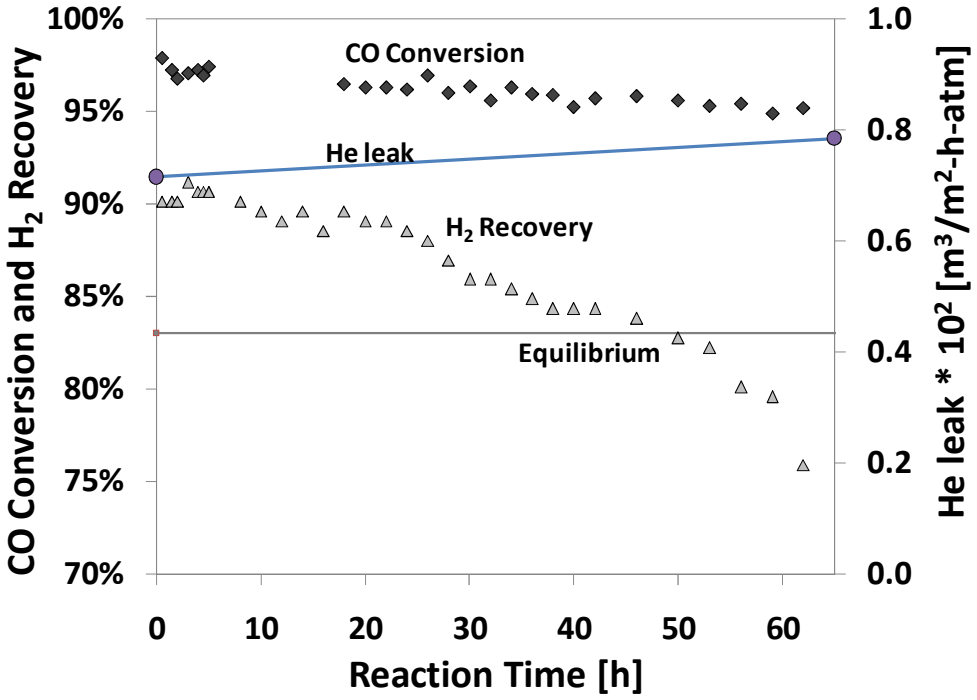

Figure 10.6. WGS CMR results and He leak development of the membrane IM-79 (23% CO, 22% H_2, 10% CO_2, and 45% H_2O; 400°C; 14.6 atma; $GHSV_{STP}$ = 2,100 h^{-1}).

Over the course of 65 hours the H_2 recovery gradually decreased due to coke formation on the membrane surface as was discussed in Chapter 8 (Section 8.4). The He leak growth rate of the membrane over the reaction period was almost three times the rate observed under pure H_2 (Table 10.3). As was discussed in the introduction of Chapter 8, the deposition and dissolution of carbon into palladium can result in a significant increase in the lattice parameter to 3.99Å. In some studies this increase has been

associated with surface distortions and leak growth in thin Pd-layers (Selman *et al.,* 1970; Galuszka *et al.,* 1998; Li *et al.,* 2007c). Since coke formation was most likely occurring on the membrane surface, it was possible that it was also dissolving into the Pd-lattice and causing accelerated leak growth (Galuszka *et al.,* 1998; Li *et al.,* 2007c). It was only speculative that the coking may have accelerated the leak growth since no analysis by XRD was conducted to determine the Pd-lattice parameter. Since a shorter testing period (65 hours) was utililized for the membrane IM-79, the accuracy of the leak growth rate calculation (equation **10.1**) was somewhat dubious.

The testing of the membrane AA-30 provided the best insight into the effects of the WGS conditions on the membrane since the reaction was conducted for the longest period of time. The membrane AA-30 was initially tested for 400 hours under pure H_2, then under the WGS reaction in 100 hour increments for 1,000 hours of reaction time and 2,500 hours total testing time. A higher H_2O/CO ratio of 3.0 was utilized to avoid possible coke formation. In between reaction tests the system was purged with He for 75 hours so that the leak could be measured, and after 500 hours of WGS conditions, the system was also switched to H_2 so that the membrane permeance could be measured. The H_2 permeance of the membrane was measured initially, after 500 hours, and after 1,000 hours of reaction time, and is shown along with the He leak over time in Figure 10.7[a]. The CO conversion and H_2 recovery for the ten-100 hour increments of reaction testing is shown in Figure 10.7[b]. The permeating CO is also shown in Figure 10.7[b].

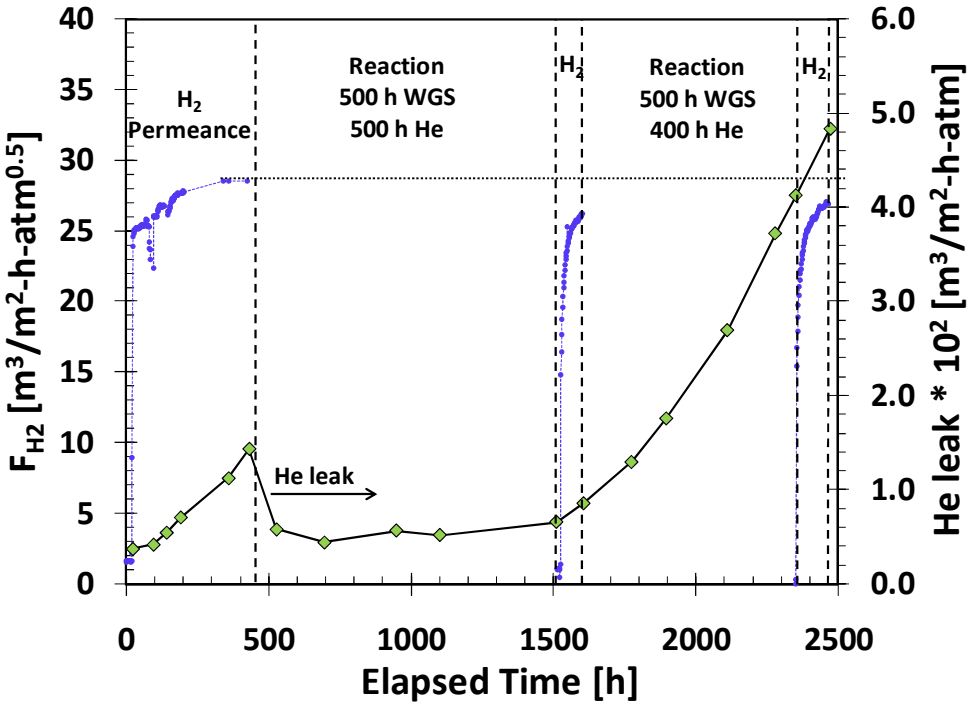

[a]

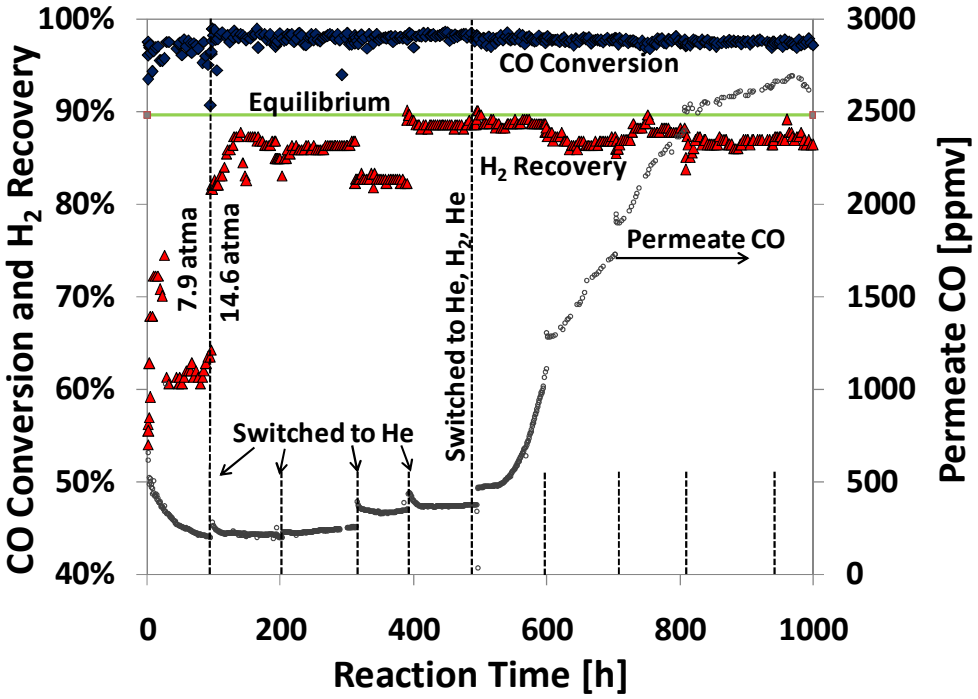

[b]

Figure 10.7. H_2, He, and WGS testing of AA-30 [a] Leak development [b] WGS CMR results and CO measured in the permeate (Feed: 19% CO, 18% H_2, 8% CO_2, and 55% H_2O; 400°C; $GHSV_{STP}$ = 2,700 h^{-1}).

When the system was switched to H_2 at 1,510 and 2,350 hours (Figure 10.7[a]) the H_2 permeance returned to within 90% of its initial value indicating that the Pd-surface was mostly free of poisoning such as coke formation. The He leak of the membrane, shown in Figure 10.7[a], and the level of CO measured in the permeate, shown in Figure 10.7[b], both decreased by a factor of 3 upon the first 200 hours of WGS conditions. The He leak remained very small until after a total time of 1,510 hours when the system was switched to H_2. During the final 500 hours of WGS conditions the He leak increased in a linear fashion with approximately the same rate as during the initial pure H_2 testing (Table 10.3).

The initial decrease in He leak observed with membrane AA-30 upon exposure to WGS conditions was unexpected, but not completely unfounded in the literature. Pomerantz and Ma (2009) observed an 80% decrease in the He leak of their 12.5 μm PI supported $Pd_{92}Cu_8$-membrane after 250 hours exposure to 54 ppmv H_2S in H_2. They attributed the leak decrease to segregation of sulfur to the grain boundaries and defects, resulting in blockage. Li *et al.* (2007b) also observed a slight but reproducible decrease in the N_2 leak of their porous ceramic supported Pd-membrane after exposure to pure CO at 350 - 450℃ which they attributed to the accelerated kinetic rate of coke formation in and around defect sites. It has been shown that carbon is soluble in palladium up to 13 at% and can be introduced via CO exposure at high temperatures (Li *et al.,* 2000; Yokoyama *et al.,* 1998; Ziemecki *et al.,* 1985). It was possible that carbon deposition could have occurred preferentially at the grain boundaries and defect sites, lowering the He leak at those locations. It seemed likely that if the carbon deposition reduced the leak by some mechanism, the effect would have been more significant during the testing of IM-79 since coke formation was occurring to a greater extent in that experiment. However, as the data in Table 10.3 show, there was a positive leak growth rate for IM-79 under the reaction conditions indicating that the effect was not significant.

Upon removal of the membrane AA-30 from the reactor, the IPA bubble test identified a single large leak on the weld at the outlet end of the membrane. A rising water leak test, shown in Figure 10.8 demonstrated that 65% of the leak was indeed localized in the 0.5 cm section adjacent to that weld. Furthermore, 23% of the leak was localized in the 1.0

cm section adjacent to the other weld, indicating that if both of the welds were covered, the remaining 5 cm length of membrane would still have had an ideal selectivity in excess of 1,500.

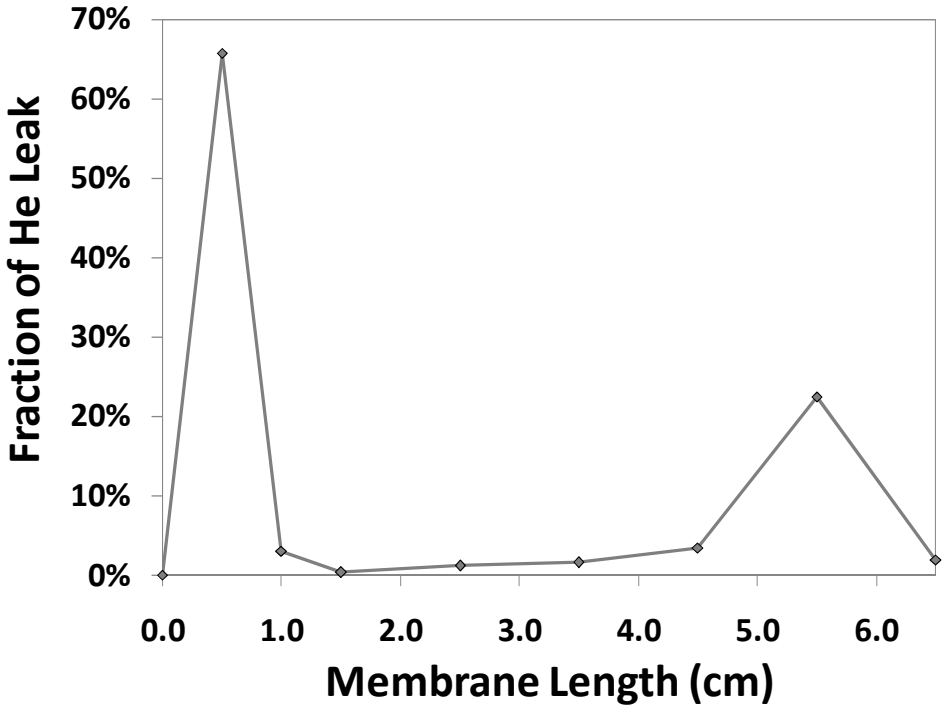

Figure 10.8. Rising water He leak test for the membrane AA-30.

The last example of WGS reaction testing was conducted with the membrane AA-38R at 400℃, 14.6 atma, and with 19% CO, 18% H_2, 8% CO_2, and 55% H_2O. The membrane was tested under WGS conditions for 124 hours, then with 1 and 2 ppmv H_2S present in the feed. The CO conversion and H_2 recovery for that reaction test were reported and discussed in Chapter 9 (Section 9.4.4). The H_2 permeance and He leak for the membrane AA-38R are shown in Figure 10.9.

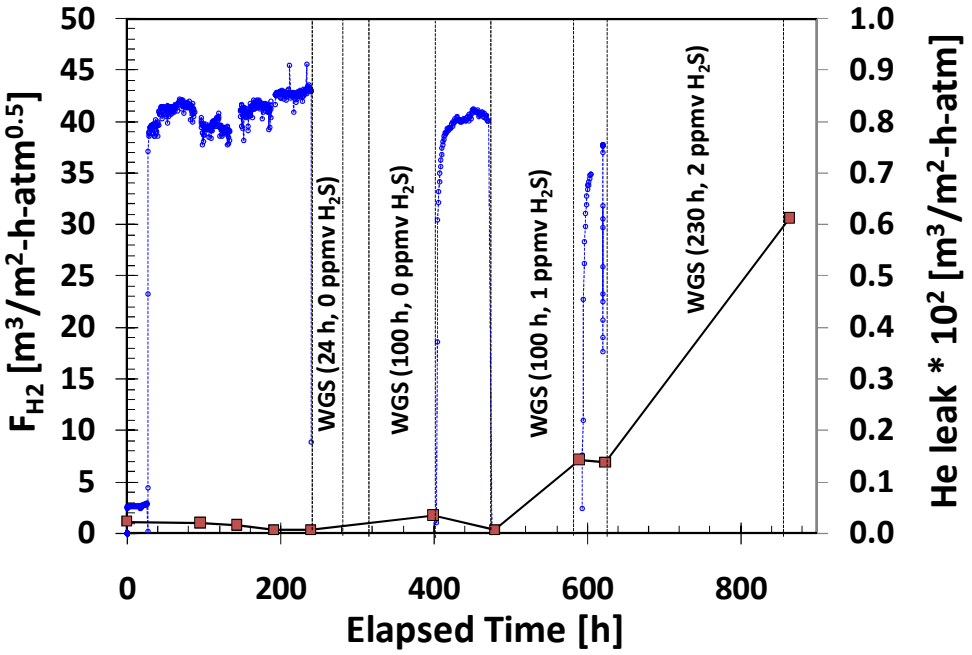

Figure 10.9. H_2 and WGS testing of the membrane AA-38R (19% CO, 18% H_2, 8% CO_2, 55% H_2O; 14.6 atma; 400°C; $GHSV_{STP}$ = 2,700 h^{-1}).

The He leak measured both before and after the first two periods of WGS testing (at a time of up to 480 hours in Figure 10.9) were below the threshold for accurate detection indicating a He permeance growth rate of less than $1.0*10^{-7}$ m^3/m^2-h^2-atm. With the membrane AA-38R there were no problematic issues during synthesis or testing, presenting a clear example that the WGS conditions did not adversely the selectivity in a well fabricated membrane with no weld defects.

The He leak growth rates during WGS testing with 1 and 2 ppmv H_2S present were more than two-orders of magnitude higher. As discussed in Chapter 9 (Section 9.4.4), there was no indication of bulk Pd_4S by XRD, but there was a significant surface morphology change at the outlet end of the membrane which was related to the H_2S poisoning phenomena previously observed in the literature (Chen, 2011; Iyoha *et al.,* 2007b). It was likely that the accelerated leak observed during WGS/H_2S testing of AA-38R was due to this surface morphology change and as a result of poisoning by H_2S.

Several of the membranes which were tested under WGS conditions (AA-24R, AA-30, and IM-79) were cut and the surface morphology was observed by SEM. The membrane AA-29 was tested under H_2 only for 1,000 hours at 400°C and is shown at two different magnifications in Figure 10.10[a] and [b]. The membranes AA-24R is also shown at two different magnifications in Figure 10.10[c] and [d]. The membrane AA-30 is shown in Figure 10.10[e] and the membrane IM-79 is shown in Figure 10.10[f].

[a] 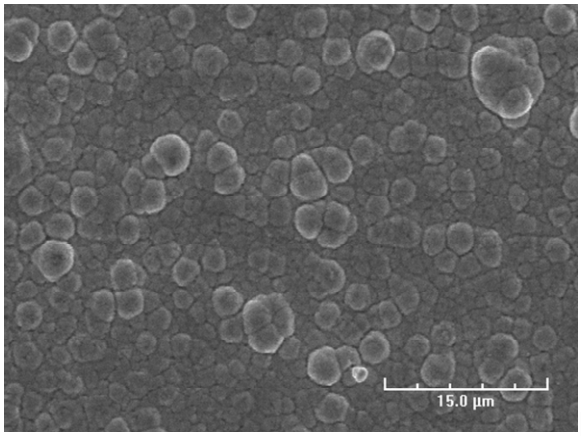

[b] 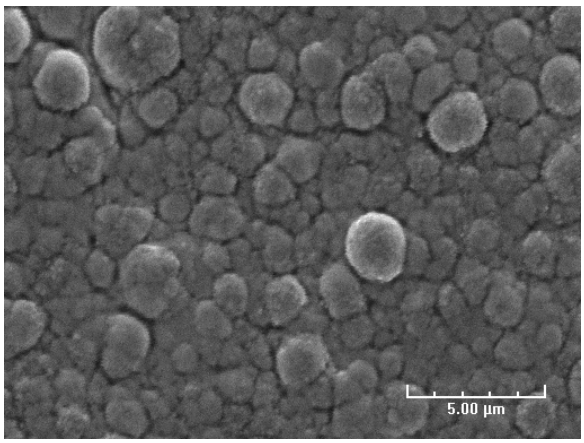

[c] 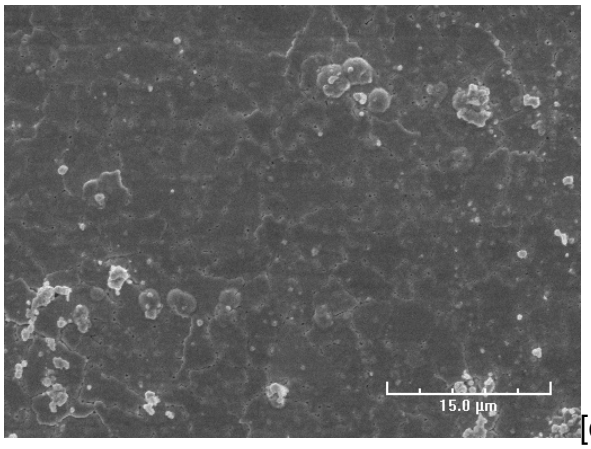

[d] 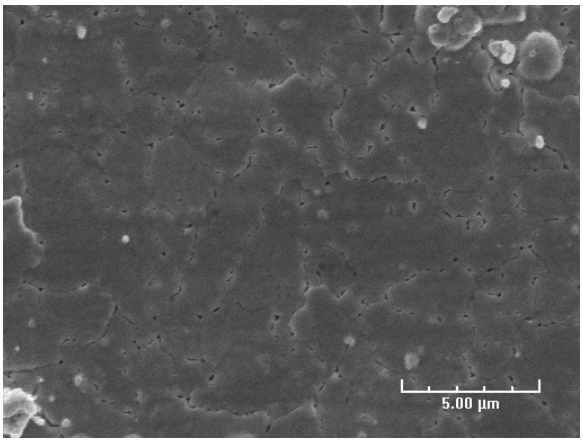

[e] 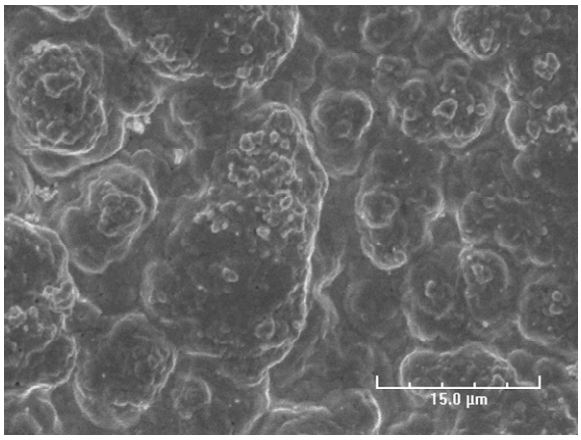

[f] 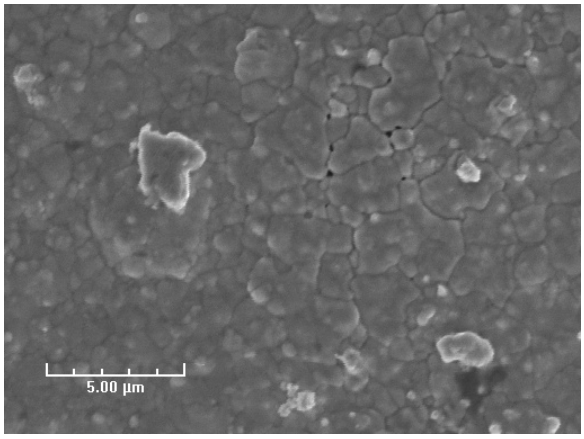

Figure 10.10. SEM images of the Pd-surface morphology [a] AA-29; 2,500X [b] AA-29; 5,000X [c] AA-24R; 2,500X [d] AA-24R; 5,000X [e] AA-30; 2,500X [f] IM-79; 5,000X.

Extensive pinhole formation was observed on AA-24R potentially due to the high temperature annealing during synthesis. Some pinholes on AA-30 and IM-79 of approximately 0.2 µm in size were apparent, but could have been attributed to the extended testing time of 2,500 and 2,000 hours respectively at 400°C. All three of the membranes AA-24R, AA-30, and IM-79 showed a higher degree of sintering among the Pd-crystallites than AA-29, similar to what had previously been observed due to higher temperature (greater than 500°C) testing in pure H_2 (Guazzone *et al.,* 2006). Unfortunately, the surface morphology varied distinctly over small distances (less than 200 µm) on the same sample of the membrane, due perhaps to the nature of electroless plating, and indicating the difficulty of surface morphology comparisons.

In some cases when platinum group metals have been exposed to reactive conditions, surface morphology changes were observed at temperatures significantly lower than the Tamman temperature, the temperature at which sintering and grain growth were expected (Flytzani-Stephanopoulos and Schmidt, 1979). It has been suggested that this phenomenon was the result of an increased diffusion rate of surface metal atoms due to the interaction of adsorbed gases. Kulprathipanja *et al.* (2004) reported hillock formation on the order of 150 – 400 nm in electroless plated $Pd_{65}Cu_{35}$-coupons exposed to CO and CO_2 at 450°C, but not coupons exposed to pure H_2. They also reported significant

leak growth in their 3.0 μm $Pd_{75}Cu_{25}$-membrane upon exposure to H_2/CO and H_2/CO_2 mixtures (detailed in Table 10.1). Since they observed some segregation of the copper away from the surface of the coupons, they suggested that the roughening and leak growth were most likely due to a bcc to fcc phase change taking place near the surface. However, they did not hypothesize as to how CO or CO_2 could have caused this.

In the cases of AA-24R and MA-79, the higher leak growth rate during WGS conditions than during pure H_2 testing suggested the occurrence of an alternative mechanism of leak growth such as the surface morphology rearrangement. However, the extraordinarily low rate of leak growth in AA-38R suggested that any morphology change which may have been occurring did not penetrate deeply into the Pd-layer. The testing of AA-30, where the majority of leak development in the membrane was due to weld defects (as also discussed in Chapter 4), also supported this conclusion and indicated that the WGS conditions did not significantly affect the rate of leak growth in well fabricated membranes.

Having a reasonably high, experimentally based, lifetime estimate is essential to the possibility of commercial applications. Detailed economic analysis regarding IGCC applications have identified cost effective options assuming a membrane lifetime of 5 years (Gray *et al.,* 2009). The membrane lifetime was defined as the length of time during which the membrane produced a H_2 purity of greater than 94%, suitable for a gas turbine in the power block of IGCC (Klara *et al.,* 2007; Gray *et al.,* 2009). Assuming that membranes in this study were utilized at a high pressure (14.6 atma) and a low flow such that H_2 fluxes of 5 – 9 m^3/m^2-h were achieved as in the WGS and H_2/H_2O experiments respectively, the viable lifetime was as great as ten or more years for AA-38R, 1.1 years for IM-79, and 0.25 years for AA-30. This was a conservative lifetime estimate because helium was used as the impermeable gas for the leak measurements. Since the leak through the membrane was mainly due to Knudsen diffusion, the leak of other gases such as CO, CO_2, and H_2O would be lower than that of He since the molecular mass of those species is greater (Perry and Green, 1997). The purity of H_2 in the permeate stream during the WGS CMR experiments with AA-30 (measured by collection of residual H_2O by cold trap and analysis of the dry permeate gas by GC)

dropped below 94% at approximately 2,200 hours, in close agreement with the estimated lifetime calculation.

10.4. Conclusions

Membranes were tested for up to 2,500 hours under H_2, H_2/H_2O, syngas, and WGS conditions at 400°C and exhibited stable H_2 permeance and gradual leak development (as low as $1.0*10^{-7}$ m^3/m^2-h^2-atm) which was in line with testing in pure H_2. Experiments with H_2/H_2O mixtures indicated that H_2O did not adversely affect the membrane selectivity. Long-term testing under WGS conditions also indicated that CO and CO_2 did not increase the leak growth rate or decrease the H_2 permeance of the membranes. Moreover, due to the stable membrane behavior, stable CO conversion and H_2 recovery of over 96% and 88% respectively were achieved for over 900 hours. Given the low leak growth rates observed in several membranes under reaction conditions, a membrane lifetime of greater than 10 years was projected to be possible.

A surface morphology change was observed in several membranes that were tested under WGS conditions at 400°C which resembled higher temperature annealing effects. Given the low rate of leak growth, it was unlikely that this change penetrated deeply into the Pd-layer. The gradual leak growth observed under WGS conditions was attributed to the observed pinhole formation. For the membranes which exhibited significant leak growth, the primary cause was shown to be weld defects inherent in the low cost porous stainless steel supports.

Membranes tested under syngas with 1 – 20 ppmv H_2S exhibited higher leak growth rates (up to four times greater) than that measured under syngas only. A Pd-membrane tested under WGS conditions with 2 ppmv H_2S exhibited the same trend, indicating that H_2S resulted in leak development, potentially due to a gradual penetration of sulfur into the Pd-layer forming bulk sulfides.

11. CONCLUSIONS

- The most reliable and reproducible method for membrane synthesis involved repetitive alumina grading treatments with successively smaller particle sizes from 10 to 0.01 μm, and resulted in thin (less than 5 μm), leak free Pd-membranes. Membranes prepared by this method exhibited H_2 permeance as high as 61.7 m^3/m^2-h-$atm^{0.5}$, with stable selectivity of 3,900 at 400°C.
- The primary obstacle to the reliable production of thin, leak free Pd-membranes on low cost PSS_{316L} supports was defects greater than 10 μm in size, present near the welded regions on about half of all supports. The best way of repairing these defects was through additional alumina grading and Pd-plating steps applied solely to the welded regions.
- At H_2 pressure exceeding 4 atma, the H_2 flux was found to exceed Sieverts' law by as much as 56% due to the influence of both the mass transfer resistance in the porous support and grading layers and the increased solubility of H-atoms in the Pd-layer at higher pressure (greater than 4 atma).
- The H_2 permeance inhibition was found to be significant for CO at temperatures below 400°C, and that of H_2O was significant at 400°C. The gas phase mass transfer resistance was significant over the whole range of feed flow rates tested (with Reynolds numbers from 10 to 200).
- The WGS CMR allowed for the simultaneous recovery of H_2 (up to 90%) and CO conversion of 98%, significantly in excess of the packed-bed equilibrium conversion. Similar results were obtained for both CO/steam feed mixtures and simulated syngas mixtures.
- The WGS CMR was capable of high CO conversion at higher throughput (5,400 h^{-1} space velocity) than previous packed-bed and membrane reactor experiments by utilization of a higher operating temperature of 450°C and a reaction pressure of 14 atma.
- Indications of coke formation were observed in the WGS CMR for H_2O/CO ratios as high as 1.6 at 300 – 400°C, and as high as 1.1 at 450 – 500°C. A thermodynamic analysis indicated that coke formation was not preferred due to the

potential for CH_4 formation when sufficient H_2 was present. The rate of coke formation on the Pd-surface was found to vary widely depending on the feed conditions and the presence of the iron-chrome oxide catalyst.

- A Pd-membrane tested under shifted syngas (50% H_2, 30% CO_2, 19% H_2O, and 1% CO) including up to 2.5 ppmv H_2S maintained a stable H_2 flux of 14.0 m^3/m^2-h with 90% H_2 recovery for 25 hours at 400°C. A $Pd_{90}Au_{10}$-membrane tested under shifted syngas with up to 20 ppmv H_2S achieved a stable H_2 flux of 7.8 m^3/m^2-h with 44% H_2 recovery for 25 hours indicating significant sulfur tolerance by the Pd/Au-alloy.
- The WGS CMR incorporating a Pd-membrane was operated with 0, 1, and 2 ppmv H_2S in the feed for 440 hours. A stable CO conversion of 96% and H_2 recovery of 78% was achieved for the final 80 hours of testing with 2 ppmv H_2S present.
- Only a slight amount of Pd_4S phase was observed on the pure Pd-membranes tested with up to 2.5 ppmv H_2S in shifted syngas and WGS conditions, potentially indicating that the thermodynamic threshold for Pd_4S formation (P_{H2S}/P_{H2}) was increased by a side reaction of H_2S with one of the syngas species. Under the test conditions, up to 2.5 ppmv of H_2S did not behave as a significant poison to the Pd-surface.
- Membranes were tested for up to 1,000 hours under H_2/H_2O, syngas, and WGS conditions at 400°C and exhibited stable H_2 permeance and gradual leak development which was in line with testing in pure H_2. The leak growth rates under H_2, mixed gas, and WGS conditions were in line with the pinhole formation mechanism.
- Considering the low leak growth rate under WGS conditions at 400°C, a membrane lifetime in excess of 10 years was projected for defect free membranes.
- When both Pd and Pd/Au-membranes were tested under either mixed gas or WGS conditions, first with no H_2S, then with 2 – 20 ppmv H_2S, a higher rate of leak growth was observed for higher concentrations of H_2S, potentially due to the gradual penetration of sulfur into the Pd-layer. This effect was not correlated to the formation of bulk Pd_4S on the membrane.

12. RECOMMENDATIONS FOR FUTURE RESEARCH WORK

In order to better establish the utility of Pd-membranes for the IGCC process, and to develop a more complete understanding of the science, the following recommendations are made for future work:

- For the purpose of a more reliable synthesis methodology, work must be done to develop a method of identifying and fixing weld defects in the low cost PSS supports. The solution may also consist of a better powder sintering procedure or a better welding procedure used in the support manufacturing.
- There is a discrepancy in the literature between estimated binding energies of CO, H_2O, and CO_2 on the Pd-surface based on adsorption isotherm data (primarily collected at temperatures below 200°C) and the observed phenomenon of H_2 permeation inhibition at temperature above 300°C. The study and resolution of this discrepancy will lead to a more thorough understanding of surface adsorption phenomenon on precious metals.
- Increased pressure of up to 14 atma in the WGS CMR allowed for significantly higher CO conversion and H_2 recover for a given feed rate at 400°C. It can be theorized from this trend, and by way of the 1-D model, that high CO conversion and H_2 recovery would still be possible at feed rates of up to 30,000 h^{-1} at a reaction pressure of 50 atma. The potential application of the WGS CMR to the IGCC process would be fortified by lab or pilot scale testing at 50 atma to confirm this performance potential.
- Coke formation from CO on the Pd-surface has not been widely studied in the literature, thus, the mechanisms and rate expression are unknown. A better understanding of this process may have significant implications in the field of precious metal catalysis.
- The interaction of H_2S and the syngas species with the Pd-surface is not well understood. The potential exists for competitive adsorption and also possibly surface reaction producing COS and/or SO_2. Either of these phenomena have the potential to alter the poisoning effect of H_2S on the Pd-membrane. The interactions

of these species on the Pd-surface should be further studied by both computational chemistry and experimental methods.

- Long-term tests (up to 1,000 hours) should be conducted with the WGS CMR utilizing Pd and Pd/Au-membranes and syngas feed from a coal gasifier that has been scrubbed and de-sulfurized (to less than 2 ppmv H_2S). Care should be taken to identify trace contaminants in the syngas and on the membrane surface after the tests, which may correlate to the probable reduction in H_2 flux. With this information, consideration can be made for more effective gas clean-up or different Pd/alloy compositions.
- When Pd-membranes were tested for extended periods of time (greater than 100 hours) under H_2/H_2O and WGS conditions, surface morphology changes were observed suggesting the possibility of reaction enhanced sintering. This phenomenon has not been previously observed for palladium. The surface morphology change should be investigated by exposing both PSS supported Pd-coupons and Pd-foils to various mixed gas and reaction conditions then observing the surface morphology and grain structure.

NOMENCLATURE

Roman Letters

A - Area [m^2]
C - Concentration [$kmol/m^3$]
D - Diffusivity [m^2/h]
d - Hydraulic diameter of reactor or particle diameter in packed bed [m]
E - Energy of a reaction or surface binding energy [kJ/mol]
F - Permeance of inert gas [m^3/m^2-h-atm], of H_2 [m^3/m^2-h-$atm^{0.5}$]
G - Gibbs free energy of formation or of reaction [kJ/mol]
J - Volumetric flux [m^3/m^2-h]
H - Enthalpy of formation or of reaction [kJ/mol]
h - Plank's constant [6.626×10^{-34} J-s]
K - Equilibrium constant (unitless), or Langmuir adsorption equilibrium constant, or Sieverts' constant [atm^x, x = 0, ½, 1]
k - Rate constant for surface reaction [$kmol/m^2$-h-atm^x], rate constant for catalyzed WGS reaction [kmol/kg-h], mass transfer coefficient [m/h], Boltzmann constant [1.381×10^{-23} J/K]
L - Length [m] or concentration of active sites on a surface [$kmol/m^2$]
m - Molecular mass [kg/mol]
N - Molar flow rate, feed flow rate [kmol/h]
P - Pressure [atma]
Q - Permeability [μm-m^3/m^2-h-atm]
R - Radius [m] or ideal gas constant [0.008314 kJ/mol-K, or 0.0821 m^3-atm/kmol-K] or mass transfer resistance [atm-h/m]
r - Reaction rate [kmol/kg-h]
Re - Dimensionless Reynolds number
Sc - Dimensionless Schmidt number
Sh - Dimensionless Sherwood number
S - Entropy of adsorption or reaction [J/mol-K]
T - Temperature [K]
t - Time [h]
V - Volume [m^3]
v - Velocity of gas stream [m/h]
w - Weight of support plus membrane (for gravimetric thickness) [g]
X_{CO} - CO conversion (always with subscript 'CO')
x - Mole fraction of a gas species (for selectivity, referring to feed composition, unitless)
Y_{H2} - H_2 recovery (always with subscript H_2)
y - Mole fraction of a gas species (for selectivity, refering to permeate composition, unitless)
z - Dimension parallel to the primary axis of flow, axial coordinate in the reactor system [m]

Greek Symbols

α - Selectivity (unitless), alternately Pd/H phase
β - $\beta = P_{CO2}P_{H2}/K_{WGS}P_{CO}P_{H2O}$ is the reaction quotient, alternatively Pd/H phase
γ - Inhibition coefficient (unitless)
Δ - Change in variable
δ - Thickness [μm]
ε - Catalyst bed void fraction or porosity (unitless)
η - Catalytic effectiveness factor (unitless)
θ_i - Fraction of surface sites occupied by species *i* (unitless), molar ratio of two species in feed gas (unitless)
κ - Molar density of Pd [$1.13*10^5$ mol/m^3]
λ - Adsorption equilibrium constant [atm^{-1}]
μ - Dynamic viscosity [kg/m-h], Length prefix 'micro', or chemical potential [kJ/mol]
ν - H/Pd atomic ratio (unitless), reaction coefficient (unitless)
ξ - $\xi = z/L$, dimensionless axial coordinate in the reactor system
π - Mathematical constant truncated to 3 significant digits: 3.14
ρ - Density [kg/m^3]
τ - Residence time [s]

Subscripts

A - Activation (as in energy)
B - Boundary layer (referring to gas boundary layer)
a - Adsorption
b - Bulk gas
d - Desorption or dissolution
cat - catalyst
c - Cross-section
H - Atomic hydrogen in the Pd-lattice
i - Gas species index
j - Gas species index or rate step index
K - Knudsen
m - Molar (referring to molar volume V_m)
out - Outlet end of the membrane separator or reactor
perm - Permeate
r - Reaction, reactor
ret - Retentate
S - Sieverts' (referring to Sieverts' constant K_S)
s - Surface
shell - Reactor outer wall or casing
tube - Membrane tube
x - Surface index

0 - ‘pre’ or initial, ‘standard’ temperature (273 K) or pressure (1.0 atma)

Exponents

i - Ideal (referring to separation factor)
m - Exponent of the pressure of CO in the empirical rate formula (equation **2.4**)
n - Exponent of the pressure of H_2O in the empirical rate formula
o - Exponent of the pressure of CO_2 in the empirical rate formula
p - Exponent of the pressure of H_2 in the empirical rate formula
* - Unoccupied or free surface site

Acronyms

AA - Designation used for membranes prepared by Alexander Augustine
AGR - Acid gas removal
bcc - body-centered cubic (crystal structure)
C - Designation for coupons
CMR - Catalytic membrane reactor
CSTR - Continuous stirred tank reactor
CVD - Chemical vapor deposition
D - Dimension (referring to one or two dimensional system)
EA - Designation used for membranes prepared by Dr. M. Engin Ayturk
EDS - Energy dispersive x-ray spectroscopy
EP - Electroplating
EDTA - Ethylenediaminetetraacetic acid
FPD - Flame-photometric detector
fcc - face-centered cubic (crystal structure)
GC - Gas chromatography
GHSV - Gas hourly space velocity
IGCC - Integrated gasification combined cycle
IM - Designation used for membranes prepared by Dr. Ivan Mardilovich
IPA - Isopropyl alcohol
ML - Mono-layer
MS - Magnetron sputtering
MSR - Methane-steam reforming ($CH_4 + H_2O \rightarrow CO_2 + 3H_2$)
NR - Not reported (referring to documentation in a literature study)
NTU - Number of transfer units (referring to heat transfer)
PBR - Packed-bed reactor
PH - Porous Hastelloy (high Ni-steel alloy)
PI - Porous Inconel (high Ni-steel alloy)
PID - Proportional, integral, differential (referring to a control circuit)
ppmv - Part-per-million by volume
ppbv - Part-per-billion by volume
PSS - Porous stainless steel
PVD - Physical vapor deposition
RK - Designiation used for membranes prepared by Reyyan Koc

rpm	-	revolutions per minute (referring to angular velocity)
sccm	-	Standard cubic centimeters per minute (gas at 273 K, 1 atma)
SEM	-	Scanning electron microscope
SS	-	Stainless steel (high Cr-steel alloy) or surface-site
SR	-	Steam reforming
STP	-	Standard temperature pressure (273 K, 1 atma)
Syngas	-	‘Synthesis gas’, mixture of H_2, CO, CO_2, and H_2O
WGS	-	Water-gas shift ($CO + H_2O \rightarrow CO_2 + H_2$)
XRD	-	X-ray diffraction or X-ray diffractometer

REFERENCES

Abdollahi, M.; Yu, J.; Liu, P. K. T.; Ciora, R.; Sahimi, M.; Tsotsis, T. T. "Hydrogen production from coal-derived syngas using a catalytic membrane reactor based process." *Journal of Membrane Science,* 363(2010), 160-169.

Albers, P.; Pietsch, J.; Parker, S. "Poisoning and deactivation of palladium catalysts." *Journal of Molecular Catalysis A: Chemical,* 173(2001), 275-286.

Alfonso, D. R. "Comparative studies of CO and H_2O interaction with the Pd(111) surface: A theoretical study of poisoning." *Applied Physics Letters*, 88(2006), 051908.

Alfonso, D. R. "First-principles study of sulfur overlayers on Pd(111) surface" *Surface Science,* 596(2005), 229-241.

Amadeo, N. E.; Laborde, M. A. "Hydrogen production from the low-temperature water-gas shift reaction: kinetics and simulation of the industrial reactor." *International Journal of Hydrogen Energy,* 20(1995), 12, 949-956.

Arstad, B.; Venvik, H.; Klette, H.; Walmsley, J. C.; Tucho, W. M.; Holmestad, R.; Holmen, A.; Bredesen, R. "Studies of self-supported 1.6 um Pd/23 wt.% Ag membranes during and after H_2 production in a catalytic membrane reactor." *Catalysis Today*, 118(2006), 63-72.

Augustine, A. S.; Ma, Y. H.; Kazantzis, N. K. "High pressure palladium membrane reactor for the high temperature water-gas shift reaction." *International Journal of Hydrogen Energy,* 36(2011) 5350-5360.

Ayturk, M. E. "Synthesis, annealing strategies and in-situ characterization of thermally stable composite thin Pd/Ag alloy membranes for H_2 separation." PhD Thesis 2007, Worcester Polytechnic Institute, Worcester, MA.

Ayturk, M. E.; Kazantzis, N. K.; Ma, Y. H. "Modeling and performance assessment of Pd- and Pd/Au-based catalytic membrane reactors for hydrogen production." *Energy & Environmental Science,* 2(2009), 430-438.

Ayturk, M. E.; Ma, Y. H. "Electroless Pd and Ag deposition kinetics of the composite Pd and Pd/Ag membranes synthesized from agitated plating baths." *Journal of Membrane Science,* 330(2009), 233-245.

Ayturk, M. E.; Mardilovich, I. P.; Engwall, E. E.; Ma, Y. H. "Synthesis of composite Pd-porous stainless steel (PSS) membranes with a Pd/Ag intermetallic diffusion barrier." *Journal of Membrane Science,* 285(2006), 385-394.

Balovnev, Y. A. “Diffusion of hydrogen in palladium.” *Russian Journal of Physical Chemistry,* 48(3), 1974, 409-410.

Barbieri, G.; Brunetti, A.; Tricoli, G.; Drioli, E. “An innovative configuration of a Pd-based membrane reactor for the production of pure hydrogen. Experimental analysis of water gas shift.” *Journal of Power Sources*, 182(2008), 160-167.

Barbieri, G.; Marigliano, G.; Perri, G.; Drioli, E. “Conversion-temperature diagram for a palladium membrane reactor. Analysis of an endothermic reaction: methane steam reforming.” *Industrial & Engineering Chemistry Research,* 40(2001), 2017-2026.

Barrer, R. M. Diffusion in and Through Solids, © Cambridge University Press, 1951.

Basile, A.; Chiappetta, G.; Tosti, S.; Violante, V. “Experimental and simulation of both Pd and Pd/Ag for a water gas shift membrane reactor.” *Separation and Purification Technology*, 25(2001), 549-571.

Basile, A.; Criscuoli, A.; Santella, F.; Drioli, E. “Membrane reactor for water gas shift reaction.” *Gas Separation & Purification*, 10(1996a), 4, 243-254.

Basile, A.; Drioli, E.; Santella, F.; Violante, V.; Capannelli, G.; Vitulli, G. “A study on catalytic membrane reactors for water gas shift reaction.” *Gas Separation & Purification*, 10(1996b), 1, 53-61.

Basile, A.; Paturzo, L.; Fausto, G. “Co-current and counter-current modes for water gas shift membrane reactor.” *Catalysis Today,* 82(2003), 275-281.

Battersby, S.; Ladewig, B. P.; Duke, M.; Rudolph, V.; Diniz da Costa, J. C. “Membrane reactor modelling, validation and simulation for the WGS reaction using metal doped silica membranes.” *Asia-Pacific Journal of Chemical Engineering,* October, 2009.

Behm, R. J.; Christmann, K.; Ertl, G. “Adsorption of CO on Pd(100).” *Journal of Chemical Physics,* 73(1980), 6, 2984-2995.

Bi, Y.; Xu, H.; Li, W.; Goldbach, A. “Water-gas shift reaction in a Pd membrane reactor over $Pt/Ce_{0.6}Zr_{0.4}O_2$ catalyst.” *International Journal of Hydrogen Energy,* 34(2009), 2965-2971.

Bissett, L. “Equilibrium constant for shift reactions.” *Chemical Engineering,* Oct. 24, 1977, 155.

Bohlbro, H. “The kinetics of the water gas conversion at atmospheric pressure.” *Acta Chemica Scandinavica,* 16(1961), 502-520.

Bohlbro, H. “The kinetics of the water gas conversion III. Influence of H_2S on the rate equation.” *Acta Chemica Scandinavica,* 17(1963), 1001-1011.

Bracht, M.; Alderliesten, P. T.; Kloster, R.; Pruschek, R.; Haupt, G.; Xue, E.; Ross, J. R. H.; Koukou, M. K.; Papayannakos, N. "Water gas shift membrane reactor for CO_2 control in IGCC systems: techno-economic feasibility study." *Energy Conversion and Management,* 38(1997), S159-S164.

Bredesen, R.; Jordal, K.; Bolland, O. "High-temperature membranes in power generation with CO_2 capture." *Chemical Engineering and Processing,* 43(2004), 1129-1158.

Brinker, C. J.; Scherer, G. W. Sol-gel Science, © 1990, Academic Press Limited, San Diego, CA.

Brunetti, A.; Barbieri, G.; Drioli, E.; Lee, K.-H.; Sea, B.-K.; Lee, D.-W. "Porous stainless steel supported silica membrane for WGS reaction." *Desalination,* 200(2006), 681-683.

Brunetti, A.; Barbieri, G.; Drioli, E.; Lee, K.-H.; Sea, B.; Lee, D.-W. "WGS reaction in a membrane reactor using a porous stainless steel supported silica membrane." *Chemical Engineering and Processing,* 46(2007a), 119-126.

Brunetti, A.; Caravella, A.; Barbieri, G.; Drioli, E. "Simulation study of water gas shift reaction in a membrane reactor." *Journal of Membrane Science,* 306(2007b), 329-340.

Bryden, K. J.; Ying, J. Y. "Nanostructured palladium-iron membranes for hydrogen separation and membrane hydrogenation reactions." *Journal of Membrane Science,* 203(2002), 29-42.

Burch, R. "Gold catalysts for pure hydrogen production in the water-gas shift reaction: activity, structure and reaction mechanism." *Physical Chemistry Chemical Physics,* 8(2006), 5483-5500.

Bustamante, F.; Enick, R. M. "High-temperature kinetics of the homogeneous reverse water-gas shift reaction." *AIChE Journal,* 50(2004), 5, 1028-1041.

Caravella, A.; Barbieri, G.; Drioli, E. "Concentration Polarization analysis in self-supported Pd-based membranes." *Separation and Purification Technology*, 66(2009), 613-624.

Catalano, J.; Baschetti, M. G.; Sarti, G. C. "Influence of the gas phase resistance on hydrogen flux through thin palladium-silver membranes." *Journal of Membrane Science,* 339(2009), 57-67.

Catalano, J.; Baschetti, M. G.; Sarti, G. C. "Influence of water vapor on hydrogen permeation through 2.5 μm Pd-Ag membranes." *International Journal of Hydrgen Energy,* 36(2011), 8658-8673.

Chen, C. H. "Sulfur Tolerance of Pd/Au Alloy Membranes for Hydrogen Separation from Coal Gas." PhD Thesis 2011, Worcester Polytechnic Institute, Worcester, MA.

Chen, C. H., Ma, Y. H. "The effect of H_2S on the performance of Pd and Pd/Au composite membrane." *Journal of Membrane Science*, 362(2010), 535-544.

Chiappetta, G.; Clarizia, G.; Drioli, E. “Design of an integrated membrane system for a high level hydrogen purification.” *Chemical Engineering Journal,* 124(2006), 29-40.

Chiappetta, G.; Clarizia, G.; Drioli, E. “Theoretical analysis of the effect of catalyst mass distribution and operation parameters on the performance of a Pd-based membrane reactor for water-gas shift reaction.” *Chemical Engineering Journal,* 136(2008), 373-382.

Christain, D. C.; Boyd, P. B. Jr. “What to Look For in CO Conversion Catalysts.” *Chemical Engineering*, May 1949, 148.

Collins, J. P.; Harper-Nixon, D. L. “A New Preparation Technique for Pd/Alumina Membranes with Enhanced High-Temperature Stability.” *Industrial & Engineering Chemistry Research,* 38(1999), 1925-1936.

Collins, J. P.; Way, J. D. “Preparation and Characterization of a Composite Palladium-Ceramic Membrane.” *Industrial & Engineering Chemistry Research,* 32(1993), 3006-3013.

Coulson, J. M.; Richardson, J. F.; Backhurst, J. R.; Harker, J. H. Chemical Engineering, Volume 1, Sixth Edition, *Fluid Flow, Heat Transfer and Mass Transfer.* © Elsevier, 1999.

Criscuoli, A. Basile, A.; Drioli, E. “An analysis of the performance of membrane reactors for the water-gas shift reaction using gas feed mixtures.” *Catalysis Today,* 56(2000), 53-64.

Criscuoli, A.; Basile, A.; Drioli, E.; Loiacono, O. “An economic feasibility study for water gas shift membrane reactor.” *Journal of Membrane Science*, 181(2001), 21-27.

Cussler, E. L. Diffusion Mass Transfer in Fluid Systems. © Cambridge University Press 1997.

Damle, A.; Richardson, C.; Powers, T.; Love, C.; Acquaviva, J. “Demonstration of a Pilot-Scale Membrane Reactor Process for Hydrogen Production.” *ECS Transactions*, 12(2008), 1, 499-510.

deRosset, A. J. “Diffusion of Hydrogen through Palladium Membranes.” *Industrial & Engineering Chemistry,* 52(1960), 6, 525-528.

Doering, D. L.; Poppa, H.; Dickinson, J. T. “UHV Studies of the Interaction of CO with Small Supported Metal Particles, Pd/Mica.” *Journal of Catalysis,* 73(1982), 104-119.

Dulaurent, O.; Chandes, K.; Bouly, C.; Bianchi, D. “Heat of Adsorption of Carbon Monoxide on a Pd/Al_2O_3 Solid Using *in situ* Infrared Spectroscopy at High Temperatures.” *Journal of Catalysis*, 188(1999), 237-251.

Faraji, F.; Safarik, I.; Strausz, O. P. “CO-Catalyzed Conversion of H_2S to H_2 + S. 1. Reaction between CO and H_2S.” *Industrial & Engineering Chemistry Research,* 35(1996), 3854-3860.

Flytzani-Stephanopoulos, M.; Schmidt, L. D. “Morphology and etching processes on macroscopic metal catalysts.” *Progress in Surface Science,* 9(1979), 83-111.

Fogler, H. S. Elements of Chemical Reaction Engineering Third Edition, © Prentice Hall PTR 1999, Upper Saddle River, NJ.

Frieske, H.; Wicke, E. “Magnetic Susceptibility and Equilibrium Diagram of PdH_n.” *Berichte der Bunsen-Gesellschaft fur Physikalische Chemie*, 77(1973), 48-52.

Gade, S. K.; Coulter, K. E.; Way, J. D. “Effects of fabrication technique upon material properties and permeation characteristics of palladium-gold alloy membranes for hydrogen separations.” *Gold Bulletin,* 43(2010), 4, 287-297.

Gade, S. K.; DeVoss, S. J.; Coulter, K. E.; Paglieri, S. N.; Alptekin, G. O.; Way, J. D. “Palladium-gold membranes in mixed gas streams with hydrogen sulfide: effect of alloy content and fabrication technique.” *Journal of Membrane Science,* 378(2011), 35-41.

Gallucci, F.; Chiaravalloti, F.; Tosti, S.; Drioli, E.; Basile, A. “The effect of mixture gas on hydrogen permeation through a palladium membrane: Experimental study and theoretical approach.” *International Journal of Hydrogen Energy,* 32(2007), 12, 1837-1845.

Galuska, J.; Pandey, R. N.; Ahmed, S. “Methane conversion to syngas in a palladium membrane reactor.” *Catalysis Today,* 46(1998), 83-89.

Gielens, F. C.; Knibbeler, R. J. J.; Duysinx, P. F. J.; Tong, H. D.; Vorstman, M. A. G.; Keurentjes, J. T. F. “Influence of steam and carbon dioxide on the hydrogen flux through thin Pd/Ag and Pd membranes.” *Journal of Membrane Science,* 279(2006), 176-185.

Gielens, F. C.; Tong, H. D.; van Rijn, C. J. M.; Vorstman, M. A. G.; Keurentjes, J. T. F. “High-flux palladium-silver alloy membranes fabricated by microsystem technology.” *Desalination,* 147(2002), 417-423.

Gotti, A.; Prins, R. “Basic metal oxides as Co-catalysts in the conversion of synthesis gas to methanol on supported palladium catalysts.” *Journal of Catalysis,* 175(1998), 302-311.

Graham, T. “On the Absorption and Dialytic Separation of Gases by Colloid Septa.” *Philosophical Transactions of the Royal Society of London*, 156(1866), 399-439.

Gray, D.; Plunkett, J.; Salerno, S.; White, C.; Tomlinson, G. “Current and future technologies for gasification-based power generation”, Volume 2, DOE/NETL-2009/1389.

Gronvold, R. *Acta Chemical Scandinavica,* 10(1956), 1620.

Gryaznov, V. M.; Serebryannikova, O. S.; Serov, Y. M. “Preparation and catalysis over palladium composite membranes.” *Applied Catalysis A: General,* 96(1993), 15-23.

Guazzone, F. “Engineering of substrate surface for the synthesis of ultra-thin composite Pd and Pd-Cu membranes for H_2 separation.” PhD Thesis 2005, Worcester Polytechnic Institute, Worcester, MA.

Guazzone, F.; Ma, Y. H. “Leak Growth Mechanism in Composite Pd Membranes Prepared by the Electroless Deposition Method.” *AIChE Journal,* 54(2008), 2, 487-494.

Guazzone, F.; Payzant, E. A.; Speakman, S. A.; Ma, Y. H. “Microstrains and Stresses Analysis in Electroless Deposited Thin Pd Films.” *Industrial & Engineering Chemistry Research,* 45(2006), 8145-8153.

Guo, X.; Yates, J. T. “Dependence of effective desorption kinetic parameters on surface coverage and adsorption temperature: CO on Pd(111).” *Journal of Chemical Physics,* 90(1989), 11, 6761-6766.

Gusovius, A. F.; Watling, T.C. “Ca promoted Pd/SiO_2 catalysts for the synthesis of methanol from CO: the location of the promoter.” *Applied Catalysis A: General,* 188(1999), 187-199.

Hagg, May-Britt, Handbook of Membrane Separations: Chemical, Pharmaceutical, Food, and Biotechnological Applications, © CRC Press, Taylor & Francis Group, 2009.

Hilair, S.; Wang, X.; Luo, T.; Gorte, R. J.; Wagner, J. “A comparative study of water-gas-shift reaction over ceria-supported metallic catalysts.” *Applied Catalysis A: General,* 258(2004), 271-276.

Hla, S. S.; Park, D.; Duffy, G. J.; Edwards, J. H.; Roberts, D. G.; Ilyushechkin, A.; Morpeth, L. D.; Nguyen, T. “Kinetics of high-temperature water-gas shift reaction over two iron-based commercial catalysts using simulated coal-derived syngases.” *Chemical Engineering Journal,* 146(2009), 148-154.

Holleck, G. L. “Diffusion and solubility of hydrogen in palladium and palladium-silver alloys” *Journal of Physical Chemistry,* 74(1970), 3, 503-511.

Hou, K.; Hughes, R. “Preparation of thin and highly stable Pd/Ag composite membranes and simulative analysis of transfer resistance for hydrogen separation.” *Journal of Membrane Science,* 214(2003), 43-55.

Hou, K.; Hughes, R. “The effect of external mass transfer, competitive adsorption and coking on hydrogen permeation through thin Pd/Ag membranes.” *Journal of Membrane Science*, 206(2002), 119-130.

Howard, B. H.; Killmeyer, R. P.; Rothenberger, K. S.; Cugini, A. V.; Morreale, B. D.; Enick, R. M.; Bustamante, F. “Hydrogen permeance of palladium-copper alloy membranes over a wide range of temperatures and pressures.” *Journal of Membrane Science,* 241(2004), 207-218.

Hsiung, T. H.; Christman, D. D.; Hunter, E. J.; Homyak, A. R. “Methane Formation on H_2 Purification Using a Commercial Pd-Ag Membrane.” *AIChE Journal,* 45(1), 1999, 204-208.

Iida, H.; Igarashi, A. “Characterization of a Pt/TiO_2 (rutile) catalyst for water gas shift reaction at low-temperature.” *Applied Catalysis A: General,* 298(2006), 152-160.

Iyoha, O.; Enick, R.; Killmeyer, R.; Howard, B.; Ciocco, M.; Morreale, B. “H_2 production from simulated coal syngas containing H_2S in multi-tubular Pd and 80 wt% Pd-20 wt% Cu membrane reactors at 1173K.” *Journal of Membrane Science*, 306(2007a), 103-115.

Iyoha, O.; Enick, R.; Killmeyer, R.; Morreale, B. “The influence of hydrogen sulfide-to-hydrogen partial pressure ratio on the sulfidization of Pd and 70 mol% Pd-Cu membranes.” *Journal of Membrane Science,* 305(2007b), 77-92.

Iyoha, O.; Howard, B.; Morreale, B.; Killmeyer, R.; Enick, R. “The Effects of H_2O, CO, and CO_2 on the H_2 Permeance and Surface Characteristics of 1 mm Thick Pd80wt%Cu Membranes.” *Topics in Catalysis,* 49(2008), 97-107.

Johanek, V.; Stara, I.; Tsud, N.; Veltruska, K.; Matolin, V. “CO adsorption on Al_2O_3-supported Pd clusters: XPS study.” *Applied Surface Science,* 162-163(2000), 679-684.

Jorgensen, S. L.; Nielsen, P. E. H., Lehrmann, P. “Steam reforming of methane in a membrane reactor.” *Catalysis Today,* 25(1995), 303-307.

Jun, C.-S.; Lee, K.-H. “Palladium and palladium alloy composite membranes prepared by metal-organic chemical vapor deposition method (cold-wall).” *Journal of Membrane Science,* 176(2000), 121-130.

Kajiwara, M.; Uemiya, S.; Kojima, T.; Kikuchi, E. “Rhodium- and iridium-dispersed porous alumina membranes and their hydrogen permeation properties.” *Catalysis Today,* 56(2000), 83-87.

Keeling, R. F.; Piper, S. C.; Bollenbacher, A. F.; Walker, S. J., *Carbon Dioxide Research Group,* Scripps Institution of Oceanography, University of California La Jolla, 2009.

Keiski, R. L.; Salmi, T.; Niemisto, P.; Ainassaari, J.; Pohjola, V. J. “Stationary and transient kinetics of the high temperature water-gas shift reaction.” *Applied Catalysis A: General,* 137(1996), 349-370.

Keuler, J. N.; Lorenzen, L. “Developing a heating procedure to optimize hydrogen permeance through Pd-Ag membranes of thickness less than 2.2 μm.” *Journal of Membrane Science,* 195(2002), 203-213.

Kikuchi, H.; Uemiya, E. S.; Sato, N. Inoue, H.; Ando, H.; Matsuda, T. “Membrane Reactor Using Microporous Glass-Supported Thin Film of Palladium. Application to the Water Gas Shift Reaction.” *Chemistry Letters,* 3(1989), 489-492.

Kim, C. H.; Thompson, L. T. “Deactivation of Au/CeO_x water gas shift catalysts.” *Journal of Catalysis,* 230(2005), 66-74.

Klara, J. M.; Woods, M. C.; Capicotto, P. J.; Haslbeck, J. L.; Kuehn, N. J.; Matuszewski, M.; Pinkerton, L. L.; Rutkowski, M. D.; Schoff, R. L.; Vaysman, V. “Cost and Performance Baseline for Fossil Energy Plants, Volume 1: Bituminous Coal and Natural Gas to Electricity Final Report.” DOE/NETL-2007/1281.

Knapton, A. G. “Palladium Alloys for Hydrogen Diffusion Membranes.” *Platinum Metals Reviews,* 21(1977), 2, 44-50.

Knudsen, M. “The laws of molecular flow and of inner friction flow of gases through tubes.” *Journal of Membrane Science,* 100(1995), 23-25.

Koc, R. “Technical and Economic Performance Assessment of Pd/Alloy Membrane Reactor Technology Options in the Presence of Uncertainty” PhD Thesis 2012, Worcester Polytechnic Institute, Worcester, MA.

Kodama, S.; Fukui, K.; Tame, T.; Kinoshita, M. “Reaction Rate of Water-Gas Shift Reaction.” *Shokubai,* 8(1952), 50.

Korens, N.; Simbeck, D. R.; Wilhelm, D. J. “Process screening analysis of alternative gas treating and sulfur removal for gasification.” SFA Pacific, Inc. Engineering & Economic Consultants, DOE/NETL-2002/739656-00100.

Koukou, M. K.; Papayannakos, N.; Markatos, N. C. “Dispersion Effects on Membrane Reactor Performance.” *AIChE Journal,* 42(1996), 9, 2607-2615.

Koukou, M. K.; Papayannakos, N.; Markatos, N. C.; Bracht, M.; Alderliesten, P. T. “Simulation Tools for the Design of Industrial-scale Membrane Reactors.” *TransIChemE,* 76A(1998), 911-920.

Krishnankutty, N.; Vannice, M. A. “The Effect of Pretreatment on Pd/C Catalysts, I. Adsorption and Absorption Properties.” *Journal of Catalysis,* 155(1995), 312-326.

Kul’kova, N. V.; Temkin, M. I. *Zhurnal Fizicheskoi Khimii*, 23(1949), 695.

Kulprathipanja, A.; Alptekin, G. O.; Falconer, J. L.; Way, J. D. “Effects of water gas shift gases on Pd-Cu alloy membrane surface morphology and separation properties.” *Industrial & Engineering Chemistry Research* 43(2004) 4188-4198.

Kumar, S.; Shankar, S.; Shah, P. R.; Kumar, S. “A Comprehensive Model for Catalytic Membrane Reactor.” *International Journal of Chemical Reactor Engineering,* 4(2006), A5.

Latyshev, V. V.; Bystritskiy, V. M. “Interaction of Hydrogen Isotopes and Diffusion Membranes Made From Palladium Alloys.” *The Physics of Metals & Metallography,* 71(1991), 6, 1-20.

Lewis, F. A. The Palladium/Hydrogen System, © New York, Academic Press Inc., 1967.

Li, A.; Grace, J. R.; Lim, C. J. “Preparation of thin Pd-based composite membrane on planar metallic substrate. Part I: Pre-treatment of porous stainless steel substrate.” *Journal of Membrane Science,* 298(2007a), 175-181.

Li, A.; Liang, W.; Hughes, R. “The effect of carbon monoxide and steam on the hydrogen permeability of a Pd/stainless steel membrane.” *Journal of Membrane Science*, 165(2000), 135-141.

Li, F.; Fan, L.-S. “Clean coal conversion process – progress and challenges.” *Energy & Environmental Science,* 1(2008a), 248-267.

Li, H.; Goldbach, A.; Li, W.; Xu, H. “CO_2 Decomposition over Pd Membrane Surfaces.” *Journal of Physical Chemistry B,* 112(2008b), 12182-12184.

Li, H.; Goldbach, A.; Li, W.; Xu, H. “On CH_4 decomposition during separation from H_2 mixtures with thin Pd membranes.” *Journal of Membrane Science,* 324(2008c), 95-101.

Li, H.; Goldbach, A.; Li, W.; Xu, H. “PdC formation in ultra-thin Pd membranes during separation of H_2/CO mixtures.” *Journal of Membrane Science,* 299(2007b), 130-137.

Li, H.; Pieterse, J. A. Z.; Dijkstra, J. W.; Haije, W. G.; Xu, H. Y.; Bao, C.; van den Brink, R. W.; Jansen, D. “Performance test of a bench-scale multi-tubular membrane reformer.” *Journal of Membrane Science,* 373(2011), 43-52.

Lin, Y.-M.; Rei, M.-H. “Separation of hydrogen from the gas mixture out of catalytic reformer by using supported palladium membrane.” *Separation and Purification Technology,* 25(2001), 87-95.

Ludtke, O.; Behling, R.-D.; Ohlrogge, K. “Concentration polarization in gas permeation.” *Journal of Membrane Science,* 146(1998), 145-157.

Luyben, W. L. “Design and Control of Gas-Phase Reactor/Recycle Processes with Reversible Exothermic Reactions.” *Indusctrial & Engineering Chemistry Research,* 39(2000), 1529-1538.

Lwin, Y. “Chemical equilibrium by Gibbs energy minimization on spreedsheets.” *International Journal of Engineering Education,* 16(2000), 4, 335-339.

Ma, D.; Lund, C. R. F. “Assessing High-Temperature Water-Gas Shift Membrane Reactors.” *Industrial & Engineering Chemistry Research,* 42(2003), 711-717.

Ma, Y. M.; Akis, B. C.; Ayturk, M. E.; Guazzone, F.; Engwall, E. E.; Mardilovich, I. P. “Characterization of Intermetallic Diffusion Barrier and Alloy Formation for Pd/Cu and Pd/Ag Porous Stainless Steel Composite Membranes.” *Industrial & Engineering Chemistry Research,* 43(2004), 2936-2945.

Ma, Y. H.; Guazzone, F. “Method for fabricating a composite gas separation module.” June 1, 2010, US Patent 7,727,596.

Ma, Y. H.; Mardilovich, I. P.; Engwall, E. E. “Composite gas separation modules having high Tamman temperature intermediate layers.” August 14, 2007, US Patent 7,255,726.

Ma, Y. H.; Mardilovich, I. P.; Engwall, E. E. “Method for fabricating composite gas separation modules.” June 24, 2008, U. S. Patent 7,390,536.

Ma, Y. H.; Mardilovich, P. P.; She, Y. “Hydrogen gas-extraction module and method of fabrication.” November 28, 2000, US Patent 6,152,987.

Ma, Y. H.; Shipman, C. W. “On the computation of complex equilibria” *AIChE Journal,* 18(1972), 2, 299-304.

Maciejewski, M.; Baiker, A. “Incorporation of Carbon into Palladium during Low-Temperature Disproportionation of CO over Pd/ZrO_2 Prepared from Glassy Pd-Zr Alloys.” *Journal of Physical Chemistry,* 98(1994), 285-290.

Magnouche, A.; Fromageau, R. “Hydrogen dissolution in palladium: A resistometric study under pressure” *Journal of Applied Physics*, 56(1984), 6, 1617-1622.

Marcano, J. G. S.; Tsotsis, T. T. Catalytic membranes and membrane reactors, © Weinheim: Wiley-VCH, 2002.

Mardilovich, I. P.; Engwall, E. E.; Ma, Y. H. “Dependence of hydrogen flux on the pore size and plating surface topology of asymmetric Pd-porous stainless steel membranes.” *Desalination,* 144(2002), 85-89.

Mardilovich, I. P.; Engwall, E. E.; Ma, Y. H. “Thermally Stable Composite Palladium Membranes Having Intermediate Porous Metal Intermetallic Diffusion Barrier Layers Formed by Bi-Metal Multi-Layer Deposition.” *Proceeds from the 9th Conference on Inorganic Membranes,* Lillehammer – Norway, June 25-29, 2006.

Marigliano, G.; Barbieri, G.; Drioli, E. “Equilibrium conversion for a Pd-based membrane reactor. Dependence on the temperature and pressure.” *Chemical Engineering and Processing,* 42(2003), 231-236.

Markatos, N. C.; Vogiatzis, E.; Koukou, M. K.; Papayannakos, N. “Membrane Reactor Modeling: A Comparative Study to Evaluate the Role of Combined Mass and Heat Dispersion in Large-scale Adiabatic Membrane Modules.” *Chemical Engineering Research and Design,* 83(2005), A10, 1171-1178.

McKinley, D. L. “Metal Alloy for Hydrogen Separation and Purification.” US Patent 3,350,845 (1967).

Mendes, D.; Mendes, A.; Madeira, L. M.; Iulianelli, A.; Sousa, J. M; Basile, A. “The water-gas shift reaction: from conventional catalytic systems to Pd-based membrane reactors – a review.” *Asia-Pacific Journal of Chemical Engineering,* 5(2010) 111-137.

Moe, J. M. “Design of water-gas shift reactors.” *Chemical Engineering Progress,* 58(1962), 3, 33-36.

Morreale, B. D.; Ciocco, M. V.; Enick, R. M.; Morsi, B. I.; Howard, B. H.; Cugini, A. V.; Rothenberger, K. S. “The permeability of hydrogen in bulk palladium at elevated temperatures and pressures.” *Journal of Membrane Science,* 212(2003), 87-97.

Morreale, B. D.; Ciocco, M. V.; Howard, B. H.; Killmeyer, R. P.; Cugini, A. V.; Enick, R. M. “Effect of hydrogen-sulfide on the hydrogen permeance of palladium-copper alloys at elevated temperatures.” *Journal of Membrane Science,* 241(2004), 210-224.

Morreale, B. D.; Howard, B. H.; Iyoha, O.; Enick, R. M.; Ling, C.; Sholl, D. S. “Experimental and Computational Prediction of the Hydrogen Transport Properties of Pd_4S.” *Industrial & Engineering Chemistry Research,* 46(2007), 6313-6319.

Mundschau, M. V.; Xie, X.; Evenson IV, C. R.; Sammells, A. F. “Dense inorganic membranes for production of hydrogen from methane and coal with carbon dioxide sequestration.” *Catalysis Today,* 118(2006), 12-23.

Nam, S.-E.; Lee, K.-H. “A study on the palladium/nickel composite membrane by vacuum electrodeposition.” *Journal of Membrane Science,* 170(2000), 91-99.

Nam, S.-E.; Lee, K.-H. “Hydrogen separation by Pd alloy composite membranes: introduction of diffusion barrier.” *Journal of Membrane Science,* 192(2001), 177-185.

Nam, S.-E.; Lee, K.-H. “Preparation and Characterization of Palladium Alloy Composite Membranes with a Diffusion Barrier for Hydrogen Separation.” *Industrial & Engineering Chemistry Research,* 44(2005), 100-105.

Nam, S.-E.; Lee, S.-H.; Lee, K.-H. “Preparation of a palladium alloy composite membrane supported on a porous stainless steel by vacuum electrodeposition.” *Journal of Membrane Science,* 153(1999), 163-173.

Neurock, M. “First-principles analysis of the hydrogenation of carbon monoxide over palladium.” *Topics in Catalysis,* 9(1999), 135-152.

Newsome, D. S. “The Water-Gas Shift Reaction.” *Catalysis Reviews: Science and Engineering*, 21(1980), 2, 275-318.

Niemantsverdriet, J.W.; van Langevelt, A.D. “Coke formation on platinum metals studied by auger electron spectroscopy and secondary ion mass spectrometry.” *Fuel,* 65(1986), 1396-1399.

Obama, B. H., State of the Union 2011, United States Capitol, Washington D.C.

Okamoto, H. “C-Pd (Carbon Palladium).” *Journal of Phase Equilibria and Diffusion,* 28(3), 2007, 313.

Pan, X. L.; Stroh, N.; Brunner, H.; Xiong, G. X.; Sheng, S. S. “Pd/ceramic hollow fibers for H_2 separation.” *Seperation and Purification Technology,* 32(2003), 265-270.

Pedernera, M. N.; Pina, J.; Borio, D. O. “Kinetic evaluation of carbon formation in a membrane reactor for methane reforming.” *Chemical Engineering Journal,* 134(2007), 138-144.

Perry, R. H.; Green, D. W. Perry’s chemical engineers’ handbook; seventh edition, © McGraw-Hill, USA, 1997.

Peters, T. A.; Kaleta, T.; Stange, M.; Bredesen, R. “Hydrogen transport through a selection of thin Pd-alloy membranes: Membrane stability, H_2S inhibition, and flux recovery in hydrogen and simulated WGS mixtures.” *Catalysis Today,* 193(2012), 8-19.

Peters, T. A.; Stange, M.; Klette, H.; Bredesen, R. “High pressure performance of thin Pd-23%Ag/stainless steel composite membranes in water gas shift mixtures; influence of dilution, mass transfer and surface effects on the hydrogen flux.” *Journal of Membrane Science,* 316(2008), 119-127.

Peters, T. A; Tucho, W. M.; Ramachandran, A.; Stange, M.; Walmsley, J. C.; Holmestad, R.; Borg, A.; Bredesen, R. “Thin Pd-23%Ag/stainless steel composite membranes: Long-term stability, life-time estimation and post-process characterization.” *Journal of Membrane Science,* 326(2009), 572-581.

Podolski, W. F.; Kim, Y. G. “Modeling the Water-Gas Shift Reaction.” *Industrial Engineering Chemical Process Development,* 13(1974), 4, 415-421.

Pomerantz, N.; Ma, Y. H. “Effects of H_2S on the Performance and Long-Term Stability of Pd/Cu Membranes.” *Industrial & Engineering Chemistry Research*, 48(2009), 8, 4030-4039.

Ramaswami, A.; Milford, J. B.; Small, M. J. Integrated Environmental Modeling. © John Wiley & Sons, Inc. 2005.

Reid, R. C.; Prausnitz, J. M.; Poling, B. E. The Properties of Gases & Liquids. © McGraw-Hill, Inc. 1987.

Reyes, F.; Luyben, W. L. "Steady-State and Dynamic Effects of Design Alternatives in Heat-Exchanger/Furnace/Reactor Processes." *Industrial & Engineering Chemistry Research,* 39(2000), 3335-3346.

Rhodes, C.; Williams, B. P.; King, F.; Hutchings, G. J. "Promotion of Fe_3O_4/Cr_2O_3 high temperature water gas shift catalyst." *Catalysis Communications,* 3(2002), 381-384.

Roa, F.; Block, M. J.; Way, J. D. "The influence of alloy composition on the H_2 flux of composite Pd-Cu membranes." *Desalination,* 147(2002), 411-416.

Roa, F.; Way, J. D. "Influence of Alloy Composition and Membrane Fabrication on the Pressure Dependence of the Hydrogen Flux of Palladium-Copper Membranes." *Industrial & Engineering Chemistry Research,* 42(2003a), 5827-5835.

Roa, F.; Way, J. D.; McCormick, R. L.; Paglieri, S. N. "Preparation and characterization of Pd-Cu composite membranes for hydrogen separation." *Chemical Engineering Journal,* 93(2003b), 11-22.

Robeson, L. M. "The upper bound revisited." *Journal of Membrane Science,* 320(2008), 390-400.

Rogal, J.; Reuter, K.; Scheffler, M. "CO oxidation on Pd(100) at technologically relevant pressure conditions: First-principles kinetic Monte Carlo study." *Physical Review B,* 77(2008), 155410.

Rupprechter, G.; Kaichev, V. V.; Unterhalt, H.; Morkel, M.; Bukhtiyarov, V. I. "CO dissociation and CO hydrogenation on smooth and ion-bombarded Pd(111): SFG and XPS spectroscopy at mbar pressures." *Applied Surface Science,* 235(2004), 26-31.

Salmi, T.; Bostrom, S.; Lindfors, L.-E. "A Dynamic Study of the Water-Gas Shift Reaction over an Industrial Ferrochrome Catalyst." *Journal of Catalysis,* 112(1988), 345-356.

Salmi, T.; Hakkarainen, R. "Kinetic Study of the Low-Temperature Water-Gas Shift Reaction over a Cu-ZnO Catalyst." *Applied Catalysis,* 49(1989), 285-306.

Scura, F.; Barbieri, G.; De Luca, G.; Drioli, E. "The influence of the CO inhibition effect on the estimation of the H_2 purification unit surface." *International Journal of Hydrogen Energy,* 33(2008), 4183-4192.

Selman, G. L.; Ellison, P. J.; Darling, A. S. "Carbon in Platinum and Palladium." *Platinum Metals Review,* 14(1970), 1, 14-20.

Shchibrya, G. G.; Morozov, N. M.; Temkin, M. I. "Kinetics and Mechanism of the Catalytic Reaction of Carbon Monoxide with Water Vapor II. Reaction of Zinc-Chromium-Copper Oxide Catalyst." *Kinetics and Catalysis,* 6(1965), 1010-1011.

Sheintuch, M.; Dessau, R. M. “Observations, modeling and optimization of yield, selectivity and activity during dehydrogenation of isobutane and propane in a Pd Membrane Reactor.” *Chemical Engineering Science,* 51(1996), 4, 535-547.

Shirasaki, Y.; Tsuneki, T.; Ota, Y.; Yasuda, I.; Tachibana, S.; Nakajima, H.; Kobayashi, K. “Development of membrane reformer system for highly efficient hydrogen production from natural gas.”, *International Journal of Hydrogen Energy,* 34(2009), 4482-4487.

Shu, J.; Adnot, A.; Grandjean, B. P. A.; Kaliaguine, S. “Structurally stable composite Pd-Ag alloy membranes: Introduction of a diffusion barrier.” *Thin Solid Films,* 286(1996), 72-79.

Shu, J.; Grandjean, B. P. A.; Van Neste, A.; Kaliaguine, S. “Catalytic Palladium-based Membrane Reactors: A Review.” *Canadian Journal of Chemical Engineering,* 69(1991), 1036-1060.

Shukla, R.; Ranjith, P.; Haque, A.; Choi, X. “A review of studies on CO_2 sequestration and caprock integrity.” *Fuel,* 89(2010), 2651-2664.

Sieverts, A. “Zur Kenntnis der Okklusion und Diffusion von Gasen durch Metalle.” *Zeitschrift fur Physikalische Chemie*, 60(1908), 129-201.

Siller, R. H.; Oates, W. A.; McLellan, R. B. “The solubility of carbon in palladium and platinum.” *Journal of Less Common Metals,* 16(1968), 71-73.

Singer, C. J. A History of Technology, v.5, © Oxford, Clarendon Press, 1954.

Singh, C. P. P.; Saraf, D. N. “Simulation of High-Temperature Water-Gas Shift Reactors.” *Industrial & Engineering Chemistry Process Design and Development,* 16(1977), 3, 313-319.

Smigelskas, A. D.; Kirkendall, E. O. “Zinc Diffusion in Alpha Brass.” *Transactions of the Metallurgical Society of AIME,* 171(1947), 130-142.

Smith, D. P. Hydrogen in Metals, © University of Chicago Press, Chicago IL, 1948.

Stuve, E. M.; Maddix, R. J. “Bonding and dehydrogenation of ethylene on palladium metal. Vibrational spectra and temperature-programed reaction studies on palladium(100).” *Journal of Physical Chemistry,* 89(1985) 105-112.

Swanson, H. E.; Tatge, E., *National Bureau of Standards Circular,* v. 359(1953).

Tiemersma, T. P.; Patil, C. S.; van Sint Annaland, M.; Kuipers, J. A. M. “Modelling of packed bed membrane reactors for autothermal production of ultrapure hydrogen.” *Chemical Engineering Science,* 61(2006), 1602-1616.

Tinkle, M.; Dumesic, J. A. “Isotopic Exchange Measurements of the Rates of Adsorption/Desorption and Interconversion of CO and CO_2 over Chromia-Promoted Magnetite: Implications for Water-Gas Shift.” *Journal of Catalysis,* 103(1987), 65-78.

Tong, J.; Matsumura, Y. “Thin Pd membrane prepared on macroporous stainless steel tube filter by an *in-situ* muli-dimensional plating mechanism.” *Chemical Communications,* 2004, 2460-2461.

Tong, J.; Suda, H.; Haraya, K.; Matsumura, Y. “A novel method for the preparation of thin dense Pd membrane on macroporous stainless steel tube filter.” *Journal of Membrane Science,* 260(2005), 10-18.

Torkelson, J.; Ye, N.; Li, Z.; Coutinho, D.; Fokema, M. “Robust low-cost water-gas shift membrane reactor for high-purity hydrogen production from coal-derived syngas.” DOE/DE-FC26-05NT42452, August 2008.

Tosti, S. “Supported and laminated Pd-based metallic membranes.” *International Journal of Hydrogen Energy,* 28(12), 2003, 1445-1454.

Tosti, S.; Basile, A.; Chiappetta, G.; Rizzello, C.; Violante, V. “Pd-Ag Membrane Reactors for Water Gas Shift Reaction.” *Chemical Engineering Journal*, 93(2003), 23-30.

Uchida, H.; Isogai, N.; Oba, M.; Hasegawa, T. “The zinc oxide-copper catalyst for carbon monoxide-shift conversion. I. The dependence of the catalytic activity on the chemical composition of the catalyst.” *Bulletin of the Chemical Society of Japan,* 40(1967), 1981-1986.

Uchida, H.; Oba, M.; Isogai, N.; Hasegawa, T. “The Zinc Oxide-Copper Catalyst for Carbon Monoxide-Shift Conversion. II. The Catalytic Activity and the Catalyst Structures.” *Bulletin of the Chemical Society of Japan,* 41(1968), 479-485.

Uemiya, S.; Ando, N. S. H.; Kikuchi, E. “The Water Gas Shift Reaction Assisted by a Palladium Membrane Reactor.” *Industrial & Engineering Chemistry Research*, 30(1991a), 585-589.

Uemiya, S.; Kato, W.; Uyama, A.; Kajiwara, M.; Kojima, T.; Kikuchi, E. “Separation of hydrogen from gas mixtures using supported platinum-group metal membranes.” *Separation and Purification Technology,* 22-23(2001), 309-317.

Uemiya, S.; Sato, N.; Ando, H.; Matsuda, T.; Kikuchi, E. “Steam reforming of methane in a hydrogen-permeable membrane reactor.” *Applied Catalysis,* 67(1991b), 223-230.

Unemoto, A.; Kaimai, A.; Sato, K.; Otake, T.; Yashiro, K.; Mizusaki, J.; Kawada, T.; Tsuneki, T.; Shiraski, Y.; Yasuda, I. “The effect of co-existing gases from the process of steam reforming reaction on hydrogen permeability of palladium alloy membrane at high temperatures.” *International Journal of Hydrogen Energy,* 32(2007), 2881-2887.

United States Energy Information Administration (US EIA), 2008, http://www.eia.doe.gov/.

Wakao, N.; Funazkri, T. “Effect of fluid dispersion coefficients on particle-to-fluid mass transfer coefficients in packed beds.” *Chemical Engineering Science,* 33(1978), 1375-1384.

Wang, D.; Flanagan, T. B.; Shanahan, K. L. “Permeation of hydrogen through pre-oxidized Pd membranes in the presence and absence of CO.” *Journal of Alloys and Compounds,* 372(2004), 158-164.

Ward, T. L.; Dow, T. “Model of hydrogen permeation behavior in palladium membranes.” *Journal of Membrane Science*, 153(1999), 211-231.

Wilke, C. R. “A Viscosity Equation for Gas Mixtures.” *Journal of Chemical Physics,* 18(1950), 517-519.

Wilke, S.; Scheffler, M. “Poisoning of Pd(100) for the dissociation of H_2: a theoretical study of co-adsorption of hydrogen and sulfur.” *Surface Science,* 329(1995), L605-L610.

Yang, R. T.; Goethel, P. J.; Schwartz, J. M; Lund, C. R. F. “Solubility and Diffusivity of Carbon in Metals.” *Journal of Catalysis,* 122(1990), 206-210.

Yokoyama, H.; Numakura, H.; Koiwa, M. “The Solubility and Diffusion of Carbon in Palladium.” *Acta Materialia,* 46(1998), 8, 2823-2830.

Zhang, Y.; Wang, Z.; Wang, S. C. “Selective permeation of CO_2 through new facilitated transport membranes.” *Desalination,* 145(2002), 385-388.

Zhao, H.-B.; Xiong, G.-X.; Baron, G. V. “Preparation and characterization of palladium-based composite membranes by electroless plating and magnetron sputtering.” *Catalysis Today,* 56(2000), 89-96.

Ziemecki, S. B. “Catalytic reaction based on diffusion of carbon atoms through a palladium membrane.” *Studies in Surface Science and Catalysis* (Book Series), Catalysis 1987, © Elsevier Science Publishers B. V. Amsterdam, 1988.

Ziemecki, S. B.; Jones, G. A.; Swartzfager, D. G. “Coexistance of hydrogen and carbon solutes in the palladium lattice.” *Journal of Less-Common Metals,* 131(1987), 157-162.

Ziemecki, S. B.; Jones, G. A.; Swartzfager, D. G.; Harlow, R. L. “Formation of Interstitial Pd-C Phase by Interaction of Ethylene, Acetylene, and Carbon Monoxide with Palladium.” *Journal of the American Chemical Society,* 107(1985), 4547-4548.

APPENDIX A: DERIVATION OF EQUATIONS AND OTHER EXPRESSIONS

A.1. WGS equilibrium constant (Bisset, 1977)

A highly accurate expression for the WGS equilibrium expression was proposed by Bisset (1977) given by the equation:

$$K = exp\left(-13.148 + \frac{5639.5}{T} - \frac{49,170}{T^2} + 1.077ln(T) + 5.44 * 10^{-4}T - 1.125 * 10^{-7}T^2\right)$$

A.2. Derivation of equation 2.30

Ficks Law:

$$J = (D/t_{Pd})(C_1 - C_2) \qquad \textbf{2.24}$$

The flux of a substance diffusing in solution between two points is equal to the diffusivity of the substance in solution, multiplied by the concentration gradient, divided by the distance between the points. The law has been applied to both solid and fluid solutions. The concentration of atomic H in bulk Pd was given by equation **2.25**.

$$C_x \equiv \kappa \nu_x \qquad \textbf{2.25}$$

For convenience, the concentration of atomic hydrogen in the palladium was expressed as the H/Pd atomic ratio multiplied by a concentration factor, $\kappa = 1.13 * 10^5 \mathbf{mol/m^3}$, which was the molar density of palladium. The overall flux of H_2 being adsorbed onto the surface was given by equation **2.26.**

$$J_a = k_a P_x(1 - \theta_H)^2 - k_d \theta_H^2 \qquad \textbf{2.26}$$

The overall flux of H_2 being adsorbed onto the surface was equal to the adsorbing flux minus the desorbing flux. The adsorbing flux was proportional to the partial pressure of H_2 above the surface and the concentration of adjacent free surface sites, $(1 - \theta_H)^2$. The desorbing flux was proportional to the concentration of adjacent occupied surface sites, θ_H^2. The flux of H_2 being dissolved into the bulk was given by equation **2.27**.

$$J_d = \kappa k_i \theta_H (1 - v_x) - \kappa v_x k_o (1 - \theta_H) \qquad \textbf{2.27}$$

The overall flux of H_2 being dissolved into the bulk was equal to the dissolving flux minus the evolving flux. The dissolving flux of atomic hydrogen into the bulk was proportional to the fraction of atomic hydrogen occupied surface sites and the fraction of vacant spaces in the lattice. The evolving flux of atomic hydrogen onto the surface was proportional to the fraction of unoccupied surface sites and the fraction of occupied spaces in the lattice.

Assuming that the bulk diffusion step was rate limiting, equation **2.24** defined the flux. The fluxes of adsorption and desorption and dissolution and evolution were at equilibrium such that the overall fluxes from equations **2.26** and **2.26** were equal to zero. The equations **2.26** and **2.27** were thus simplified to equations **2.26a** and **2.27a**.

$$k_a P_x (1 - \theta)^2 = k_d \theta^2 \qquad \textbf{2.26a}$$

$$k_i \theta (1 - v_x) = v_x k_o (1 - \theta) \qquad \textbf{2.27a}$$

The equations **2.26a** and **2.27a** were combined to create an equilibrium expression relating the hydrogen partial pressure above the surface to the H/Pd atomic ratio just below the surface. The definition of atomic H-concentration in the bulk, equation **2.25** was also incorporated resulting in equation **2.28**.

$$\frac{\kappa k_i}{k_o} \sqrt{\frac{k_a}{k_d}} \sqrt{P_x} (1 - v_x) = v_x \kappa = C_x \qquad \textbf{2.28}$$

The terms k_i, k_o, k_a, and k_d were combined to form a single term, K_s, which is known as Sieverts' constant, $K_s = \frac{k_o}{k_i} \sqrt{\frac{k_d}{k_a}}$. Incorporating equation **2.28** into equation **2.24** for both C_1 and C_2 yielded equation **2.24a**.

$$J = \frac{D\kappa}{t_{Pd} K_s} \left(\sqrt{P_1} (1 - v_1) - \sqrt{P_2} (1 - v_2) \right) \qquad \textbf{2.24a}$$

This equation was commonly simplified by the assumption that v_1 and v_2 were much less than one so that $(1 - v_1) \approx 1$. When this simplification was made, the relationship between flux and pressure known as Sieverts' law, equation **2.29**, was arrived at.

$$\boldsymbol{J = \frac{D\kappa}{t_{Pd}K_s}\left(\sqrt{P_1} - \sqrt{P_2}\right)} \qquad \textbf{2.29}$$

Instead of simplifying equation **2.24a**, $\boldsymbol{v_1}$ and $\boldsymbol{v_2}$ could be solved for in terms of pressure by the substitution shown below resulting in equation **2.28a** (a rearrangement of equation **2.28**).

$$\boldsymbol{v_x = \frac{\sqrt{P_x}}{K_s + \sqrt{P_x}}} \qquad \textbf{2.28a}$$

Substituting equation **2.28a** into equation **2.24a** then simplifying yielded equation **2.30**.

$$\boldsymbol{J = \frac{D\kappa}{t_{Pd}}\left(\frac{\sqrt{P_1}}{K_s + \sqrt{P_1}} - \frac{\sqrt{P_2}}{K_s + \sqrt{P_2}}\right)} \qquad \textbf{2.30}$$

Equation **2.30** implies that at very high pressure ($\sqrt{P_x} > K_s$), the Pd-lattice will be nearly saturated with H-atoms, so there will no longer be a strong concentration gradient for hydrogen diffusion, resulting in a maximum achievable driving force. In other words, for a P_1 much greater than K_s, there will no longer be greater flux by further increasing P_1.

A.3. Derivation of equation 4.10

The resistance of the dense Pd-layer, R_{Pd}, was defined by equation **4.10a**.

$$R_{Pd} = \frac{\Delta P}{J_{H2}} = \frac{P_1 - P_2}{J_{H2}} \qquad \textbf{4.10a}$$

Where P_1 and P_2 [atma] were the partial pressures of H_2 on sides 1 and 2 of the membrane and J_{H2} [m^3/m^2-h] was the flux of H_2 across the membrane. The Sievert's law equation **2.31**, was used to substitute for J_{H2}, resulting in equation **4.10b**.

$$R_{Pd} = \frac{\delta_{Pd}(P_1 - P_2)}{Q_{H2}\left(\sqrt{P_1} - \sqrt{P_2}\right)} \qquad \textbf{4.10b}$$

Where δ_{Pd} [μm] was the thickness of the Pd-layer and Q_{H2} [m^3-μm/m^2-h-$atm^{0.5}$] was the permeability of hydrogen in the metal. Equation **4.10b** was simplified by the equality $P_1 - P_2 = \left(\sqrt{P_1} + \sqrt{P_2}\right)\left(\sqrt{P_1} - \sqrt{P_2}\right)$ resulting in equation **4.10**.

$$R_{Pd} = \frac{\delta_{Pd}\left(\sqrt{P_1} + \sqrt{P_2}\right)}{Q_{H2}} \qquad \textbf{4.10}$$

A.4. 1-D simulation output

Numerical integration of the 1-D modeling equations described in Chapter 5 (equations **5.4** – **5.18**) resulted in a profile of the state variables (X_{CO} and Y_{H2}) with regard to the axial position in the reactor. As an example, the model was solved with the parameters listed in Table A.1. The system dimensions were that of the experimental system described in the Experimental, Section 3.5.1. The gas boundary layer mass transfer coefficient, k_B, was estimated by an empirical correlation as described in Chapters 5 and 6 (Perry and Green, 1997). The surface inhibition coefficient was estimated from the literature binding energies of CO (Guo and Yates, 1989) and H_2O (Catalano et al., 2011) via equations **5.9** – **5.10** described in Chapter 5.

Table A.1. Modeling parameters utilized for the example.

Catalyst Properties	Fe/Cr-oxide
Catalyst density, ρ_{cat} [kg/m^3]	1.06*10^3
Catalyst void fraction, ε	0.47
Particle size, d_p [m]	3.5*10^{-4} (average particle size)
Rate expression, $r_{CO}/(1-\beta)$ [kmol/kg-h]	$2.52 \times 10^6 e^{-111/RT} P_{CO} P_{CO2}^{-0.36} P_{H2}^{-0.09}$ (Equation **5.20**, Hla *et al.,* 2009)
Effectiveness factor, η	1.0 (assumed)
Reactor Dimensions	Tube-in-tube
Reactor Length, L [m]	0.065
Cross-sectional area, A_c [m^2]	2.33*10^{-4}
Aspect ratio	14.8
Membrane Properties	Tubular
Membrane area, A_{Pd} [m^2]	2.5*10^{-3}
Permeance, $F_{H2,0}$ [m^3/m^2-h-atm$^{0.5}$]	26.7
Binding energy, ΔE_i [kJ/mol]	CO: -149 (Guo and Yates, 1989) H_2O: -125 (Catalano *et al.,* 2011)
Feed Properties	
Feed composition, θ_i	θ_{H2O} = 2.6, θ_{CO2} = 0, θ_{H2} = 0
Feed rate, $N_{CO,r,0}$ [kmol/h]	A: 4.79*10^{-4}, B: 1.44*10^{-3}
Inert sweep, $N_{i,p,0}$ [kmol/h]	None
Temperature, T [°C]	400
Reaction pressure, P_s [atma]	14.6
Tube-side pressure, P_t [atma]	0.98
Dynamic viscosity, μ [kg/h-m]	0.084
Diffusivity of H_2, D_{H2} [m$_2$/h]	0.0796
Sherwood number approximation, *Sh*	$1.15Sc^{0.333}\left(\frac{Re}{\varepsilon}\right)^{0.5}$ (Equation **5.16**, Perry and Green, 1997)

The solution consisted of three datasets: ξ, X_{CO}, and Y_{H2} as are plotted in Figure A.1.

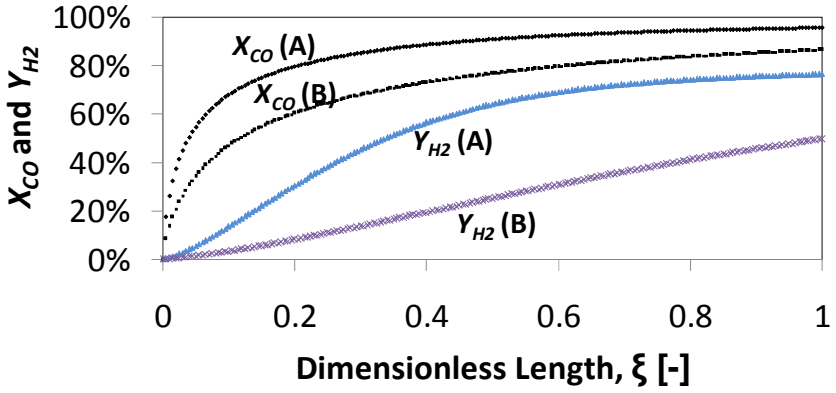

Figure A.1. CO conversion and H_2 recovery versus dimensionless length (A: GHSV = 2,900 h^{-1}, B: GHSV = 8,700 h^{-1}).

The H_2 recovery, Y_{H2}, could be used to determine the H_2 flux, J_{H2}, at each point along the membrane by equation **5.5a**, derived from the definition of H_2 recovery, equation **5.5**, and incorporating the parameters listed in Table A.1. The H_2 flux versus dimensionless length is plotted in Figure A.2.

$$Y_{H2} \equiv \frac{N_{H2,p}}{N_{CO,r,0}} \qquad \textbf{5.5}$$

$$J_{H2} = Y_{H2} \frac{N_{CO,r,0} R T_0}{A_{Pd} P_0} \qquad \textbf{5.5a}$$

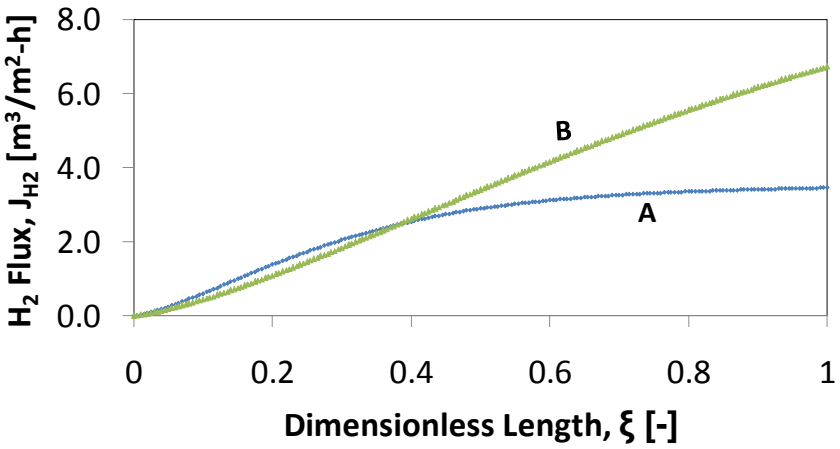

Figure A.2. H_2 flux versus dimensionless length (A: GHSV = 2,900 h^{-1}, B: GHSV = 8,700 h^{-1}).

The CO conversion and H_2 recovery were algebraically related to the partial pressure of H_2 on the retentate side, $P_{H2,r}$, by equation **5.6** and the partial pressure of each other species on the retentate side, $P_{i,r}$, by equation **5.7** (and incorporating the parameters listed in Table A.1). The partial pressure of H_2 on the retentate side versus dimensionless length is plotted in Figure A.3[a]. The partial pressures of CO and CO_2 on the retentate side versus dimensionless length are plotted in Figure A.3[b]. The output of the model corresponding to $\xi = 1$ was used for comparison with data from the experimental system.

$$P_{H2,r} = P_{T,r}\frac{\theta_{H_2}+X_{CO}-Y_{H_2}}{1+\theta_{H_2O}+\theta_{H_2}+\theta_{CO_2}-Y_{H_2}} \qquad \textbf{5.6}$$

$$P_{i\neq H2,r} = P_{T,r}\frac{\theta_i+v_iX_{CO}}{1+\theta_{H_2O}+\theta_{H_2}+\theta_{CO_2}-Y_{H_2}} \qquad \textbf{5.7}$$

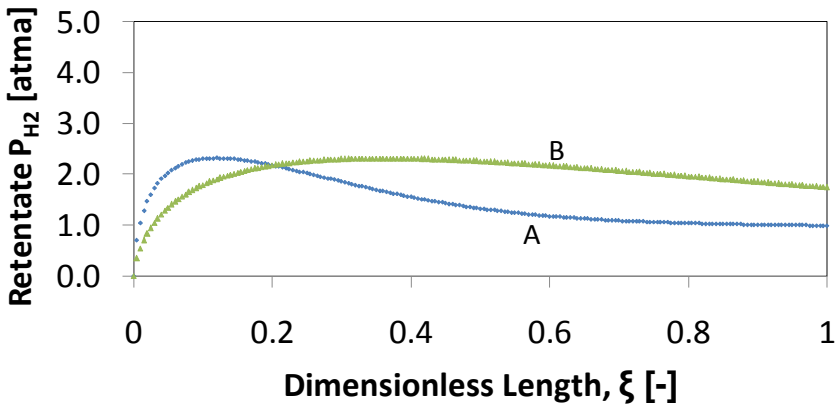

[a]

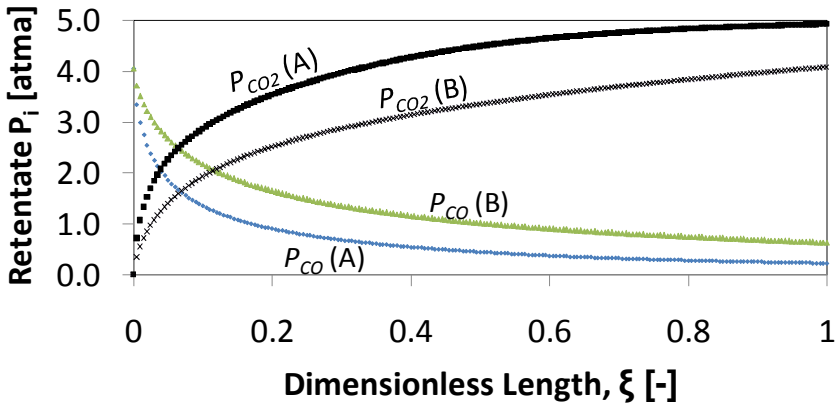

[b]

Figure A.3. [a] $P_{H2,r}$ versus dimensionless length [b] $P_{CO,r}$ and $P_{CO2,r}$ versus dimensionless length (A: GHSV = 2,900 h^{-1}, B: GHSV = 8,700 h^{-1}).

The partial pressure of H_2 versus the dimensionless length (Figure A.3[a]) indicated that there was initially no H_2 present at the reactor inlet. H_2 was formed by the reaction more rapidly than it was removed so that the partial pressure of H_2 increased to a maximum level at ξ = 0.12 and 0.36 for the feed space velocities of 2,900 and 8,700 h^{-1} respectively. The partial pressure of CO versus the dimensionless length (Figure A.3[b]) decreased exponentially since CO was consumed by the WGS reaction. The partial pressure of CO_2 (Figure A.3[b]) increased over the dimensionless length since CO_2 was both generated by the WGS reaction and concentrated by the recovery of H_2.

APPENDIX B: MEMBRANE FABRICATION PROCEDURE

Included in this section are two detailed procedures (Synthesis Methods A and B) for membrane preparation. A list of all the solutions utilized during membrane fabrication is shown in Table B.1.

For both synthesis methods the support was first cleaned by submerging in **Basic Cleaning Solution** (see Table B.1) at 40℃ and sonicated for 30 min. The support was then submerged in flowing water for 60 min. The support was sonicated in deionized water for 3x5 min (3 submersions of 5 minutes each), IPA for 5 min, and then dried in air at 120℃.

Table B.1. Solutions used in membrane synthesis.

Basic Cleaning Solution (200 mL) (components added and mixed in order)	190 mL H_2O 9 g Na_3PO_4*12H_2O 13 g Na_2CO_3 9 g NaOH ~1 mL Detergent (added just before use)
Alumina Slurry 0.01 – 1.0 µm (1 L) (components added and mixed in order)	1 L H_2O 0.1 mL HCl (aqueous concentrated, ~10M) 0.85 g α-Al_2O_3 (0.3 µm particles) 0.14 g α-Al_2O_3 (1.0 µm particles) 0.09 g α-Al_2O_3 (0.01 µm particles)
Alumina Slurry 10 µm (1 L) (components added and mixed in order)	1 L H_2O 0.1 mL HCl (aqueous concentrated, ~10M) 4.0 g α-Al_2O_3 (10 µm particles)
Alumina Slurry 3 - 5 µm (1 L) (components added and mixed in order)	1000 mL H_2O 0.1 mL HCl (aqueous concentrated, ~10M) 10 g α-Al_2O_3 (3 µm particles) 10 g α-Al_2O_3 (5 µm particles)
Alumina Slurry 0.02 - 1.0 µm (1 L) (components added and mixed in order)	1 L H_2O 0.1 mL HCl (aqueous concentrated, ~10M) 0.5 g α-Al_2O_3 (0.02 µm particles) 2 g α-Al_2O_3 (0.3 µm particles) 2 g α-Al_2O_3 (1.0 µm particles)
Alumina Slurry 0.02-0.3 µm (1 L) (components added and mixed in order)	500 mL H_2O 0.1 mL HCl (aqueous concentrated, ~10M) 0.5 g $SnCl_2$*2H_2O 0.5 g α-Al_2O_3 (0.02 µm particles) 2 g α-Al_2O_3 (0.3 µm particles) 500 mL Palladium (II) Chloride Solution (added after 15 min)
Tin(II) Chloride Solution (500 mL) (prepared immediately prior to use, components added and mixed in order)	500 mL H_2O 0.5 mL HCl (aqueous concentrated, ~10M) 0.5 g $SnCl_2$*2H_2O

Palladium(II) Chloride Solution (1 L)	1 L H_2O 1.0 mL HCl (aqueous concentrated, ~10M) 0.1 g PdCl2 (heat to ~40℃ and stir to dissolve)
Pd(II) Plating Solution (1 L) (components added and mixed in order)	200 mL H_2O 200 mL NH_4OH (aqueous concentrated, ~14M) 4.0 g $Pd(NH_3)_4Cl_2*H_2O$ 40.1 g $Na_2EDTA*2H_2O$ 600 mL H_2O (fill to 1 L)
Ag(I) Plating Solution (1 L) (components added and mixed in order)	200 mL H_2O 200 mL NH_4OH (aqueous concentrated, ~14M) 0.52 g $AgNO_3$ 40.1 g $Na_2EDTA*2H_2O$ 600 mL H_2O (fill to 1 L)
Hydrazine (1 M, 40 mL) (99% Hydrazine is extremely corrosive, toxic, and flammable, handle with extreme care)	1.30 mL Hydrazine (98.5% anhydrous) 39 mL H_2O (fill to 40 mL)

Synthesis Method A

The support was oxidized by heating in air at 5℃/min to 600℃ (PSS) or 700℃ (PI) for 12 hours. Full vacuum (~0.1 atma) was applied to the tube-side of the support and the support was submerged in water for 5 min. With vacuum still applied, the support was dipped into 1M HCl for ~2 sec, then water for 5 more min. The support was dipped into **Alumina Slurry (0.02 – 1.0 µm)** for 10 sec then withdrawn from the solution into the air. When the tube was withdrawn from the solution, care was taken to prevent drips from running down from the non-porous section to the porous section of the support causing trails. The support was allowed to dry for 5 min. The support was dipped into water for 5 min, then turned up-right into the air again for 5 min. Care was again taken to prevent drips. The vacuum line was detached and the support was dried in air at 120℃ for at least 5 hours.

Partial vacuum (~0.5 atma) was applied to the tube-side of the support and the support was submerged in water for 5 min. The support was put through one **Activation Cycle** (see Table B.2) then into water for 5 min. **Pd(II) Plating Solution** (70 mL) was heated to 60℃ and **Hydrazine** (0.4 mL) was added. The support, from here on to be referred to as ‘the membrane’, was submersed in the plating solution for 10 min followed by water for 10 min. When the membrane was submerged in Pd(II) Plating Solution nitrogen bubbles could be seen eminating from the membrane surface, confirming that the

plating reaction was occurring. The vacuum line was detached, the vacuum was turned off, and the membrane was dried in air at 120℃.

Table B.2. **Activation Cycle** procedure; the membrane was dipped into each solution sequentially for the prescribed time.

Solution	Time (min)
Tin(II) Chloride Solution	5
H_2O (1)	2
H_2O (2)	3
Palladium (II) Chloride Solution	5
0.01 M HCl	2
H_2O (3)	3

A **Pd/Ag Barrier Treatment** was applied by immersing the membrane in the solutions listed in Table B.3.

Table B.3. **Pd/Ag Barrier Treatment** procedure.

Solution	**Time (min)**	**T (℃)**	**Details**
H_2O	5	25	
1M HCl	0.5	25	Sensitization treatment
H_2O	5	25	
3 **Activation Cycles**			(See Table B.2)
H_2O	10	25	
Pd (II) Plating Sol'n	30	60	0.25 mL **Hydrazine** added to 70 mL
H_2O	5	60	
Ag(I) Plating Sol'n	60	60	0.4 mL **Hydrazine** added to 70 mL
H_2O	5	60	
Pd(II) Plating Sol'n	60	60	0.25 mL **Hydrazine** added to 70 mL
H_2O	5	60	
Ag(I) Plating Sol'n	60	60	0.4 mL **Hydrazine** added to 70 mL
H_2O	5	60	
Pd(II) Plating Sol'n	60	60	0.4 mL **Hydrazine** added to 70 mL
H_2O	10	25	

The membrane was dried in air at 120°C and then lightly polished by hand with 2,400 grade SiC paper. The membrane was plated with palladium, 3x90 minutes, by immersion in the solutions listed in Table B.4.

Table B.4. 1st palladium plating, 3x90 minutes.

Solution	**Time (min)**	**T (°C)**	**Details**
H_2O	5	25	
1M HCl	0.5	25	Sensitization treatment
H_2O	5	25	
5 **Activation Cycles**			(See Table B.2)
H_2O	10	25	
Pd(II) Plating Sol'n	90	60	0.4 mL **Hydrazine** added to 70 mL
H_2O	10	60	
Pd(II) Plating Sol'n	90	60	0.4 mL **Hydrazine** added to 70 mL
H_2O	10	60	
Pd(II) Plating Sol'n	90	60	0.4 mL **Hydrazine** added to 70 mL
H_2O	10	25	

The membrane was dried in air at 120°C and then a **Mechanical Treatment** was performed. The Mechanical Treatment is described in Table B.5. The membrane was plated with palladium, 3x90 minutes, by immersion in the solutions listed in Table B.6.

Table B.5. **Mechanical Treatment** procedure; the membrane was treated on a lathe at ~200 rpm sequentially with each grade of SiC paper for the prescribed time.

SiC Paper Grade	Time (min)
600	1
1,200	2
2,400	5

Table B.6. 2nd palladium plating, 3x90 minutes.

Solution	Time (min)	T (°C)	Details
H_2O	5	25	
1M HCl	0.5	25	Sensitization treatment
H_2O	5	25	
3 **Activation Cycles**			(See Table B.2)
Pd(II) Plating Sol'n	90	60	0.4 mL **Hydrazine** added to 70 mL
H_2O	10	60	
Pd(II) Plating Sol'n	90	60	0.4 mL **Hydrazine** added to 70 mL
H_2O	10	60	
Pd(II) Plating Sol'n	90	60	0.4 mL **Hydrazine** added to 70 mL
H_2O	10	25	

The membrane was dried in air at 120°C and then a **Mechanical Treatment** (see Table B.5) was performed. The membrane was plated the third time with palladium, 2x90 minutes, by immersion in the solutions listed in Table B.7.

Table B.7. 3rd palladium plating, 2x90 minutes.

Solution	Time (min)	T (°C)	Details
H_2O	5	25	
1M HCl	0.5	25	Sensitization treatment
H_2O	5	25	
2 **Activation Cycles**			(See Table B.2)
H_2O	10	25	
Pd(II) Plating Sol'n	90	60	0.4 mL **Hydrazine** added to 70 mL, partial tube-side vacuum
H_2O	10	60	
Pd(II) Plating Sol'n	90	60	0.4 mL **Hydrazine** added to 70 mL, full tube-side vacuum
H_2O	10	60	

The membrane was dried in air at 120°C and leak tested by applying 2.4 atmg He to the shell-side of the membrane and measuring the tube-side flow. If the flow was less than 0.05 sccm, the membrane was considered 'dense'.

Synthesis Method B

The cleaned support was graded before and after oxidation by applying the **Alumina Slurries** in the order listed in Table B.8. The support was oxidized by heating in air at

5℃/min to 600℃ (PSS) or 700℃ (PI) for 12 hours. After each 30 sec alumina slurry treatment the support was withdrawn into the air and brushed with a nitrile glove to remove excess slurry cake. The glove brushing was done aggressively to make sure that no excess alumina particles remained free on the surface and to slightly polish the support surface (using the alumina particles as polishing grit). Following the oxidation, a small amount of Pd was electroless plated after each grading treatment to secure the alumina particles to the surface.

Table B.8. Alumina grading treatments for Synthesis Method B.

Solution	**Time**	**T (℃)**	**Details**
Alumina Slurry 10 µm	3x30 sec	25	Full tube-side vacuum
Alumina Slurry 3-5 µm	3x30 sec	25	Full tube-side vacuum
Oxidation	12 hours		
Alumina Slurry 3-5 µm	3x30 sec	25	Full tube-side vacuum
1 Activation Cycle		25	Full tube-side vacuum
Pd(II) Plating Sol'n	5 min	60	0.4 mL **Hydrazine** added to 70 mL, full tube-side vacuum
Alumina Slurry 0.02-1 µm	3x30 sec		Full tube-side vacuum
1 Activation Cycle		25	Full tube-side vacuum
Pd(II) Plating Sol'n	5 min	60	0.4 mL **Hydrazine** added to 70 mL, full tube-side vacuum
Alumina Slurry 0.02-0.3 µm	3x30 sec		Full tube-side vacuum
1 Activation Cycle		25	Full tube-side vacuum
Pd(II) Plating Sol'n	10 min	60	0.4 mL **Hydrazine** added to 70 mL, full tube-side vacuum

The membrane was plated with palladium, 3x90 minutes, by immersion in the solutions listed in Table B.9.

Table B.9. Palladium plating for Synthesis Method B.

Solution	**Time (min)**	**T (°C)**	**Details**
2**Activation Cycles**			(See Table C.2)
H_2O	10	25	
Pd(II) Plating Sol'n	60	60	0.4 mL **Hydrazine** added to 70 mL
Alumina Slurry 0.02-0.3 µm	3x30 sec		Full tube-side vacuum
1 Activation Cycle			Full tube-side vacuum
Pd(II) Plating Sol'n	10 min	60	0.4 mL **Hydrazine** added to 70 mL, full tube-side vacuum
1**Activation Cycle**			
H_2O	10	25	
Pd(II) Plating Sol'n	60	60	0.4 mL **Hydrazine** added to 70 mL

The membrane was dried in air at 120°C and leak tested by applying 2.4 atmg He to the shell-side of the membrane and measuring the tube-side flow. If the flow was less than 0.05 sccm, the membrane was considered 'dense'.

APPENDIX C: GC METHOD DETAILS

A Gas Chromatograph (HP 5890 Series II) equipped with a TCD detector and a Carboxen 1000 column was used to analyze the compositions of gas mixtures from the retentate and permeate streams for mixed gas and WGS reactor experiments. Argon was used as the carrier gas at a flow rate of 20 ml/min and at a column head pressure of 300 kPa. The details of the GC method are summarized in Table C.1 and a sample chromatograph of an equimolar mixture of H_2, N_2, CO, and CO_2 is shown in Figure C.1.

Table C.1. GC method details for the HP 5890 GC.

Column	60/80 Carboxen 1000 (15' x 1/8")
Carrier	Ar, 20 mL/min (~300 kPa head pressure)
Oven	Isothermal, 150℃ (10 min)
Detector	TCD, negative polarity, high sensitivity T = 200℃
Loop Volume	10 µL gas injection, 10 sec injection delay
Retention Time	H_2: 1.30 min, N_2: 2.41 min, CO: 2.85 min, CO_2: 7.55 min

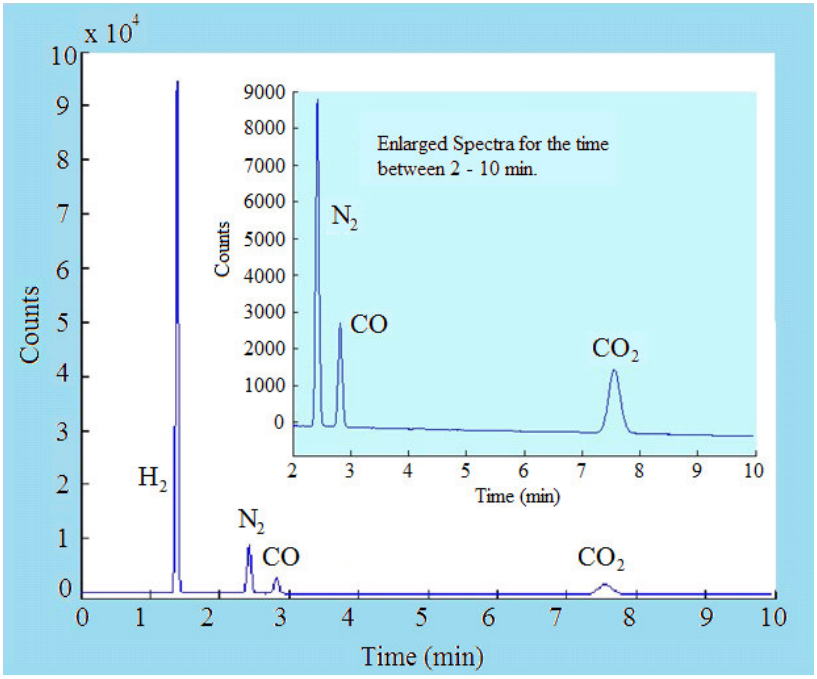

Figure C.1. Sample gas chromatograph of a 1:1:1:1 mixture of H_2, N_2, CO, and CO_2.

The calibration for different gases (hydrogen, nitrogen, carbon monoxide, and carbon dioxide) was performed by using samples of gas with varying composition from flow controllers, 50:50-95:5 H_2:CO_2, and 0:50:50-49:2:49 H_2:CO:CO_2. Additional calibration points were included from a mixed gas cylinder, 80:10:10 CO_2:H_2:He (AIM Products Inc.). Atleast three runs of each gas composition were conducted. The calibration curves for H_2, CO, and CO_2 are shown in Figure C.2. A high degree of linearity was observed between the integrated peak area and the concentration of each species. At a 95% confidence interval, the standard error for the area calculations was 0.2 - 3.6%

[a]

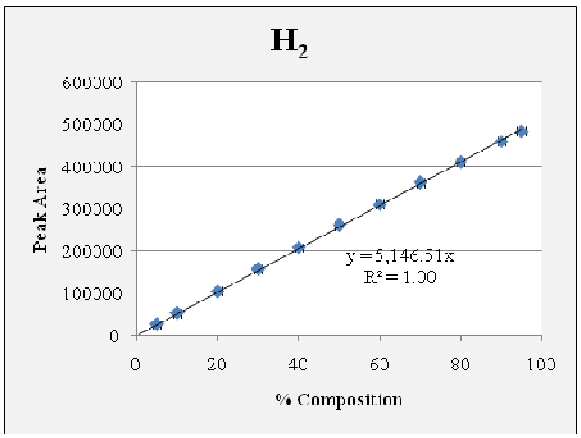

[b]

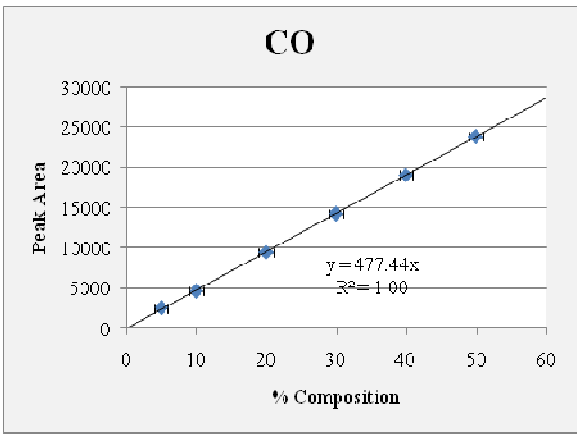

[c]

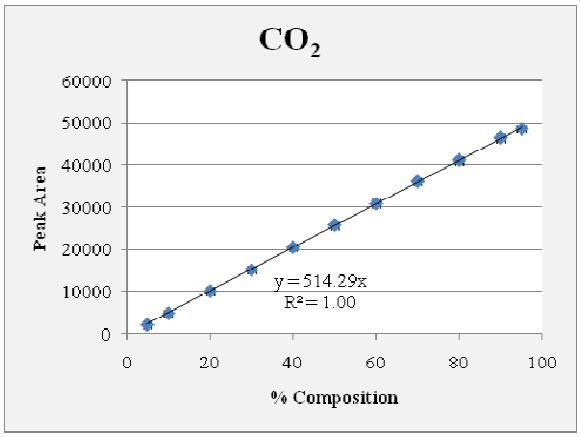

Figure C.2. Calibration curves for each of the WGS species [a] H_2 [b] CO [c] CO_2.

A Gas Chromatograph (SRI Model 8610C) equipped with a FPD detector and a 1/32" MXT stainless steel capillary column was used to analyze the feed and retentate

streams for concentrations of H_2S between 0.1 and 50 ppmv during mixed gas experiments as well as WGS reactor experiments. Helium was used as the carrier gas at a flow rate of 5 ml/min and at a column head pressure of 300 kPa. The details of the GC method are summarized in Table C.2 and a sample chromatogram of a 5 ppmv H_2S in shifted syngas mixture is shown in Figure C.3.

Table C.2. GC method details for the SRI 8610C GC.

Column	MXT SS Capilary (35' x 1/32")
Carrier	He, 5 mL/min (~300 kPa head pressure)
Oven	Isothermal - 50℃ (3 min)
Detector (high sensitivity)	FPD, air: 2 psi, H_2: 35 psi T = 200℃
Detector (low sensitivity)	FPD, air: 4 psi, H_2: 30 psi T = 200℃
Loop Volume	500 µL gas injection (30 sccm flow rate)
Retention Time	COS: 1.61 min H_2S: 1.76 min

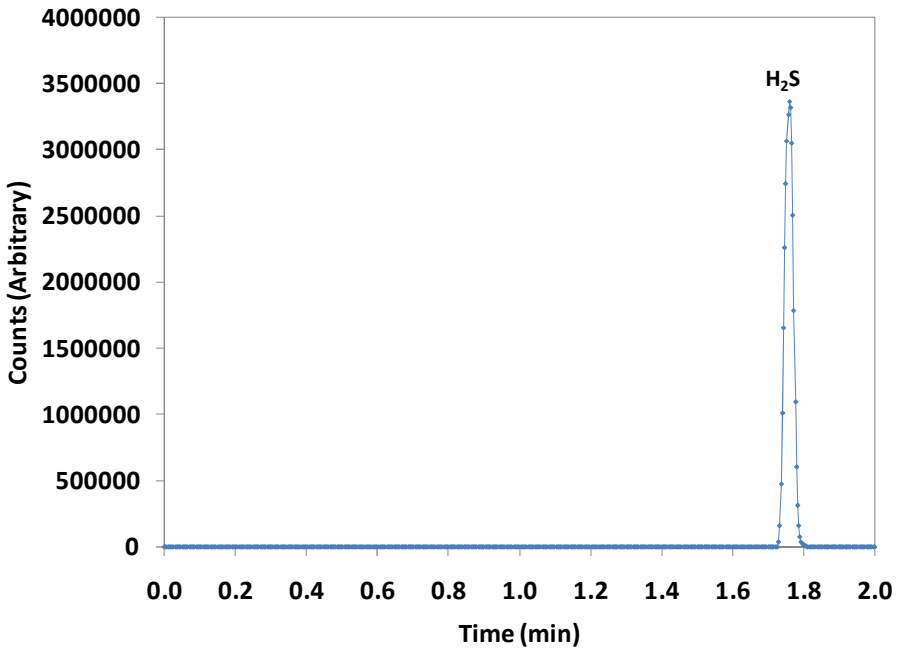

Figure C.3. Sample chromatograph of 5 ppm H_2S in 62% H_2, 37% CO_2, and 1% CO.

Only the H_2S peak is visible since the other gases have no photo-emission in the detector range. The calibration curve for H_2S in the range of 0.5 – 5 ppmv was conducted by Chen (2011) and for this study as shown in Figure C.4.

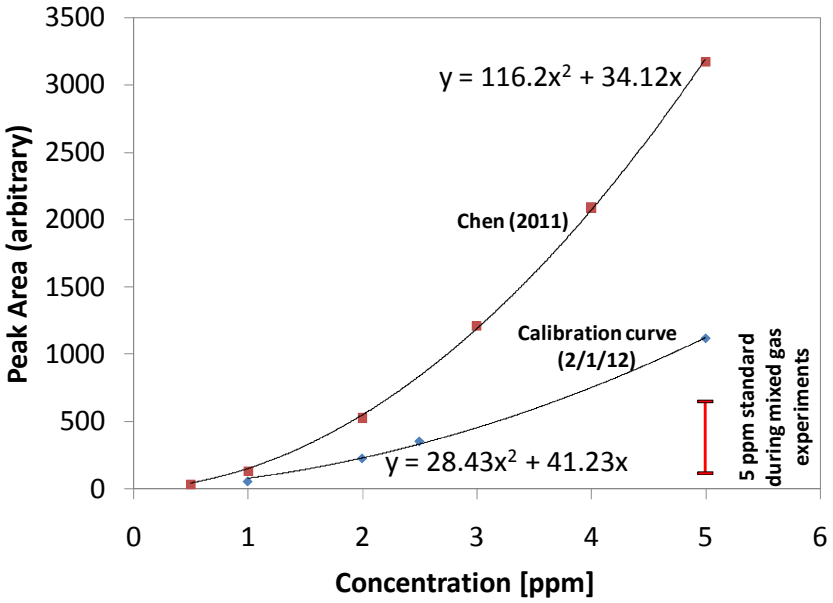

Figure C.4. Calibration curves for H_2S in H_2 with high sensitivity detector setting (conducted for this study {2/1/12} and conducted by Chen {2011}).

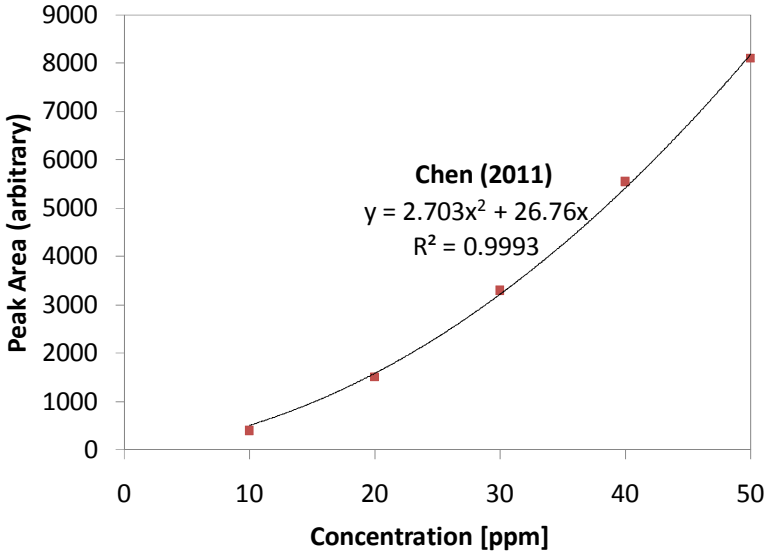

Figure C.5. Calibration curve for H_2S in H_2 with low sensitivity detector setting (conducted by Chen {2011}).

As can be seen from Figure C.4, the calibration curve measured in this study was significantly (approximately 50%) below that measured by Chen (2011). Additionally, standard samples (5 ppmv H_2S in H_2) which were run before and after mixed gas and WGS reaction samples had peak areas significantly (40 – 90%) below that. The discrepancy was potentially caused by decreased sensivity of the detector due to fouling and dust over time. The standard samples measured during the experiments were used to scale the peak area before applying the calibration curve. The error inherent in this method may have been high.

APPENDIX D: SYNTHESIS AND CHARACTERIZATION DETAILS FOR ALL MEMBRANES

Table D.1. Synthesis details of all membranes utilized in this study.

Membrane	Support provider	Support type	Area	Surface pore size	Oxidation	Grading		
		(nominal - μm)	[cm^2]	[μm]	[°C]	Material (Size, μm)	Pd-glue [μm]	Application Method
AA-1	Mott	$PI_{0.1\ um}$	23.5	10	700	-	-	-
AA-2	Mott	$PI_{0.1\ um}$	23.5	10	700	Al_2O_3 (0.01 – 1.0)	<1	Vacuum
AA-3	Mott	$PI_{0.1\ um}$	23.5	10	700	Al_2O_3 (0.01 – 1.0)	-	Vacuum
AA-4	Mott	$PI_{0.1\ um}$	23.5	10	700	Al_2O_3 (0.01 – 1.0)	2.4	Vacuum
AA-4R	Mott	$PI_{0.1\ um}$	23.5	10	700	Al_2O_3 (0.01 – 1.0)	2.4	Vacuum
AA-5	Mott	$PI_{0.1\ um}$	23.5	10	700	Al_2O_3 (0.01 – 1.0)	5.7	Vacuum
AA-6	Mott	$PI_{0.1\ um}$	23.5	10	700	Al_2O_3 (0.01 – 1.0)	5.4	Vacuum
AA-6R	Mott	$PI_{0.1\ um}$	23.5	10	700	Al_2O_3 (0.01 – 1.0)	5.4	Vacuum
AA-7	Mott	$PI_{0.1\ um}$	23.5	10	700	Al_2O_3 (0.01 – 1.0)	2.7	Vacuum
AA-7R	Mott	$PI_{0.1\ um}$	23.5	10	700	Al_2O_3 (0.01 – 1.0)	2.7	Vacuum
AA-8	Mott	$PI_{0.1\ um}$	23.5	10	700	Al_2O_3 (0.01 – 1.0)	1.2	Vacuum
AA-8R	Mott	$PI_{0.1\ um}$	23.5	10	700	Al_2O_3 (0.01 – 1.0)	1.2	Vacuum
AA-8RR	Mott	$PI_{0.1\ um}$	23.5	10	700	Al_2O_3 (0.01 – 1.0)	1.2	Vacuum
AA-8RRR	Mott	$PI_{0.1\ um}$	23.5	10	700	Al_2O_3 (0.01 – 1.0)	1.2	Vacuum
AA-9	Chand Eisenmann	$PSS310_{0.2\ um}$	23.5	Unknown	550	Al_2O_3 (0.01 – 1.0)	2.8	Vacuum
AA-10	Chand Eisenmann	$PSS310_{0.2\ um}$	23.5	Unknown	550	Al_2O_3 (0.01 – 1.0)	3.0	Vacuum
AA-11	Chand Eisenmann	$PSS310_{0.2\ um}$	23.5	Unknown	600	Al_2O_3 (0.01 – 1.0)	2.6	Vacuum
AA-12	Chand Eisenmann	$PSS316L_{0.2\ um}$	23.5	15	600	Al_2O_3 (0.01 – 1.0)	<1	Vacuum
AA-12R	Chand Eisenmann	$PSS316L_{0.2\ um}$	23.5	15	600	Al_2O_3 (0.01 – 1.0)	<1	Vacuum
AA-13	Chand Eisenmann	$PSS316L_{0.2\ um}$	23.5	15	600	Al_2O_3 (0.01 – 1.0)	<1	Vacuum
AA-14	Chand Eisenmann	$PSS316L_{0.2\ um}$	23.5	15	600	$Al(OH)_3$	None	Vacuum, brushing
AA-14R	Chand Eisenmann	$PSS316L_{0.2\ um}$	23.5	15	600	$Al(OH)_3$	None	Vacuum, brushing
AA-15	Chand Eisenmann	$PSS316L_{0.2\ um}$	23.5	15	600	$Al(OH)_3$	None	Vacuum, brushing
AA-16	Chand Eisenmann	$PH_{0.1\ um}$	23.5	50	700	Al_2O_3 (0.01 – 1.0)	1.0	Vacuum
AA-17	Chand Eisenmann	$PH_{0.1\ um}$	23.5	50	800	$Al(OH)_3$	None	Vacuum, brushing
AA-18	Chand Eisenmann	$PSS316L_{0.1\ um}$	23.5	10	600	Al_2O_3 (0.01 – 1.0)	1.0	Vacuum
AA-19	Chand Eisenmann	$PSS316L_{0.1\ um}$	23.5	10	600	Al_2O_3 (0.01 – 1.0)	1.0	Vacuum
AA-20	Chand Eisenmann	$PSS316L_{0.2\ um}$	23.5	15	600	Al_2O_3 (0.01 – 1.0)	2.2	Vacuum
AA-21	Chand Eisenmann	$PSS316L_{0.2\ um}$	23.5	15	600	Al_2O_3 (0.01 – 1.0)	1.5	Vacuum
AA-22	Chand Eisenmann	$PH_{0.1\ um}$	23.5	50	800	Al_2O_3 (0.01 – 5.0)	4.4	Vacuum
AA-23	Chand Eisenmann	$PSS316L_{0.1\ um}$	23.5	10	600	Al_2O_3 (0.01 – 5.0)	1.0	Vacuum
AA-24	Chand Eisenmann	$PSS316L_{0.1\ um}$	23.5	10	600	Al_2O_3 (0.01 – 5.0)	2.6	Vacuum
AA-24R	Chand Eisenmann	$PSS316L_{0.1\ um}$	23.5	10	600	Al_2O_3 (0.01 – 5.0)	2.6	Vacuum
AA-25	Chand Eisenmann	$PSS316L_{0.1\ um}$	23.5	10	600	Al_2O_3 (0.01 – 5.0)	3.1	Vacuum
AA-26	Chand Eisenmann	$PH_{0.1\ um}$	23.5	50	500	Al_2O_3/Sol Gel	None	Brushing, calcining
AA-27	Chand Eisenmann	$PSS316L_{0.2\ um}$	23.5	20	500	Al_2O_3/Sol Gel	None	Brushing, calcining
AA-28	Chand Eisenmann	$PSS316L_{0.2\ um}$	23.5	20	500	Al_2O_3/Sol Gel	None	Brushing, calcining
AA-29	Chand Eisenmann	$PSS316L_{0.2\ um}$	23.5	20	600	Al_2O_3 (0.01 – 5.0)	4.0	Vacuum, brushing
AA-30	Chand Eisenmann	$PSS316L_{0.2\ um}$	23.5	20	600	Al_2O_3 (0.01 – 5.0)	2.2	Vacuum, brushing
AA-31	Chand Eisenmann	$PSS316L_{0.2\ um}$	23.5	20	600	Al_2O_3 (0.01 – 5.0)	<1	Vacuum, brushing
AA-32	Chand Eisenmann	$PSS316L_{0.2\ um}$	23.5	20	600	Al_2O_3 (0.01 – 5.0)	1.8	Vacuum, brushing
AA-33	Chand Eisenmann	$PSS316L_{0.2\ um}$	23.5	20	600	Al_2O_3 (0.01 – 5.0)	<1	Vacuum, brushing
AA-34	Chand Eisenmann	$PSS316L_{0.2\ um}$	23.5	20	600	Al_2O_3 (0.01 – 5.0)	1.2	Vacuum, brushing
AA-35	Chand Eisenmann	$PSS316L_{0.2\ um}$	23.5	20	600	Al_2O_3 (0.01 – 10)	1.2	Vacuum, brushing
AA-36	Chand Eisenmann	$PSS316L_{0.2\ um}$	23.5	20	600	Al_2O_3 (0.01 – 10)	1.2	Vacuum, brushing
AA-37	Mott	$PSS316L_{0.2\ um}$	23.5	10	600	Al_2O_3 (0.3 – 3.0)	2.1	Sequential grading
AA-38	Mott	$PSS316L_{0.2\ um}$	23.5	10	600	Al_2O_3 (0.01 – 50)	3.6	Sequential grading
AA-38R	Mott	$PSS316L_{0.2\ um}$	23.5	10	600	Al_2O_3 (0.01 – 50)	3.6	Sequential grading
AA-39	Mott	$PSS316L_{0.2\ um}$	23.5	10	600	Al_2O_3 (0.01 – 10)	1.2	Sequential grading
AA-40	Mott	$PSS316L_{0.2\ um}$	23.5	10	600	Al_2O_3 (0.01 – 10)	4.5	Sequential grading
AA-40R	Mott	$PSS316L_{0.2\ um}$	23.5	10	600	Al_2O_3 (0.01 – 10)	5.1	Sequential grading
EA-054†	Chand Eisenmann	$PSS310_{0.2\ um}$	23.5	15	750	$Al(OH)_3$	None	Vacuum, brushing
IM-79‡	Chand Eisenmann	$PSS316L_{0.2\ um}$	23.5	10	600	Al_2O_3 (0.01 – 1.0)	4.5	Vacuum
IM-7616C‡	Chand Eisenmann	$PSS316L_{0.2\ um}$	23.5	10	750	Al_2O_3 (0.01 – 1.0)	<1	Vacuum
IM-86b‡	Chand Eisenmann	$PSS316L_{0.2\ um}$	23.5	10	700	Al_2O_3 (0.01 – 1.0)	2.4	Vacuum
RK-16R*	Mott	$PSS310_{0.2\ um}$	23.5	15	600	Al_2O_3 (0.01 – 10)	2.3	Sequential grading

†Prepared partially by Engin Ayturk

‡Prepared by Ivan Mardilovich

*Prepared by Reyyan Koc

Table D.1 (continued).

Membrane	Intermediate layer	Dense Pd-layer	Other details	Post-treatments	Overall thickness
	Material (Thickness, μm)	Gravimetric [μm]			[μm]
AA-1	-	10.8	-	-	10.8
AA-2	Pd/Ag (3.3)	9.0	-	-	12.3
AA-3	-	-	Crack observed in support, synthesis aborted	-	-
AA-4	Pd/Ag (4.5)	7.3	-	MT and Pd-plating	14.2
AA-4R	Pd/Ag (4.5)	9.9	AA-4 MT and Pd-plating	-	16.8
AA-5	Pd/Ag (2.7)	9.7			18.1
AA-6	Pd/Ag (2.4)	10.3		MT and Pd-plating	18.1
AA-6R	Pd/Ag (2.4)	8.8	AA-6 MT and Pd-plating		16.6
AA-7	Pd/Ag (2.5)	9.1		MT and Pd-plating	14.3
AA-7R	Pd/Ag (2.5)	9.1	AA-7 MT and Pd-plating		14.3
AA-8	Pd/Ag (3.4)	6.4		MT and Pd-plating	11.0
AA-8R	Pd/Ag (3.4)	7.0	AA-8 MT and Pd-plating	MT and Pd-plating	11.6
AA-8RR	Pd/Ag (3.4)	8.5	AA-8R MT and Pd-plating	MT and Pd-plating	13.1
AA-8RRR	Pd/Ag (3.4)	8.8	AA-8RR MT and Pd-plating		13.4
AA-9	Pd/Ag (3.5)	10.0	High He flux after Pd-plating		16.3
AA-10	Pd/Ag (4.5)	5.8	High He flux after Pd-plating		13.3
AA-11	Pd/Ag (5.7)	5.8	Oxidized after Pd-glue, high He flux after Pd-plating		14.1
AA-12	Pd/Ag (<1)	9.9	Weak Pd/Ag layer	MT and Pd-plating	10.5
AA-12R	Pd/Ag (<1)	12.1	AA-12 MT and Pd-plating		12.7
AA-13	Pd/Ag (<1)	8.7	Weak Pd/Ag layer		8.7
AA-14	None	11.4		3 x Pre-annealing and polishing	11.4
AA-14R	None	12.3	AA-14 MT, buffing, Pd-plating		12.3
AA-15	None	8.3	Ruined by H2 embrittlement	3 x Pre-annealing and polishing	8.3
AA-16	Pd/Ag (10.0)	-	No change in He flux after Pd/Ag		11.0
AA-17	None	4.7	No change in He flux after Pd		4.7
AA-18	Pd/Ag (6.0)	12.6	Weld defects	Annealing and polishing	19.6
AA-19	Pd/Ag (6.1)	-	No change in He flux after Pd/Ag		7.1
AA-20	Pd/Ag (6.8)	13.3	50% of support was non-uniform	180 μm dense Cu on 50%	22.3
AA-21	Pd/Ag (4.8)	15.7		Annealing and polishing	22.0
AA-22	Pd/Ag (<1)	10.6	Weak Pd/Ag layer		13.5
AA-23	Pd/Ag (<1)	3.1	Weak Pd/Ag layer		4.1
AA-24	Pd/Ag (6.2)	6.9		Annealing @690^{0}C and polishing	15.7
AA-24R	Pd/Ag (6.2)	7.4	AA-24 MT and Pd-plating	Annealing @690^{0}C and polishing	16.2
AA-25	Pd/Ag (9)	8.5		Annealing and polishing	20.6
AA-26	None	12.8	Peeling occurred, regraded before calcining		12.8
AA-27	None	4.2	Peeling occurred, regraded before calcining		4.2
AA-28	None	-	Peeling occurred, regraded before calcining		-
AA-29	Pd/Ag (<1)	9.3	Graded, Pd/Ag, graded again		13.3
AA-30	Pd/Ag (<1)	9.5	Graded, Pd/Ag, graded again		11.7
AA-31	Pd/Ag (1.8)	6.8	Graded, 2 x Pd/Ag		8.6
AA-32	Pd/Ag (6.2)	8.4	Graded, 2 x Pd/Ag		16.4
AA-33	Pd/Ag (3.0)	3.8	Graded, 2 x Pd/Ag	Attempted Cr-plating	7.7
AA-34	Pd/Ag (2.7)	4.1	Graded, 2 x Pd/Ag		8.0
AA-35	Pd/Ag (2.3)	4.8	2 x Grading, Pd/Ag		8.3
AA-36	Pd/Ag (2.7)	4.7	2 x Grading, Pd/Ag		8.6
AA-37	-	3.9	Peeling occurred on annealing		6.0
AA-38	-	1.5	1 heavy polishing treatment		5.1
AA-38R	-	4.4	AA-38 MT and Pd-plating		8.0
AA-39	-	2.7	Ni weld plating	0.6 μm Ag (13%wt)	4.5
AA-40	-	1.5			6.0
AA-40R	-	2.0	1 heavy polishing treatment, AA-40 MT and Pd	0.7 μm Au (9%wt)	7.9
EA-054†	None	9.3	Weld defects		9.3
IM-79‡	Pd/Ag (12.2)	10.2	heavy polishing, 4 x Pd/Ag		26.9
IM-7616C‡	Pd/Ag (5.6)	17.3			23.5
IM-86b‡	Pd/Ag (1.0)	7.5	heavy polishing, 2 x Pd/Ag		10.9
RK-16R*	-	6.0	Tested first by Reyyan Koc		8.3

†Prepared partially by Engin Ayturk
‡Prepared by Ivan Mardilovich
*Prepared by Reyyan Koc

Table D.1 (continued).

Membrane	Testing time	H_2 permeance [$m^3/m^2h*atm^{0.5}$]					E_A	Initial leak	Leak after 50 h	Initial selectivity	Leak grow th rate in H_2
	[h]	300°C	350°C	400°C	450°C	500°C	[kJ/mol]	[m^3/m^2-h-atm]	[m^3/m^2-h-atm]	[F_{H2}/F_{He}]	400°C [m^3/m^2-atm-h^2]
AA-1	500	-	12.3	15.3	18.7	-	14.37	0.000200	-	-	-
AA-2	300	23.5	27.2	33	38.1	41.1	10.82	0.003275	0.062848	125	-
AA-3							Not tested				
AA-4	250	8	-	30	-	39.5	16.85	0.000200	0.007660	13,000	-
AA-4R	100	-	-	24.7	-	-	-	0.000200	0.000200	71,600	-
AA-5	1310	11.8	14.5	18.5	21	-	11.01	0.000613	0.002400	4600	-
AA-6	2000	13.3	17.3	21.3	25.3	-	14.74	0.000200	0.001864	7100	-
AA-6R	1400	-	26.9	31.5	36.7	-	11.61	0.000200	0.000740	2,500	-
AA-7	250	17.7	21.9	23.0	29.3	-	10.67	0.000843	0.004213	14,400	-
AA-7R	350	-	-	-	27.1	-	-	0.000460	0.002272	11,600	-
AA-8	320	20.7	23.8	27.8	33.5	-	10.87	0.000332	0.001251	41,800	-
AA-8R	770	-	22.7	26.9	32.4	-	15.17	0.000200	0.000996	13,400	-
AA-8RR	1050	-	23.1	28.4	32.6	-	12.96	0.000200	0.002145	6300	-
AA-8RRR	1280	-	-	-	33.4	-	-	0.000200	0.000306	43,600	-
AA-9							Not tested				
AA-10							Not tested				
AA-11							Not tested				
AA-12	175	-	18.3	23.1	29.0	-	13.98	0.000200	0.005004	2450	-
AA-12R	125	-	-	-	36.4	-	-	0.000200	0.004366	3500	-
AA-13							Not tested				
AA-14	300	-	20.2	24.1	28.8	-	13.11	0.000536	0.000919	9840	-
AA-14R	125	-	19.1	22.7	26.2	-	11.84	0.020706	0.027830	575	-
AA-15							Not tested				
AA-16							Not tested				
AA-17							Not tested				
AA-18	450	-	10.6	14.5	18.2	-	20.23	0.003574	0.006153	2000	-
AA-19							Not tested				
AA-20							Not tested				
AA-21	864	14.3	17.2	20.2	23.7	-	12.97	0.004774	0.006689	1245	8.630E-06
AA-22	150	-	19.8	25.0	37.0	-	23.12	0.009702	0.014911	850	-
AA-23							Not tested				
AA-24	220	-	19.5	24.2	28.5	-	14.17	0.010468	0.012511	670	-
AA-24R	860	-	-	28.5	-	-	-	0.000894	0.001404	12,700	2.911E-06
AA-25	170	-	18.2	28.8	37.9	-	27.63	0.000945	0.006740	12,600	-
AA-26	290	-	12.6	17.8	22.0	26.3	19.54	0.013583	0.024587	385	1.121E-04
AA-27							Not tested				
AA-28							Not tested				
AA-29	1100	-	20.0	24.1	27.6	-	12.07	0.001251	0.003319	9100	4.596E-06
AA-30	2500	-	-	28.6	-	-	-	0.003753	0.004238	2960	3.013E-05
AA-31	780	-	-	22.0	-	-	-	0.016851	0.021702	540	5.643E-06
AA-32							Not tested				
AA-33							Not tested				
AA-34							Not tested				
AA-35							Not tested				
AA-36							Not tested				
AA-37							Not tested				
AA-38	215	-	52.6	61.7	66.8	-	9.00	0.002630	0.003753	10,500	-
AA-38R	860	-	-	41.2	-	-	-	0.000200	0.000200	75,000	6.281E-06
AA-39	290	-	-	19.0	-	30.0	-	0.024000	0.029872	345	-
AA-40	215	56.1	-	62.0	-	86.5	7.71	0.044936	0.081702	570	-
AA-40R	970	-	-	38.0	-	-	-	0.000587	0.001353	25,000	1.254E-05
EA-054†							Not tested				
IM-79‡	1800	-	-	23.2	26.9	-	-	0.000536	0.001302	17,000	1.441E-06
IM-7616C‡	450	-	2.6	-	2.9	-	-	0.023234	0.059745	35	-
IM-86b‡	2250	-	-	33.7	35.0	-	-	0.003830	0.005004	3770	1.910E-06
RK-16R*	170	-	-	37.5	-	-	-	0.013300	0.016300	1166	2.496E-05

†Prepared partially by Engin Ayturk

‡Prepared by Ivan Mardilovich

*Prepared by Reyyan Koc

Table D.1 (continued).

Membrane	Leak growth rate in H_2 450°C [m^3/m^2-atm-h^2]	Intermediate selectivity [F_{H2}/F_{He}]	Mixed or WGS conditions conditions, time	Leak growth rate [m^3/m^2-atm-h^2]	Final selectivity [F_{H2}/F_{He}]
AA-1	-	-	-	-	-
AA-2	-	105	-	-	-
AA-3			Not tested		
AA-4	-	125	-	-	-
AA-4R	-	54,600	-	-	-
AA-5	-	2150	WGS, 400 - 450°C, 24 h	1.300E-03	2800
AA-6	4.468E-05	2120	Mixed gas, 350 - 450°C,	3.600E-04	1100
AA-6R	2.783E-05	1110	WGS, 350 - 500°C, 35 h	1.100E-02	840
AA-7	-	880	-	-	-
AA-7R	-	2100	WGS, 450°C, 24 h	0, 0.146	25
AA-8	-	2560	-	-	-
AA-8R	-	-	WGS, 350 - 450°C, 72 h	2.580E-02	174
AA-8RR	2.068E-05	4000	WGS, 450°C, 72 h	8.100E-03	305
AA-8RRR	5.617E-04	500	-	-	-
AA-9			Not tested		
AA-10			Not tested		
AA-11			Not tested		
AA-12	-	1370	-	-	-
AA-12R	3.906E-04	235	-	-	-
AA-13			Not tested		
AA-14	-	190	-	-	-
AA-14R	-	300	-	-	-
AA-15			Not tested		
AA-16			Not tested		
AA-17			Not tested		
AA-18	6.587E-06	420	-	-	-
AA-19			Not tested		
AA-20			Not tested		
AA-21	2.265E-05	765	H_2/H_2O, 400°C, 70 h	1.900E-02	175
AA-22	-	80	-	-	-
AA-23			Not tested		
AA-24	-	200	-	-	-
AA-24R	-	4200	WGS, 400°C, 110 h	1.000E-02	365
AA-25	-	78	-	-	-
AA-26	2.436E-04	110	-	-	-
AA-27			Not tested		
AA-28			Not tested		
AA-29	-	1710	-	-	-
AA-30	-	825	WGS, 400°C, 1000 h	1.100E-03	240
AA-31	-	250	-	-	-
AA-32			Not tested		
AA-33			Not tested		
AA-34			Not tested		
AA-35			Not tested		
AA-36			Not tested		
AA-37			Not tested		
AA-38	2.377E-05	3900	-	-	-
AA-38R	-	75,000	WGS, 400°C, 440 h	5.200E-04	2550
AA-39	-	155	-	-	-
AA-40	-	200	-	-	-
AA-40R	-	1600	Syngas, 400°C, 0 - 20 ppm	7.450E-05	340
EA-054†			Not tested		
IM-79‡	2.911E-05	1350	WGS, 400°C, 65 h	3.750E-04	330
IM-7616C‡	-	5	-	-	-
IM-86b‡	-	2130	H_2/H_2O, 400°C, 190 h	1.000E-04	20
RK-16R*	-	920	Syngas, 400°C, 0 - 2.5 ppm	6.310E-05	675

†Prepared partially by Engin Ayturk

‡Prepared by Ivan Mardilovich

*Prepared by Reyyan Koc

APPENDIX E: CODE FOR MODELING

The following Matlab® code was utilized to solve the 1-D model simulations conducted in this study. The model which the code is based on was discussed in Chapter 5. The code is structured as follows:

1. Constants: system specifications, catalyst properties, membrane properties, and temperature

2. Feed conditions: flow rate, pressure, and gas composition

3. Thermodynamic and rate calculations: equilibrium constant and reaction rate constant

4. Flow dynamics: Reynolds number, Schmidt number, velocity, viscosity, and diffusivity

5. Reaction and separation coefficients: dimensionless rate constant and mass transfer coefficients for membrane and gas boundary layer

6. Integration: Integration of function containing steady state mass balance equations from $\zeta = 0$ to 1. Integration was conducted with the Matlab® algorithm ODE23S, a stiff differential equation solver which utilizes the Runge-Kutta method.

7. Plotting of the results: Generally the results were first viewed by plotting in Matlab®, then transferred to Excel® for preparation of figures.

When run, the code initially calculated the H_2 flux and CO conversion for each of 200 points along the reactor length. For most cases, only the overall CO conversion and H_2 recovery were saved from each set of initial conditions.

```
%Program to simulate the WGS CMR via a 1-D model, incorporating iron-chrome
%oxide catalyst rate law, gas boundary layer mass transfer resistance and Pd-
%surface inhibition. Program is currently configured to vary GHSV from 50 to
3500 h-1
%Written by Alex Augustine

global k m n o p K B C D PT thT thH2O thH2 thCO2 thHe Pp a b c;
q = 40;              %Simulation runs 'q' times with 1 variable changing
X = zeros(q,3);      %Matrix to store results from each run
for i = 1:1:q;

% 1. Constants
    d = 10;               %Pd-layer thickness (um)
    r = 0.5*2.54/(2*100);    %membrane tube radius (m)
    L = 0.065;                %membrane tube length (m)
    Ri = (27/32)*2.54/(2*100);    %reactor shell radius (m)
    Ap = pi*2*r*L;       %membrane surface area (m^2)
    Ac = pi*(Ri^2-r^2); %catalyst bed cross section (m^2)
    phi = 0.47;          %catalyst void fraction
    roc = 2130;          %catalyst bulk density (kg/m^3)
    ro = (1-phi)*roc;    %catalyst bed density (kg/m^3)
    T = 400+273;         %temperature (K)
    R = 0.08206;         %ideal gas constant (m^3atm/kmolK)
    Perm = 30.0;        %membrane permeance (m^3/m^2hatm^0.5

% 2. Feed conditions
    FCO = 0.00001*i;     %feed rate of CO (kmol/hr)
    thH2O = 55/19;       %ratio of H2O/CO (-)
    thH2 = 18/19;        %ratio of H2/CO (-)
    thCO2 = 8/19;        %ratio of CO2/CO (-)
    thHe = 0.01;         %ratio of inert He sweep He/CO (-)
    thT = 1+thH2O+thCO2+thH2;   %sum of all feed components (-)
    PT = 14.6;           %feed pressure (atma)
    Pp = 1.0;           %tube-side pressure (atma)

% 3. Thermodynamic and rate calculations
    %Reaction kinetics on Fe/Cr oxide catalyst
    lnk0=11.7;Ea=122;m=1;n=0;o=0;p=0; %Rhodes et al. 2002
    k = exp(lnk0-(Ea/(0.008314*T)))*3600;  %kinetic rate (kmol/kg*h)
    GH2O = -241.74+0.04174*T+7.428*10^-6*T^2;
    GCO = -109.885-0.092218*T+1.454*10^-6*T^2;
    GCO2 = -393.36-0.0038212*T+1.3322*10^-6*T^2;
    G = GCO2-GH2O-GCO;
    K = exp(-G/(0.008314*T));
    a = 101000*((6.626e-34)^3)*exp(149/(0.008314*T))/((T^2.5)*(1.38e-
23)*(6.28*(4.65e-23)*(1.38e-23))^1.5); %CO
    b = 101000*((6.626e-34)^3)*exp(135/(0.008314*T))/((T^2.5)*(1.38e-
23)*(6.28*(2.99e-23)*(1.38e-23))^1.5); %H2O

% 4. Flow dynamics
    v = FCO*thT*22.4/(phi*3600*Ac);  %flow velocity (m/s);
    Di = 0.000026*phi;          %diffusivity, H2 in mixture (m^2/s)
    u = 0.0000254;          %estimated viscosity (kg/m-s)
    car = 0.000175;         %characteristic length (m)
    rho = PT*(28+thH2*2+thCO2*40+thH2O*18)/(thT*1000*R*T)   %density of the
gas mixture (kg/m3)
```

```
%Sherwood number empirical correlation by Wakao and Funazkri
    Sh = 2 + 1.1*((rho*car*v/u)^0.6)*((u/(car*Di))^0.333);

% 5. Reaction and separation coefficients
    B = ro*Ac*L/FCO;            %inverse reaction rate on catalyst kg*h/kmol
    C = Perm*Ap/(FCO*22.4);          %membrane resistance (atm^-0.5)
    D = Sh*Di*Ap*3600/(R*T*FCO*car); %gas boundary layer resistance(atm^-1)

% 6. Integration with Matlab algorithm ODE23s (calls upon function
    %'wgsdot')
    x0 = [0; 0];
    [z,x]=ode23s(@wgsdot, (0:0.005:1), x0);
%saving results from integration
    X(i,1)=FCO*thT*1697000; %saving flow rate as GHSV (h-1)
%kmol/hr * 1697000hr/kmol*hr (13.2mL reactor)
    X(i,2)=x(201,1);
    X(i,3)=x(201,2)/(1+thH2);
end

% 7. Plotting of the results
figure('position',[20, 50, 700, 350]); %define figure dimensions
subplot(1,2,1)                         %generate first figure
plot(X(:,1), X(:,2));                  %plot XCO vs. membrane permeance
xlabel('GHSV (h-1)');
ylabel('CO Conversion');
subplot(1,2,2)                         %generate second figure
plot(X(:,1), X(:,3));                  %plot YH2 vs. membrane permeance
xlabel('GHSV (h-1)');
ylabel('H2 Recovery');
```

The code called upon the following function, ‘wgsdot’ which contained the steady state differential equations to be solved.

```
function [xdot]=wgsdot(z,x)
%function containing the steady state mass balance equations for the 1-D
%simulation 'WGS'

global k m n o p K B C D PT thT thH2O thH2 thCO2 thHe Pp a b c;

%Partial pressure of each species
PH2O = (thH2O-x(1))*PT/(thT-x(2));      %partial pressure of H2O (atma)
PCO = (1-x(1))*PT/(thT-x(2));           %partial pressure of CO (atma)
PH2 = (thH2+x(1)-x(2))*PT/(thT-x(2));   %partial pressure of H2 (atma)
PCO2 = (thCO2+x(1))*PT/(thT-x(2));      %partial pressure of CO2 (atma)
PpH2 = x(2)*Pp/(x(2)+thHe);        %partial pressure of H2 in permeate (atma)

r1 = k*(PCO^m)*(PH2O^n)*(PCO2^o)*(PH2^p)*(PCO*PH2O-PH2*PCO2/K);
%Reaction rate (kmol/kg*h)

%Square root partial pressure of H2 at Pd-surface considering membrane
%resistance, C, and gas boundary layer resistance, D (atm^0.5)
ep = -(0.5*C/D)+0.5*sqrt(((C/D)^2)+4*C*sqrt(PpH2)/D+4*PH2);
```

```
%Correction factor to account for reduction in velocity in the retentate
rgd = D*log((ep^2)/PT+1)*PT/(ep^2);
%Square root partial pressure of H2 at Pd-surface considering removalof H2
ep1 = -(0.5*C/rgd)+0.5*sqrt(((C/rgd)^2)+4*C*sqrt(PpH2)/rgd+4*PH2);

%Empirical surface activity parameters
S = 1/(1+PCO*a+PH2O*b);

%Steady state mass balance equations
dXCO2 = B*r1;              %mass balance of CO (dimensionless)
dYH2 = C*(ep1-PpH2^0.5)*S; %mass balance of H2 (dimensionless)
xdot = [dXCO2; dYH2];   %function definition
```

The following Excel® spreadsheet was utilized to determine the thermodynamic propensity for coke formation in the WGS CMR.

Chemical Equilibrium by Gibbs Energy Minimization (Ma and Shipman, 1972; Lwin, 2000)

Starting Components		C(s)	H2O	CO	CO2	H2	CH4	CH3OH
T(dC)	300	0.00	1.00	1.00	0.00	0.00	0.00	0.00
T (K)	573							
P (atm)	14.4	elements in the system:		C	H	O		
R (kJ/molK)	0.008314	moles of element (bj)		1.00	2.00	2.00		
RT (kJ/mol)	4.764							

	C(s)	H2O	CO	CO2	H2	CH4	CH3OH	
initial est.	0.1	0.5	0.05	0.7	0.2	0.1	0.05	$\sum$ ni
ni (mol)	0	0.498622	0.0001	0.750139197	0.00185678	0.2487608	0.001	1.5005
yi	0	0.3323	0.0001	0.4999	0.0012	0.1658	0.0007	
ΔGf (kJ/mol)	0	-215.384	-162.2485236	-395.1121477	0	-50.8	-162.3	

Atomic Matrix (aji)

	C(s)	H2O	CO	CO2	H2	CH4	CH3OH
C	1	0	1	1	0	1	1
H	0	2	0	0	2	4	4
O	0	1	1	2	0	0	1

C-Balance	1.00
H-Balance	2.00
O-Balance	2.00
$\sum$(ni*ΔG°f,i)	-416.600
nRT*ln(P)	19.066
RT$\sum$(ni*ln(yi))	-7.323
$\sum$G (kJ/mol)	-404.857

Confirmation: When Gibbs energy is minimized,
$\Delta\mu$ = 0, for each reaction

μC(s) (kJ/mol)	0
μH2O (kJ/mol)	-207.93
μCO (kJ/mol)	-195.35
μCO2 (kJ/mol)	-385.71
μH2 (kJ/mol)	-19.19
μXH4 (kJ/mol)	-46.65

Reaction 1: CO + H2O = CO2 + H2
$\Delta\mu 1$ (kJ/mol) -1.6164

Reaction 2: 2CO = CO2 + C(s)
$\Delta\mu 2$ (kJ/mol) 4.9966

Reaction 3: CO + H2 = H2O + C(s)
$\Delta\mu 3$ (kJ/mol) 6.6130

Coke (mol)	0
CH4 (mol)	0.248760804
$\Sigma\Delta\mu$ (kJ/mol)	9.9933

Where n_i was the mols of species *i* which was varied in order to minimize the Gibbs free energy, y_i was the mol fraction of species *i* in the gas phase, ΔG_f was the standard Gibbs free energy of formation for each species. The Excel® Solver algorithm was utilized to minimize $\sum G$ by varying the values of n_i, under the constraint that the mass balance for C, H, and O remained constant. The fugacity of the gas species CO, H_2O, CO_2, and H_2 were 0.997, 0.979, 0.997, and 1.003 respectively at 10 atma and 300°C (Perry and Green, 1997) so the ideal gas law was assumed.